UNITED KINGDOM · CHINA · MALAYSIA

FACULTY OF ENGINEERING
DEPARTMENT OF CIVIL ENGINEERING
CENTRE FOR STRUCTURAL ENGINEERING AND INFORMATICS

ANDRÉ DE ARAÚJO VIEIRA

Strengthening of Existing Reinforced Concrete Structures Against Progressive Collapse

Nottingham,

United Kingdom

2020

This page was left intentionally blank

ANDRÉ DE ARAÚJO VIEIRA

Strengthening of Existing Reinforced Concrete Structures Against Progressive Collapse

Text presented to the Department of Civil Engineering of the University of Nottingham as one of the requisites for obtaining the degree of Doctor of Philosophy in Structural Engineering.

Area: Structural Engineering

Supervisors: Dr. Savvas Triantafyllou

Dr. Tao Liu

Nottingham,

United Kingdom

2020

This page was left intentionally blank

To my family.

This page was left intentionally blank

AKNOWLEDGEMENTS

In the first place, I would like to thank my parents José Nascimento Vieira and Edna de Araújo Vieira, without whom I would have never reached so far. All the support they gave me was essential to keep my mind and soul aligned. Additionally, I would like to thank my brothers, Rafael de Araújo Vieira and Filipe de Araújo Vieira, who always gave me strength to go forward.

Moreover, I would like to thank the Brazilian government for sponsoring me through the Science Without Borders program. The present work was performed thanks to the support of CNPq (National Council for Scientific and Technological Development - Brazil).

Furthermore, I would like to thank the University of Nottingham, for accepting me to conduct this research, and for providing all the resources and support I needed to enrich my work and life quality in UK.

My special thanks to Dr. Savvas Triantaffylou and Dr. Dionysios Bournas, who kindly, patiently and wisely advised me in my way during this program, enhancing the quality of this work to high standard levels. Additionally, special thanks to all the University staff, highlighting here Nigel Rook, Sam Cook, Gary Davies, James Meakin, Balbir Loyla, both Steves, Lee and Michael Langford, who were always helpful and committed with the quality their work, and definitely without whom I would have never finished this work.

Moreover, I would like to thank all the good friends I have made in UK, who have made my experience abroad much more funny and pleasant.

Finally, my very special thanks to my companion, Gabriela Perez, who changed my life course in the very best way; who always gave me support and made me a better version of myself.

This page was left intentionally blank

"Quem sabe um dia a paz
vence a guerra, e viver
será só festejar."

Evandro Rodrigues

This page was left intentionally blank

ABSTRACT

Progressive collapse refers to the catastrophic event of structural collapse caused by an initial action of disproportionately smaller scale. Typical examples of progressive collapse involve total or partial collapse initiating from the failure of a single column. Failure events include the 1968 Ronan Point building collapse in London; the 1995 Murrah Federal building collapse in Oklahoma, and the 2001 World Trade Centre collapse in New York. These events dramatically demonstrated the need for appropriate strengthening strategies to increase the structure's resilience and prevent such failure modes. Textile-Reinforced Mortar (TRM) is a novel structural material proved very effective in strengthening and seismic retrofitting of existing reinforced concrete (RC) structures. TRM comprises a mesh of fibres woven in at least two directions and impregnated with a cement-based mortar. Recently significant research has been conducted towards optimizing the already established Near-Surface-Mounted (NSM) reinforcement strengthening method for the a-seismic retrofitting of Reinforced Concrete (RC) buildings. This technique introduces additional reinforcement in cut grooves opened in the concrete cover and filled with binder material which usually is epoxy resin or cement-based mortar. The hypothesis underpinning this research project is that an appropriate design of TRM and NSM reinforcement can bare significant advantages for strengthening of an existing reinforced concrete structure vis-à-vis progressive collapse. The methodological approach involved an experimental campaign that was suplemented by numerical simulations. In the former, four half-scaled RC frames were tested in the laboratory. The investigated parameters involved the TRM cover length and the type of flexural strengthening employed, i.e., TRM or NSM reinforcement. The results revealed that improved progressive collapse resistance can be achieved with the strengthening techniques adopted, attending to criteria of ductility and energy absorption capacity. Two simulation strategies were adopted, i..e, a micro and a macromodelling simulation procedure. In the former, a detailed 3D finite element commercial software was used, whereas in the latter a component-based model. A parametric study was conducted with the 3D model to investigate the influence of design and numerical factors. The outcome showed that the increased progressive collapse resistance of the frame was maintained on strengthened specimens regardless the parameter assessed. Moreover, the numerical investigations highlighted key indicators of progressive collapse resistance. The component based model was calibrated using the experimental data and the 3D model results and provided a reliable and cost effective simulation procedure. Furthermore, this model presented significative less oscillation when compared to the 3D one.

Keywords: *Progressive Collapse, Strengthening, Column Loss, Textile-Reinforced Mortar, Near-Surface-Mounted Reinforcement, Finite Element Analysis.*

This page was left intentionally blank

TABLE OF CONTENTS

This page was left intentionally blank

LIST OF FIGURES

LIST OF TABLES

This page was left intentionally blank

LIST OF ABBREVIATIONS

CAA	**C**ompressive **A**rch **A**ction
CDP	**C**oncrete **D**amage **P**lasticity
DIF	**D**ynamic **I**ncrease **F**actor
FEM	**F**inite **E**lement **M**ethod
LC	**L**oad **C**ell
MDR	**M**aximum **D**ynamic **R**esponse
NSM	**N**ear-**S**urface-**M**ounted
RC	**R**einforced **C**oncrete
RE	**R**igid **E**lement
SG	**S**train **G**auge
TRM	**T**extile-**R**einforced **M**ortar
UA	**O**utput **V**oltage
UE	**B**ridge **E**xcitation

This page was left intentionally blank

LIST OF SYMBOLS

A	Coefficient applied to the bond-slip curve
A_{anc}	Area of two textile-based anchors
$A_{s,bot}$	Area of steel at the bottom of the beam
$A_{s,eq}$	Equivalent area of steel
$A_{s,int}$	Area of steel at the lateral of the beam
$A_S^{`}$	Area of reinforcing steel carrying compression;
$A^{`}_{s, bot}$	Equivalent area of steel at the bottom of the beam
$A^{`}_{s,int}$	Equivalent area of steel at the lateral of the beam
$A^{`}_{s,TRM,bot}$	Steel area equivalent to the TRM at the bottom of the beam
$A^{`}_{s,TRM,lat}$	Steel area equivalent to the TRM at the lateral of the beam
C_C	Concrete compression resultant
C_{clear}	Distance between ribs on the reinforcement
C_{Con}	Column rotation on the control specimen
C_{R1}	Factor controlling the transition between elastic and plastic branches of the steel
C_{R2}	Factor controlling the transition between elastic and plastic branches of the steel
C_{St}	Column rotation on the strengthened specimen
$C_S^{`}$	Steel compression resultant
d	Depth to the tension reinforcement;
$d^{`}$	Depth to centroid of compression reinforcement
d_b	Diameter of the bar
d_c	Concrete damage in compression;
d_{CON}	Vertical deflection of the control specimen

d_{st}	Vertical deflection of the strengthened specimen
d_t	Concrete damage in tension
E_{cm}	Concrete secant modulus of elasticity
E_M	Mortar elastic modulus
E_0	Concrete elastic modulus
E_S	Steel Elastic modulus
$E_{s,hard}$	Steel stiffness at hardening phase
E_{sec}	Concrete secant modulus of elasticity
E_T	Textile elastic modulus
Ets	Concrete tensile softening stiffness
f_{ck}	Concrete characteristic value of compressive strength
f_{cm}	Concrete mean compressive strength
F_{Con}	Flexural rotation on the control specimen
$f`_c$	Concrete maximum compressive strength
$f_{f,anc}$	Tensile resistance of the textile-based anchor
$f_{fe,anc}$	Effective tensile resistance of the textile-based anchor
fpc	Maximum concrete compressive strength of the core
fpcU	Concrete crush strength of the core
fpc_{un}	Maximum concrete compressive strength of the cover
$fpcU_{un}$	Concrete crush strength of the cover
F_{St}	Flexural rotation on the strengthened specimen
f_T	Textile tensile strength
fts	Maximum concrete tensile strength of the core
fts_{un}	Maximum concrete tensile strength of the cover
f'_t	Concrete maximum tensile strength

F_t^{NSM}	Tensile capacity of the set of NSM strengthening
F_t^{TRM}	Tensile capacity of the set of textile-based anchors
f_y	Steel yield strength
G	Flow potential
G_f	Fracture energy
h_0	Distance between the top and bottom lines of potentiometers at the beam
h_w	High of the beam below the slab
l	Transmission length of the steel
I_x	Moment of Inertia around x axis
j	Factor applied to the distance between compression and tension resultants
K_1	Spring identification
K_2	Spring identification
K_c	Parameter adjusting the concrete yield surface in the deviatoric plane
k_{fc}	Ratio of core to the cover concrete strengths
k_{res}	Ratio of residual/ultimate to maximum stress
l_0	Specimen length
l_c	Element size
M_{RD}^{NSM}	Resultant moment capacity with usage of NSM strengthening
M_{RD}^{t}	Target moment capacity
$\overline{p}$	Hydrostatic pressure
P_{CON}	Vertical load of the control specimen
$P_{CON,b}$	Horizontal load on the control specimen at the beam load cells
$P_{CON,tc}$	Horizontal load on the control specimen at the top load cells

P_f	First peak load at the vertical 'Load vs Deflection' curve
P_{med}	Next peak load after P_f at the vertical 'Load vs Deflection' curve
P_{min}	Minimum load after P_f at the vertical 'Load vs Deflection' curve
P_{St}	Vertical load of the strengthened specimen
$P_{St,b}$	Horizontal load on the strengthened specimen at the beam load cells
$P_{St,tc}$	Horizontal load on the strengthened specimen at the top load cells
P_{TCA}	Maximum load at TCA phase at the vertical 'Load vs Deflection' curve
$\overline{q}$	Von Misses effective stress
R_0	Factor controlling the transition between elastic and plastic branches of the steel
R_1	Factor applied to the steel tensile stress
s	Relative displacement between concrete and steel
s_d	Distance of dowels of two consecutive textile-based anchors
S_1	Initial distance between column and the first line of potentiometers
s_1	Limit value of relative displacement between concrete and steel
S_2	Initial distance between first and second lines of potentiometers
s_2	Limit value of relative displacement between concrete and steel
s_3	Limit value of relative displacement between concrete and steel
T_{Con}	Total rotation on the control specimen
Tensoft	Factor affecting the Ets
T_{St}	Total rotation on the strengthened specimen
u_t^{ck}	Crack displacement of the concrete
u_t^{pl}	Plastic displacement in tension of the concrete
V_f	Aimed shear force

w	Width of the frame member
w_c	Compression recovery parameter on CDP
w_t	Tension recovery parameter on CDP
α	Dimensionless constant
β	Dimensionless constant
β_s	Steel hardening factor
β_u	Scale factor to account for the use of a uniform concrete compressive stress distribution in place of the true stress distribution;
γ	Parameter applied to the algebraically maximum principal stress
Δ	Potentiometer reading
δ	Spring displacement
$\Delta_{failure}$	Vertical deflection of the frame at the failure load
ΔS_1	Variation of S_1 at the outer side of the curvature
$\Delta S_1'$	Variation of S_1 at the inner side of the curvature
ΔS_2	Variation of S_2 at the outer side of the curvature
$\Delta S_2'$	Variation of S_2 at the inner side of the curvature
Δ_{yield}	Vertical deflection of the frame at the yield point
ε_0	Concrete strain at maximum strength
ε_{c0}	Concrete strain at maximum strength of the core
ε_{0c}^{el}	Concrete compressive elastic strain
ε_c^{el}	Compressive strain in the concrete after unloading, considering the damage
$\tilde{\varepsilon}_c^{in}$	Concrete compressive inelastic strain
$\tilde{\varepsilon}_c^{pl}$	Concrete compressive plastic strain
ε_{c0un}	Concrete strain at maximum strength of the cover

ε_{cU}	Concrete strain at ultimate stress core
ε_{cr}	Concrete tensile crack strain
ε_{cUun}	Concrete strain at ultimate stress cover
$\varepsilon_{s,eq}$	Steel equivalent strain
$\varepsilon_{s,eq1}$	First limit value for the steel equivalent strain
$\varepsilon_{s,eq2}$	Second limit value for the steel equivalent strain
$\varepsilon_{s,eq3}$	Third limit value for the steel equivalent strain
ε_{0t}^{el}	Concrete tensile elastic strain
ε_{t}^{el}	Tensile strain in the concrete after unloading, considering the damage
$\tilde{\varepsilon}_{t}^{ck}$	Concrete tensile crack strain
$\tilde{\varepsilon}_{t}^{pl}$	Concrete tensile plastic strain
ε_{u}	Steel ultimate strain
$\varepsilon_{u,eq}$	Steel equivalent ultimate strain
ε_{y}	Steel yield strain
$\varepsilon_{y,eq}$	Steel equivalent yield strain
η_{e}	Correction factor for the textile-based anchor tensile resistance
θ	Fan angle of the textile-based anchor
θ_{f}	Flexural Rotation
θ_{tot}	Total Rotation
λ	Ratio between unloading slope at ε_{cU} and initial slope E_0
ν	Poisson's ratio
$\bar{\sigma}\|_0$	Initial concrete yield stress
σ_{b0}	Biaxial compressive yield stress of the concrete
σ_{c0}	Concrete maximum compressive strength

σ_c	Concrete compressive strength
σ_{cu}	Concrete ultimate compressive strength
$\hat{\bar{\sigma}}_{max}$	Algebraically maximum principal stress
σ_s	Steel tensile stress
$\sigma_{s,1}$	Steel tensile stress between 0 and $\varepsilon_{s,eq1}$
$\sigma_{s,f}$	Final steel tensile strength
$\sigma_{s,max}$	Maximum steel tensile stress
σ_{t0}	Concrete maximum tensile strength
σ_t	Concrete tensile strength
τ_{b0}	Bond stress between concrete and steel
τ_{bf}	Final bond stress between concrete and steel
τ_{bmax}	Maximum bond stress between concrete and steel
τ_1	Bond stress between s=0 and s=s_1
ψ	Dilation angle
ϵ	Eccentricity
$Ø_{eq}$	Equivalent diameter of the reinforcement
$\langle x \rangle$	Macaulay bracket function

This page was left intentionally blank

CHAPTER 1 INTRODUCTION

1.1 Problem Statement

The term progressive collapse (also called disproportionate collapse), refers to the type of structural failure where small and locally defined initial damage spreads through the structure and rapidly evolves into a disproportionally larger event that may lead to total or partial collapse of the structure (American Society of Civil Engineers (ASCE), 2005). According to the USA General Services Administration (GSA, 2003), "Progressive collapse is a situation where local failure of a primary structural component leads to the collapse of adjoining members which, in turn, leads to additional collapse".

The 1968 Ronan Point collapse in London, UK was the first ever registered case of disproportionate collapse leading the to definition of the term and hence becoming a milestone on the design of structures against this failure mechanism. From this point onwards, structural engineers and governmental user agencies provided design guidelines and criteria (GSA, 2003, Eurocode, 2006, Committee and Standardization, 2008, DoD, 2009) with the objective of mitigating the susceptibility of buildings to this form of failure (Nair, 2006).

In the Ronan Point event, a gas explosion in the kitchen of one apartment on the 18th floor blew out an outer panel. The loss of a bearing wall in this story caused the progressive collapse of floors nineteen to twenty-two. The dynamic loading imparted by the falling debris caused the progressive collapse of the floors below (Figure 1.1) (NIST(Ellingwood et al., 2007)). In this case, the effect was quite out of proportion to the cause, i.e., the initial damage. The walls of the Ronan Point were unreinforced and joint forces were resisted only by bond, friction and gravity. With the explosion, this resistance was reduced considerably or even reversed the gravity loads. So, the friction force and bond between the panels were eliminated leading to failure (Ellingwood et al., 2007). The authors stated that the build design attended to all standard requisites of that period. These standards presented detailed requirements for the design of individual members but provided little guidance for the stability design of all structural system.

Another case of progressive collapse is the Murrah Federal Building in Oklahoma, United States, 1996, where the explosion of a truck lead to the collapse of great part of structure. Other known cases are the Twin Towers in the United States of America on September 11, 2001, and the attack on the Pentagon, also in the United States on the same date.

Figure 1.1 - Ronan Point partial collapse. (Pearson and Delatte, 2005)

Kiakojouri et al. (2020) have listed the major structural failures since 1968 (Table 1.1) where most of the buildings were designed prior 1968. It becomes essential to note that standards conceived before the Ronan Point incident did not consider progressive collapse as a potential failure mode in their provisions. A large number of pre-1968 RC buildings are still operational and in many cases involve public buildings (schools, hotels, museums, hospital, government administration buildings). Hence, strengthening of such structures against progressive collapse becomes a timely and pressing design challenge. In this work pre-1968 buildings are referred to as old buildings.

Incident	Year	Location	Structural System	N$_o$. floor	Triggering Event	Casuality D/I	Damage
Ronan Point	1968	London, UK	Large-panel	22	Gas explosion	4/17	Partial
Skyline Plaza Towers	1973	Farifax, US	RC frame	26	Premature shoring removal	14/34	Partial
Hotel New World	1986	Little India, Singapore	RC frame	6	Static fatigue	33/17	Total
L'ambiance Plaza	1987	Bridgeport, US	Steel frame/ Lift-slab	16	Failure of lifting system	28D	Total
Alfred P. Murrah Federal Bldg.	1995	Oklahoma City,US	RC frame with shear wall	9	Truck bomb	169/800	Total
Sampoong Dept. Store	1995	Seoul, South Korea	RC frame	5	Overload	502/937	Partial
Khobar Towers	1996	Khobar, Saudit Arabia	Precast Concrete Bldg.	8	Bomb explosion	20/372	Partial
WTC Bldg 1	2001	New York, US	Steel frame	110	Aircraft impact and fire	1462	Total
WTC Bldg 2	2001	New York, US	Steel frame	110	Aircraft impact and fire	630	Total
WTC Bldg 7	2001	New York, US	Steel frame	47	Debris impact and fire	0	Total
Windsor Tower	2005	Madrid, Spain	Steel frame – RC core	32	Fire	71	Partial
Pyne Gould Corporation Bldg.	2011	Christchurch, New Zeland	RC frame	5	Earthquake	18/28	Total
Rana Plaza	2013	Savar, Bangladesh	RC frame	8	Misuse, overload	1129/2515	Partial
Plasco Bldg.	2017	Tehran, Iran	Steel frame	17	Fire	22/235	Total

Table 1.1 – Major structural failures since 1968 (Kiakojouri et al., 2020).

As presented in Table 1.1, many different causes can be the source of the disproportional propagation of the failure through the building, depending also on its structural material. The loss of a load carrying member is a potential cause to a disproportional collapse. In this event the redistribution of internal forces propagates the damage what possibly leads to failure rather disproportional.

When a column is removed, the frame of which this column was part achieves large displacements. With the evolution of the vertical deflection, internal mechanisms of the system, additional to the flexural resistance, are developed as last resource of resistance against the total failure (Figure 1.2). In the beam those mechanisms are the Compressive Arch Action (CAA) (Figure 1.2a) and the Tensile Catenary Action (TCA) (Figure 1.2b).

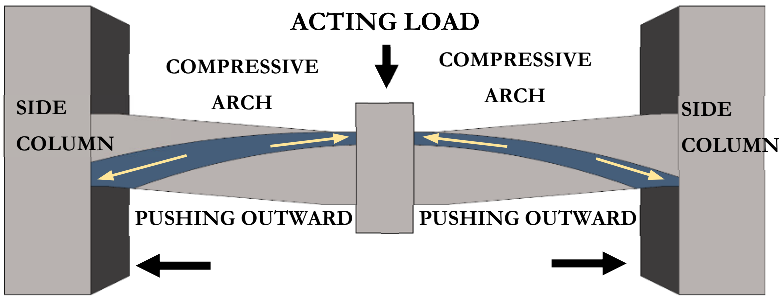

a)

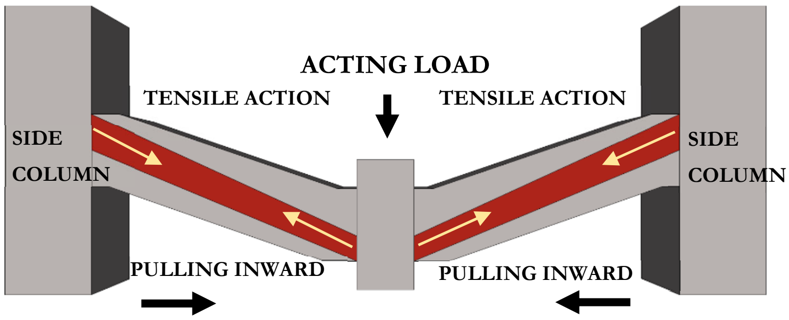

b)

Figure 1.2 – Internal mechanisms of defense of the beam a) CAA b) TCA.

This dynamic event is composed by a set of localized failures which are further connected with the evolution of the vertical deflection of the column above of the removed one. Once the load above the removed column has no more a reaction to equilibrate the system, it is redistributed to the neighbour elements of the structure through the Alternate Load Paths (ALP). This redistribution of the load is dependent on the conditions of the structure, namely rotational capacity, redundancy of the structure, materials' strengths, reinforcement ratio and the structure's dimensions. Those characteristics will determine how the the compressive arch as well as the tension will reach the neighbour elements. Moreover, it will determine the deformation and load carrying capacity of the frame prior to the collapse. Works addressing those topics can be found on Chapter 2.

For new designs it is possible to arrange the internal reinforcement in order to take advantage of the CAA and TCA (Yu and Tan, 2013b). However, for old buildings, depending on the type of building, historical value, and the conditions of the internal reinforcement, doing a repair internally to the structure is sometimes cost prohibitive. Furthermore, the logistic to do such repair is complex and maybe dangerous to be done. For those reasons, external strengthening emerges as the most appropriate solution.

A potential solution to increase the progressive collapse resistance of existing buildings was seen on the novel material named *Textile-Reinforced Mortar (TRM)* as well as on the strengthening technique known as *Near-Surfaced-Mounted (NSM) reinforcement*. Those techniques do not require extensive labour, have a significantly lower footprint compared to other methods and and impose minimum disruptions on the structure. Rather, only a surface treatment (Figure 3.28) or small cover grooves (Figure 3.21) are required. This simplicity on the execution is contrasted with the valuable contribution to the element resistances in flexure or shear (see chapter 2), as well as to its stiffness.

As it can be seen in Chapter 2, research efforts have focused on the application of structural strengthening to increase the progressive collapse resistance of buildings with diverse materials and techniques. However, no work was identifyied to study the benefits of using Textile-Reinforced Mortar (TRM) or Near-Surfaced-Mounted (NSM) reinforcement addressing the topic on existing buildings designed prior the first registered event. Since the need of strengthening those buildings is evident, due the lack of concern of those designs on progressive collapse prevention, this work provides a feasible and reliable solution to address the problem.

1.2 Project Scope

Strengthening the structure in select locations can effectively lead to an increment of the building progressive collapse resistance by reducing the disproportional damage propagation. A novel material named Textile-Reinforced Mortar (TRM) as well as a strengthening technique known as Near-Surfaced-Mounted (NSM) reinforcement will be adopted in this work. The benefits of its usage on old designed structures against the progressive collapse generated due the removal of an internal column of an external frame is examined. The investigation comprises an experimental and a numerical assessment, involving both 2D and 3D FEM computational models. External frame here is understood as those composing the perimeter of the building. Internal column is referred to those which are not the corner or the immediately after the corner columns. As mentioned before, old structures are referred to those designed prior 1968 incident.

1.3 Justification

Accounting for and mitigating the detrimental effects of disproportional collapse not only results in direct economic benefits but most importantly protects the human life. This can be achieved by increasing the resisitance of the building against progressive collapse. The overarching aim of this research was to examine the application of low footprint external strengthening as a means to achieve this design objective.

To the authors' knowledge, few research has been conducted on quantifying the response of existing RC buildings to progressive collapse (Sasani and Sagiroglu, 2008, Kazemi-Moghaddam and Sasani, 2015). Furthermore, the design of old buildings did not take into account progressive collapse scenario. Therefore, a strengthening method that increases the progressive collapse resistance of an old building is needed. This method must to be the less invasive possible, as it is the case of TRM and NSM reinforcement techniques. Thus, studying such materials in progressive collapse scenarios generated by the loss of a column is justified by the suitability of the material to the problem conditions, as well as the potential of those on increasing the progressive collapse resistance of the building.

1.4 Objectives

The main aim of this research project is to examine the applicability of TRM and NSM stainless steel bars for increasing the robustness and resilience of reinforced concrete (RC) frames with respect to progressive collapse. To achieve that, the following set of individual and measurable objectives is identified:

- To establish a robust methodology for the application of TRM and NSM reinforcement for the strengthening of existing structural elements against progressive collapse.

- To determine the influence of specific design parameters on the efficiency of the strengthening scheme, i.e., TRM and textile-based anchors and NSM stainless steel bars.

- To develop and assess by numerical modelling, through nonlinear finite element analysis, the strengthening of RC portal frames.

- To build an analytical model that can reproduce the physical response with adequate accuracy but at a significantly reduced computational cost.

1.5 Methodology

To conduct the present work, the following steps were considered to study the influence of the strengthening of frames against progressive collapse due a column removal.

1. A literature review to identify the mechanics of progressive collapse, study current advances in experimental and numerical investigation over the theme, explore the current state-of-the-art in strengthening strategies for mitigating progressive collapse in reinforced concrete members, and to develop an experimental set-up for the column removal scenario of a middle column of a frame.

2. An experimental program with four half-scale specimens to obtain the response of the frames facing a column removal situation.

3. A computational program applying nonlinear finite element analysis with the commercial software Abaqus (Hibbitt et al., 1997), using the experimental results as basis to validate the models. With those models, performing a parametric study to identify the most influent parameters on the progressive collapse resistance of a frame. Furthermore, to study different scenarios which could not be assessed in laboratory.

4. A component-based RC joint model capable to successfully reproduce the results from the experiments as well as the numerical parametric study.

5. Finally, a synthesis of experiments, numerical nonlinear analysis and parametric studies will be done in order to reach the research objectives and therefore to achieve a greater understanding of the use of TRM and NSM in a column removal scenario.

1.6 Original Contribution

This work extrapolates the boundaries of knowledge on strengthening old structures against progressive collapse generated by the loss of an internal column of an external frame. The innovation on the field is:

- The strengthening in such situation with two types of strengthening methods:
  - TRM (Textile-Reinforced Mortar);
  - NSM (Near-Surface-Mounted) reinforcement.
- A numerical procedure was established to simulate the response of concrete subassemblies strengthened with NSM reinforcement and TRM.
- Key parameters controlling the overall response and the failure mode of the strengthened subassemblies are identified.
- Insights are provided on the overall energy absorption of the strengthened specimens and the corresponding DIFs are evaluated.
- The recent method of anchorage of TRM with textile-based anchors is used in a column loss scenario.

CHAPTER 2 LITERATURE REVIEW

2.1 Introduction

The case of progressive collapse has met the increased interest of the scientific community since the occurrence of the first event, i.e., the Ronan Point Building. According to Ellingwood et al. (2007), immediately after this event, some countries, including the UK and Canada, began to worry about the progressive collapse, creating standards to help prevent the buildings against this type of breakdown. During the 1980s, US design standards started to incorporating requirements for obtain quantifiable measures of the overall structural integrity (General Structural Integrity). These were based on definition of the notions of continuity, redundancy and ductility in structures.

In this chapter the state of art is reviewd and critically assessed hence providing the point of departure for this work. To perform both the experimental and the numerical work, the decisions over the design, methodology, techniques, materials and expected values shall be well established and fundamented. Therefore, an extensive literature review on the state-of-the-art involving progressive collapse and strengthening techniques, with a focus on both experimental and numerical procedures, is performed in the following sections.

As mentioned before, the Ronan Point building collapse was the event which brought to light the existence of progressive collapse. From this point onward, the scientific community turned their attention to the theme. As a result, design guidelines started to be developed by governments around the world addressing the topic. The recent work of Kiakojouri et al. (2020) correlates the progressive collapse events with the development of books and standards including progressive collapse provisions in its guidelines Figure 2.1.

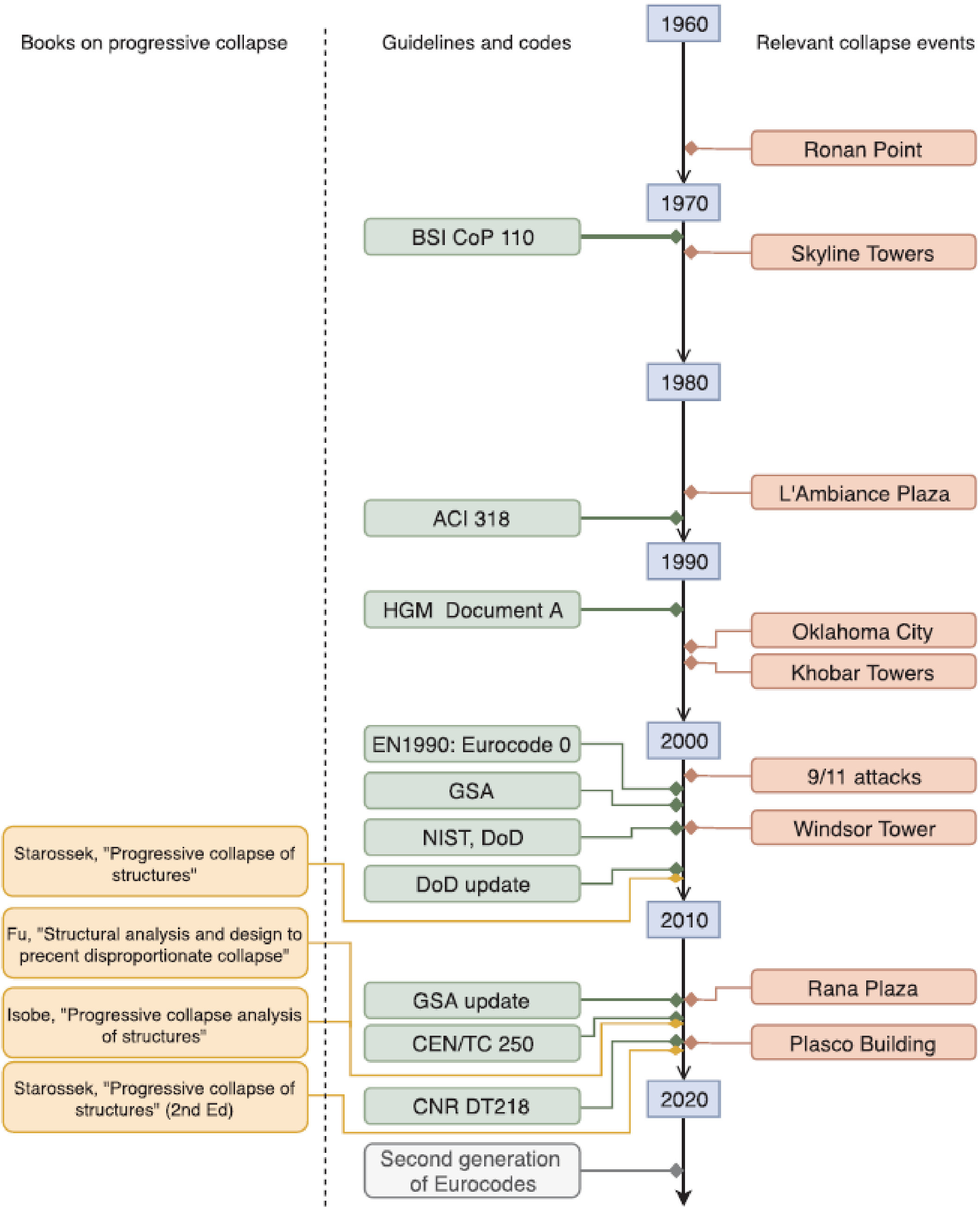

Figure 2.1 – Progessive colapse related events (Kiakojouri et al., 2020).

In general, two methods are considered on existing design standards to qualitatively describe and quantify the event of progressive collapse: (i) the indirect method and (ii) the direct method. These methods are described in the following sections.

2.1.1 The Indirect Method

This method does not require special calculations. It provides the engineer a qualitative framework to assess the robustness of a building with respect to progressive collapse. Between the two methods of design, this is a more subjective method; it provides design guidelines that will result in alternate load paths when an element is lost.

In general, the following four factors are considered crucial when designing with the objective of improving the integrity and resilience of a structure, namely:

- Continuity
- Redundancy
- Ductility
- Resistance

Figure 2.2 – Structure without redundancy, on Bahia Administrative Centre (*CAB - Centro Administrativo da Bahia*), in Salvador, Brazil (Laranjeiras, 2013).

Continuity increases the resistance against progressive collapse by enhancing the load transfer mechanism in case of loss of any element. Furthermore, redundancy introduces alternate load transfer mechanisms to the structure so that when an element is lost the corresponding structural assembly, e.g., a portal frame will be able to redistribute loads in a controlled and preferably ductile manner. Figure 2.2 illustrates a structure without redundancy located in Salvador, Bahia, Brazil. It is possible to imagine the total collapse if a tie rod is lost, for example. Figure 2.3 illustrates a redundant construction, where the forces would have alternative ways to be transferred in the case of loss of a cable.

Figure 2.3 – Structure with redundancy, Octávio Frias de Oliveira Bridge, Sao Paulo. (Laranjeiras, 2013).

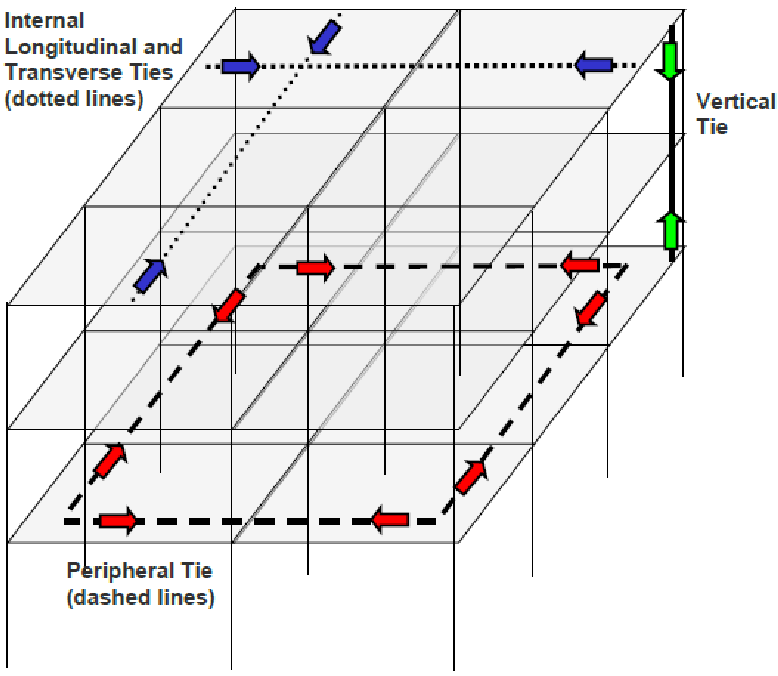

Figure 2.4 – Tie forces in a building (DoD, 2009).

The ductility is quantifies the capacity of the structure to sustain plastic deformation prior to collapse. The more the structure deforms in its plastic regime the higher is its ductility. In RC structures the deformation in large stages is characterized by the steel, so with adequate amount of steel it is possible to reach deformation enough to avoid failure. On the structure where the deformation capacity is higher, the energy stored on the structure, due some specific event, is better spread and dissipated, thus avoiding the failure to propagate.

Finally, the resistance is an key factor for the structure's ability to develop all the previous features. In DoD (2009), Figure 2.4 is used as a reference figure to qualitatively describe the crucial mechanisms one would need to examine when seeking to secure or "tie up" a structure against progressive collapse.

2.1.2 The direct method

The direct method can be implemented by either one of the following approaches, the *Specific Load Resistance Method (SLR)* or the *Alternate Load Path Method (ALP)*. In the former method the building resistance to progressive collapse is increased by increasing the resistance of specific structural members. In the latter, the design considers alternate pathways to facilitate load redistribution after initial collapse (Ellingwood et al., 2007, American Society of Civil Engineers (ASCE), 2005).

Also named *Key Element Design* on literature, the SLR characterizes by explicitly evaluating the critical load bearing components of a building to resist the design level threat, such as blast pressure. As an example, the blast pressure for a defined threat may be considered explicitly on the design by using non-linear dynamic analysis methods. This is a threat specific design approach and the design threats may be in form of explosive, impact or fire loading as per stated in the National Institute of Standards and Technology - NIST (Ellingwood et al., 2007)

The ALP method is a tool to ensure redundancy on the structure. It does not require characterization of the threat which caused the element loss, so it is therefore a threat independent approach. This method promotes ductility, continuity and energy absorbing properties to the structural systems. This is advantageous to design against progressive collapse (Ellingwood et al., 2007).

Following, the most recent advances in progressive collapse research will be presented, where both the direct and indirect methods are adopted. First, experimental investigations, followed by numerical and analytical studies addressing progressive collapse will be discussed. Moreover, works on strengthening methods with respect to progressive collapse will be assessed.

2.2 Experimental Investigation in Progressive Collapse

Yu and Tan (2012) investigated the effect of reinforcement detailing on the existence of alternative load-paths that could be triggered in a column loss scenario.

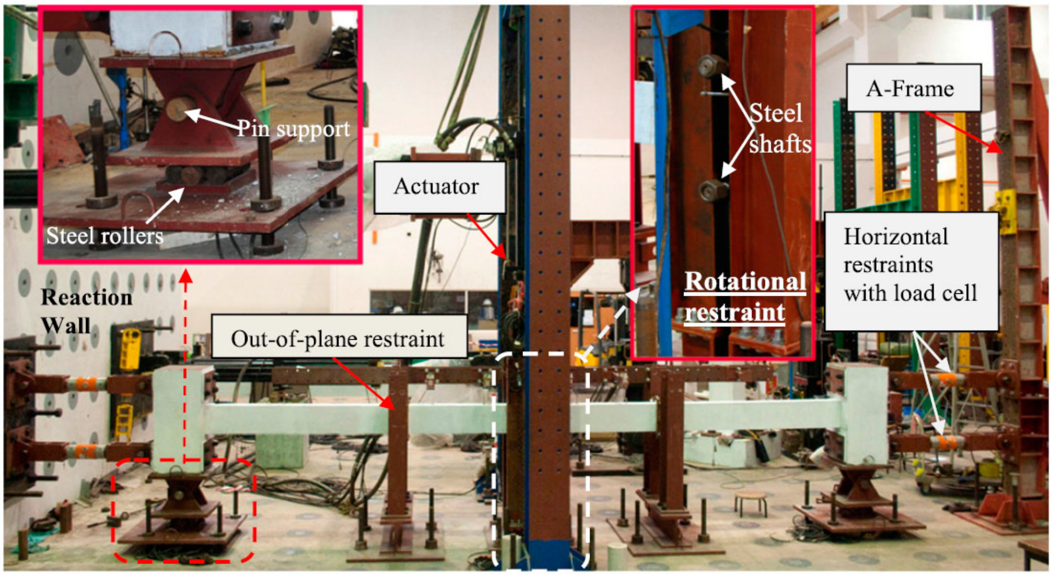

Figure 2.5 –Test set-up used by Yu and Tan (2012).

Six half-scale specimens of a continuous two-span reinforced concrete beam varying top and bottom steel reinforcement ratios were tested. The experimental set-up comprised three column stubs; one at each side of the beam and one simulating the removed column at the middle (Figure 2.5). The tests were conducted with quasi-static approach through the imposition of a displacement at the top of the middle joint.

Results derived from two specimens are shown in Figure 2.6, where the vertical displacements where CAA and TCA initiate were clearly identified.

According to the authors, with adequate rotational and axial restraints, CAA and the TCA were developed contributing significantly in order to increase the progressive collapse resistance. The middle joint tends to rotate toward the most severe cracked side, thus affecting the development of the mechanism.

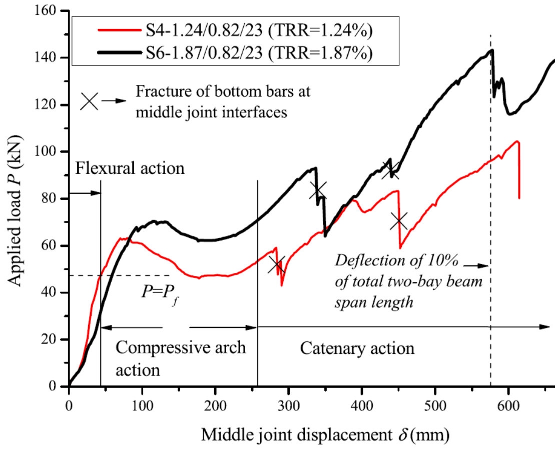

a)

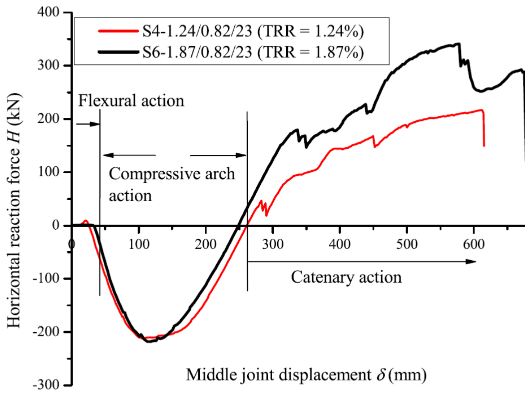

b)

Figure 2.6 – Behaviour of two specimens over applied load at the middle joint. a) applied Load b) horizontal reaction (Yu and Tan, 2012).

The authors demonstrated that the CAA action is favourable in beams with small span-to-depth ratio and low longitudinal reinforcement ratio. Contrary, the catenary action is favourable in beams with large span-to-depth ratios and high longitudinal reinforcements, particularly with a high ratio on top reinforcement. This is due the fact that the tensile load on the beam when the TCA is activated was resisted by the top bars, since in large displacements all the bottom bars fractured in the middle joint. All specimens failed at the middle joint interfaces and the end column stub interfaces.

Yu and Tan (2013a) examined the influence of the detailing on the increment progressive collapse resistance. Two half-scale models were tested, one with seismic detailing and one with non-seismic detailing. According to the authors, the seismic detailing typically enlarges the sections of structural members and increases the longitudinal reinforcement ratio. The behaviours of CAA and TCA with those detailing criteria were assessed as well as a computational model with finite element modelling with variations in geometric and material nonlinearity.

The authors verified the influence of CAA and TCA on the progressive collapse resistance. TCA had no clear difference between the seismic and non-seismic detailed specimen. This occurs because the seismic detailing increases the shear capacity and the structural mechanisms are dominated by flexural and axial actions. They also noted that the top reinforcement bars are more important to TCA.

The authors concluded that to assess the behaviour of the structure with a computational model the joints should be accounted explicitly. A component-based joint model was developed and showed useful comparing structural response at different structural mechanisms. Finally, the stiffness of the joint will influence on the beginning and duration of the structural mechanisms.

Yu and Tan (2013b) tested four specimens in reinforced concrete suggesting also different detailing. The difference between the detailing improved the rotational capacity and deformation limits to increase the potential of the TCA. Also in this work, the DIF, recommended by DoD (2009), is used to address the dynamic nature of the progressive collapse. The author confirmed the acceptability of the purposed detailing on the increasing of catenary action.

Yu et al. (2014) tested RC specimens with explosion loads in a column removal scenario. The initial configuration had three columns: one in the middle and two others in each side, connected through a beam. The central column was removed by explosion with no actuator applying load or displacement above it. Instead, a dead load was installed over the central column and the response (CAA and TCA) was measured at both columns in each side, at the beam level. At this point, two concrete rings, properly installed with gauges, worked as reaction walls, measuring the axial response of the beam.

In that work the tests were dynamic and compared with quasi-static experiments. The Dynamic Increase Factor (DIF) and the Dynamic Load Amplification Factor (DLAF) were assessed and discussed. The authors defined DLAF as the ratio of loads which results in the same deformation of a structure in nonlinear static (NLS) and nonlinear dynamic (NLD) analysis. Moreover, the effect of contact detonation was also evaluated (Figure 2.7). Figure 2.8 shows the comparison of the horizontal reaction between the dynamic and the static test in one of the authors' specimens.

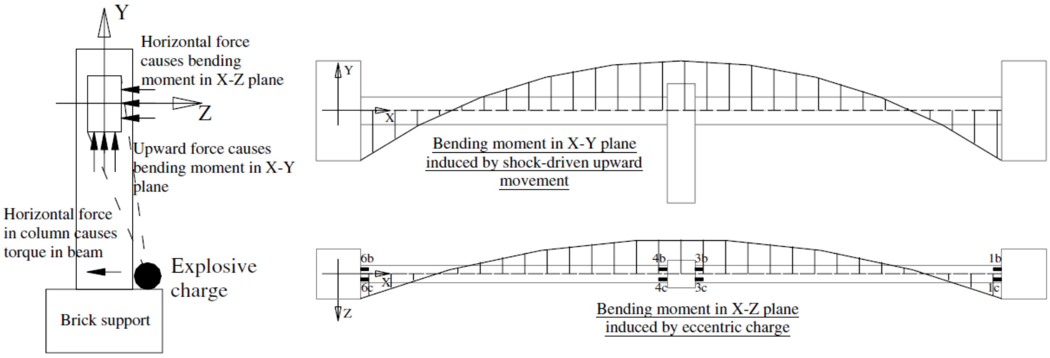

a)

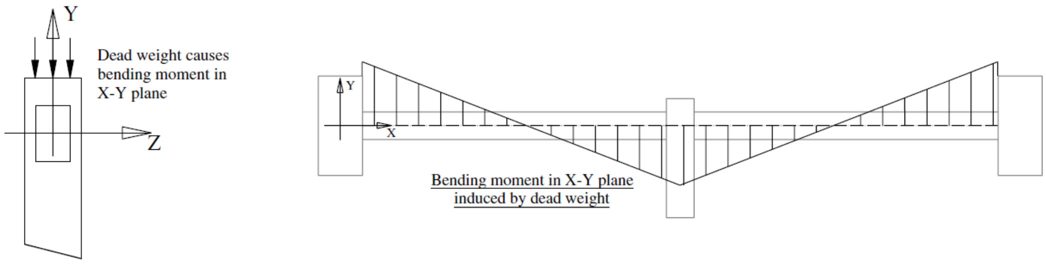

b)

Figure 2.7 – Effect of explosion of a column in a frame a) bending moments in X-Y and X-Z planes induced by explosion ; b) bending moment in X-Y plane due the dead load (Yu et al., 2014).

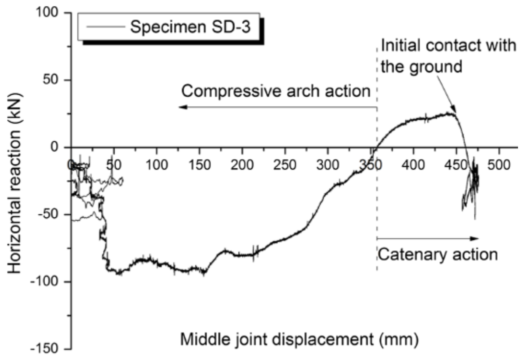

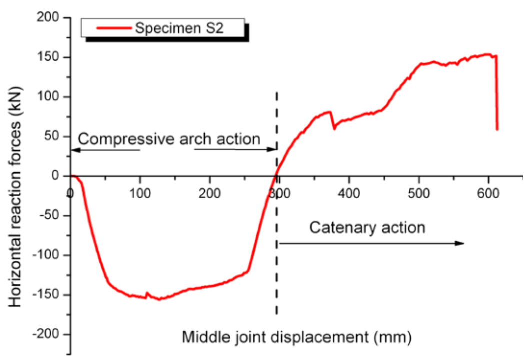

a) **b)**

Figure 2.8 – Comparison between dynamic and static test a) dynamic; b) static (Yu et al., 2014).

It was found that the DIF of material strength is small, and the DLAF achieved on the experiment is different from the prediction. The reason of this difference is that the prediction did not consider the initial damage caused by the contact detonation. If this initial damage was not considered the resistance would be overestimated and a large DLAF would be obtained. However, using an energy equilibrium approach without considering the initial damage leads to underestimated DLAF, which is not safe.

Orton and Kirby (2013) measured the dynamic response of a building in a column removal scenario through a quarter-scaled, two-story, specimen subjected to four drop tests. The experiment was performed by removing a temporary support for the first column, resetting to the original position and repeating the support removal procedure. The applied load was kept constant for the two first iterations but was further increased on iterations 3 and 4. Through this series of tests the authors were able quantify the dynamic increase factor.

The authors also introduced a Single Degree of Freedom (SDOF) model to simulate the structures response. The model predictions were compared to the experimental test and showed very close results. The DIF found from the experiment results was consistent to predict the dynamic behaviour according to the authors.

Qian et al. (2014) worked to identify load-carrying mechanisms to resist progressive collapse in RC structures through six one-quarter specimens. Such mechanisms include the CAA, TCA, the Compressive Membrane Action (CMA) and the Tensile Membrane Action (TMA). The former two are developed in the beam and the other two are developed in the slabs.

Four specimens were composed by columns stubs and beams connecting the columns, without slabs, with different configurations. The authors introduce the term “3D effect” to denote the presence of a beam on the transversal direction of the of the frame at the central column. Hence, two specimens had two beams at opposite sides of the central column (2D), and other two had beams at each side of the central column (3D). Other two additional specimens had 4 slabs, with the same size, supported on the beams in each side. The tests were performed with quasi-static approach. The authors made use of DIF to adapt their results to a dynamic scenario. Furthermore, the authors did analytical assessments with computational models.

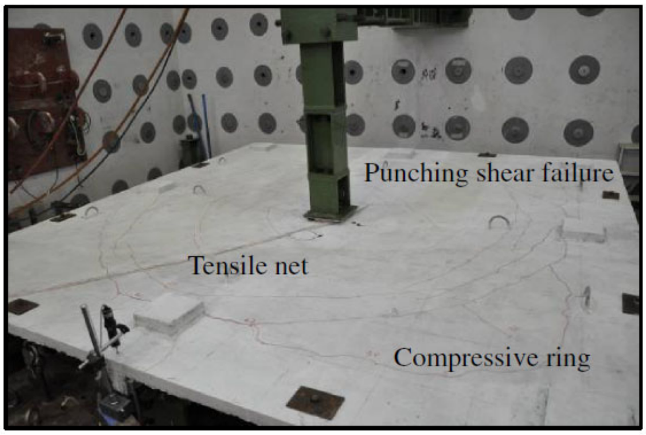

a)

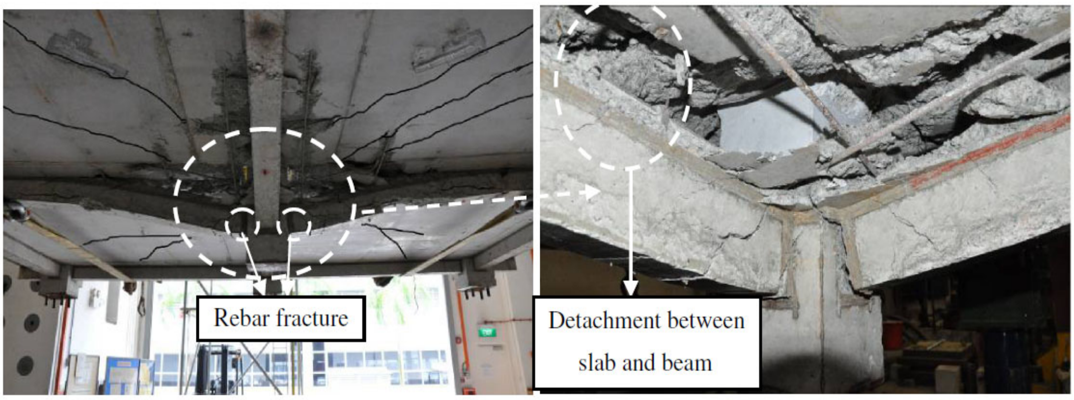

b)

Figure 2.9 – Damage configuration in one specimen a) top; b) bottom (Qian et al., 2014).

They noted that simulating such kind of collapse is complex due the large displacement that occur at the beam. Also noted that the 3D effect, without considering slabs, increase the beam action on the frame by 100%, while when the slab is added this increment goes to 246.2%. For the specimens with slabs, it was observed that the initial resistance was by flexural action, followed by CMA, CAA, TMA and TCA. The tests also concluded that the slabs are the main source of structure capacity, carrying around 68% of the load in large displacements. Figure 2.9 shows the damage in a specimen with slab.

Finally, it was observed that their analytical assessment can overestimate the first and ultimate peak load in beam slabs structures because the model did not include the strain compatibility between beam and slab.

Dat and Tan (2014) assessed the effect of a penultimate-external column removal considering the influence of the neighbour beams and slabs. The authors tested three one-third scaled specimens through a static load procedure. The variation was on the beam' stirrups, longitudinal reinforcement on the slabs, and the aspect ratio of the slab panel. Figure 2.10 shows the idealized structural behaviour after a penultimate external and internal column loss.

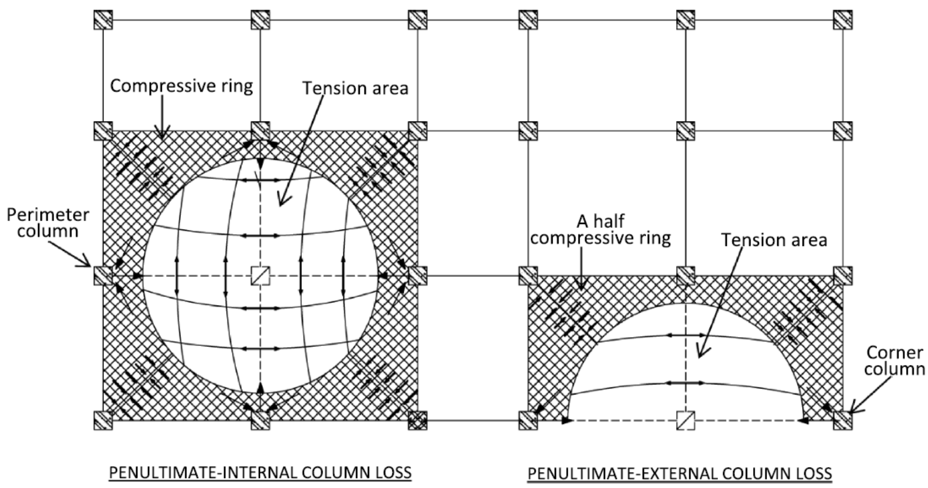

Figure 2.10 – Idealized structural behaviour in a penultimate column loss scenario (Dat and Tan, 2014).

The tests revealed that the three specimens presented the same pattern of failure, three rigid bodies connected by two diagonal cracks, ending on the column removed corner, on the bottom of the slabs. Concrete crushing and fracture of beam bottom bars at each beam end, along the doubled beam was also observed. The presence of longitudinal reinforcement on the slabs and additional stirrups on the beams ends allowed the specimens to reach higher load capacity and displacement ductility.

When increasing the aspect ratio of the slabs, it was observed that higher negative moments were acting on the perimeter beams. Several cracks appeared on the regions of the slabs close to the beams in those specimens with higher aspect ratios on the slabs. Additionally, torsional cracks were also observed in those specimens. This last behaviour promoted a lower load-carrying capacity of the structure. On the other two specimens, with lower aspect ratio of the slab, torsional failure was not observed, and higher load-carrying capacity was observed.

Kang et al. (2015) assessed the progressive collapse of a precast structure filled with an Engineered Cementitious Composite (ECC) material, in a column removal scenario. The mixture the authors used for this material was ordinary Portland cement, water, micro-sand, ground granulated blast-furnace slag (GGBS), and Polyvinyl Alcohol (PVA) fibres. Six half-scaled specimens with different detailing and longitudinal reinforcement ratio were tested to evaluate the resistance to progressive collapse and the failure modes. The specimens varied from each other by: the presence of ECC (in the last five specimens); the change of the anchor mechanism from 90º bended bars to lap-sliced bars at the middle joint; the ratio of the top and, alternatively, the bottom reinforcement bars.

Using ECC instead of conventional concrete did not result in significant differences on the specimens' response in a column removal scenario. The specimens with 90º bended anchor and higher top reinforcement bars mobilised higher TCA. Using different anchorage system resulted in the same CAA capacity. Specimens with lap-spliced anchorage, but without changing the bottom reinforcement ratio, demonstrated greater horizontal compression forces at the CAA stage. Regarding to the top reinforcement ratio, specimens with lower ratio showed lower CAA and TCA capacity. The top reinforcement bar and the ECC deformed similarly, but in the specimen with ECC major cracks were formed after its tensile capacity, in the plastic hinge region, near the side column, resulting on top reinforcement bars premature fracture. Finally, the presence of ECC reduced the deformation capacity of the sub-assemblages due the stiffness of ECC in tension.

Tsai and Chang (2015) tested six 3/8 scaled-down specimens of RC in a column removal scenario. The specimens had varied span-to-depth ratio and the stirrup spacing. The steel ratio was maintained in an average of 0.78%.

The authors observed that for deeper beam sections the CAA may be more pronounced, and the peak arch resistance should be considered as the ultimate strength in a column loss scenario. It was also noted that the variation of stirrups has minor effect on the

CAA and TCA, being this variation more influent on the first mechanism of resistance. In this work the authors assessed the DIF recommended by DoD (2009), and reached the conclusion that the empirical formula presented by Unified Facilities Criteria (UFC) are only suitable for static progressive collapse without considering TCA.

Stathas et al. (2017a) studied experimentally and analytically the membrane action on one-way slabs supported on external beams which suddenly lost one column. The authors observed the influence of different reinforcement configurations on the membrane action. Moreover, different cases, where different perimetral columns were removed, were assessed.

The results showed that the studied specimens were able to develop the membrane action, highlighting the better behaviour of that specimen where the top reinforcement was continuous through the specimen. Moreover, the authors concluded that regardless of the continuity of the slab reinforcement, the structure was able to sustain tha applied loads. Furthermore, they observed that the membrane action is the major source of resistance of the structure after the beam' flexural and CAA peak are surpassed.

The analytical model showed that if the geometric nonlinearities are not considered, the results are not realistc. Moreover, the model is more representative if tension stiffening in the material properties is not considered.

Stathas et al. (2017b) complemented the previous work by studying experimentally and analytically the performance of a portal frame under a sudden loss of a middle column. The authors designed the subassemblage considering the correspondent Eurocodes provisions and, instead of applying a displacement or a load at the top of the middle column, they investigated the appliance of a distributed load over the beam.

The authors studied two types of subasemblage, one with monolithic concrete; and the second with precast beam with dry jonts and concentric unbonded posttensioning. Moreover, the analytical model developed in the paper aimed to effectively simulate the studied frame in a fast way. The analytical model, capable of simulate both concentrated and distributed load situations showed that a distributed load better reflects the beam behaviour under a sudden column loss. Furthermore, the authors observed that the CAA phase is more important to enhance the frame resistance under sudden loss of a column. Finally, limits to the monolithic and precast beams where drawn under the same condition of loads, where the monolithic reached larger vertical deflections.

A key point emerging from this literature review is that the case of old/ existing structures and their strengthening against progressive collapse is not addressed. However, the current state-of-the-art provides significant insight on the typology of experimental setups, the appropriate instrumentation, as well as the necessary laboratory capacity to perform such tests. Moreover, the behaviour of the frame under such scenario could be anticipated, as well as the beam failure mode (Yu and Tan, 2012, Orton and Kirby, 2013, Yu and Tan, 2013a, Yu and Tan, 2013b, Kang et al., 2015, Tsai and Chang, 2015, Stathas et al., 2017b). A further key point rests on the fact that the abscense of slabs and transversal beams is justifiably if the TCA is not of concern. Additionally, the understanding over the DIF definitions could be enlighted by those studies (Yu and Tan, 2013b, Dat and Tan, 2014, Qian et al., 2014, Kang et al., 2015, Tsai and Chang, 2015, Pham et al., 2017, Stathas et al., 2017b, Stathas et al., 2017a).

2.3 Analytical/ Numerical Investigation in Progressive Collapse

Husain and Tsopelas (2004) assessed the contribution of redundancy on the strength of RC structures. They aimed to quantify the deterministic and probabilistic effects of redundancy by proposing two indices: the redundancy strength index; and the redundancy variation index. Furthermore, the influence of ductility capacity on the proposed index in a two-dimensional frame was studied. The authors used a nonlinear pushover analysis. Moreover, it was considered an inverted triangular lateral load distribution monotonically increasing until collapse.

The redundancy-strength index (r_s) accounts for the ability of a structural system to redistribute loads from irreversible damaged members towards elements with higher resistance. The second proposed index, the redundancy-variation index (r_v), quantifies the effects of element strength on the structural system. The nature of the former index is deterministic, while the second is probabilistic.

The index r_s was defined as the ratio of the mean ultimate strength to the mean yield strength of the structure. Therefore, a structure with $r_s = 1$ means a structure without redundancy. The index r_v is a function of the number of plastic hinges and their average correlation coefficient between their strengths. This index can assume values from 0 to 1. If a single plastic hinge can cause a collapse, it means $r_v = 1$ and this structure is not redundant. If it is needed an infinite number of plastic hinges to cause the collapse, or when element strength in a structure are uncorrelated, the structure is considered redundant and $r_v = 0$.

The model considered was a two-dimensional frame. The number of floors and bays were varied, as well as the capacity of rotation of each beam. As stated by the authors, the lower is the value of the rotational ductility capacity the lower is its redundancy, while the redundancy grows when the rotational ductility capacity grows. The beams were modelled using a nonlinear hysteretic element, which includes strength deterioration, stiffness degradation and pinching effects. For the columns the same model was considered, however the strength deterioration, stiffness degradation and pinching effects were not considered.

It was observed that r_s increases with the increment of the member ductility, also that beyond four bays, increasing the number of bays does not mean significant increment of redundancy. For all cases r_s increased more quickly within low ductility range. The authors also observed that as members ductility increases the number of plastic hinges to failure increases as well. Similarly, as the number of floors and bays is enlarged the number of plastic hinges also raises. The results showed that by providing ductility capacity higher than a limit, little is gained by increasing the number of developed plastic hinges at failure, thus not too much increment is expected on the probabilistic effects of the redundancy. The index r_v decreases when the number of bays is increased but increases when the number of floors rises. Effectively the authors evaluated the indices for the case of earthquake induced damage.

Izzuddin et al. (2008) presented a method of analysis of multiple floors structure robustness in a sudden loss of a column. According to the authors, from the observation of the progressive collapse in Ronan Point building in 1968, measurements have been taken in an attempt to mitigate this effect or prevent progressive collapse, and project guides can be divided into three parts: (i) conditions for mooring methods of the structure; (ii) provisions for significant members of the structures that have been removed, if the mooring method cannot be satisfied; (iii) and provisions for key elements of the structure whose excess damage removal to prescribed limits.

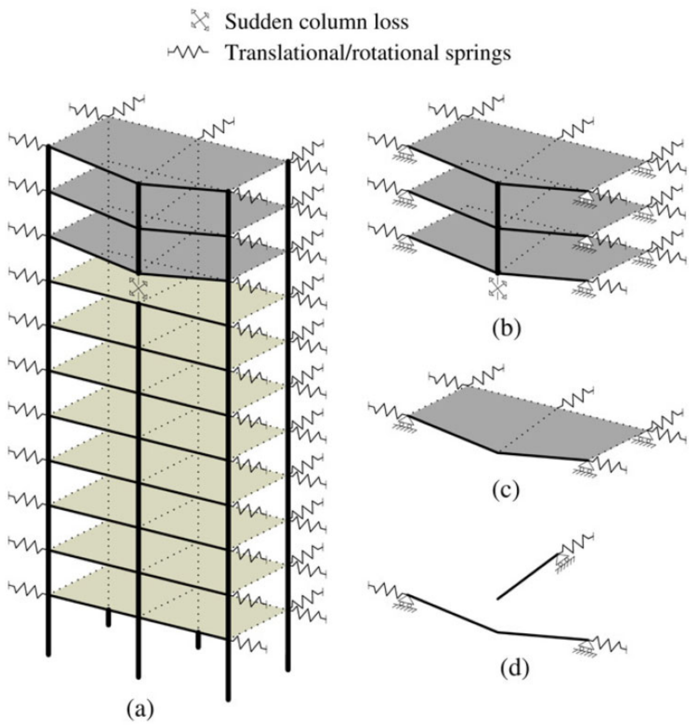

Figure 2.11 – Multi-level analysis (Izzuddin et al., 2008).

Since the response of the structure of a multiple building floors to lose a column is dynamic and the response is greatly affected by material and geometrical nonlinearities the most accurate method for analysis would be a nonlinear dynamic analysis using a refined finite element model of the structure. However, such analysis would require significant computational time to be completed. Therefore, the authors introduced a simplified, yet accurate, method to reduce the corresponding computational toll, in which only the nonlinear static response of the structure is needed. The following stages are used by the method: (i) nonlinear static response of the damaged structure under gravity loading; (ii) simplified dynamic assessment to determine the maximum response in a column removal scenario; (iii) ductility assessment of the connections.

With four different levels of model idealization, as shown in Figure 2.11, the author presented an assessment framework to study a sudden removal of column from the structure through a static non-linear approach rather than dynamic. As stated by the authors, varying the level of structural modelling will only affect the first stage of the method, i.e., the nonlinear static response. The proposed assessment framework is deterministic, evaluating whether the stories above the failed column will fail due excessive dynamic ductility demands.

According to the authors, the individual measure of energy absorption capacity, redundancy or ductility is not an adequate way to measure the robustness. Instead, it is suggested the usage of the proposed approach, which considers the influence of those three indicators together.

Liu (2013) proposed a new method of structural analysis in a column removal scenario. According to the author, the conventional method used is the pushdown, where the gravity load is amplified, while in this work a pulldown analysis was suggested (Figure 2.12).

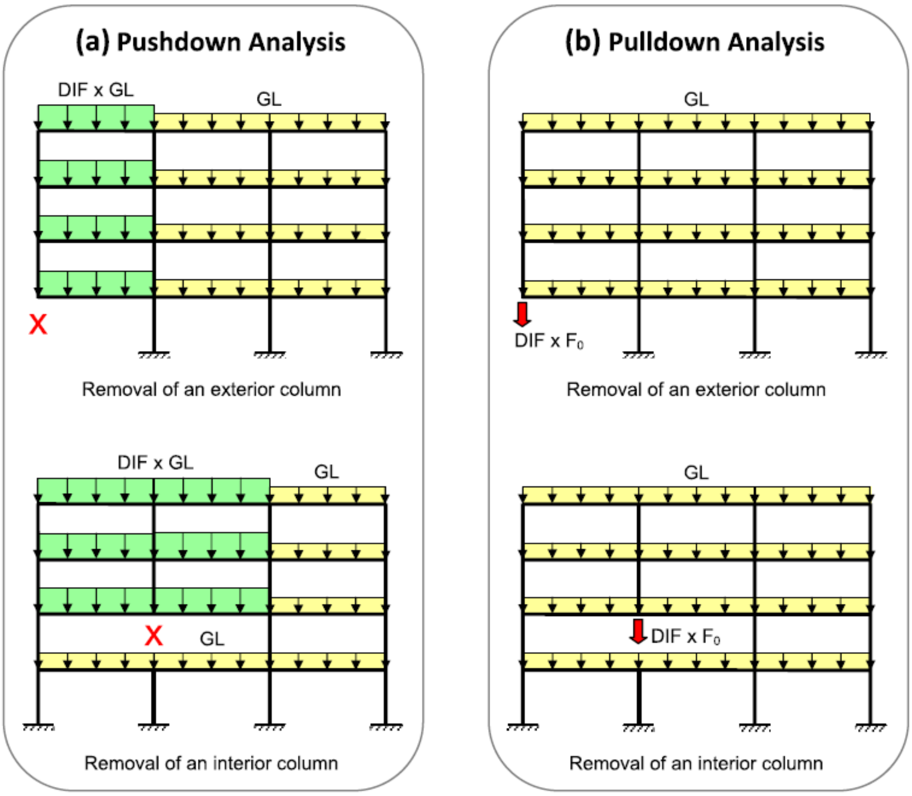

Figure 2.12 – Pushdown and Pulldown method (Liu, 2013).

As stated in the work, the pulldown is equal in value to the axial compression force on the column which will be removed of the intact frame multiplied by a DIF. The author tested a nine-story steel frame and compared the results from assessments between a pushdown and pulldown analysis.

It was observed the same accuracy on the estimation of the peak dynamic response of a pulldown analysis with the pushdown. The predictions of some structural responses were better with the proposed technique, for example, the peak axial forces on columns next to the removed column. For the previous example, the error on the same analysis with pulldown and pushdown analysis were 1.6 % and 26.3% respectively. Besides, curve-fitting of data points were made for the example to show how empirical DIF formulas can be derived for practical applications.

Le and Xue (2014) developed a two-scale stochastic numerical model to analyse the probabilistic collapse behaviour of 2D RC frames considering a scenario of initial damage. The authors developed what they call a coarse-scale model to facilitate the simulation of progressive collapse of RC structures. This coarse-scale model consists of several elastic blocks connected by a set of cohesive elements. These represent the potential damage zones. Here, the constitutive relation of the proposed cohesive element had to be determined from structural behaviour of the individual potential damage zone.

According to the authors, the model is capable to capture the difference in fracture energies under normal and shear loading, also their interaction under multi-axial loading. As it was stated, it was included on the model the compressive failure by allowing a small negative cohesive separation. Bond-slip of the longitudinal bars was also considered in the model.

The authors calibrated the coarse model through fine-scale stochastic simulations and then applied the two-scale model to analyse a two dimensional 30-story RC frame structure. Two types of simulation were performed: stochastic and deterministic. In the deterministic mode the mean material properties and a set of factored loads suggested by DoD (2009) were used. In the stochastic procedure uncertainties were considered both for material properties and gravity loads. The simulations were performed using the commercial software Abaqus (Hibbitt et al., 1997).

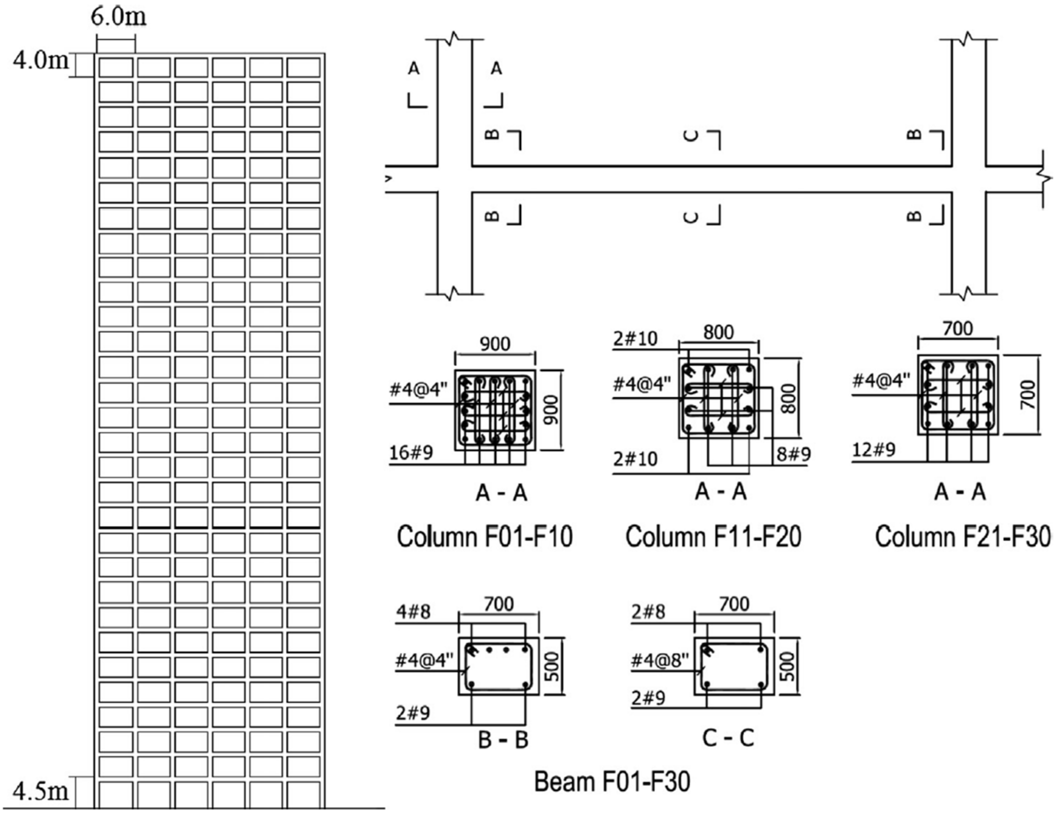

Figure 2.13 – Model studied by Le and Xue (2014).

The scenario that the authors considered to address progressive collapse was the sudden removal of a column. The building used had 30 floors (Figure 2.13). Once per time, the perimeter columns of the 1st, 8th, 16th, 26th and 29th story were removed. The authors also considered the impact which might occur between a damaged and an intact element. To address this scenario, a default contact algorithm present on the commercial software utilized was adopted in the studies. The simulation was established to finish when the calculated probabilities of each collapse extent converge within a relative error of 5%. Deterministic simulations were performed to the same scenarios and the same procedures of the original examinations.

The authors divided the general collapse in four levels to assess the degree of the propagation of local structural damage: (1) intact: the crush front does not propagate; (2) local collapse: the crush front only propagates through the area where the columns are removed and it is arrested within one story; (3) partial collapse: the crush front propagates further than the local region defined in (2); (4) total collapse: the crush front propagates into the entire structure.

In the scenario considered by the authors, the probability of no collapse reduced from 99.14% to 63.80%. Null probability was presented to promote a local collapse. Removing a column from the 26th story showed to be the most likely to result in a partial collapse, with the corresponding probability equal to 46%. Lower values were found to the other scenarios following the sequence of removing a column from the 8th, 16th, 1st and 29th story. Total collapse probability attained its maximum value when the 8th story column was removed. Removing columns from 1st, 16th, 26th and 29th presented lower probabilities of total collapse. The authors attribute this fact to the movement downward, the contact with the floor below and the load above the column removed.

When a deterministic model was processed a partial collapse was attributed to a removal column from the 1st story, a total collapse when the column was removed from the 8th or 16th floors and intact in the other situations. These predictions showed that the deterministic approach can be used but it is not as accurate as the probabilistic method.

Fascetti et al. (2015) assessed the robustness of RC frames to progressive collapse due a removal of one or more load carrying members. The authors performed analysis with dynamic and static procedures. With the called Local Robustness Evaluation (LRE) methodology, pushdown procedures are combined with nonlinear time-history simulations trying to compare robustness of different systems. By considering mechanisms involving different failures, the LRE is adapted to capture the local failures. The methodology attempts to estimate the load redistribution resulting from local damages and is provided an overview of the weak point of the building.

The effect of modelling with 2D and 3D model was assessed, as well as the contribution of the slab on the resistance to the progressive collapse. The authors noted that the 2D model can overestimate the dynamic displacements induced by the column failure. Therefore, the 3D model was more adequate to do such simulation. Furthermore, it was observed that the slab can slightly increase the stiffness of the elements as well as it strength.

In the mentioned work a global and local pushdown analysis were performed. The local analysis consists in a single load applied at the top of the column which had a part of it “removed”. The global consist in a distributed load applied along the beams at each side of the removed column. The global analysis resulted in a smoother force-deformation response, whereas the local approach presented local yielding and redistribution. The collapse on the global approach occurred at a slightly lower force, and on the local analysis the failure happened at a smaller displacement.

On a ten-story building, assessed in this work, a computational model simulated a pushdown analysis. Several columns from a peripheral frame at the ground floor were removed independently to check which column removed is more harmful to the building. After that, the adjacent columns were removed individually to check the next critical column to be removed, as well as the amount of columns that when are removed promote the beginning of the progressive collapse. According to the authors, the number of removed columns can be a representative “robustness index”. The other index proposed used the named Axial Load Multiplier for the total amount of columns removed. This multiplier is obtained when the pushdown force is normalized with the force which was acting on the column before being removed.

Kazemi-Moghaddam and Sasani (2015) studied analytically the progressive collapse of the Murrah Federal building after the sudden loss of column G20 (Figure 2.14). According to the authors, previous studies have concluded that the building would have collapsed even if exterior column G20 was statically removed, but in this paper is shown a different conclusion: the building would have resisted to the progressive collapse, even if the column was suddenly removed.

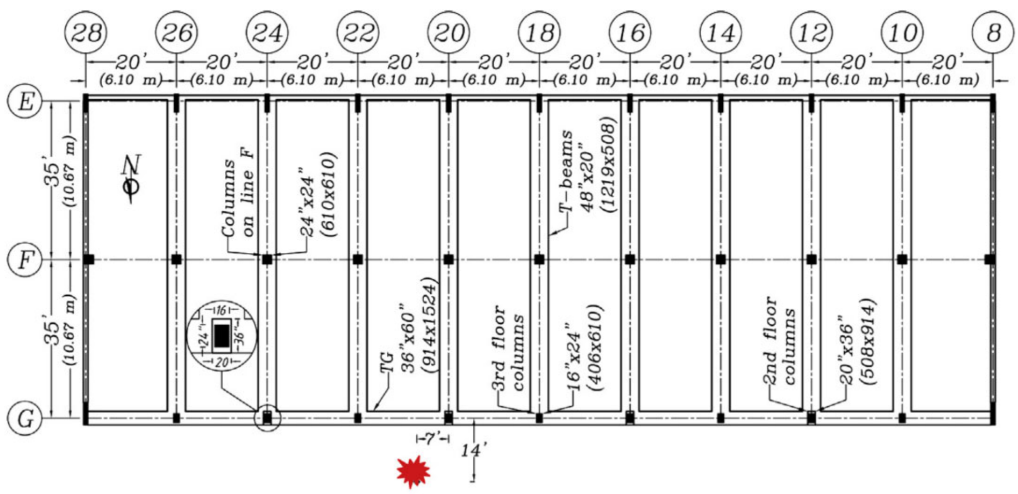

Figure 2.14 – Plan view of the Third floor (Kazemi-Moghaddam and Sasani, 2015).

With the open-source program OpenSees (Mazzoni et al., 2004), the authors simulated the structure of the building in a 3D model. It was concluded that the maximum vertical displacement the building would reach would be 86 mm, after the G20 column removal, and the damage would have been more severe than a sudden removal of this column. They also noted that the gravity load transferred by the transition grid on the third floor after the column removal is smaller than before the loss of this column.

Livingston et al. (2015) used 2D computational models and experimental results to assess the response of a continuous beam bridging a column lost. The specimens tested in laboratory were 3/8 scaled of a continuous beam from an exterior frame of a 7-story ordinary RC building where a central column was removed. The test was performed with a pushdown method, where a continuous displacement was imposed at the central (removed) column.

For the finite element analysis, a two-dimensional element was developed using the open-source program OpenSees (Mazzoni et al., 2004). The same pushdown procedure of the experimental test was used here. The authors compared the model and the experiment to validate the analytical model. In both it was observed similar results to the mechanisms of resistance to progressive collapse.

By varying the lateral restraint stiffness, the authors observed that the vertical load carrying capacity is affected. A higher lateral stiffness results in a lager vertical load carrying capacity. Also, it was varied the influence of rebar yield strength, and it was concluded that higher yield strength bars support means more vertical load resistance. Finally, the influence of the span was assessed, and concluded that it would be better assessed by analysing they configuration of the reinforcement bars, which had significant influence over the performance of the beam.

Dat et al. (2015) proposed an approach to assess the progressive collapse of RC building which lost its penultimate column. This approach considers the contribution of the beams and slabs in such resistance. A Single Degree of Freedom (SDOF) system is used to evaluate the structural dynamic response of the building (Figure 2.15).

By calculating the structural ultimate load capacity in penultimate internal and penultimate external column, the progressive collapse resistance for each scenario was determined.

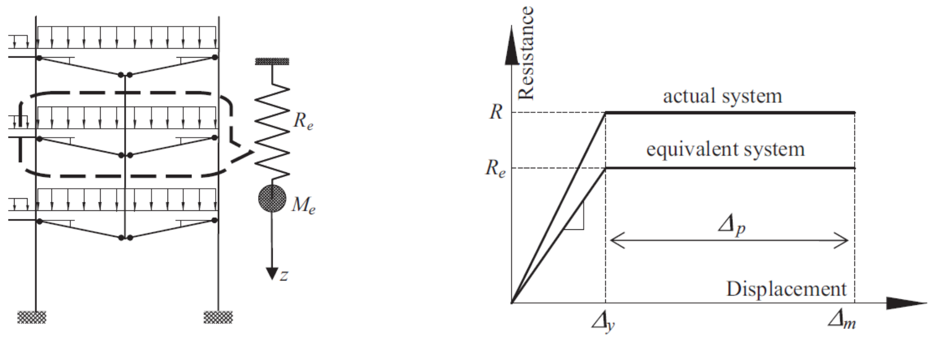

a) b)

Figure 2.15 – a) SDOF system; b) Resistance functions (Dat et al., 2015).

As it was stated by the authors, vertical displacements are mainly governed by rotational deformations of various beam plastic hinges. Hence, the displacement ductility, which reflects the dynamic effect of the event, is calculated and related to the curvature ductility ratio of the critical hinge component of the system.

By testing two series of RC specimens the authors validated the proposed approach. Each series had six specimens: one for the penultimate external columns, one-third scaled down; and the other for the penultimate internal columns, one-quarter scaled down. The tests were conducted statically until the specimen failure through distributed load with a 12-point load system. Comparing the test with the proposed approach, it was achieved that the last is conservative in its values, being this way safer to be used.

Chen et al. (2016) propose a robustness index which accounts both for the topology of the structure and assessment of robustness under specific corresponding events. The robustness index was obtained by quantifying the opposite property of robustness, in other words, the vulnerability, through component importance and vulnerability coefficients.

The authors divided the collapse stages in four parts. Undamaged, when there is no collapse or event which could cause this. Locally damaged stage, when an explosion occurred removing a column inducting internal forces in all components of the structure, but without enough time to present deformations. According to the authors, in most cases, this stage is selected to evaluate the vulnerability of the structure because it starts the closest to the undamaged stage. The damage propagation stage, when an increasing number of components fail due the redistribution of internal forces. As it was said, the structural robustness deteriorates, while the vulnerability increases until the end of the collapse. The collapsed stage, when the structure responds no more, and the structural collapse ended.

The authors considered the structure as an assembly of its components. So, they divided the components in four groups. Key elements, which include the elements with high importance that are vulnerable to a certain event; important but not vulnerable (INV); vulnerable but not important (VNI) elements; and the neither important nor vulnerable (NINV) elements.

The authors associated the vulnerability with the failure criteria, and thus with the structural type (truss or RC frame). For each structural type a failure criterion was defined according to its material behaviour. Each type of failure criteria led to a vulnerability coefficient. Basically, for truss it was used a stress strain relation as failure criteria and for RC members a more complex formulation depending on shear, bending moment and axial force was presented.

To define the level of importance of the component, the authors proposed a coefficient based on the structural bearing capacity. Basically, it is the ratio between the difference of the initial and final structural bearing capacity and the initial structural bearing capacity.

Considering a structure as an assembly of discrete components and the structural vulnerability as a contribution of component vulnerability it is possible to achieve the robustness of the structure, since the robustness is seen as the antonymous of vulnerability. So, the authors defined the structural robustness index to single and different simultaneous events which can lead to collapse.

The authors conducted numerical simulations to assess the vulnerability, thus the robustness index, for RC frame and truss structures. The simulations showed concise results, highlighting the components of the structures which were more vulnerable and when removed would lead to a partial or total collapse. As an indication on how to improve the robustness of a structure, the authors suggested increasing its local resistances and providing redundancy, which was proved through simulations with truss structures.

The literature review on numerical simulation provides insights on the current state-of-the-art vis-à-vis progressive collapse. Therefore, it was possible to define adequate tools (as Abaqus (Hibbitt et al., 1997) and OpenSees (Mazzoni et al., 2004)) to be used in the present work to conduct the simulations, see, also, (Izzuddin et al., 2008, Yu and Tan, 2013a, Le and Xue, 2014, Kazemi-Moghaddam and Sasani, 2015, Livingston et al., 2015). Moreover, the method of analysis (pushover), material definitions (bond-slip behaviour and hysteretic material), model characteristics (lateral stiffness) to be considered, as well as the importance of the structural element characteristics on the overall behaviour of the frame could be identified (Husain and Tsopelas, 2004, Liu, 2013, Le and Xue, 2014, Fascetti et al., 2015, Livingston et al., 2015, Chen et al., 2016). Finally, the importance of the assessment using the energy approach in conjunction with ductility and redundancy considerations was crucial for the proper assessment of the behaviour of a reinforced concrete frame (Izzuddin et al., 2008).

2.4 Retrofitting methods with respect to progressive collapse

In the following, a review on the state-of-the-art vis-à-vis structural strengthening with externally bonded systems is provided. The review does not focus solely on the case of progressive collapse with the objective of providing a more thorough description of the available strengthening techniques, especially for the case of RC buildings and hence examine their applicability for the specific case of progressive collapse.

2.4.1 Fibre Reinforced Polymer (FRP)

2.4.1.1 Experimental investigation

Bournas and Triantafillou (2011) assessed the bond strength in columns confined with Fibre-Reinforced Polymer (FRP) and TRM in regions of lap-splice of reinforcement bars. The experiments consisted in seven full-scaled columns cantilevers which were tested under cyclic uniaxial flexure with constant axial load. Three of the seven columns were control specimens, without retrofitting, one without lap-splice, one with 20 bars diameters of lap-splice, and other with 40. Other specimens varied in type of jacket, FRP or TRM. The failure was controlled by flexure in all specimens with lap-splices.

Columns without retrofitting and with lap-splices presented splitting bond failure followed by spalling of the concrete cover. Specimens with short lap-splice and retrofitted with FRP and TRM presented splitting longitudinal cracking followed by pull-out bond failure of lapped bars. Specimens with long lap-splice retrofitted with FRP and TRM did not reached bond failure or spalling of concrete.

Assessing the stress on the steel, the authors concluded that the short lap-splice is not adequate for the development of the longitudinal bars' yield stress, while the longer lap-splice was sufficient to the development of yielding in the push direction only.

By resisting the propagation of cracks, the retrofitting with FRP and TRM was effective on increasing the bond strength. However, the FRP was found to be more effective when compared to TRM.

Analytical program was conducted with bond models according to formulation proposed on literature. It was found good relation with the results extracted from the tests. After that, these models were adapted to address the usage of FRP and TRM.

Qian and Li (2012) used FRP on retrofitting against progressive collapse in a load carrying removal scenario. The authors studied the effects of strengthening and retrofitting flat slabs to mitigate the progressive collapse by using externally bonded unidirectional carbon fibre-reinforced polymer (CFRP) laminates.

Six flat slabs of one-third scaled were tested in laboratory to assess the influence of the proposed retrofitting scheme. Two of those were tested without strengthening, one with low and other with medium amount of slab reinforcement. Two more specimens had also low and medium slab reinforcement but were strengthened on the top face of the slab orthogonally. The last two specimens had low and medium slab reinforcement as well, but were strengthened diagonally on the top face of the slab. Figure 2.16 presents the specimen without retrofitting. Figure 2.17(a) and (b) present the two strengthening schemes used.

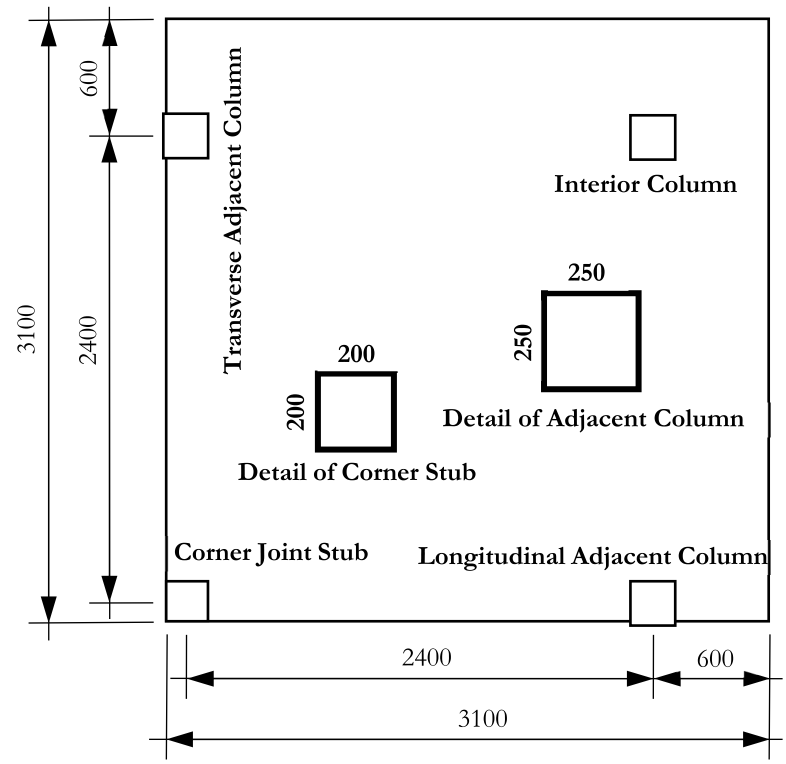

Figure 2.16 – Plan view of the specimen adopted in Qian and Li (2012).

The failure modes of both control specimens were very similar. Flexural cracks were observed on the top face of the slabs near the adjacent columns and the bottom face of the slab close to the corner column. Crack patterns differed in the two control specimens. Significantly more diagonal cracks distributed over a wider area were observed in the specimen with medium reinforcement. For large displacements TMA was also observed for both specimens and it was noted that both specimens would collapse if the corner column was suddenly removed. Since the critical column to be removed is the corner column, the authors proposed the retrofitting scheme presented in Figure 2.17.

The dynamic strength was predicted for each specimen. Since the progressive collapse is a dynamic event, the specimens tested should be assessed with this concern. The method used is named the energy-based capacity curve method. The authors approximately evaluated the strain energy accumulated in the structure by directly integrating the experimental load-displacement paths. By implementing an equivalence of energy approach, the authors postulated that the dissipated energy measured from the experimental curves should be equal to the work produced by the external load (actuator) over the induced displacement. Collapse was then defined as this state where the work produced by the external loads was larger than the dissipated energy. In this way, the authors obtained a set of capacity curves by dividing the accumulated stored energy by its corresponding displacement. It was observed that the strengthening reduced the vulnerability of the specimens against progressive collapse in such a way that it could be avoided.

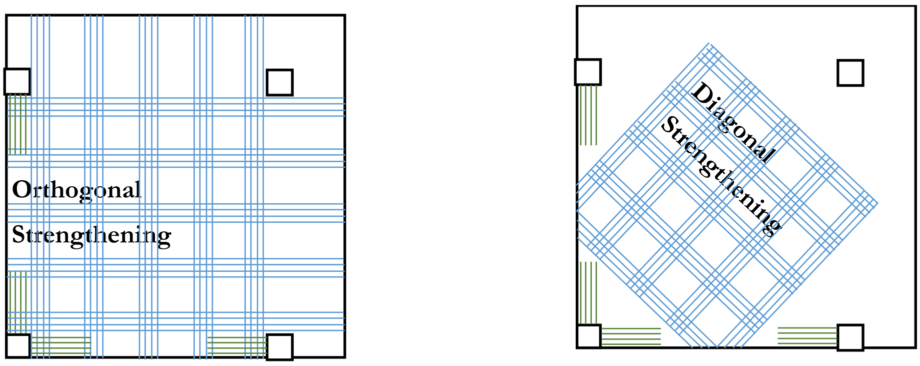

a) b)

Figure 2.17 – Strengthening schemes adopted in Qian and Li (2012) a) orthogonal b) diagonal.

The strengthened specimen with low reinforcement presented in Figure 2.17(a) had its first peak capacity, initial stiffness, peak tensile membrane action, and dynamic ultimate strength increased by 97.7%, 77.6%, 28.9% and 74% respectively when compared to the control specimen of the same reinforcement. The corresponding increment for the specimen presented on Figure 2.17(b) was 118.8%, 90.3%, 30.1% and 82% respectively. The energy dissipation capacity increased by 119.5% on the strengthened specimens. Those with diagonal strengthening showed better performance given that the fibres were placed diagonally to the expected cracks opening.

The strengthened specimen with medium reinforcement and orthogonal strengthening had its first peak capacity, peak tensile membrane action, and dynamic ultimate strength increased by 49.0%, 28.6% and 47.9% while the same results on the specimen with diagonal strengthening were 57.3%, 38.4% and 52.1%. The energy dissipation was increased by 39.7% and 0.0% for the specimens with orthogonal and diagonal fibres respectively. The authors stated that the last specimen could not increase the energy dissipation due a local failure concentrated in the cut-off point of the central CFRP strips.

Bournas et al. (2015) assessed the behaviour of FRP anchors when connected to FRP and TRM sheets to concrete (Figure 2.18). Eight specimens consisting in RC columns and foundations, with no reinforcement crossing the interface between the column and foundation block, were connected with FRP anchors. Tests were conducted applying an uniaxial load on the column part. The parameters varied during the tests were the number of anchors, the anchor cross sectional area, the type of externally bonded sheet connected with the anchor, the bonding agent used to bind the sheet-anchor system, and the presence of external confinement with composite material jacket. Figure 2.19 presents all the specimens tested. 'F' means if it is FRP and 'T' is Textile; the number after this letter is the number of strengthening layers; followed by the total amount of anchors, which will be divided equally in opposite sides of the column; the following number is the nominal diameter of the spike anchor; 'R' means the usage of resin as binder material and 'M' refers to mortar; 'J' was added at the end to indicate jacketing.

Failure of specimens strengthened with FRP unidirectional sheets were controlled by tensile rupture of the carbon spike at the column-base block interface. Specimens strengthened with textile bidirectional fibres had its failure mode also through the rupture of the anchors. According to the authors this last system was less effective due the lower continuity between the anchor protruding fibres and the vertical fibres on textile.

Comparing the effective strain (defined by the authors as the average tensile strain in the fibre anchors at failure) of fibre anchor, it was observed that specimens strengthened with FRP had higher effective strain than those with textile-based reinforcement.

By comparing the number of anchors, it was possible to observe that the specimen with FRP carbon sheet using one anchor with one 9.25 mm diameter were 15% more effective than that using two 6.25 mm. Also, the usage of one anchor with 12.7 mm diameter was 14% less effective than two with 9.25 mm diameter.

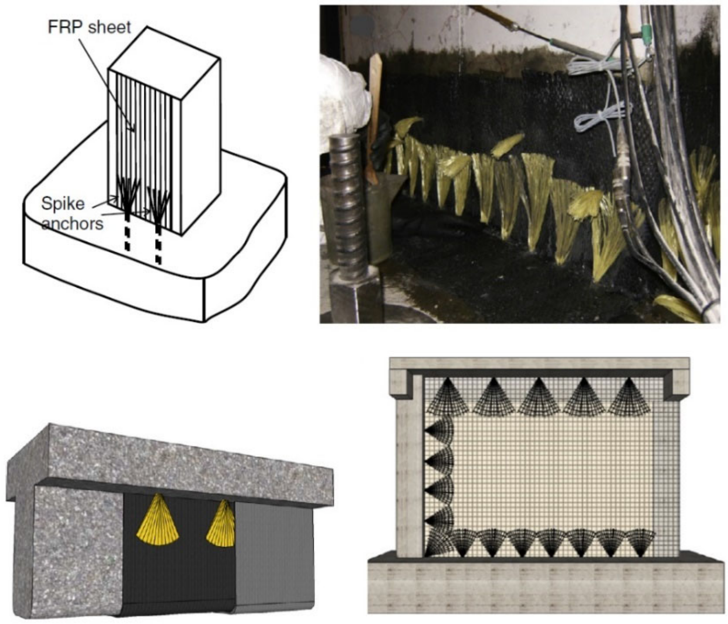

Figure 2.18 – Usage of FRP anchors (Bournas et al., 2015).

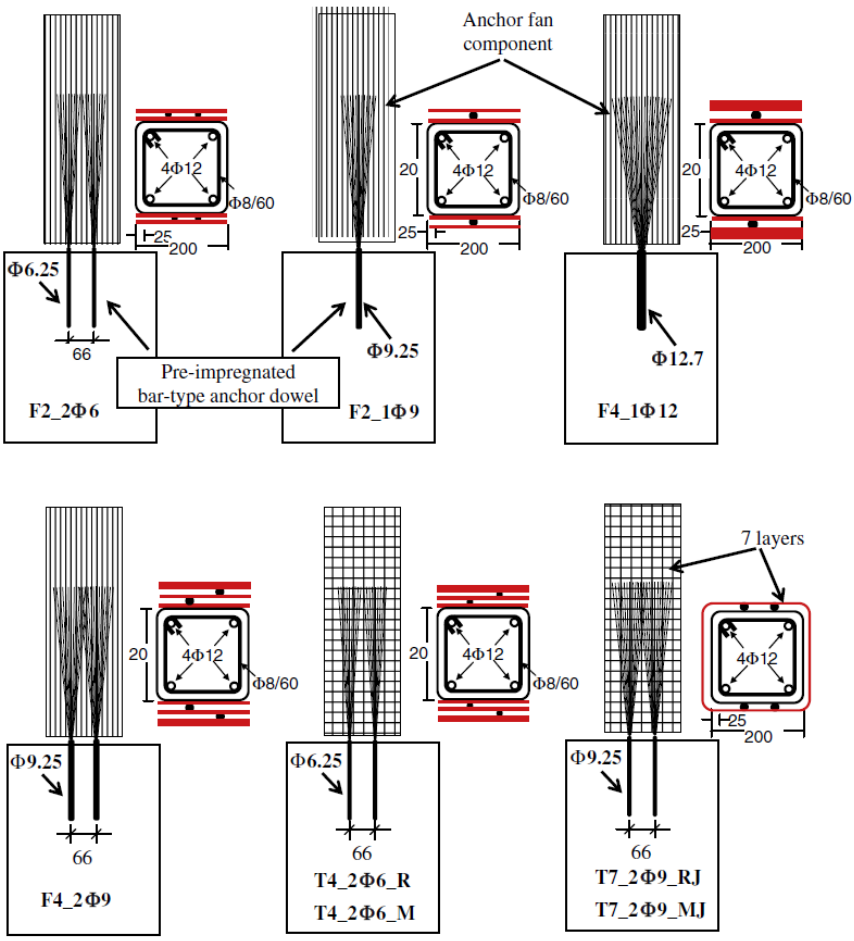

Figure 2.19 – Specimens tested (Bournas et al., 2015).

Assessing the anchor cross sectional area, it was observed that doubling this parameter the tensile capacity is increased 70%, although this increment is only 50% when the same anchor was used to connect TRM sheets to concrete.

The effectiveness of the anchors is more than twice when the specimens with externally bonded FRP uniaxial sheets and bidirectional textile fibre sheets are compared.

Finally, when connecting externally bonded bidirectional textile reinforcement the effectiveness of the anchors is 15% lower when mortar is used as bond agent instead of resin, and failure is controlled by anchor debonding instead of rupture.

2.4.1.2 Numerical investigation

Elkoly and El-Ariss (2014) also presented a strengthening technique to mitigate progressive collapse. A numerical procedure to assess the potential of progressive collapse of RC continuous beams in a column removal scenario was also presented. The main aim of the authors was to analyse the flexural behaviour of beams retrofitted with external fibre-reinforced plastic (FRP) rods after the removal of a column. Figure 2.20 presents the scheme of positioning the cables (represented as A_{FRP}).

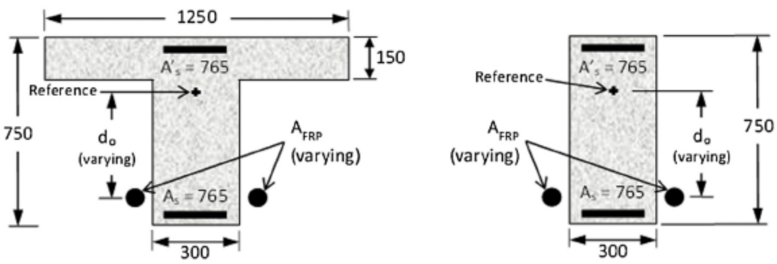

Figure 2.20 – Scheme of the external cables (Elkoly and El-Ariss, 2014).

The procedure proposed involves the installation of external unbounded FRP cables attached to the beams. The cables considered were made from the following materials: Arapree, a tendon made with aramid fibres embedded in epoxy resin; Leadline, a pith-based carbon FRP rod; Technora, a spirally-wound pultrude rod, impregnated with a vinyl ester resin; and Carbon Fibre Composite Cable (CCFC), formed by a twisted number of small diameters rods. The analytical model was performed with an open source finite element package for structural analysis, ZEUZ-NL (Elnashai et al., 2010).

Two sets of specimens were considered. In the first set, straight cables were used along the beam length. In the second, cables were deviated to follow the trajectory of the bending moment diagram corresponding to a two-span beam.

On the models, where the cables were not deviated along the beam length all, specimens presented considerable increment of the maximum vertical displacement (up to 485%), failure load (up to 250%), energy absorption (up to 500%), and small increment of the ultimate load (up to 10%) when compared to the control beam. The Technora and Arapree cables presented similar behaviour in each of the aforementioned performance indicators. These were larger than the corresponding indicators of the Leadline and CCFC cables.

The authors also assessed the behaviour of structures retrofitted with external Arapree FRP with one deviation point along the beam and varying the number of cables from 2 to 16. It was observed that compared to control beam, the beam with 2 cables had it failure load increased in 100% and the vertical displacement increased in 210%. On the beam with 16 cables these values were 320% and 235% respectively. The authors concluded that strengthening with 14 cables is an optimal choice for both rectangular and T-beams.

By using two deviation points to the cables at the beams the authors concluded that a ratio of 65% of L_s/L (distance between the deviators/beam length) is the optimal deviator location to mitigate the effects of progressive collapse in a column removal scenario. These deviators are placed symmetrically to the beam centre. The optimal ratio assumed a value of L_s/L = 85% when three deviators were used (considering the deviators at the end of beam). In this case the third would be placed at the centre of the beam.

Hao et al. (2015) presented a numerical approach to assess the reliability of RC columns and frame strengthened with FRP subjected to explosive loads. The reliability of the structure is used to estimate the failure probabilities of RC columns in different damage levels. The authors used a set of curves termed Pressure-Impulse (P-I) curves (developed in Mutalib and Hao (2011)) to estimate the column damage. As stated, the analysis considered random fluctuations of RC column dimensions, reinforcement ratios, material properties, FRP configurations, thickness, and strength and the random fluctuations of blast loadings corresponding to different scaled distances.

A computational model was developed and validated through drop weight impact tests and field blasting tests. After that, several P-I diagrams of RC columns with or without FRP strengthening were constructed under blast loads. The authors then used these diagrams to model the RC column capacities to resist blast loads.

The authors divided the damage into three levels (where D represents the damage level): D = 0.2, represents low damage; D = 0.5, represents medium damage; D = 0.8 represents a high level of damage or almost collapse of the column. According to Mutalib and Hao (2011), these damage levels are defined regarding the remaining axial load-carrying capacity of the column with respect to its design load-carrying axial capacity.

To assess the effectiveness of FRP strengthening in RC columns to resist blast loads, the authors considered three different retrofitting schemes: with FRP strips (Figure 2.21(a)); with FRP wrap (Figure 2.21(b)); and with FRP strips and wrap (Figure 2.21(c)). Results were compared to an unretrofitted control specimen.

The software CALREL (Liu et al., 1989) was used to evaluate the probability of failure for the RC columns at different damage levels, which were defined using the P-I diagrams. Eight cases of FRP strengthened columns were considered in this study, varying the thickness, 2, 4, 6 mm (C2FRP1, C2FRP2, C2FRP3 respectively), with constant strength of 1700 MPa; and varying the strength, 1000, 2400 MPa (C2FRP4, C2FRP5 respectively), with constant thickness of 4 mm.

Table 2.1 presents the results of pressure and impulse asymptotes achieved for the examples processed. The column chosen to be retrofitted was the control example C2. The blast charge was maintained constant. These results demonstrate that FRP strengthened specimens performed better than the control specimen. According to the authors, these P-I curves indicate that FRP is highly efficient on increasing the blast load resistance of RC columns.

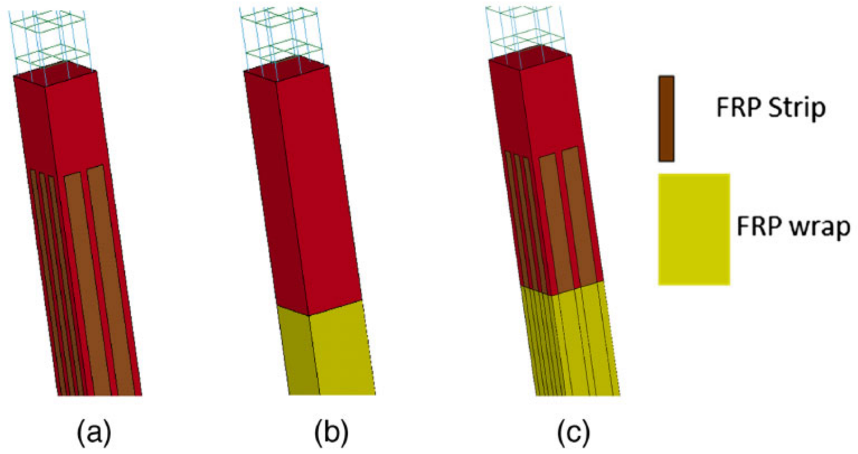

Figure 2.21 – Strengthening schemes used in Hao et al. (2015) a) with strips b) with wrap c) with strips and wrap.

Furthermore, by varying the distance of the blast load in these specimens, the authors observed that the FRP increased the load blasting resistance of the columns. For example, considering the damage level of D = 0.5, the failure probability decreased for the same scaled distance of applied load applied when used FRP (Figure 2.22).

	Damage $D = 0.2$		Damage $D = 0.5$		Damage $D = 0.8$	
Column	P_0 (kPa)	I_0 (kPa · ms)	P_0 (kPa)	I_0 (kPa · ms)	P_0 (kPa)	I_0 (kPa · ms)
C1	605	1,096	847	1,869	1,180	2,094
C2	1,095	3,256	1,535	3,997	1,639	4,849
C3	1,661	5,700	2,354	6,318	2,179	7,651
C2FRP1	1,197	3,572	1,753	4,216	1,797	5,061
C2FRP2	1,264	3,840	1,862	4,468	1,857	5,483
C2FRP3	1,375	4,336	1,971	5,008	1,939	6,749
C2FRP4	1,207	3,828	1,830	4,195	1,820	5,107
C2FRP5	1,351	3,853	1,893	5,117	1,902	6,409

Table 2.1 - Results of pressure and impulse achieved by Hao et al. (2015).

Finally, the same model was applied to assess the collapse probability of an example frame structure subjected to blast attack. A two-bay six-story frame was considered for the analysis. Frame columns were considered to be strengthened with FRP. The results presented the probability of failure of such structure and reaffirmed the effectiveness of FRP on enhancing the resistance of structures subjected to blast loads.

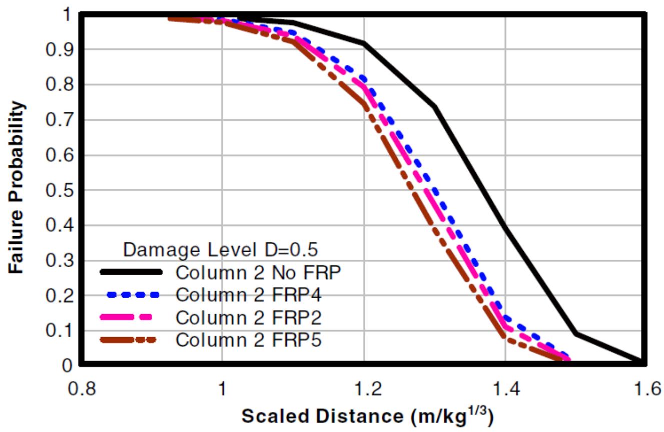

Figure 2.22 – Failure probability (Hao et al., 2015).

Based on the aforementioned, the comparative advantages of the TRM against the FRP are established. A key point that stands out is that the application of CFRP has been shown to be effective in mitigating the progressive collapse of reinforced concrete buildings (Qian and Li, 2012). The performance of textile-based anchors interacting with FRP and TRM (Bournas et al., 2015) is shown to be critical for the effectiveness of textile fibre reinforced materials, either FRPs or TRMs. Finally, the performance of RC strengthened frames under explosion was observed, as well as methods of simulating those frames in progressive collapse events (Elkoly and El-Ariss, 2014, Hao et al., 2015).

2.4.2 Near-Surfaced-Mounted Reinforcement

2.4.2.1 Experimental investigation

Bournas and Triantafillou (2009) studied the performance of Near-Surface-Mounted (NSM) FRP strips and bars in RC columns as a method for increasing its flexural resistance. A total of 11 large-scaled cantilever columns were tested under cyclic uniaxial flexure with constant axial load applied at the cantilever end. Several parameters were analysed, including: the type of NSM reinforcement (CFRP strips, Glass Fibre-Reinforced Polymer bars and stainless steel reinforcement bars); the configuration of NSM reinforcement; the amount of NSM reinforcement; and the presence of jacketing at the members end on NSM reinforced specimens.

Amongst the examined specimens, of particular interest is the one with two stainless steel bars placed symmetrically on the most critical sides. These were positioned in square holes opened in the column surface which were filled with epoxy resin. Moreover, this specimen was retrofitted with a TRM confining jacket on the first 600 mm counting from the column base. This strategy led to an increment of the ultimate load of nearly 100% when compared to the non-strengthened control specimen. The corresponding drift ratio at failure (defined by the authors as a reduction of peak resistance in a cycle below 80% of the maximum recorded resistance in that direction of load) was also increased (the maximum stroke of the piston was reached). Consequently, energy dissipation was higher in this column, as well as the stiffness which was higher than the other specimens.

A column with only stainless steel as strengthening had its peak load increased in around 65% compared with the control specimen and its energy dissipation was the second best performance compared with the other columns. Other specimens, with NSM FRP or glass FRP bars, showed minor contribution than that with stainless steel bars.

Mofidi et al. (2015) assessed the influence of NSM FRP reinforcement for shear rehabilitation of RC beams. Six full-scaled T-beams were tested in laboratory with different shear reinforcement ratios. The specimens varied on the presence of NSM FRP rods and the presence of stirrups. The rods were applied in both lateral sides of the beam. Two cases of transversal reinforcement were considered based on their spacing; a moderate reinforcement (with 260 mm spacing) and a high reinforcement (with 175 mm spacing). The tests were conducted through a three-point load, where the applied load was not in the mid-span.

Comparing the specimens without NSM FRP rods, the shear resistance was increased by 139% and 185%, for the moderate and high shear reinforced specimens respectively, compared to the control. The deflection of each specimen was 11.2 mm and 11.9 mm for the moderate and high reinforcement specimens respectively, the control specimen deflection was 2.9 mm. The failure mode of each non-strengthened specimen was through diagonal shear cracks.

The shear resistance of the NSM FRP rod strengthened specimens (without stirrups, but with NSM FRP rods) was improved by 91% and 84% (for moderate and high reinforcement, respectively) when compared to the corresponding control specimen. The deflections were 11.7 mm and 13.1 mm for the moderate and high shear reinforced specimens respectively. The control reached a deflection of 6.1 mm. The failure mode for each retrofitted specimen was through concrete cover splitting on the side of the beam. However, the specimens with steel reinforcement also failed in flexure.

Comparing each unstrengthened specimen with its corresponding strengthened one, the gain in shear resistance due to additional strength was 61% when compared to the control specimen, 29% to the specimen with moderate reinforcement, and 4% to the specimen with high reinforcement. The corresponding values for the relation increase in deflection were 135%, 4% and 10% respectively.

The authors compared their study with results presented in a database collected by them using the literature. More than 69 RC beams strengthened with NSM FRP rods and laminate were used in this database. The comparison showed that the presence of steel stirrups did not diminish the NSM FRP shear contribution.

Finally, the authors proposed a shear design model for RC beams strengthened with NSM FRP rods and laminates, which can predict the possible failure modes of the elements. This model presented adequate correlation with the results achieved on their experiments, producing accurate and conservative values.

Reda et al. (2016) studied the flexural behaviour of RC beams strengthened with NSM glass fibre reinforced polymer (GFRP) bars. The anchorage angles of the bars were varied to prevent debonding and concrete cover separation. To perform this study, 11 beams were tested under four-point bending. The parameters analysed were the following: the presence of hooks on the anchorage; the angle of anchorage; the bar length; and the length of the epoxy which was used as bonding agent. Figure 2.23 presents the test configuration, specimens with different lengths and epoxy lengths.

The load-carrying capacity of the beam strengthened with NSM GFRP bars without hooks and 1800 mm length increased in 77%, compared to the control specimen. The stiffness of this beam was increased by 49% and the maximum deflection at the failure load decreased 12.7% compared to the control specimen. Its failure mode was through debonding of NSM GFRP bar.

The anchorage with 45º hook presented better performance than those with 90º hooks, when comparing the load-carrying capacity. Comparing the former with the control specimen the increment of the ultimate load capacity was approximately 101% higher when 1400 mm length of strengthening with fully epoxy length on the ending zones was considered. The failure mode of the specimen with 45º hooks was through compression of the concrete. Moreover, the strain in this specimen was higher than that one with 90º hook and slightly lower than the control specimen.

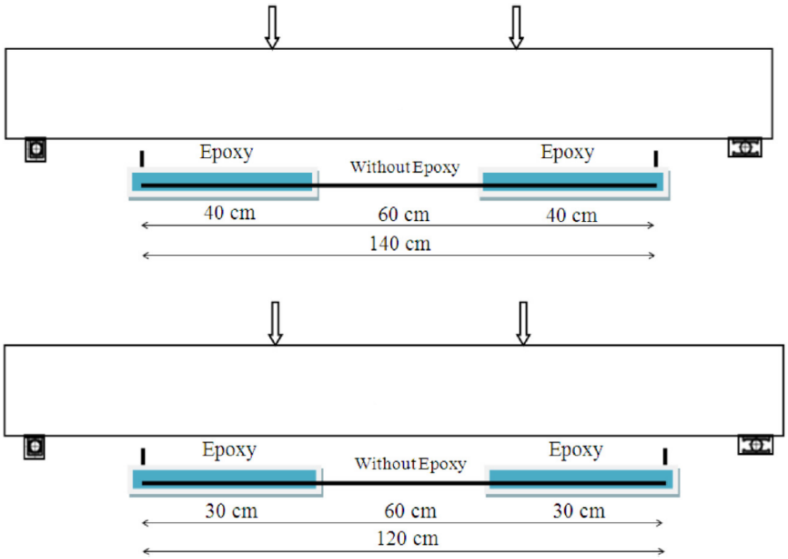

Figure 2.23 – General specimens used by Reda et al. (2016).

Specimens with lower epoxy length at the end of the GFRP bars presented lower load-carrying capacity than its counterparts. For example, comparing the specimen with 1400 mm of strengthening length and 90º hooks on anchorage, the ultimate load was 5% lower on the specimen with lower epoxy length. On the same comparison between the specimens with 1200 mm strengthening length, the specimen with lower epoxy length had its ultimate load capacity 25% lower than its counterpart with major epoxy length.

Specimens with equal or lower than 1200 mm strengthening length and 90º hooks on the anchorage failed due shear at the end of NSM GFRP bars. Specimens with 1400 mm of strengthening length failed by compression. Furthermore, the specimen with

1400 mm of strengthening length, 90º hooks and partially bonded with epoxy, undergone crushing of the concrete in a small portion behind the hook. The specimen with no hook and 1400 mm of strengthening length had also debonding and cut of the NSM GFRP bars.

The authors proposed an elastic-plastic analysis to compare with experimental results, which presented good correlation with the real scenario in terms of load-deflection, load-GFRP strain and moment curvature.

2.4.2.2 Numerical investigation

Kim et al. (2015) performed a numerical investigation on the flexural behaviour of pre-stressed concrete retrofitted with post-tensioned NSM CFRP strips over service load. A three-dimensional finite element model was built to assess the performance of the anchorage depending on its position along the girders. The effectiveness of the post-tensioned NSM CFRP stripes was also assessed using the concept of potential energy.

The NSM CFRP strips were placed at the bottom of each girder as shown in Figure 2.24. Various post-tensioning levels were addressed for the CFRP going from 0% to 60% of its ultimate capacity. Also, a strengthening coefficient was proposed, $\alpha = Lp/L$. Where Lp is the bond length and L is the girder length. Figure 2.24 presents the girders to be studied and the retrofitting scheme.

Simulation was conducted using the commercial software ANSYS (Moaveni, 2003). Concrete was modelled with elastic shell elements. Three-dimensional spar elements were used to represent the pre-stressing strands and the NSM CFRP stripes. The model was validated using theoretical solutions and published literature.

The external retrofitting resulted in a shared load mechanism between the strands and the NSM CFRP strips. When the level of post-tensioning was varied from 0% to 60% of those strips' ultimate capacity, the mid-span steel strain was reduced by 2.3%. The authors justified this small value with the fact that the girder was loaded in service load. By varying the strengthening coefficient, a rapid increase of the CFRP strain was observed. This increment reached a limit value after which it remained constant in its development length. Moreover, it was observed that the reduction of mid-span steel strain was independent of the strengthening coefficient. When increased the girder length it was observed that the NSM CFRP strengthening efficacy was reduced.

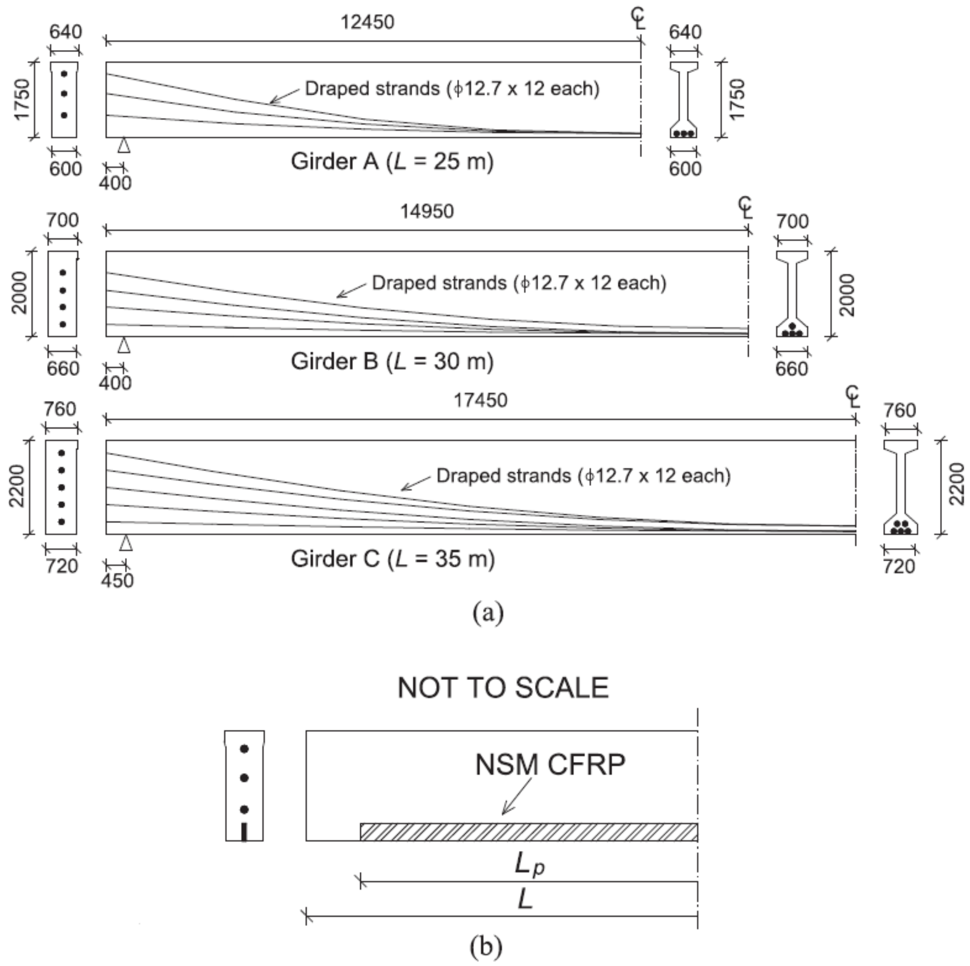

Figure 2.24 – a) Girders b) position of NSM CFRP (Kim et al., 2015).

By increasing the post-tensioning stress of NSM CFRP reinforcement up to 60% and strengthening coefficient up to 0.9, the deflection was decreased by 42%, when compared with an unstrengthened specimen. The authors suggested a minimum of 0.6 to strengthening coefficient for design purposes.

Finally, the authors concluded that post-tensioning NSM CFRP increased the usable potential energy of strengthened elements. A functionality index (FI) was proposed to quantify the flexural performance of girders which could be extended to FRP strengthened concrete members. Using the FI to NSM CFRP reinforcement it was observed that this reinforcement has limited advantage from flexural performance perspective.

The literature review on NSM reinforcement demonstrated how the technique is being currently used on the strengthening of structural elements under flexure. Amongst the materials used for NSM reinforcement, the stainless steel excelled on reinforcing RC elements in flexure (Bournas and Triantafillou, 2009). Furthermore, the technique showed to be well stablished as a solution for flexure, even with different materials and configurations (Kim et al., 2015, Mofidi et al., 2015, Reda et al., 2016).

2.4.3 Textile-Reinforced Mortar

2.4.3.1 Experimenta/Numerical work

Bournas et al. (2007) compared the effect of using TRM and FRP as method for RC column strengthening. Experiments were carried out on 15 RC short prisms and on three nearly full-scale non-seismically detailed RC columns. These last columns were tested over a cyclic uniaxial flexure under constant axial load, while the formers were tested ensuring the longitudinal bars to buckling.

Short prisms were divided in three groups, each one with five specimens: the first with no reinforcement; the second with longitudinal reinforcement and stirrups spaced by 200 mm; and the third one with also longitudinal reinforcement and stirrups spaced each 100 mm. Amongst the 5 specimens in each group, one was not retrofitted, two were retrofitted with different amounts of layers of FRP, and other two with different amounts of layers of TRM. The TRM strengthened prisms were similar in stiffness and strength to the FRP specimens.

Experiments with prisms showed that the TRM did not fail abruptly like their FRP counterparts. Failure on TRM prisms initiated on a small portion of fibres then propagated slowly to the others, resulting in a more ductile collapse than the FRP specimen. Moreover, it was observed that the TRM improved the compressive strength and deformation capacity of the specimens, and this improvement was slightly smaller compared to the FRP counterpart.

The three full-scale RC columns assessed differed from each other by the presence of jackets: one had no jacket; other had two layers of CFRP, and a third one had four layers of TRM. It was observed the force and cyclic deformation, the rate of strength and stiffness degradation, and the energy dissipation. The results were similar to FRP and TRM jacketed specimens, which had better responses than the unretrofitted specimen.

Finally, the authors compared the test results with derivations for retrofitted reinforced concrete members introduced in Eurocode 8, Part 3. This comparison demonstrated that the code specification estimated are much more conservative than the results obtained on the experiments.

Bournas et al. (2009) compared the performance of TRM and FRP when used for seismic retrofitting of RC columns with continuous or lap-spliced deformed bars. Ten large-scaled cantilevers columns were tested under cyclic uniaxial flexure with constant axial load. Four specimens had continuous longitudinal reinforcement and six had lap-spliced rebars at the base. Amongst the first four specimens there was the control without retrofitting, a specimen with carbon fibre reinforced polymer (CFRP) and resin as binder, another with TRM with the same stiffness of the CFRP and mortar as binder, and a last one, similar to the previous, but with glass fibres instead of carbon fibres on the textile of TRM. The other six varied the lap-splice length and the presence of FRP or TRM. In both cases, with continuous or lap-spliced longitudinal bars, the failure mode was controlled by flexure.

An important observation was that, in specimens with longitudinal bars, both FRP and TRM did not mitigate bar buckling in the specimens. However, this buckling was developed in later cycles compared to the control specimen. The FRP jacketed specimen demonstrated a highly brittle response, with minimum energy dissipation up until failure. This resulted to an abrupt bar buckling right above the retrofitted area.

TRM specimens on the other hand resulted in more dissipative, i.e., ductile response. Carbon fibre TRM did not fail; glass fibre TRM developed cracks without reaching the ultimate limit load. Thus, TRM was more effective as means of increasing cyclic deformation capacity and energy dissipation.

Lap-spliced specimens showed similar results using TRM and FRP and were far better than the control specimens. For short lap-splices the FRP was slightly better in terms of deformation capacity, and similarly good to TRM in specimens with long lap-splice on its rebars.

The authors also compared the test results with predictions from code formulations and concluded that the Eurocode 8-based modified formulation is in moderate to good agreement for members with continuous deformed bars jacketed with FRP or TRM. For elements with deformed short lap-spliced bars the prediction from Eurocode 8 of drift ratios are in good agreement for TRM and FRP retrofitted members, while for long lap-splices the predictions are conservative.

Koutas et al. (2013) examined manufacturing methods and testing for textile-based anchors. The authors assessed the strengthening of masonry infills with TRM with the idea to change its brittle failure to a more ductile behaviour. The main objective in this work was to assess two cases: when the thickness of the masonry is less than the RC frame above, so the TRM can be connected to the frame through anchors inserted on the beams; when the thickness of the masonry is equal to the RC frame above. In this second case, if the beam above the masonry is a T-beam, the TRM could be extended up to the slab and possibly anchored, or if the concrete element is a rectangular column, it could be covered by TRM layers in its two faces or even be wrapped around.

A total of 19 specimens were tested in laboratory, divided in two series. Each one represented a different boundary condition. The first group (Series A) (Figure 2.25(a)) had six specimens where anchors would be used to improve the transference of loads. The parameters observed were the quantity of fibres in the anchors and the depth at which the anchors were inserted in the concrete. Each specimen was retrofitted in both sides of the wall with one layer of glass-fibre textile combined with a commercial polymer-modified mortar.

The second group (Series B) (Figure 2.25(b)) had 13 specimens where RC T-beams prisms were considered. The parameters assessed in this group were the type of textile used on the wall, the number of layers of this textile, the quantity of fibres in the anchors, the length of the anchors on the infill, and the orientation of part of the anchors placed into the concrete. All the series were subjected to monotonically tensile load applied on the top of the beam.

The results of Series A showed that all the specimens failed due the rupture of one anchor, which resulted in a sudden load drop. The maximum capacity load of this series was around 15 kN. The results also indicated that reducing the anchor length from 150 mm to 75 mm led to a small change in the load capacity (around 7%). Moreover, it was observed that increasing the amount of fibres in 50% led to an increment of 19% on the failure load.

The effectiveness of each anchor was analysed by dividing the load that each anchor supported by the tensile strength of fibres in a straight configuration. It was reached a maximum of 24% on the specimen with a textile width of 400 mm on it anchors and an anchor length of 150 mm.

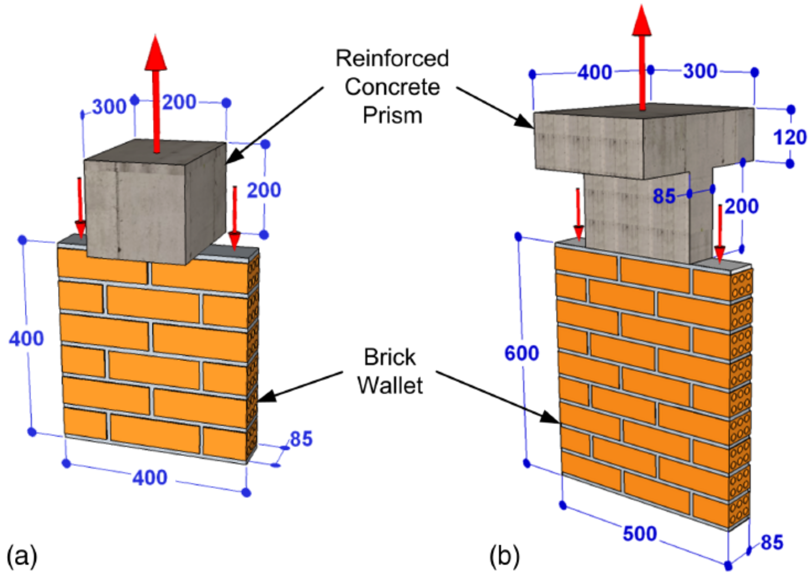

Figure 2.25 – Specimens of Koutas et al. (2013) a) Series A b) Series B.

On Series B, the specimens presented different failure modes, varying between textile rupture, anchor rupture, anchor debonding and brick crushing. One layer of the control with heavy textile resisted a force of 16.75 kN, while the control with light textile resisted to 11.95 kN. The term heavy and light resume the volume of fibres on the textile. Thus, considering the volume of fibres supporting the load, the capacity was similar in both specimens. The same conclusion was reached for two layers of textile. Generally, the anchors contributed significantly on the specimen capacity of load-carrying. Two specimens had its anchors debonded prematurely, the specimens with heavy textile, 400 mm anchor width and 350 mm of fan length (i.e., the part of anchor set-up in contact with the textile). The author attributed this behaviour to the combination of relatively short bond length, and the fact it was bonded on the top of the heavy textile, which produced high shear stresses between the anchor and the textile.

The authors concluded that typical failure of anchors involves debonding through the mortar of TRM system, in their part over the concrete, followed by rupture of the fibres in their bent parts. Also, it was concluded that placing anchors between two layers of TRM is effective due the behaviour of the conjunction.

Larrinaga et al. (2014) performed an experimental program and numerical modelling of basalt TRM behaviour under axial tensile stress. Thirty-one specimens were tested in laboratory, three unreinforced and twenty-eight with internal reinforcement. Four series of one to four layers of TRM were defined. The specimens had cross-section of 100 x 10 mm² and 600 mm in length. Furthermore, a numerical investigation was conducted with two different models: the Aveston-Cooper-Kelly (AKC) (Aveston et al., 1971) theory for inorganic-based composites; and a finite element analysis (FEA).

The test results revealed that while the rupture of the specimen with one layer was smooth, by increasing the number of layers the failure mode became more brittle. Moreover, the crack pattern changed with the amount of layers. The number of cracks increased and the distance between them diminished with the increment of the number of layers. It was noted that the stiffness reduced prior to rupture strain. This behaviour was explained by the debonding between the textile and the matrix, or the progressive rupture of the filaments inside rovings.

From the numerical modelling the results revealed that FEA model presented more close results to the experimental than the ACK theory. At stage III (after the crack being formed and until rupture) the ACK model failed to predict the actual experimental response. That was attributed to the progressive rupture of the filaments inside the rovings and the debonding at the textile-matrix interface, which is not expected by the ACK model.

The FEA model showed to be a good way to simulate TRM in tension, although it presented some discrepancies. The authors suggested simulating the basalt-to-mortar interface as rigid elements, since it will provide accurate results in the three stages (stiffness of the mortar; multiple-crack stage; from the second up to failure, controlled by the basalt elasticity modulus) observed on experiments.

Tetta et al. (2015) conducted an experimental program to study the shear strengthening of rectangular RC beams with TRM and FRP. Fourteen half-scaled beams were tested as simply supported in (non-symmetric) three-point bending scheme. Specimens were designed to fail in shear, so, the load was applied not in the mid-span. In this configuration, the short span had no shear reinforcement while the longer had 8 mm diameter bars spaced each 75 mm. Where the beam had no shear reinforcement, the specimens, excluding the control, were strengthened with FRP or TRM. The parameters analysed were: (i) the strengthening system, (ii) the strengthening configuration, (iii) the number of layers.

Amongst specimens strengthened with FRP, those wrapped laterally and in a 'U' shape configuration failed in shear at an ultimate load considerably higher than the control specimen. For example, the specimen with two layers of FRP and U-shaped system increased 143% of shear capacity from the control specimen. Some beams of this group failed by debonding of FRP with a layer of concrete attached to the jacket. Fully wrapped beam with one layer of FRP increased 2.8 times the shear capacity, reached the ultimate moment capacity and failed by the crushing of concrete after yielding of the longitudinal reinforcement.

About the TRM group, with exemption of the fully wrapped with two layers of TRM, which failed in flexure, all the others failed in shear, increasing the shear capacity up to 150%. Failure of specimens with one layer was associated to the damage of TRM jackets. On those specimens with two layers (excluding the fully wrapped), the failure was associated to debonding of TRM jacket at approximately 2/3 of the shear span which was accompanied by peeling off the concrete cover. Specimens with three layers failed in similar way to those with two layers. The specimen with U-shaped jacket and three layers of TRM failed with total debonding of the jacket and had it failure as explosive as any other specimen.

It was observed that applying U-shaped jackets was more effective than applying only lateral strengthening, and it was more representative on TRM specimens. Fully wrapped specimens were by far better than the others.

Considering the number of layers, it was observed that adding more layers enhance more the shear capacity in specimens with TRM than in FRP. From two to three layers this increment followed the same pattern described before, with exemption of the fully wrapped specimen, where the shear capacity was increased in the same proportion on TRM and FRP retrofitted beams.

It was observed that the failure mode has changed by increasing the number of layers from one to two or three on TRM-wrapped specimens. It passed from slippage of the vertical fibre rooving through the mortar and partial fibre rupture, in one-layer jackets, to debonding of the jacket, in two or three layers or strengthening. The authors associated this fact to the interlocking mechanism created by two or more layers of textile.

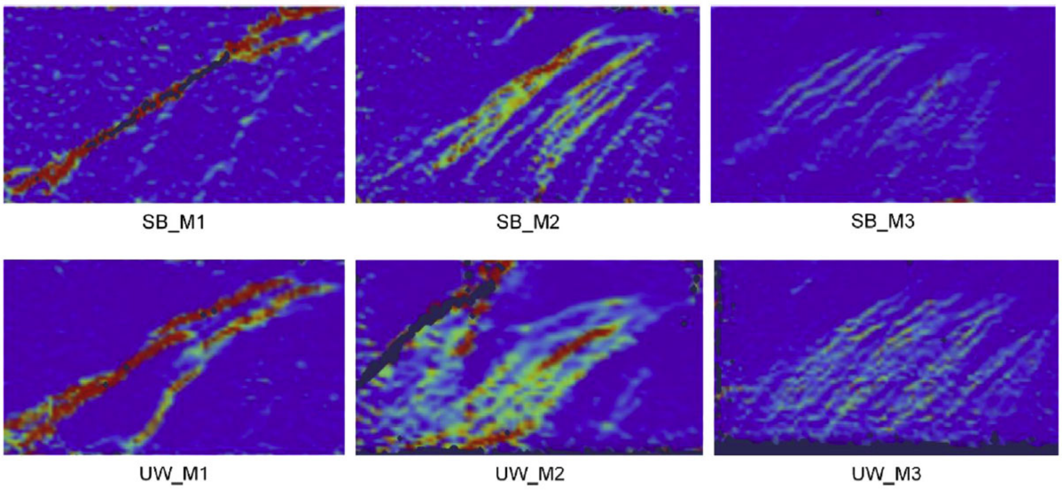

Figure 2.26 – Crack pattern on TRM-wrapped specimens (Tetta et al., 2015).

Figure 2.26 shows the cracks formed in some specimens. It is possible to analyse the change from one major crack on specimens with one layer of TRM to better distributed smaller cracks on specimens with two or three layers. 'SB' means side-bonded and 'UW' U-shaped wrapped. 'M' refers to the binder material, in this case mortar, and the number after that is the amount of layers.

The authors used the concept of effective strain, defined by them as the effective stress divided by the modulus of elasticity. Effective stress is defined as the average stress of the fibres crossing the shear crack. It was noted that TRM jackets were less effective than FRP jackets, although this parameter can be influenced by factors as the number of layers and the strengthening configuration.

Tetta et al. (2016) have studied the shear strengthening of RC T-beams with TRM associated to textile-based anchors. To perform such study, tests were conducted on simply supported T-beams, with a point of load appliance at an assymetrical position considering the supports. A total of 11 beams were tested observing the usage of textile-based anchors for U-shaped TRM jacket, the numbers of TRM layers, the textile geometry, the textile material, the comparison between TRM and FRP.

The equivalence between number of layers and material was provided according to the stiffness of the element, where carbon fibre was highlighted amongst materials. Comparing heavy and light carbon fibres, it was observed that 3 layers of light carbon was equivalent ot 2 layers of heavy carbon fibres. Moreover, an upper limit to the anchor strength was provided, derived from cupon test, reaching 2455 MPa of tensile strength and 1.85% of ultimate strain. Additionally, a strengthening procedure was provided.

Results demonstrated that U-shaped jackets without anchors lead to an increment of the shear resistance in up to 77.4% compared to the non-strengthend one. Moreover, to achieve similar value with glass fibres, seven layers had to be used. When textile-based anchors were used the shear resistance of the beam increased in up to 191.1%. Additionally, the debonding of the jacket was delayed when compared to the non-anchored counterpart. Depending on the characteristics of the strengthening, the failure was associated to debonding of the sheet, rupture of the fibres, pull out of the anchors, and fracture of the jacket. In cases as the beam strengthened with three layers of light carbon fibre and presence of anchors, the failure was due to the rupture of some anchors and pull-off of others. Differences on specimens with TRM and FRP were negligible.

The authors also provide a design methodology to be used when designing strengthening of RC members agains shear. This methodology also includes a reduction factor to the anchorage strength due to the local concentration of stress and the non-uniform distribution of stress amongst anchors.

Current studies on TRM have demonstrated the potential of the technique on strengthening structural elements both for flexure and for shear. The solution was compared to other existing well stablished solution, the FRP. TRM was observed to be more ductile in flexure (Bournas et al., 2007), as well as in shear when associated to textile-based anchors (Tetta et al., 2016). When those anchors were not used, the failure of the strengthened beam was presented to be more explosive (Tetta et al., 2015). The parameters of the textile-based anchors, method of appliance, failure modes, its interaction with TRM, as well as the adequate type of textile to be used could be identified (Koutas et al., 2013, Tetta et al., 2016). Moreover, the simulations involving TRM were shown to be more representative when using FEM (Larrinaga et al., 2014).

2.4.4 Alternative Methods

Hadi and Saeed Alrudaini (2012) proposed a new method to retrofit RC structures against progressive collapse. In an effort to provide Alternate Load Paths (ALP) to the loads after the collapse of a column, the authors aimed to increase the redundancy of the building. The method consisted on placing vertical cables connected at the end of beams and hung on a hat steel braced frame which redistribute these loads to adjacent columns. This scheme is proposed to be applied after the building being constructed. Figure 2.27 provides an overview of this method. Numerical investigation of a 10-story RC building was conducted in this work to address the new scheme proposed.

The authors further conducted numerical simulations using three-dimensional frame elements. To account for the potential plastic hinges, the inelastic behaviour of beams was modelled with help of nonlinear rotational springs at the end of each beam. The moment of inertia of beams used was half of the un-cracked moment of inertia, and for columns the moment of inertia was 0.7 of the un-cracked moment of inertia. Members of the top hat-braced frame were modelled using 3D frame elements and the bracings were modelled using axial elements capable of carrying axial compression and tension forces.

Cables were modelled using axial elements with tension-only capability. Hat-braced frame was linked to the columns using contact elements allowing only the transference of compression forces from the hat-braced frame to the columns. To connect the cables nodes with the hat-braced frame nodes, rigid beam elements were used. This allowed the loads to be transferred from the cable to the hat-braced frame.

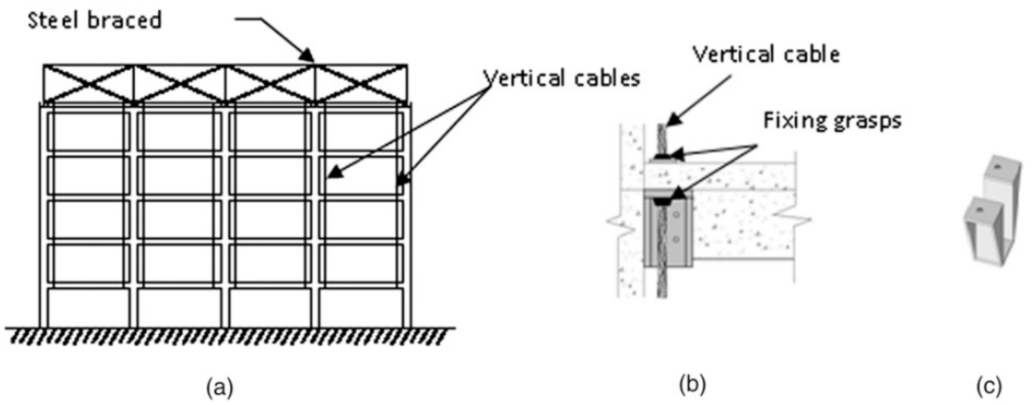

Figure 2.27 – System proposed a) cable configuration; b) cable connection at the beam c) hanging seat of the beam (Hadi and Saeed Alrudaini, 2012).

To address the different column compressive and tensile stiffness, for the columns above the removed one, the authors combined two elements: a 3D elastic frame element, with only a defined section moment of inertia to account for the bending capacity; and a nonlinear axial line element, accounting for the compressive and tensile stiffness. The method of assessment was a nonlinear dynamic analysis in conjunction with ALP method. The load was imposed until the full capacity and it was kept constant for a time. Then, the column was removed suddenly, and the time history response of the building was tracked.

A 10-story building consisting in four longitudinal by four transverse bays of 6.5 m centre-to-centre span length was assessed. The height of the first story was 5 m and the others had 3 m height. Three independent columns removal scenarios were considered in this study. The first was the penultimate internal column, the second was the penultimate external, and the third was the corner column.

The effectiveness of the proposed scheme was confirmed on the simulations where the displacements and rotations measured were lower than those of the unretrofitted model. Furthermore, it was observed that the lower floors (close to the lost column) suffer higher displacements than those on the top floors. It was also observed that instantaneously to the loss of the column the cables were tensioned above the failed column. Moreover, the tension developed in those cables was less than their capacity, working in the elastic range.

Tsai (2012) proposed a performance-based approach to promote the collapse resistance of regular building frames under sudden column loss using steel braces. The author idealized a SDOF system, from which were developed analytical formulations of the proposed design approach accordingly with its pseudo-static response. Nonlinear dynamic analyses were carried out to evaluate the validity of the approach for practical applications.

The SDOF model consisted of three parallel springs presented in Figure 2.28. K_b comprises the elastic stiffness of frame members while K_a stands for the elastic stiffness provided by the braces added. P_{cc} is obtained through a step force function representing the dynamic load of the model under column loss.

The author obtained the pseudo-static response of the SDOF system with and without the brace spring. This was determined from a nonlinear static analysis procedure. Maximum dynamic displacements, acquired from nonlinear time-history analyses in a sudden released downward loading scenario, were compared to the pseudo-static predictions.

It was observed that the pseudo-static prediction agrees with the maximum dynamic response and it can be used to estimate the performance of structural frames with added elasto-plastic braces under specific load demands.

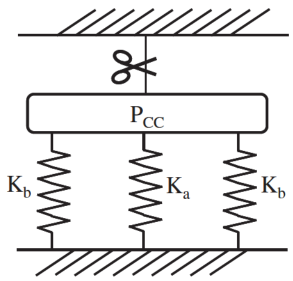

Figure 2.28 – Idealized SDOF system by Tsai (2012).

To assess the application of the model to building frames, two steel (Figure 2.29(a) and (b)) models and one RC (Figure 2.29(c)) moment-resisting frame model were constructed by using the commercial analysis program SAP2000 (Wilson, 1997). Figure 2.29 shows the models, the continuous line are the frame and the dashed lines are the braces.

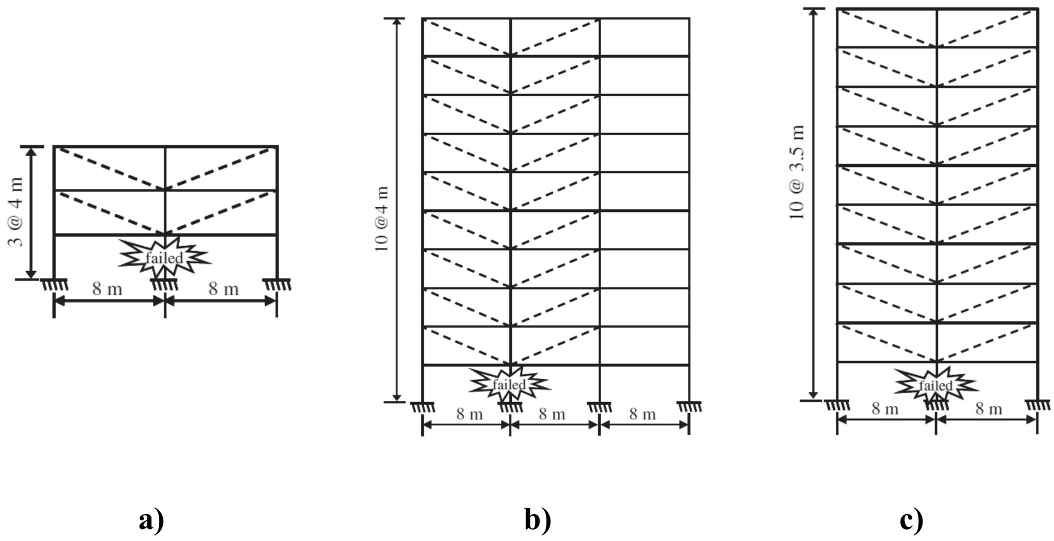

Figure 2.29 – Models a) three-story steel frame b) ten-story steel frame c) ten-story RC frame (Tsai, 2012).

The models without retrofitting had its resistance and ductility capacity determined from nonlinear static pushdown analyses. After that, elasto-plastic axial members, designed intentionally to sustain tensile loading, were placed to simulate the braces.

The results showed that stiffness and strength of the retrofitted frames were generally larger than the expected structural response. By comparing the collapse resistance and the displacements of the braced frames the author observed that the proposed design may result in a conservative structural performance.

The performance precision was revised to present results closer to the real behaviour. After that, nonlinear static analyses were carried out to update the pseudo-static response curves. Both the unretrofitted and retrofitted model had, after few iterations, its ductility demand and collapse resistance approximated to the design targets and the desired pseudo-static response. Consequently, the maximum dynamic demand of the braced frame was well captured with the model.

Finally, for frame models with braces with strength of 248 MPa, nonlinear time history analysis was carried out to assess the accuracy of the proposed retrofit design procedure, which is based on nonlinear static approach. It was observed that the design procedure is accurate and conservative and can provide satisfactory results.

Kim and Shin (2013) studied RC structures retrofitted against progressive collapse in a column removal scenario by prestressing tendons positioned strategically on the frame (Figure 2.30). Analytical models were prepared to conduct the research, consisting in six-story structures with three-by-four bays and twenty-story structures with three-by-three bays.

Both nonlinear static and nonlinear dynamic analyses were conducted. In the former the load was applied on the spans bearing the removed column (Figure 2.31(a)), whereas in the last the load was imposed on all spans (Figure 2.31(b)). On the dynamic analysis the axial load acting on the column was applied before this column being removed. After that, the column was replaced by a load equivalent to its member forces as a reaction force. To simulate the sudden removal, the authors removed the member force suddenly after few seconds were elapsed, while the gravity load was maintained constant.

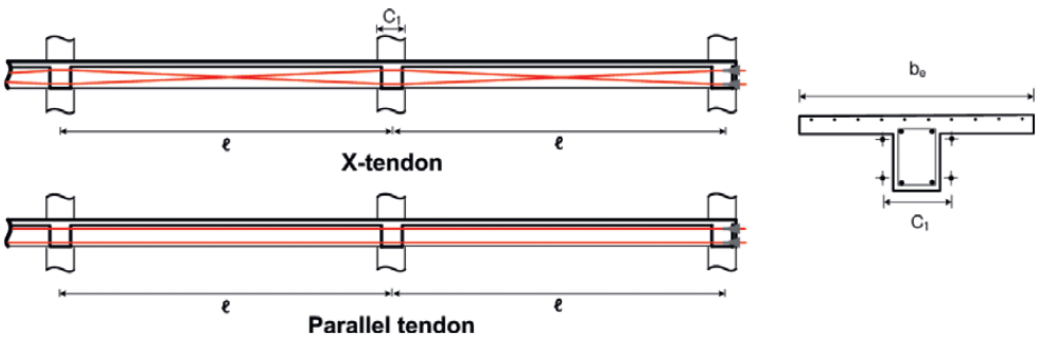

Figure 2.30 – Configuration of tendons (Kim and Shin, 2013).

It was observed after the simulation with the first frame (six-story) that the unretrofitted structure failed right after the column was removed. On the other hand, the retrofitted structures remained stable and the vertical displacement decreased as the initial tension and cross-sectional area of the tendons increased. The authors observed that when the initial tension on the tendons was 2372 kN the structure remained elastic after column removal. However, when the initial tension was not applied, large inelastic deformations were observed.

For this same frame, it was observed that when the number of floors fitted with tendons increased (above the failed column), the resistance to progressive collapse was increased as well. Moreover, the effectiveness of the tendons was observed more significant when an interior column is removed. Furthermore, X-tendon were more effective than the parallel tendons.

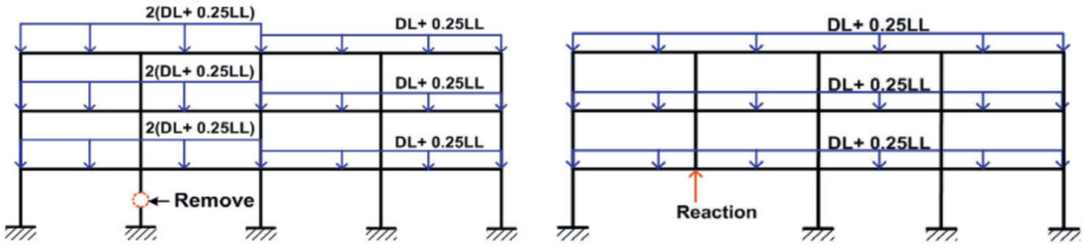

a) **b)**

Figure 2.31 – Load applied in Kim and Shin (2013) a) nonlinear static load b) nonlinear dynamic load.

For the second frame (twenty-story) the usage of the x-tendon was assessed. The same observations on the last frame applied to this one. Structures retrofitted remained stable after the column removal, while those unretrofitted failed.

The authors concluded that the General Service Administration, GSA (2003), recommendation to the dynamic response factor to ensure safety against progressive collapse may be too conservative since they found values 40% lower than that presented on the guidelines.

Finally, the seismic performance of a six-story building was assessed through computational model and it was observed that the structures did not have their natural periods changed after retrofitted with the tendons.

In this last section, the most recent alternative methods of retrofitting structures against progressive collapse generated by the loss of a column could be presented. In these it was possible to identify the current practices on modeling the problem with different approaches, be it analytical or complex FEM model (Hadi and Saeed Alrudaini, 2012, Tsai, 2012, Kim and Shin, 2013). Moreover, the modeling approach to simulate static scenarios, as well as the assessment of the DIF and the confirmation of the conservative values adopted by GSA (2003) stands out as a robust methodology to assess the effectiveness of a strengthening solution in a concise manner (Kim and Shin, 2013).

This page was left intentionally blank

CHAPTER 3 EXPERIMENTAL PROGRAM

3.1 Introduction

In this project, an experimental program was conducted to assess the structural behaviour of a reinforced concrete (RC) frame, designed based in pre-1968 UK specifications, in a column removal scenario, strengthened with TRM and NSM reinforcement. More specifically, the influence of anchored TRM jacketing and NSM reinforcement on the RC frames' internal mechanisms of defence, i.e., flexural resistance, the CAA and the TCA, is examined. Furthermore, the influence of shear strengthening of the beam with TRM U-shaped jacket on the RC frame progressive collapse mechanism is also examined.

From the literature review (Husain and Tsopelas, 2004, Dat and Tan, 2014, Qian et al., 2014, Dat et al., 2015) it could be observed that the continuity of the structure in adjacent bays to the failed one is important to the progressive collapse resistance of the building. When a penultimate column is removed, the redistribution of load is asymetrical (Dat and Tan, 2014). When a corner column is removed, the resistance is associated to the structural elements in both orthogonal directions of the column (Qian et al., 2014). Moreover, the presence of slabs and transversal beams have significant influence on the structure resistance. Therefore, to simplify the complexity, the case of a portion of 2D peripheral frame of a multi-story building is considered where the middle column is removed (Figure 3.1). Additionally, given that a peripheral frame is assessed, the slab above the beam would be expected to be at one side of the beam only. However, this configuration would cause an out-of-plane asymmetry on the failure, since the TRM for shear would wrap the beam at one side and be anchored at the other side. Therefore, to simplify the assessment of the performance of the textile-based anchors, a T-beam was considered.

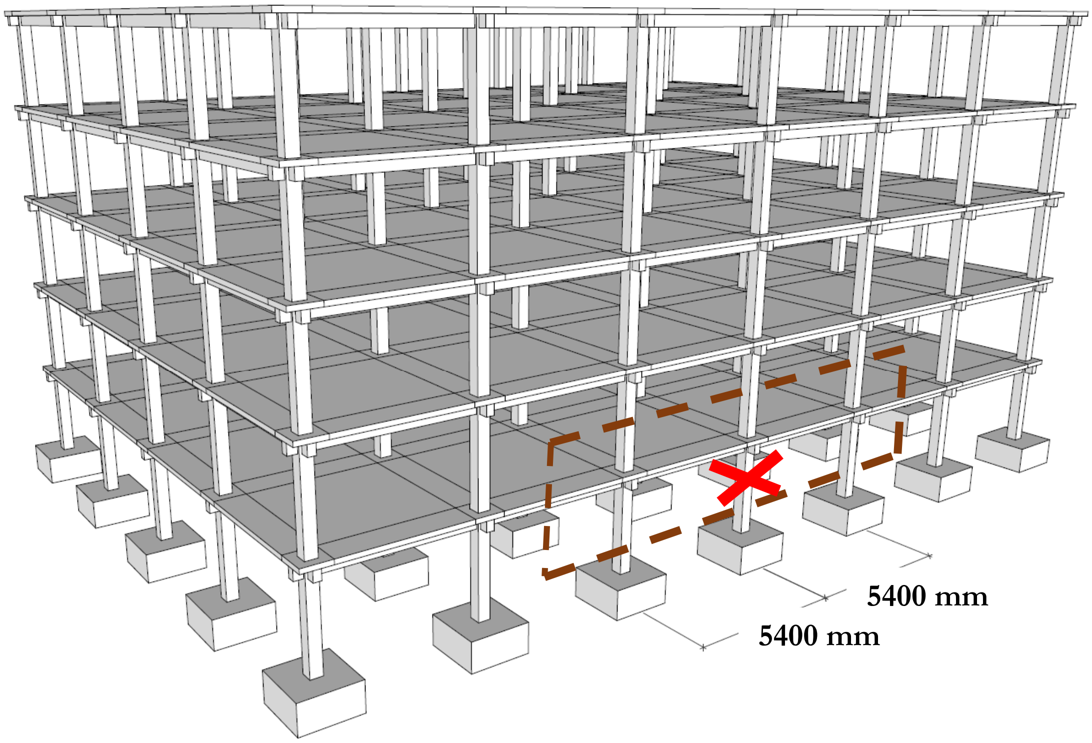

Figure 3.1 – Structure assessed.

The contrubition of the strengthening methods adopted will be assessed vis-à-vis the response of a control, i.e., non-strengthened specimen. This control specimen is a half-scaled subassemblage of a portion of a multistorey building. In the original structure each beam was assumed to carry a 27.5 kN/m of uniformly distributed load accounting to a 5kN/m² dead load and a 6 kN/m² distributed over the area of one-span slabs. The loads were assumed to pertain to a high congregation building, e.g., a concert hall.

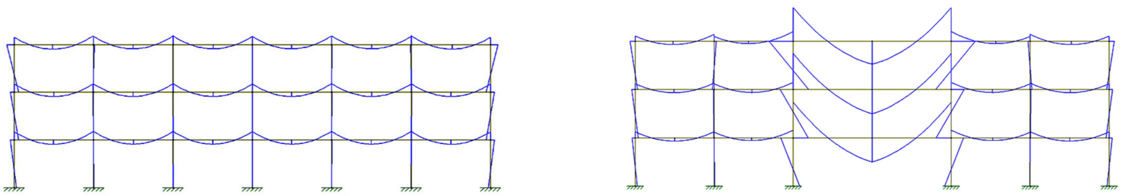

a) b)

Figure 3.2 – Change in the moment diagram caused by a column removal a) frame with the column b) frame without the column.

In Figure 3.2 one can see that the moment diagram is dramatically changed when a column is removed from a frame. As mentioned, in new designs it is possible to adapt the internal reinforcement to resist the new moment diagram. However, for old designed buildings an intervention is needed, such as an external strengthening.

The assessment of the efficiency of the strengthening methods was performed through half-scale specimens via quasi-static procedure. Its results were properly adapted to obtain estimates for the corresponding dynamic response as per literature suggestions (GSA, 2003, Izzuddin et al., 2008, DoD, 2009, McKay et al., 2012).

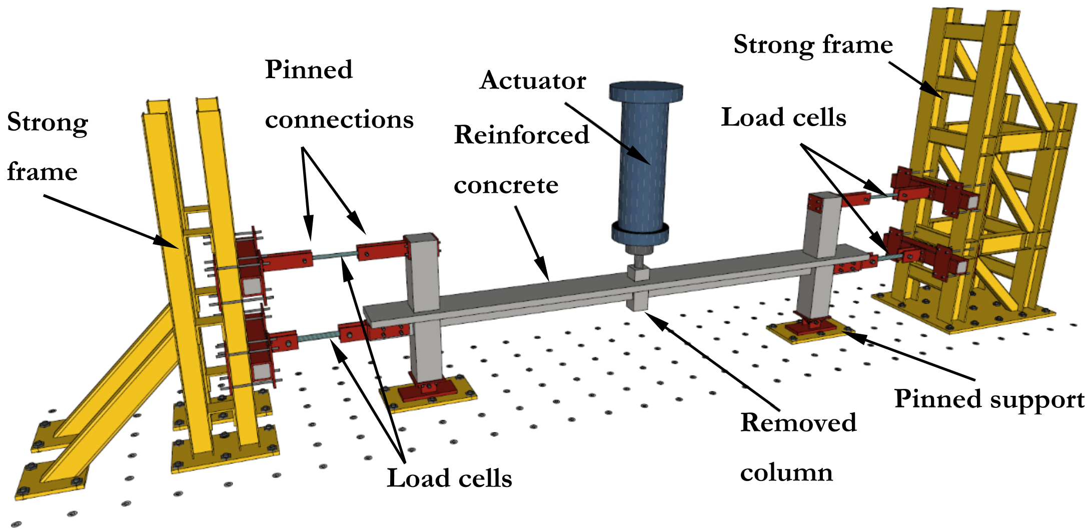

Figure 3.3 – Experiment configuration.

The experiments consisted of a subassembly of a peripheral frame of a multi-story building, composed by two side columns (300x300 mm) and a middle column (200x200 mm) connected by a 'T' beam. The beam extended beyond side columns to account for the continuity of the frame, where were connected through a steel set-up to strong frames at each side. Moreover, the side columns were pin-jointed at the strong floor, while at the top were connected to the strong frames through a steel set-up as well. An hydraulic actuator applied a displacement at the top of the middle column using a rate of 0.1mm/s. Figure 3.3 presents the experiment's configuration.

It is of interest to note that the increased axial loads transmitted to the side columns from the upper stories during a column removal scenario would affect the response of the sub-assemblage primarily by acting on the strength and rotational capacity of the edge columns. Since the aim of the present work is to perform a comparative study on the effectiveness of different strengthening procedures, as previously mentioned, the idea is to reduce the complexity of the experimental setup. Therefore, a similar test set-up with other experimental works, e.g. Yu and Tan (2012, 2013) and Stathas et al. 2017b, that did not consider the end columns axial load was adopted for brevity. Since the strengthening strategy focused on the span rather than on the side columns, we expect that the relative gains to be similar to these if the axial forces have been accounted.

Considering the above described subassembly, the failure mode, as witnessed in the literature (Yu and Tan, 2012, Yu and Tan, 2013b, Tsai and Chang, 2015), is expected to be composed by: flexural cracks at the beginning; then concrete crush at the bottom of the beam at the vicinity of the side joints; this will be followed by plastic hinges formed at the beam near the columns; following, with catenary action working, tensile cracks along the entire beam; finally, the reinforcement, which slipped during the evolution of the verical deflection, can be lead to fracture at the position of the plastic hinges.

Specimen	Description
CON	Control specimen
NSM_PR	Stainless steel reinforcement NSM reinforcement for flexural strengthening. Epoxy resin was used in this specimen as binder material. Partial strengthening for shear was used, it means that part of the beam was retrofitted with TRM, while part of it remained without strengthening.
TRM_TR	Anchored TRM for flexural strengthening. Total strengthening of the beam for shear was used
NSM_TR	Stainless steel NSM reinforcement for flexural strengthening. Epoxy resin was used in this specimen as binder material for NSM. Total strengthening of the beam for shear was used.

Table 3.1 - Specimens Identification.

Considering the expected failure mode, the strengthening layout should delay the occurrence of the main failure mechanisms in the beam, preferably result in a distributed rather than localised evolution of damage. In parallel, it should allow the frame to rotate when reaching large deflections to facilitate the development of the TCA. Moreover, this strengthening scheme should increase the load capacity of the frame while providing a better energy absorption capacity. Therefore, TRM and NSM reinforcement were adopted as strengthening materials given its deformation capacities, as well as load carrying potentials.

In total 4 specimens were tested with different configurations and materials of strengthening (Table 3.1). Each specimen was designed as a two-span beam considering detailing practices typical to pre-1968 design specifications in the UK. Following, the diagrams of the mould, reinforcement, continuity, instrumentation and strengthening of each specimen are presented.

3.2 Test Set-up

3.2.1 Mould

Figure 3.4 shows the specimen mould. The length of the side columns is regard to the point of null moment considering the undamaged structure. Likewise, the length of the beams beyond side columns were extended following the same principle. The position of the pins on the test set-up (Figure 3.3) correspond to those mentioned points.

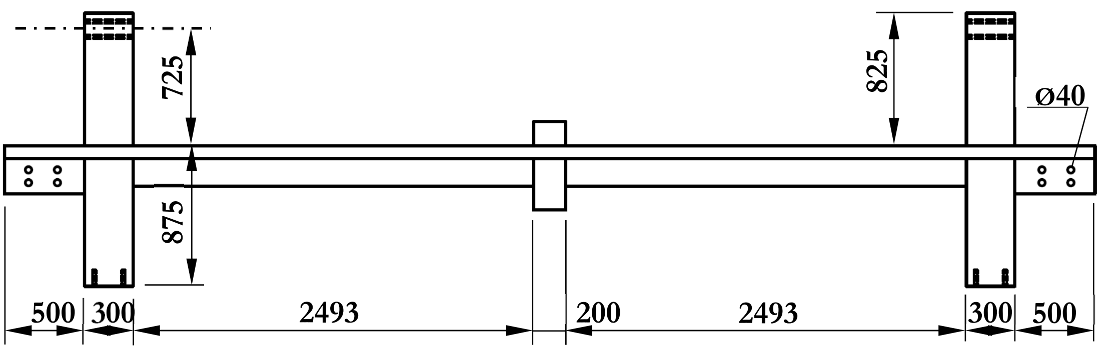

Figure 3.4 – Specimen mould (dimensions in mm).

In each side beam there are four 40 mm holes, designed to perform the transference of load from the concrete to the strong frames. The slab was considered to simulate the portion which contributes on the beam flexural resistance, as well as to anchor the TRM (Figure 3.5).

At the bottom of this column a support was used up to the test day, when it was removed. Figure 3.6 shows the mould in the place where it was casted. The casting process was divided in two steps: first, all the volume of concrete below the slab was applied; then, in the following day, the concrete of the top of the columns. Before casting the specimen, an anti-adherent was applied on the mould to facilitate its removal.

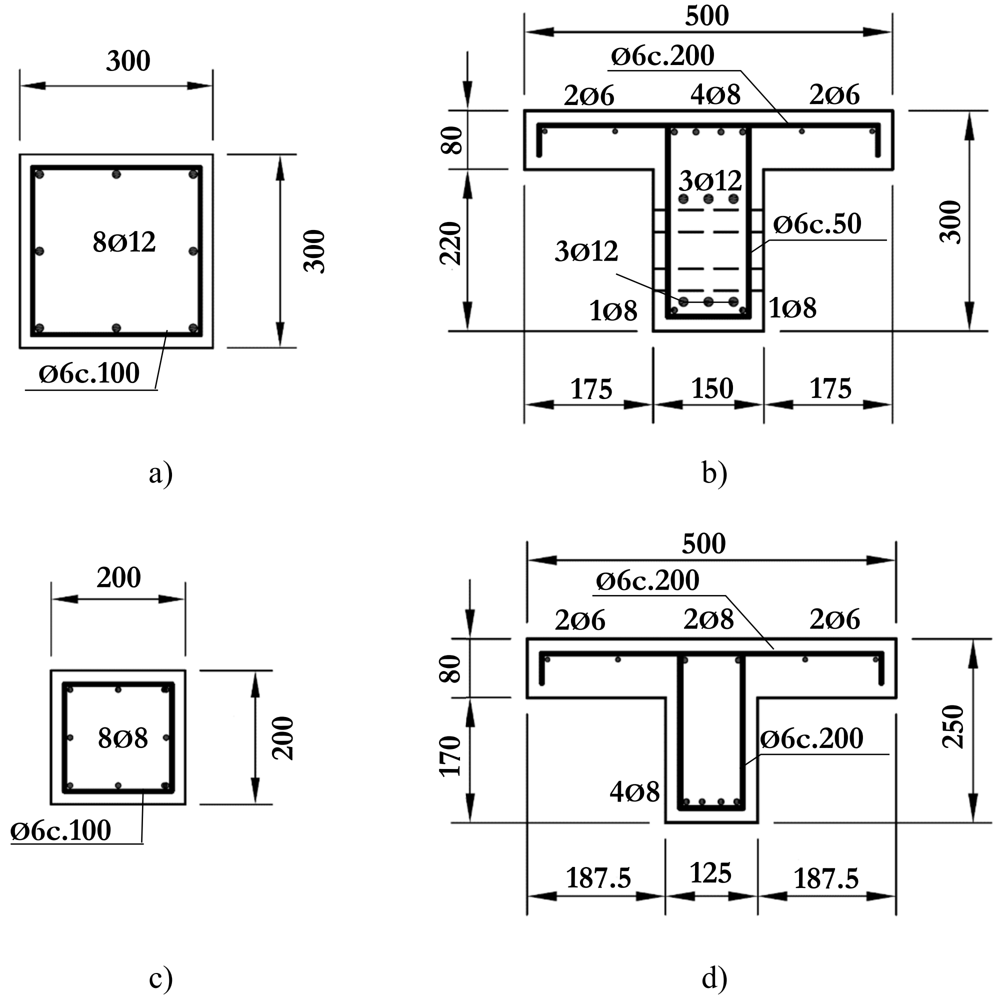

Figure 3.5 – Cross sections of the frame elements a) side columns b) beam, beyond side columns c) middle column d) beam, mid-span between columns (dimensions in mm).

a)

b)

Figure 3.6 – Specimen mould a) Assembling the mould b) Casted specimen.

3.2.2 Reinforcement

The general reinforcement is presented in Figure 3.5 and Figure 3.7, where the former shows the cross sections of the frame elements with the respective reinforcements, and the second presents an additional data of the frame reinforcement, designed originally as a two-span beam. Longitudinal reinforcement comprised two 8 mm bars at the bottom of the beam and two at the top, both with a lap-splice after the middle column. Two additional 8 mm longitudinal bars were used as midspan reinforcement (considering the original 3 columns configuration) and bent upwards at the supports (see N1 on Figure 3.7).

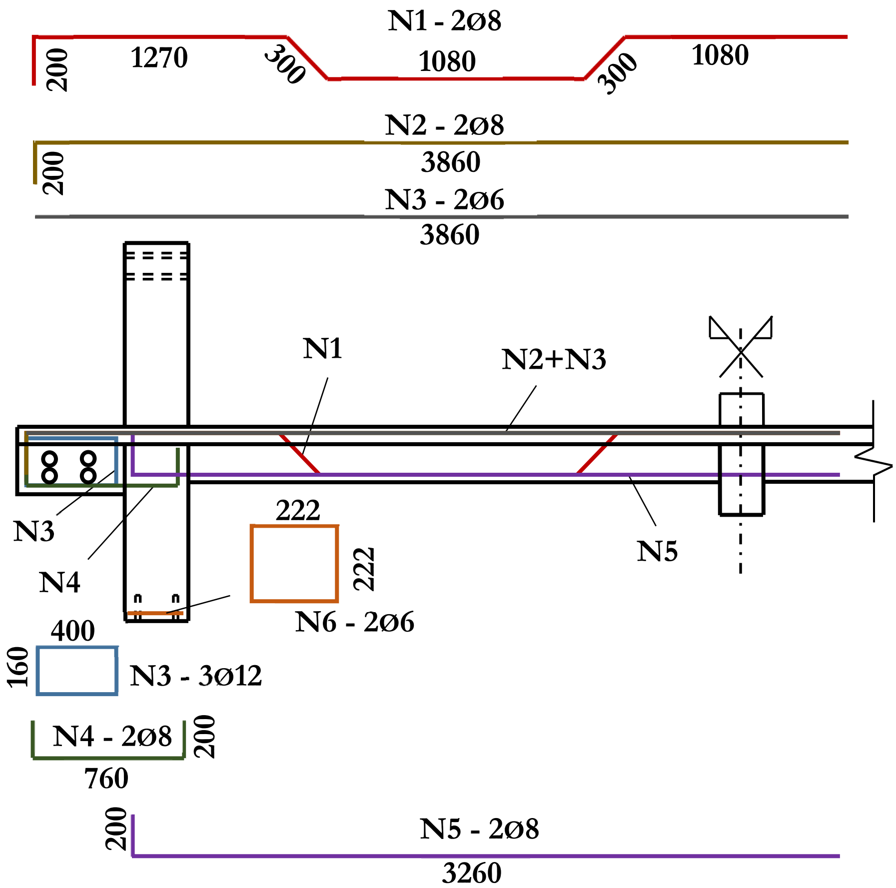

Figure 3.7 – Internal reinforcement (dimensions in mm).

Shear reinforcement comprised 6 mm smooth bars centered at 200 mm spacing, i.e., 13 in each side of the middle columns. To prevent shear failure at the supports, spacing was reduced to 50 mm at the beam extensions to the left and right of the corresponding columns. The T-beam flange had a 500 mm width and 4 longitudinal bars of 6 mm diameter each. The transversal reinforcement for the slabs comprised 6 mm smooth bars spaced each 200 mm.

The side columns were overdesigned to force the collapse to happen at the beam between those columns. Each side column had 8 of 12 mm bars as longitudinal reinforcement, while the middle one had 8 of 8 mm. Each column had 6 mm smooth bars for transversal reinforcement separated each 100 mm. Hence, the side columns have been designed to sustain a maximum applied load at the assembly equal to 300 kN, i.e, 3 times higher than the failure load of the control specimen. Additional reinforcement (N3 and N6 on Figure 3.7) was provided to mitigate any localized failure modes at the beam to column joints. Furthermore, the length of each part of the bar is given close the correspondent part. Figure 3.8 shows the assemblage of the reinforcement.

Figure 3.8 – Assemblage of the internal reinforcement.

3.2.3 Continuity

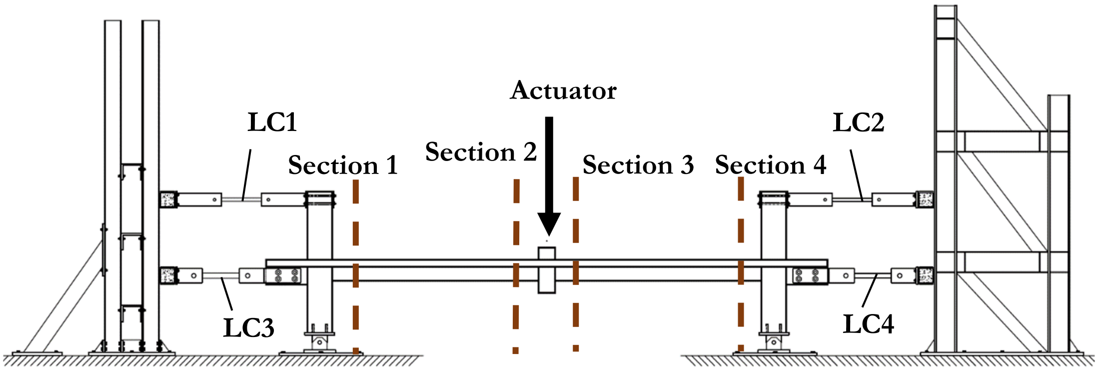

Figure 3.9 – Experiment frontal view.

To simulate the actual scenario, where the beam continues beyond both side columns, a steel set-up was appropriately designed. As mentioned previously, the specimen was attached in four points to strong frames, two at both sides, additionally, at the bottom of the side columns to a strong floor. To achieve the simulation of real behaviour steel plates, pins, threaded rods, steel tubes filled with concrete, lifting eyes and bars were used as per shown in Figure 3.9 and Figure 3.10.

a)

b)

Figure 3.10 – Test Set-up a) Assembled b) Detail.

3.2.4 Instrumentation

3.2.4.1 Strain Gauges

Despite the information from the strain gauges could not be used due to malfunction of the equipment, here the scheme adopted to measure strains along the beam is presented. In total, 16 SGs were installed in the beam, the distribution of each one was designed as following: 4 SGs on the longitudinal reinforcement at the top of the beam, on sections 1 and 4 (see Figure 3.9); 2 SGs on the longitudinal reinforcement at the bottom of the beam, sections 2 and 3 (see Figure 3.9); and 4 SGs on the longitudinal reinforcement at the bottom of the beam, inside the middle column. The distribution of the SGs on the reinforcement can be observed in Figure 3.11. In Figure 3.12 a demonstration of SGs placed on the reinforcement is presented.

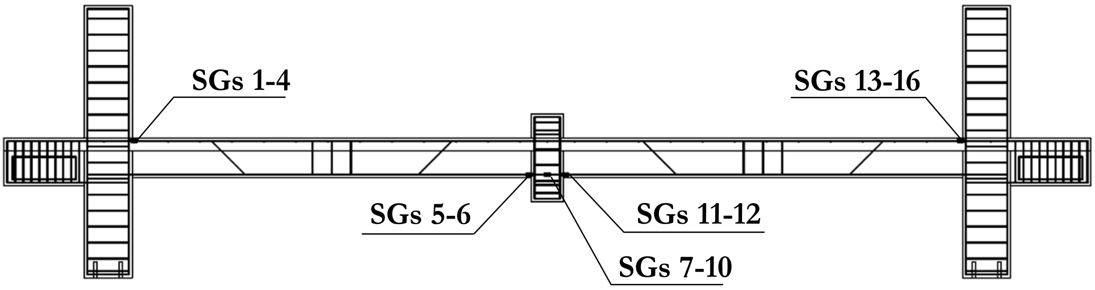

Figure 3.11 – Strain gauges on the beam reinforcement.

Figure 3.12 – Strain Gauges attached to the reinforcement.

3.2.4.2 Load Cells

Apart of the 16 SGs installed on the longitudinal reinforcement, other 16 were used on steel bars identified in Figure 3.9 as LC1, LC2, LC3 and LC4. With 4 SGs strategically positioned in each steel bar (see Wheatstone Bridge section), its axial displacements could be converted in strains. Thus, with the strains and the properties of each steel bar, those strains could be converted in loads. Therefore, each steel bar positioned as presented in Figure 3.9 worked as a load cell, measuring both compression and tension. These were calibrated through three compression tests, from where the elastic modulus of each one was achieved, which was around 212 GPa.

Wheatstone Bridge

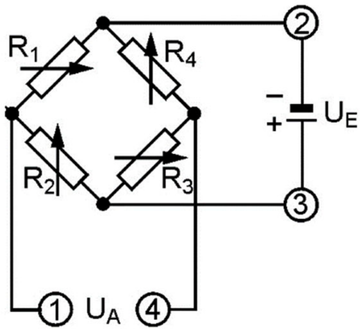

Figure 3.13 – Example of full Wheatstone Bridge connection (Hoffmann, 1974).

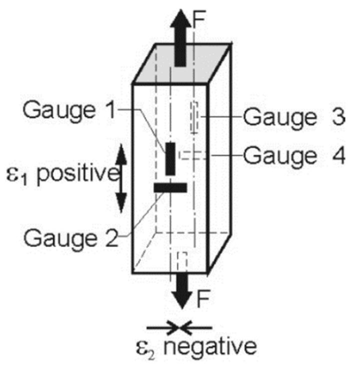

Figure 3.14 – Configuration of the strain gauges in a bar over axial tension, (Hoffmann, 1974).

The Strain Gauge (SG) works with an internal resistance and for each deformation of the piece measured there is a change in resistance. By using a conversion factor, provided in each strain gauge package, the changes in resistances can be represented as changes in strains. In the full Wheatstone Bridge connection, the SGs are arranged in a specific way so the strains in both longitudinal and transversal directions are addressed in its measurement. Figure 3.13 presents this connection.

Figure 3.15 – Full Wheatstone Bridge connection on the steel bars.

Each "R" is a resistance (SG) and each numbered node is a connection point. UE stands for the bridge excitation (input) voltage and UA is the output voltage. The resistances R1 and R3 are put in the same direction as well as the resistances R2 and R4. Figure 3.14 presents the configuration for a bar over axial tension.

Figure 3.15 shows the full Wheatstone Bridge connection installed in one of the experiment steel bars. For a more detailed explanation about Wheatstone Bridge it is suggested consulting Hoffmann (1974).

3.2.4.3 Potentiometers

A total of 23 potentiometers was used to measure rotations and displacements along the beam during the tests. Based on Yu and Tan (2013b) work, the configuration of potentiometers to measure beam rotations are those numbered from 1 to 16. Potentiometers 17 to 19 measured vertical displacements along the beam. At the column, the potentiometers, numbered from 20 to 23, were placed in a typical X configuration. All the potentiometers positions are presented in Figure 3.16.

A set of 4 potentiometers was used to measure the rotations at sections 1 to 4 (see Figure 3.9) (see also Section 3.5.2). According to Yu and Tan (2013b), the rotations of the beam-column connection are formed by shear, flexural, and fixed-end rotations. The former can be ignored due the small contribution of shear on the failure mechanism in a two-bay beam. The flexural is affected by many factors, namely material properties of reinforcement and concrete, reinforcement ratios, and beam depth.

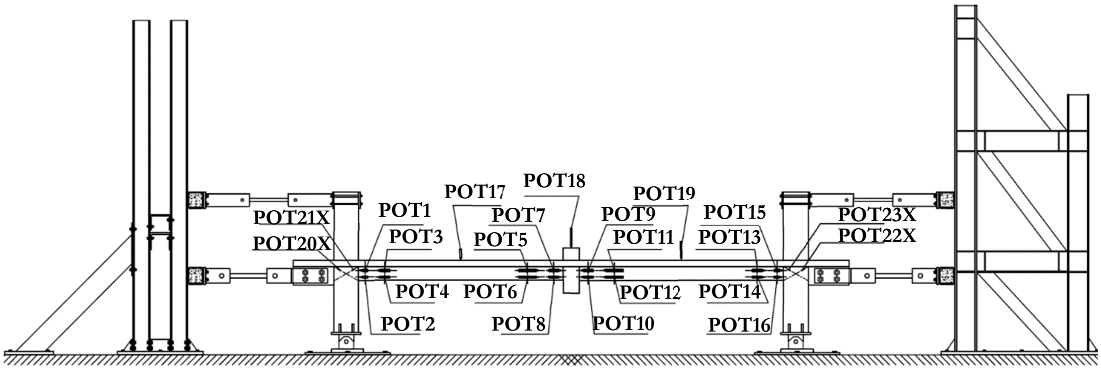

Figure 3.16 – Potentiometers distribution.

3.3 Material Properties

A steel grade S500 was used for the longitudinal steel reinforcement and S250 for the smooth shear links. The target compressive strength of concrete was determined through sample tests on the day of testing, according to BS EN 12390-3:2009 (EN, 2009), and was found to be 19.5 MPa for the control specimen and 21.5 MPa, 22.3, and 23.0 MPa for specimens NSM_PR, TRM_TR and NSM_TR, respectively. The mean value, standard deviation and corresponding coefficient of variation are shown in Table 3.2. Compression tests were conducted with 150 mm cubes and tensile tests through cylinders with 150 mm diameter and 300 mm high.

Specimen	Mean Compressive Strength (MPa)	Mean Tensile Strength (MPa)	Standard Deviation		Coefficient of Variation	
			Compressive Strength	Tensile Strength	Compressive Strength	Tensile Strength
CON	19.5	2.1	0.66	0.06	0.035	0.032
NSM_PR	21.5	2.1	0.36	0.13	0.017	0.062
TRM_TR	22.3	2.3	0.38	0.08	0.018	0.042
NSM_TR	23.0	2.2	1.52	0.16	0.066	0.072

Table 3.2 - Concrete data.

Stainless-steel bars were used for the NSM reinforcement with a tensile strength of 650 MPa and an elastic modulus of 200 GPa. The binder material chosen to fill the NSM groove was an epoxy resin with 30 MPa of tensile strength and an elastic modulus equal to 3.8 GPa as per the manufacturer datasheets.

Two types of textile fibre material were used in this work, i.e., light carbon and heavy carbon fibre textile. The corresponding material properties are shown in Table 3.3 as per manufacturer datasheet.

The strengthening mortar employed had a water to binder ratio of 0.23:1 measured by weight. The compressive and flexural strengths of the mortar were obtained according to EN1015-22 (EN, 1999) through tests on groups of three 40 x 40 x 160 mm prisms, performed on the day of the test. The corresponding material properties with respective standard deviation are shown in Table 3.4.

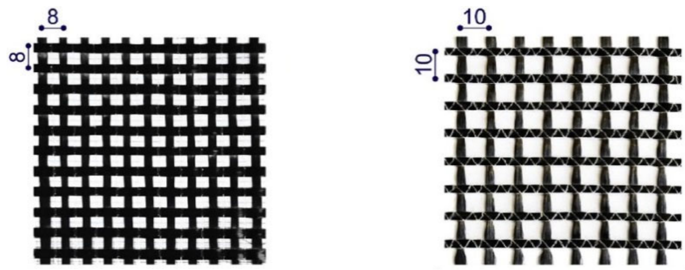

Type of fibre	Light Carbon Fibres	Heavy Carbon Fibres
Elastic Modulus [GPa]	225	225
Tensile Strength [MPa]	4800	3800
Nominal Thickness [mm]	0.062	0.095
Weight [g/m²]	220	348

Table 3.3 – Carbon fibres properties

Specimen	Mortar strength (MPa)	
	Compressive	Flexural
CON	-	-
NSM_PR	30.1 (2.11)	10.23 (0.46)
TRM_TR	31.8 (0.78)	9.48 (1.00)
NSM_TR	36.8 (2.16)	7.60 (0.57)

Table 3.4 – Mortar strengths.

Two types of textile-based anchors, i.e., for shear and flexural TRM reinforcement, respectively were manufactured in-house (Figure 3.17). In both cases, the anchor dowel had a 20mm² area and a 50 mm length. For the case of shear strengthening, the fan had a length of 140 mm, comprising 30 mm of dry fibres and 110 mm of stiff fibres (Figure 3.17a). For the case of flexural strengthening a 50mm length of dry fibres and a 110mm length of stiff fibres was used (Figure 3.17b). The fan angle was 45º in both cases. The average tensile strength and ultimate strain of the anchors were 2455 MPa (or 49.1 kN) and 1.85%, respectively and a 0.37 reduction factor on the anchor capacity was considered as suggested in Tetta et al. (2016).

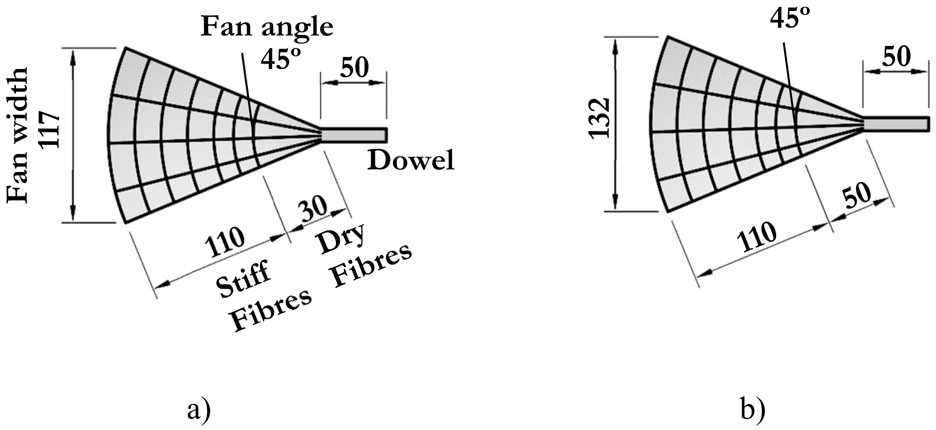

Figure 3.17 – Anchors detail a) Shear anchors b) Flexure anchors (all dimensions in mm).

Resin	Compressive Strength	Tensile Strength	Bond Strength with Concrete	Young's Modulus
A	52	37	4.0	1800
B	42	25	2.5	3000

Table 3.5 – Anchors epoxy resins data (MPa).

The anchors were bonded to concrete using two different types of epoxy resin following the recommendations provided in Koutas et al. (2013). Prior to the anchor installation, a high strength epoxy resin (Type A) was applied on the anchor dowel and stiff fibres (Figure 3.17a) and in the slab groove. The second resin (Type B) was applied on the dry fibres (Figure 3.17a) during the installation of the anchors. The mechanical properties of the epoxy resins used are shown in Table 3.5.

3.4 Strengthened Specimens

In the column removal scenario considered herein, the resilience and robustness of the sub-assemblage relies on the internal mechanisms of defense of the frame (flexural capacity, CAA and TCA). TCA is the last resource of resistance of the frame, and, according to the guidelines (Ellingwood et al., 2007, DoD, 2009), the internal reinforcement should have enough continuity and enough axial capacity to allow the frame to reach this mechanism and support the horizontal loads, considering the large deflections.

Since strengthening of the end sections (Sections 1 and 4 in Figure 3.9) with respect to sagging is challenging from a practical standpoint, a realistic strengthening objective would be to increase the flexural capacity of the bottom mid-span section (i.e., Sections 2 and 3 in Figure 3.9). From a limit analysis standpoint, this capacity would optimally assume a value equal to the capacity of the end sections, i.e., the critical sections of the assembly. Driven by these considerations and given the reinforcement layout and the corresponding material properties, the target moment capacity is found to be $M_{RD}^{t} = 21$ kNm.

Hence, the NSM and TRM configurations employed for flexural strengthening were designed accordingly as discussed in the following sections. Additionally, U-shaped TRM jackets were adopted to prevent the concrete crush at the bottom of the side joints, as well as to avoid the shear failure due the increased applied load on the middle column. The partial strengthening aimed to reach those goals with a minimum amount of strengthening material. The full cover was chosen to address the drawbacks from the usage of a partial strengthening.

To the author knowledge, there is not an explicity provision on the current guidelines with regards to a "design" load bearing capacity of the frame during the TCA. UFC (2009) suggests that a structural integrity assesment should always be performed for a load case scenario defined by DIF(2DEAD+0.5LIVE), where DIF>1 a dynamic increase factor. Hence, the strengthening strategy investigated in this work was to take full advantage of the existing strength of the structure at the end supports while providing the minimum required reinforcement to do so at the mid-joint.

3.4.1 NSM Specimen (NSM_PR and NSM_TR)

Two stainless-steel bars with a diameter of 6 mm were installed via the NSM technique in 20x20 mm grooves (Figure 3.18a). The tensile capacity of the NSM reinforcement was $F_t^{NSM} = 37$ kN and the resulting moment capacity was $M_{RD}^{NSM} = 18$ kNm for sections 2 and 3 (see Figure 3.9); this was comparable to the target strength M_{RD}^{t}.

The anchorage length of the NSM bars was evaluated to be equal to 750 mm (Figure 3.18b) considering the position of the plastic hinge to be formed at the vicinity of the middle column. The material chosen to be the bonding agent between the NSM reinforcement and the concrete inside the grooves was the epoxy resin following the results in Bournas and Triantafillou (2009).

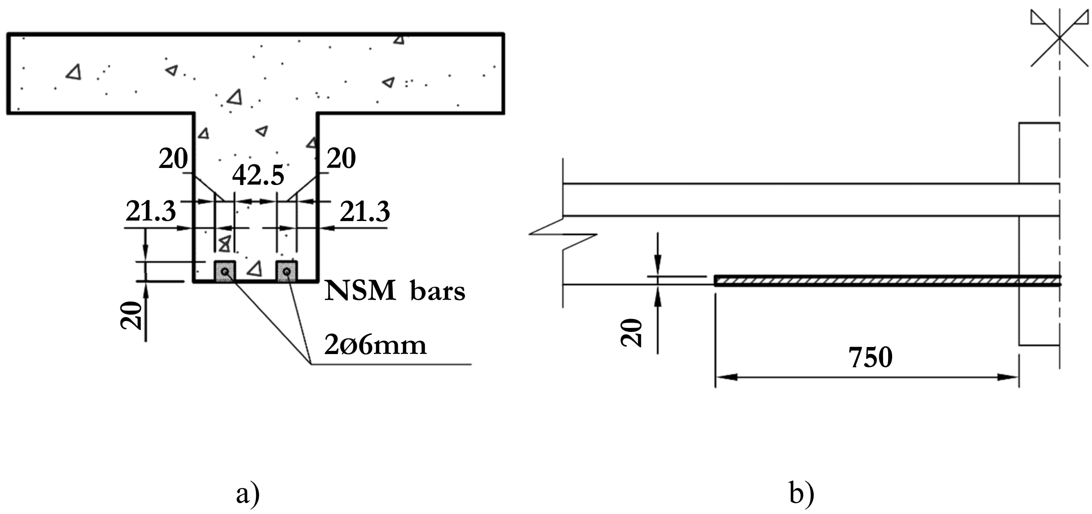

Figure 3.18 – Position of NSM stainless steel bars a) cross section b) frontal view.

The beam was strengthened with 3 layers of light carbon TRM U-jackets as shown in Figure 3.19. The jackets were anchored to the beam flange using heavy carbon fibre textile anchors. It is important to note that the TRM layers were not anchored in the longitudinal direction and hence did not contribute to the flexural capacity of the mid-section.

To apply the NSM system, two square-shaped pieces of wood were left in the mould for the grooves, before casting the concrete, (Figure 3.20). Then, when the concrete completed 7 days of casted, the moulds and the wood pieces were removed (Figure 3.21a). After that, the surface of the concrete receiving the epoxy resin was prepared manually with an abrasive disc (Figure 3.21b). To apply the NSM bars first the resin was applied on the top half of the groove, then the bars were inserted on the resin by manual pressure. Sequentially, the second half of the groove was filled with resin (Figure 3.21c). To positioning the reinforcement two spacers were used per bar, to make sure it would be centralized inside the groove. Figure 3.21 presents the appliance of the NSM reinforcement and its final configuration (Figure 3.21d).

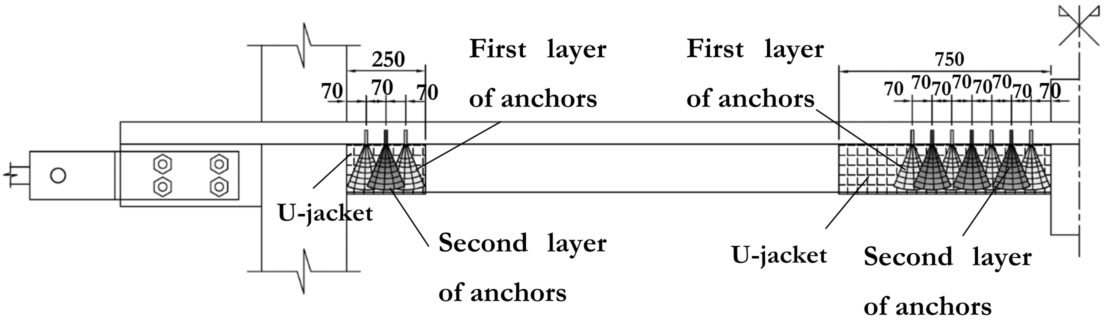

Figure 3.19 – TRM configuration for shear strengthening of the partially reinforced specimen (NSM_PR).

Figure 3.20 – Position of the NSM groove in the mould.

The NSM_TR specimen reinforcement was the same of specimen NSM_PR (Figure 3.18). Its shear reinforcement comprised 3 layers of U-shaped light carbon textile fibre TRM jackets as in specimen TRM_PR, which will be presented following.

Similar to the strain gauges attached to the internal reinforcement, the readings from the strain gauges inserted on the NSM reinforcement could not be used. However, the scheme of these gauges is presented here. Six strain gauges were placed in each stainless-steel bar, one right after the column, one close to the end, and one between those two. Figure 3.22 shows the configuration of the SGs on the NSM bars, where values inside brackets are the correspondent SGs for the other side of the middle column, and values put together are the SG number in each stainless-steel bar.

a)

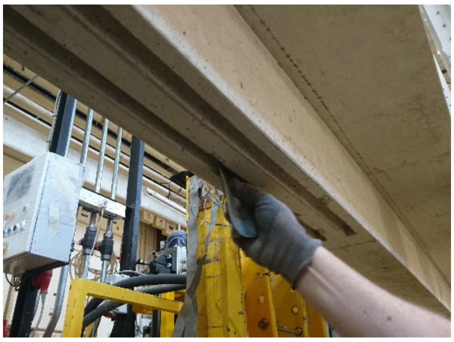

b)

c)

d)

Figure 3.21 – Appliance of NSM reinforcement a) grooves exposed b) surface treatment c) hand pressure to remove eventual air bubbles d) final configuration.

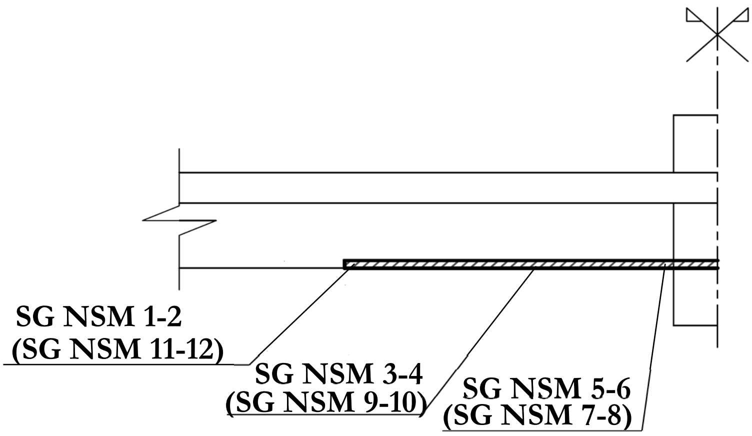

Figure 3.22 – Strain Gauges on NSM bars.

3.4.2 Anchored TRM (TRM_TR)

The TRM flexural strengthening reinforcement was designed to have a tensile capacity similar to the NSM reinforcement employed in specimen NSM_PR. The TRM reinforcement comprised 3 layers of U-shaped jackets plus one additional 125x1000 mm strip reinforcement applied at the bottom of the beam as shown in Figure 3.23.

The tensile capacity F_T of the TRM reinforcement contributing to flexure was evaluated using the following relation:

$$F_T = n b_w t_w f_t \tag{3.1}$$

where n is the number of textile layers, b_w is the beam width; t_w is the textile nominal thickness, and f_t is the tensile strength of the textile. The TRM tensile strength was defined according to the TRM coupon tests provided in Raoof and Bournas (2017), where $f_t =$ 1434 MPa and the elastic modulus was 116.8 GPa. Hence, the tensile strength of the TRM reinforcement was evaluated as

$$F_T^{TRM} = 4 \cdot 125 \cdot 0.062 \cdot 1434 \approx 44.4kN \tag{3.2}$$

It is of interest to note that the TRM strength employed is significantly lower than the values reported by the manufacturers in Table 3.3. It is however considered here the former to be more representative of the actual stress state on the TRM layers; this assumption is indeed verified by the experimental results presented in Section 3.5.

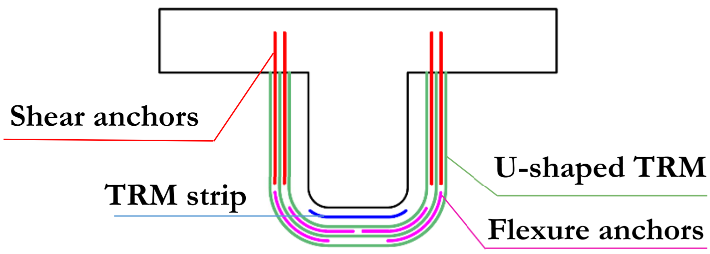

Figure 3.23 – Textile-based anchors.

In this specimen, the TRM layers were anchored to the middle column through textile-based anchors. Two anchors were installed between the first and the second TRM layer;

the remaining were installed between the second and third layer (Figure 3.23). Contrary to NSM_PR, the U-shaped jackets were installed along the entire length of the beam (Figure 3.24) hence uniformly increasing the stiffness and strength of the specimen; this was proven to be beneficial as discussed in Section 3.6.3.

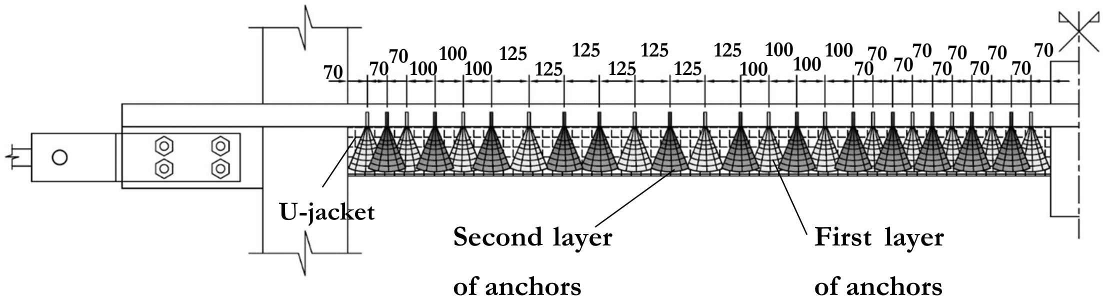

Figure 3.24 – TRM configuration for shear strengthening for the totally reinforced specimens (TRM_TR, NSM_TR).

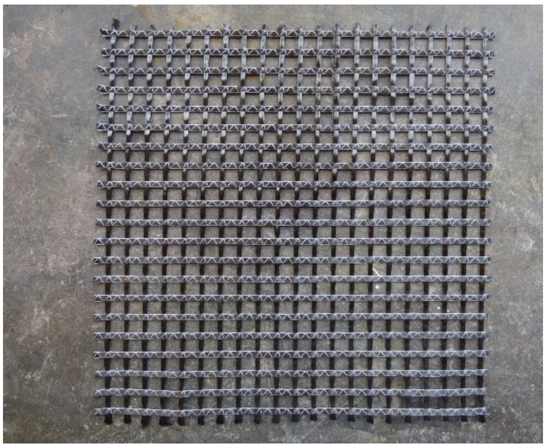

a)

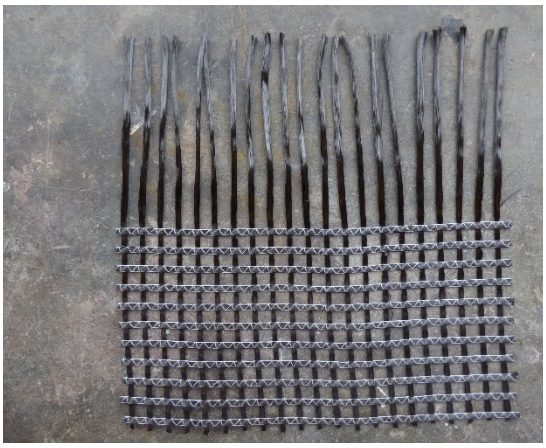

b)

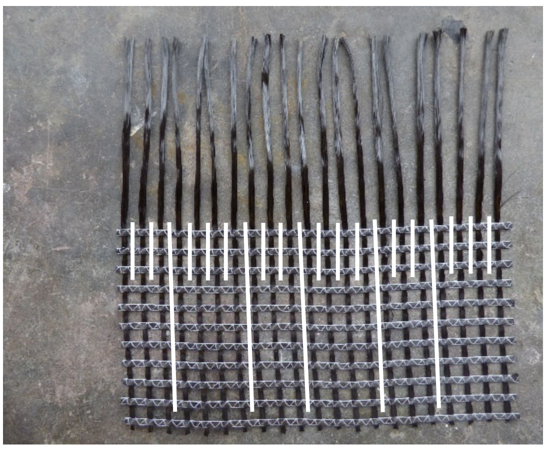

c)

d)

e) f)

Figure 3.25 – Textile-based anchors preparation a) Portion of textile to make the anchor b) fibres removed from the mesh c) cutting areas d) mesh shaped as a fan ready for resin on the dowel e) resin on the fan f) anchor ready.

To prepare the anchors, the same procedure found in Koutas et al. (2013) and Tetta et al. (2016) was adopted here. First the textile was cut in the desired size (Figure 3.25a).

After that, some fibres were removed to create the dowel (Figure 3.25b). Following, the remaining mesh was cut as presented in Figure 3.25c. Then, the mesh was shaped as a fan, with the help of plastic bracers, to receive the resin on the dowel (Figure 3.25d). It is suggested to leave the last row of the mesh uncut (Figure 3.25c) until the resin of the dowel is dry.

Usually, after this point part of the fan is also coated with resin days before its insertion on the beam (Figure 3.25e). This procedure was not adopted for the anchors used as flexural strengthening. Therefore, the fan of those anchors remained uncoated up to the day of appliance of those on the beam. This is due the fact that to insert the flexural anchors on the beam the fan needed to be molded during the process (Figure 3.26) to be shaped on the beam corner. However, the fan coating with resin was used for the anchors reinforcing the beam against shear. The part of the fan without resin is called here dry fibres (Figure 3.17). A different kind of resin is applied on the dry fibres of the anchor during its insertion on the beam. Since the flexural anchors had the fan uncoated, this second resin was applied all over the fan during the insertion of the anchor on the beam.

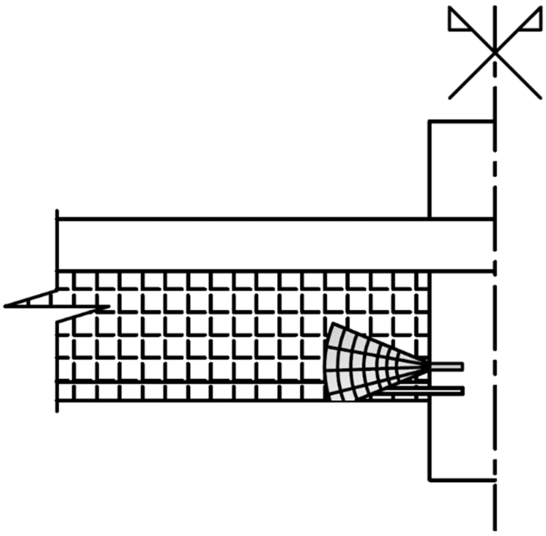

Figure 3.26 – Frontal view of flexural anchors.

The appliance of the anchor is a process which must be made in conjunction with the appliance of the U-shaped TRM. For that reason, the procedure to install both strengthening methods will be described in the following section. The additional reinforcement against shear is applied in all strengthened specimens, however with different configurations.

3.4.2.1 Shear Strengthening

Additional shear reinforcement was also provided in all strengthened specimens. The aim of this strengthening was to mitigate the shear failure modes, which were observed on the control specimen. Given the material properties and dimensions, as well as the reinforcement arrangement adopted, the shear strength of the control specimen was estimated at $V_{RD} = 52$ kN. To avoid any premature failure due to shear, the additional shear reinforcement was designed to sustain the maximum load applied on the beam during the TCA, which was equal to 90kN.

The shear strengthening comprised a U-shaped anchored TRM with light carbon fibres for the textile and heavy carbon fibre for the anchors. This was applied first on part of the beam (Figure 3.19), then on the full length of the beam (Figure 3.24).

In Tetta et al. (2016), anchored TRM was used to strengthen a beam against shear. In that work the anchors were activated in different times, therefore proportionating different stress concentrations per anchor. This behaviour, added to the fact that the failure was governed by the anchors, lead to an expression to calculate the system TRM + anchors in U-shaped jackets to resist the shear stresses of the beam:

$$V_f = A_{anc} f_{fe,anc} \frac{h_w}{s_d} \cot\theta \quad \textbf{(3.3)}$$

Where V_f is the aimed shear force to be resisted; A_{anc} is the area of two anchors, accounting both sides of the beam, equal to 40 mm² (2 x 20 mm²); h_w is the high of the beam below the slab, equal to 170 mm here; and the angle θ, adopted here as 45º, corresponding to the angle formed between the longitudinal axis of the element and the compressed diagonal, similar to the one adopted in the Mörsh truss analogy to assess the shear in a beam. The parameter s_d is governed here by the geometry of the anchor, which is accounted between the dowels of two consecutive anchors (see Figure 3.19 and Figure 3.24). The parameter $f_{fe,anc}$ is the effective tensile resistance of the anchor and can be found with the following expression:

$$f_{fe,anc} = \eta_e f_{f,anc} \quad \textbf{(3.4)}$$

Where $f_{f,anc}$ is the tensile resistance of the anchor, and η_e is a correction factor for this resistance, adopted here as 0.3. Therefore, the contribution of the strengthening to the shear resistance is at least $V_{RD}^{TRM} = 40$ kN. Factoring in the shear strength of the existing beam, this would, in principle, double the maximum load applied on the structure.

Tetta et al. (2016) prepared a set-up to test the tensile capacity of the anchors. One mesh, with the same cross-sectional area of the used anchors (20 mm²) with two metallic pieces attached at each end, leaving a space of 200 mm in the central part. Three tensile tests were performed and can be seen in Figure 3.27, as well as the test set-up.

Considering the previous information and the results of the control specimen, the configuration with three layers of TRM and two layers of anchors was adopted.

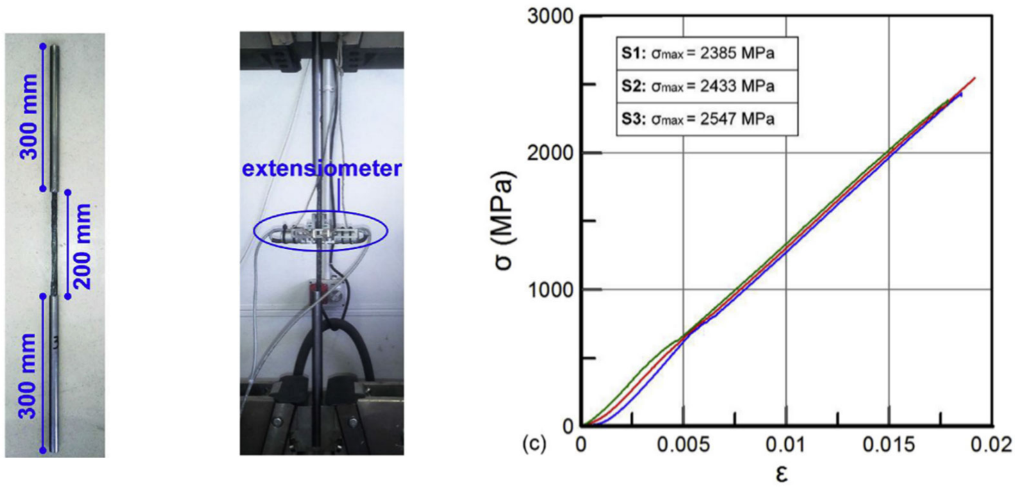

a) b) c)

Figure 3.27 – Test to the tensile resistance of the anchors a) sample b) test set-up c)results (Tetta et al., 2016).

Application of the TRM and Anchors

The same procedure to apply the system TRM + anchors (Figure 3.28) described in Koutas et al. (2013) and Tetta et al. (2016) was employed here and is the following:

(1) drilling holes into the concrete with a diameter slightly larger than the diameter of the dowel;

(2) removing the dust from the holes and the surfaces receiving TRM with air pressure;

(3) dampening the surface which will receive mortar;

(4) applying a layer of mortar;

(5) applying the textile by hand pressure over the mortar layer;

(6) application of mortar in the region where the fan part of the anchor will be placed;

(7) filling the holes with low viscosity epoxy resin;

(8) impregnating the dry fibres of the fan with epoxy adhesive;

(9) placing the anchors by inserting the dowel into the previously drilled holes and bonding of the fan part in the mortar by hand pressure;

(10) applying of mortar over the previous layer;

(11) applying a new layer of textile;

(12) repeating the steps 6 to 11 if it is necessary;

(13) applying a layer of mortar to cover.

a)

b)

c)

d)

e)

f)

g)

h)

Figure 3.28 – Installation of the U-shaped anchored TRM a) surface preparation and drilling the holes to the dowel of the anchor b) appliance of the first layer of mortar c) appliance of the first layer of textile d) filling the holes with resin e) applying resin in the dry fibres of the anchors f) placing the anchors g) applying the next layer of mortar h) retrofitting concluded after all layers being applied.

3.5 Results

3.5.1 Resistance of beam–column sub-assemblages

Overall, the examined specimens demonstrated a distinct and highly complex response. The strengthening configuration was found to significantly affect the post peak response as will be further discussed in section 3.6. All strengthened specimens reached higher first peak loads (P_f), at displacements higher than that achieved in CON.

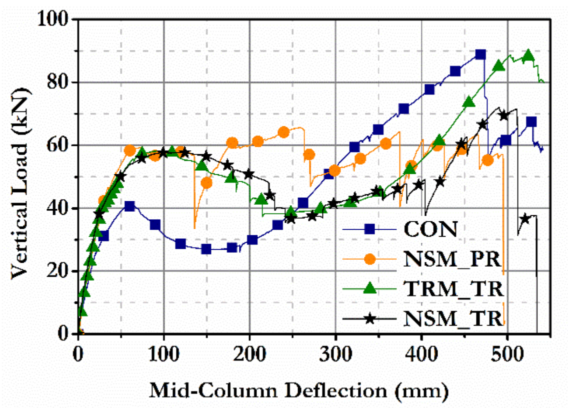

Figure 3.29 – Load vs Middle Column Displacement.

andre.vieira@nottingham.ac.uk / andre.engc@gmail.com

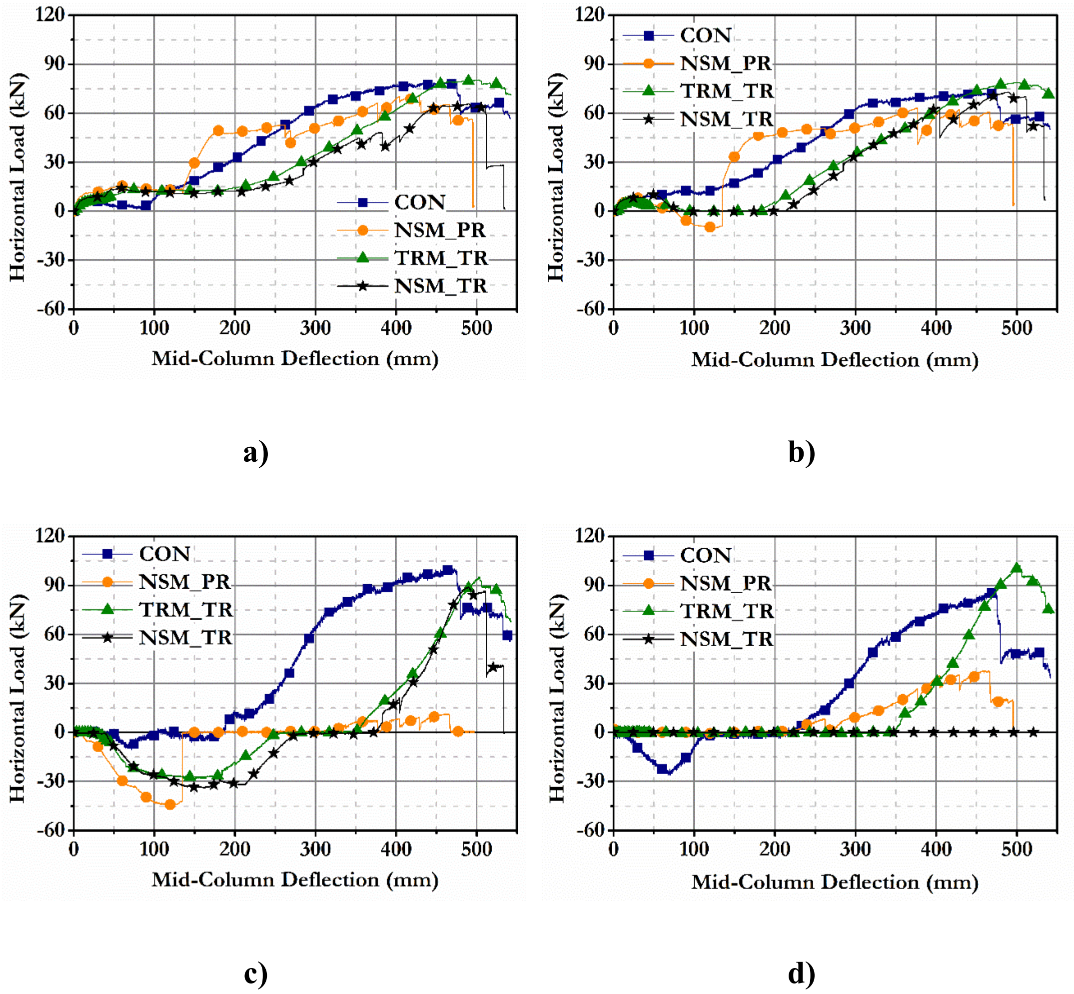

Figure 3.30 – Load Cells readings a) LC1 b) LC2 c) LC3 d) LC4.

With the exception of NSM_PR, the load dropped to a characteristic value P_{min} and then increased until the full TCA development at load P_{TCA}. The load vs mid-column vertical deflection curves for all specimens are shown in Figure 3.29. The load cell horizontal forces versus the mid-column vertical deflection are shown in Figure 3.30(a)-(d) for load cells LC1 to LC4 respectively (see also Figure 3.9). Due to malfunction of LC4 during testing of NSM_TR, no measurements were recorded.

3.5.2 Rotations

To acquire the beam rotations the potentiometer configuration presented in Figure 3.31 was adopted, where S_1 and S_2 are distances between column and section A, and between section A and B respectively. Each Δ means the measurement of each potentiometer along the test. The angle between column and section A includes the flexural and fixed-end rotations. The rotation of section B with respect to section A is only flexural rotation.

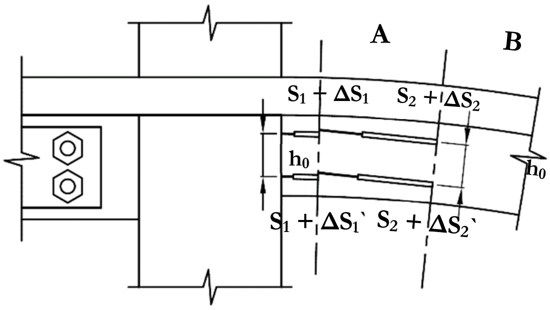

Figure 3.31 – Beam-Column rotation.

The estimative of flexural rotation θ_f is obtained if the average curvature of both sections are assumed equal (see Figure 3.31) (Yu and Tan, 2013b). Based on those assumptions the flexural rotation θ_f, could be achieved according to the following equation:

$$\theta_f = tan^{-1}\left(\frac{\Delta S_2 - \Delta S'_2}{h_0}\right) x \frac{(S_1 + S_2)}{S_2} \quad \textbf{(3.5)}$$

The total rotation, θ_{tot}, from the column to the section B can be achieved through the expression below:

$$\theta_t = tan^{-1}\left(\frac{\Delta S_1 - \Delta S'_1}{h_0}\right) + tan^{-1}\left(\frac{\Delta S_2 - \Delta S'_2}{h_0}\right) \quad \textbf{(3.6)}$$

a) **b)**

Figure 3.32 – Potentiometers installed at the bam and the column.

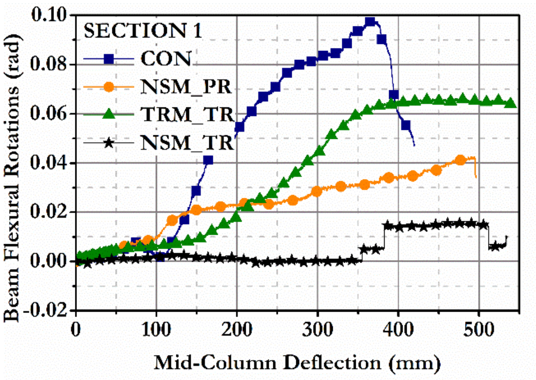

a)

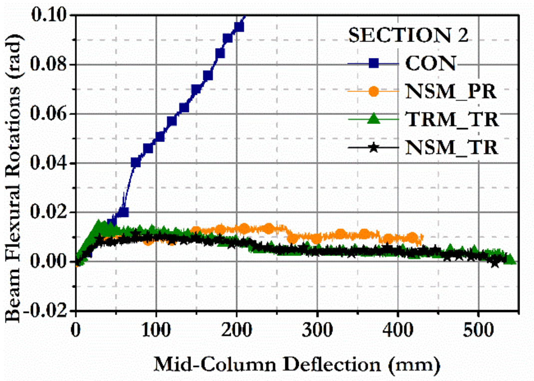

b)

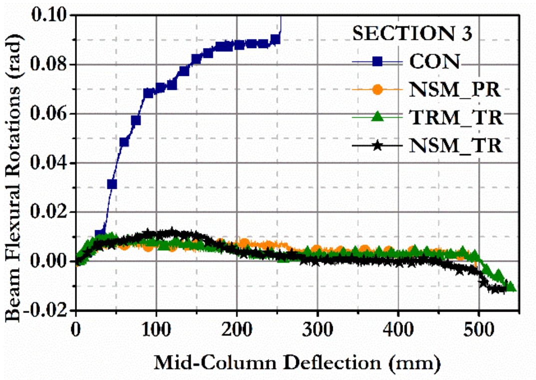

c)

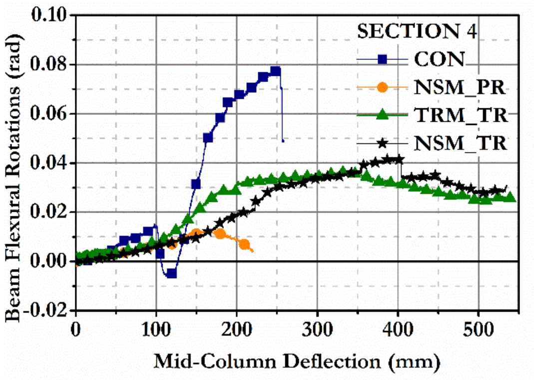

d)

Figure 3.33 – Beam flexural rotations a) Section 1 b) Section 2 c) Section 3 d) Section 4.

Potentiometers installed on the beam as well as on the column can be seen in Figure 3.32a and b respectively.

The rotations of the beam in each joint as well as the column rotations enables assessment of the overall behaviour of the strengthened beam compared with the control specimen. The flexural rotations at four critical regions along the beam identified as sections 1-4 (Figure 3.9) are shown in Figure 3.33(a)-(d). Total rotations, i.e., rotations due to flexure and fixed end rotations are presented in Figure 3.34(a)-(d). Side column rotations are summarized in Figure 3.35(a)-(b). Moreover, the failure modes of each specimen are presented in sections 3.5.2 to 3.5.5.

It should be mentioned that in cases where damage evolved at the positions where potentiometers were located, recording has been interrupted due to cracks opening or concrete crushing and spalling. These events are manifested as discontinuities in the evolution of rotation curves in Figure 3.33, Figure 3.34, and Figure 3.35.

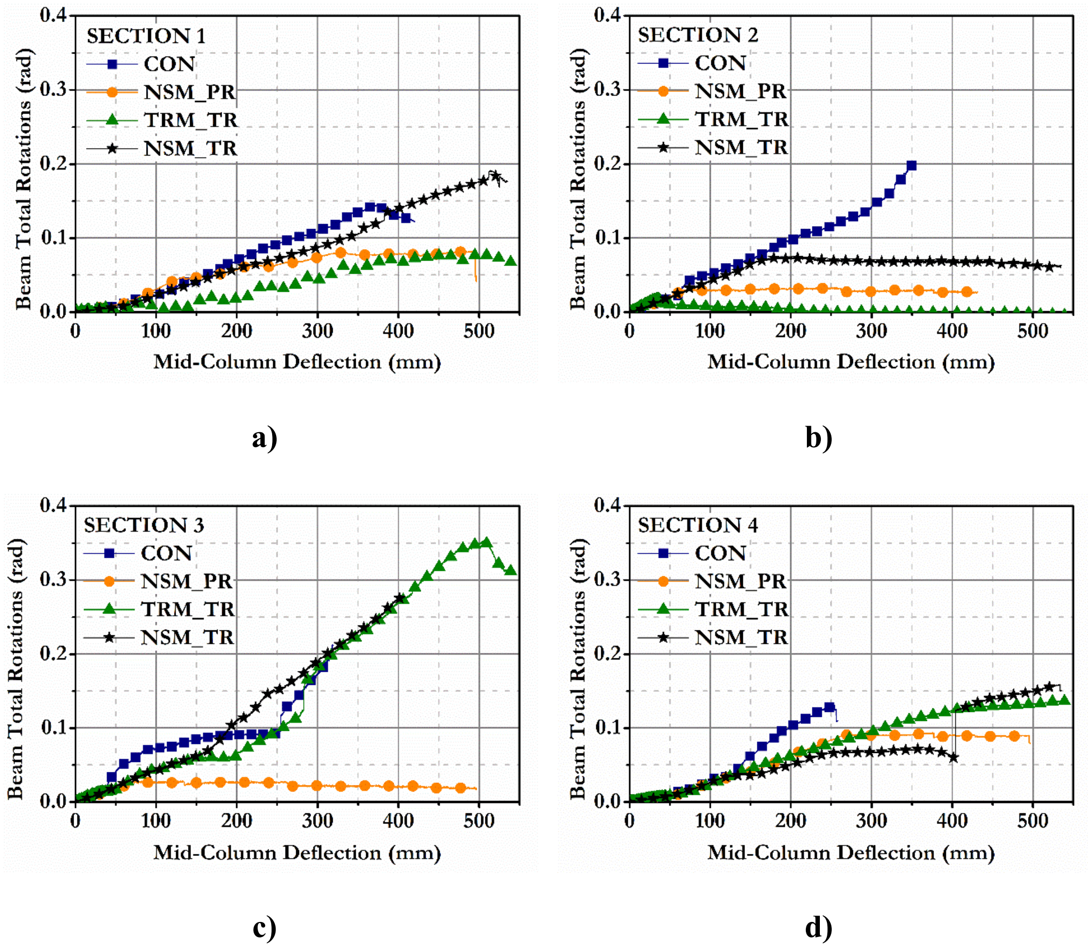

Figure 3.34 – Beam total rotations a) Section 1 b) Section 2 c) Section 3 d) Section 4.

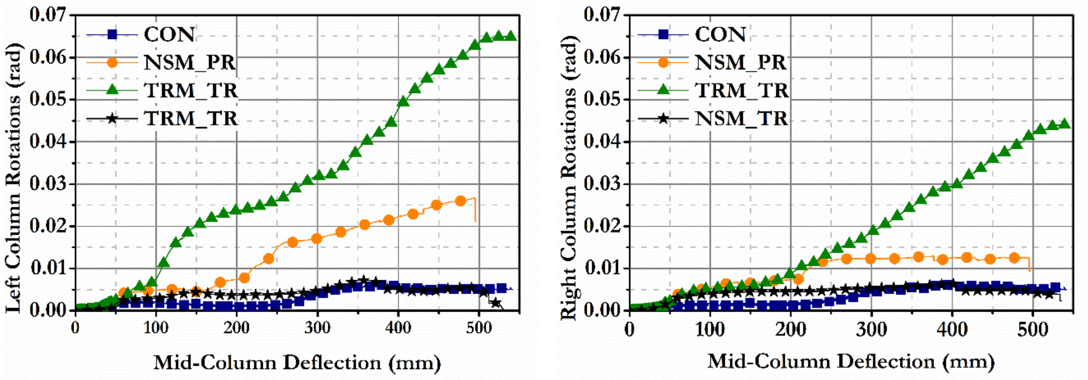

a) **b)**

Figure 3.35 – Side columns rotations a) Left side b) Right side

3.5.3 Failure Mode

3.5.3.1 CON Specimen

a) **b)**

c) **d)**

Figure 3.36 – CON Specimen failure details a) Flexural/shear cracks b) Compression at the side joints c) Reinforcement broken at the beam bottom d) Final failure.

3.5.3.2 NSM_PR Specimen

In specimen NSM_PR, strengthened in flexure with two 8-mm stainless steel bars and partially reinforced in shear with a TRM jacket (Figure 3.19), failure initiated with flexural cracks. These were however distributed over a larger length in comparison to the control specimen (Figure 3.37a) due to the favorable action of NSM reinforcement. The maximum load attained at the CAA peak was 59.5 kN (Table 3.6) at a displacement of 74.7mm. The load remained approximately constant until collapse. The sudden load drops shown in Figure 3.29 correspond to the subsequent formation of shear cracks, developed in the region of the not-anchored TRM jacket (Figure 3.37b). The CAA was again associated with concrete crushing, which however occurred at the end of the TRM jacket (Figure 3.37c). The TRM jacket was partially debonded from beam. From this point onwards damage localized at the right span of the beam eventually leading to the rupture of a longitudinal reinforcement and a shear link (Figure 3.37b). The final configuration of failure is presented in Figure 3.37d.

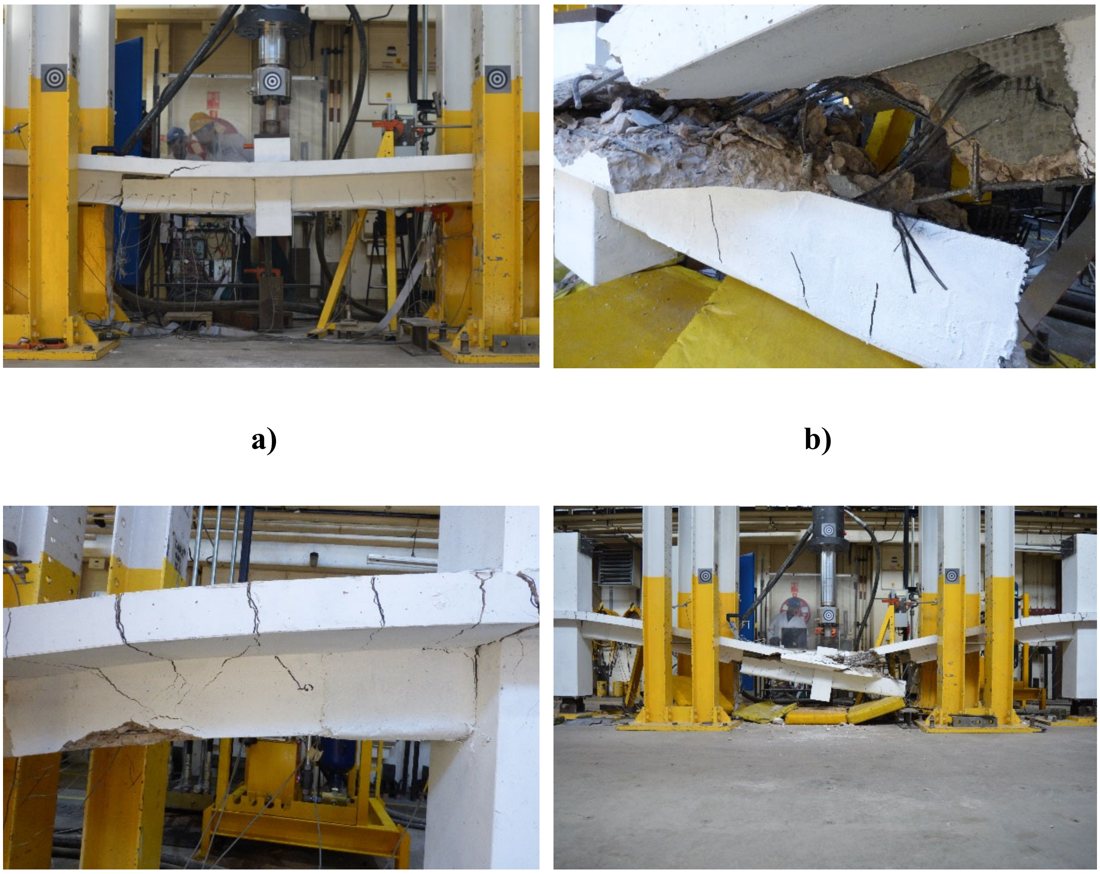

a) b)

c) d)

Figure 3.37 – NSM_PR specimen failure details a) Shear cracks b) Broken longitudinal reinforcement and shear link c) Concrete crushed due the CAA d) Final failure.

3.5.3.3 TRM_TR Specimen

Damage initiated in the form of flexural cracks at the beam in the vicinity of the middle column (Figure 3.38a). The maximum load during the CAA was 58.3 kN at 99.2 mm (Table 3.6), where a detachment of the concrete of the middle column due the presence of the flexural anchors was already visible (Figure 3.38b). The load then dropped to 38.1 kN at 216 mm of vertical deflection. Furthermore, small horizontal cracks were formed at the bottom of the beam at the side joints due the crushing of this region (Figure 3.38c). The maximum load achieved during TCA was 88.7 kN, at 503.6 mm of vertical deflection. The specimen eventually failed following the detachment of the anchors from the middle column and the associated concrete pull-off at the middle column (Figure 3.38d). Additionally, at the end of the test it was possible to observe an initiation of a punching, detaching the beam from the slab, and no rupture of the reinforcement occurred. Figure 3.38d presents the final configuration of the beam at the end of the test.

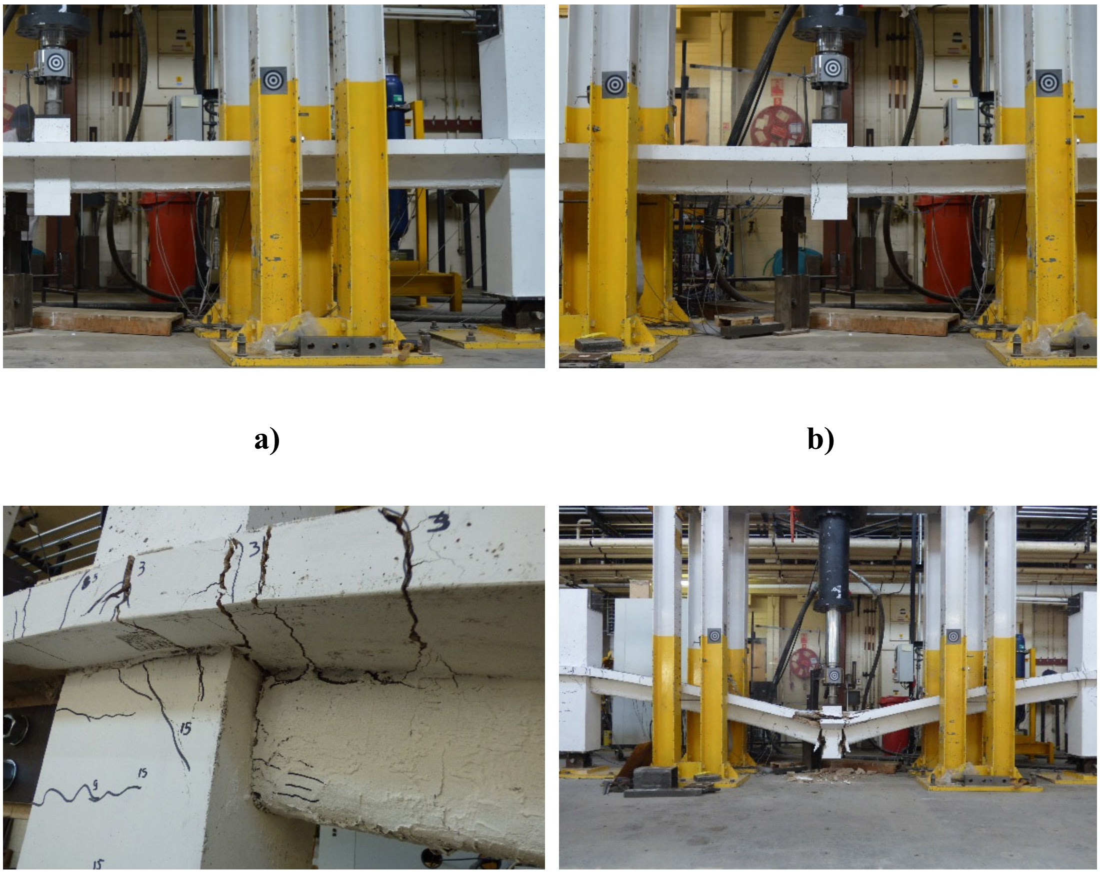

a) b)

c) d)

Figure 3.38 – TRM_TR Specimen failure details. a) Cracks along the beam b) Concrete detachment in the middle column c) Compression at the side joint d) Final Failure.

3.5.3.4 NSM_TR Specimen

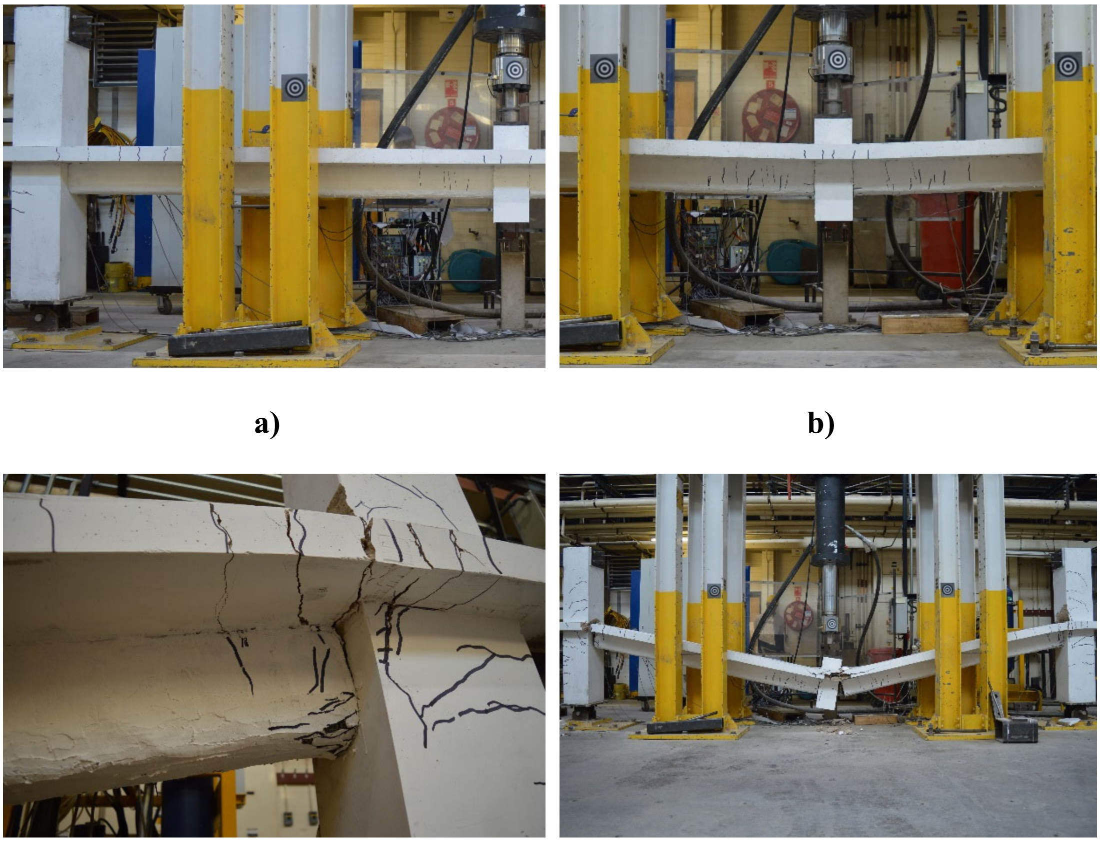

a) **b)**

c) **d)**

Figure 3.39 – NSM_TR Specimen failure details a) Flexural cracks along the beam b) Horizontal cracks at the NSM region c) Compression at the side joint d) Final failure.

The failure in this experiment was asymmetrical, initiating with the cracks at the slab, close to the side columns followed by flexural cracks at the bottom of beam at the middle span, as well as at the side columns (Figure 3.39a). Subsequently, small horizontal cracks were formed on the TRM at the bottom of the beam, close to the middle column, indicating the stainless-steel reinforcement was providing resistance (Figure 3.39b). After that, the compression below the beam at the side joints led to the TRM to be crushed (Figure 3.39c) causing the resistant load to drop up to a minimum of 36.4 kN (Table 3.6) at 244 mm of vertical deflection. Following, at the top of the beam around the middle joint the concrete was also crushed. Approaching the end, some of the longitudinal reinforcements were broken at the bottom of the beam in the region of the middle joint, as well as at the top of the beam at the side joints leading to sudden drops at the resistant load (Figure 3.29). The maximum applied load reached in this specimen was 72 kN at 490.5 mm of vertical deflection (Figure 3.39d).

3.6 Discussion

3.6.1 Overview

In all cases, the strengthening configuration significantly improved the progressive collapse resistance of the control specimen. The relative increment of the load at CAA was very similar for all strengthened specimens and equal to 1.47, 1.44 and 1.42 for NSM_PR, TRM_TR and NSM_TR, respectively, see in Figure 3.40, highlighting the effectiveness of the total length coverage strengthening techniques in delaying the evolution of localized failures (e.g., flexural cracks, concrete crushing), as well as in mitigating shear failures. Furthermore, both TRM_TR and NSM_TR resulted in a significant increment of P_{min}; in all strengthened specimens P_{min} was comparable to the load corresponding to the CAA of CON. Additionally, the deflection where the CAA concludes and the TCA takes place can be identified in Figure 3.40. This position is defined as the deflection where the compressive force on the beam vanishes and is identified by the LC3 and LC4 load cell readings. These are shown in Figure 3.30 and are summarized in Table 3.6. For the case of specimens TRM_TR and NSM_TR the midpoint between the end of compression and the beginning of tension on LC3 and LC4 reading was considered as the point of transition between CAA and TCA.

The control specimen (CON) achieved initially a peak load of 40 kN (P_f). After that, the load reduced to a value equal to 67% of the first peak load. With the development of TCA, the resistant load increased up to 219 % of the first load peak. In specimen NSM_PR, even though several failures (shear cracks, concrete crushing, TRM partial debonding, reinforcement detachment, shear links rupture) occurred along the beam, the resistant load was kept close to the initial peak P_f, ending with 96% of that load. In TRM_TR, after P_f, the load reduced to 65.5%, then increased again up to 152% of the initial peak yet reaching similar load of CON at the same stage. Similarly, in NSM_TR, after the initial major load P_f the load dropped to 63% and then increased again to 125% of the initial peak.

Specimen	CAA					P_{min}		Def.* at transition between CAA and TCA	TCA			
	Vertical		Horizontal			Vertical			Deflection (mm)	Vertical	Horizontal	
	Def.* (mm)	Applied Load (P_f)	Def.* (mm)	Beam	Top Column	Def.* (mm)	Applied Load			Applied Load (P_{TCA})	Beam	Top Column
CON	65.8	40.6	65.8	-24.1	10.3	164.7	26.9	164.7	470.9	89.1	100.3	71.6
NSM_PR	74.7	59.5	124.9	-44.7	14.9	-	-	-	464.7	64.3	37.9	65.3
TRM_TR	99.2	58.3	138.0	-27.2	12.6	216.0	38.1	305.0	503.6	88.7	102.2	80.4
NSM_TR	116.2	57.7	160.8	-34.1	11.8	244.1	36.4	325.0	490.5	72.0	88.9	72.9

All loads in kN

***Deflections**

Table 3.6 – Summary of measured loads and correspondent deflections.

Specimen	Beam Side Joints						Beam Middle Joints						Side Columns		
	CAA		P_{min}		TCA		CAA		P_{min}		TCA		CAA	P_{min}	TCA
	Flex./ Plast.	Total	Flex./ Plast.	Total	Flex./ Plast.	Total	Flex./ Plast.	Total	Flex./ Plast.	Total	Flex./ Plast.	Total			
CON	0.0092	0.0151	0.0502	0.0755	-	-	0.0511	0.0538	0.0857	0.0857	-	-	0.0019	0.0013	0.0058
NSM_PR	0.0179	0.0440	-	-	0.0399	0.0804	0.0113	0.0310	-	-	0.0015	0.0183	0.0066	-	0.0258
TRM_TR	0.0158	0.0403	0.0329	0.0687	0.0255	0.1327	0.0077	0.0551	0.0031	0.0771	0	0.3509	0.0182	0.0242	0.0643
NSM_TR	0.0107	0.0374	0.0293	0.0650	0.0151	0.1723	0.0123	0.0678	0.0031	0.1511	0	0.1326	0.0045	0.0047	0.0054

* All rotations in rad

Table 3.7 – Summary of measured rotations.

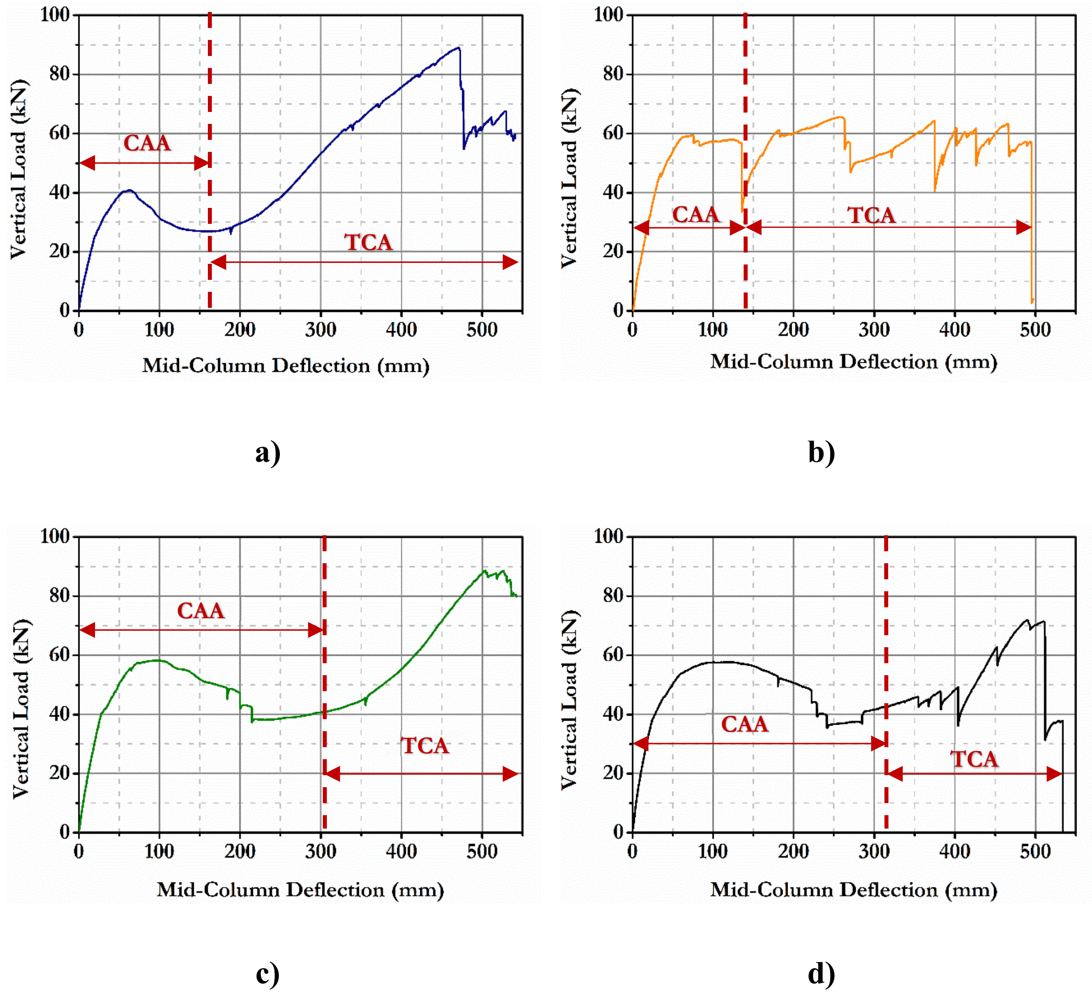

Figure 3.40 - CAA and TCA response for specimens (a) CON (b) NSM_PR (c) TRM_TR (d) NSM_TR.

The load-deflection behaviour of the specimens, even at the load-drop phase, highlights the associated benefit of the adopted strengthening methods on the structure robustness and resilience. The discussion about the specimens' performances is further presented in sections 3.6.2 and 3.6.3.

As mentioned previously, the first peak load (P_f) was up 47%, 44% and 42% higher in specimens NSM_PR, TRM_TR, and NSM_TR respectively compared to the control specimen (Table 3.8). The correspondent deflections were also increased in strengthened specimens, reaching up to 13%, 50% and 77% respectively (Table 3.8). With the confinement of the concrete at the side joints, the concrete crush was avoided or at least delayed at CAA phase. Additionally, the increased reinforcement area at the middle column joint increased the moment capacity of the two-bay beam, allowing the frame to reach higher values of resistant load in higher vertical deflections during CAA. The recoded ultimate displacement, associated to P_{TCA}, was 0%, 7% and 4% higher in NSM_PR, TRM_TR and NSM_TR, with respect to the control specimen remarking the favourable action of the full strengthening vis-à-vis the resilience of the frame.

Furthermore, during the CAA the strengthened frames were more efficient transferring the load to the neighbour elements by maintaining the integrity of the beam in critical points. The horizontal loads at the beam level (LC3 and LC4) (Figure 3.30 (c)-(d)) reached up to 185%, 13% and 41% of the CON specimen during CAA. The associated deflections were enhanced in 89%, 110% and 144% respectively. Moreover, the deflections in which the internal mechanism of resistance changes from CAA to TCA were also increased on strengthened specimens, reaching up to 97% of higher deflection. It emphasizes the capacity of the adopted strengthening technique on delaying the spread of the failure, taking advantage of eventual redundancy of the frame. At TCA phase, specimens with NSM reinforcement (NSM_PR and NSM_TR) did not reach the values of CON, and TRM_TR transferred only 2% more load to the adjacent structural elements. The strengthening prevented initial critical failures at the beam allowing higher values of load during CAA. However, the stress and strains contained at the strengthened areas reached weaker sections, leading to premature failures which prevented the frames to sustain and transfer higher loads at TCA.

The maximum loads recoded at the top load cells (LC1 and LC2) (Figure 3.30 (a)-(b)) were similar in all specimens. Hence, the side columns were not hindered by the application of strengthening on the beam. However, the side column rotations increased. The maximum column rotations recorded at P_f, P_{min} and P_{TCA}, were up to 958%, 1862% and 1109% higher when compared to the CON specimen (Table 3.9). The marginally lower performance of the NSM_PR specimen is attributed to the premature shear failures that were mitigated in TRM_TR and NSM_TR, since in all cases the TCA was bounded by the conditions of the internal reinforcement. Conversely, the strengthened beams developed lower flexural rotations ((Figure 3.33(a)-(d)) and similar total rotations (Figure 3.34(a)-(d)) to the CON specimen due to the increased stiffness provided by the strengthening.

3.6.2 The effect of the strengthening method

Both the NSM and the TRM strengthening techniques (designed to have a tensile capacity, see section (3.4.2) had similar effectiveness in increasing the robustness of the beam at CAA, reaching similar values of resistant load (Table 3.6). However, the TRM strengthening allowed for the damage to be more distributed associated with cracks opening along the entire length of the beam and eventually higher column rotations compared to the more localised damage observed in NSM strengthened specimen, associated to slippage of the reinforcement at the joints. Moreover, this contributed to the increased axial loads at the beam level during CAA, as well as the correspondent vertical deflection which were 25%, and 17% higher on NSM_TR. At the top of the columns, TRM_TR load cells registered 7% more load at CAA stage, however this value represents less than 1 kN of difference, therefore being considered similar to NSM_TR.

The beam total rotations were higher in NSM strengthened specimen (see Fig. 17) compared to the TRM strengthened specimen. In particular, the total rotations at the side columns where excessively higher by 304%, during CCA. The deflections in which the CAA changes to TCA is similar in both specimens, being only 7% higher on NSM_TR. During TCA, TRM_TR sustained 23% more load than NSM_TR at approximately similar deflections. At this stage, the loads transferred at the beam level were 15% higher on TRM_TR, while at the top load cells this value was 10%.

3.6.3 The effect of TRM shear strengthening

The length of the shear strengthening significantly affected the corresponding failure mode in specimens NSM_PR and NSM_TR. In the partially strengthened specimen the increased flexural and shear capacity prevented the formation and propagation of cracks around the middle column. Moreover, the confinement provided to sections 1 and 4 (see Figure 3.9) protected concrete crushing. However, the failure occurred in the non-strengthened region (see Figure 3.37). In NSM_TR, the continuity of the U-shaped TRM allowed the load transfer to the side joints and the stress concentration was led to the beam/columns' interfaces, which caused the reinforcement rupture in those regions in later vertical deflections.

The first peak load P_f was practically identical in both specimens, however in NSM_TR the vertical displacement in which P_f occurred was 56% higher than in NSM_PR since the premature shear failures were prevented. For the same reason, at P_{TCA}, between NSM_PR and NSM_TR, the later reached the closest value to CON, being 12% higher than NSM_PR, while the correspondent vertical deflection was 5%.

At the peak of CAA, NSM_PR transferred 30% more axial load (based on LC3 and LC4 readings) to the neighbour frames than NSM_TR. The shear crack at one side of the frame (see Figure 3.37) allowed the arch action to act only at one side, and consequently higher axial load at that side. However, the correspondent vertical deflection was 29% higher in NSM_TR, demonstrating the better performance of the full cover on the development of the CAA and consequent transference of loads to adjacent structural elements.

At the top load cells (LC1 and LC2), in general, the development of the recorded load occurred with small differences in all specimens (Figure 3.30). At the vertical deflection of P_f, NSM_PR presented 26% more load than NSM_TR, while at TCA NSM_TR showed 12% more load than NSM_PR. The transference of load was better in NSM_PR up to the CAA load peak, however the development of shear cracks restricted the achievement of higher values during TCA. Therefore, keeping the integrity of the frame and guaranteeing the transference of loads along the beam are key points to better use its internal mechanisms of resistance. Following it is shown how the strengthening length affected the rotations.

Flexural rotations were, in general, similar between both NSM_PR and NSM_TR specimens (Figure 3.33) . In NSM_PR, due to the difference of stiffness between strengthened and non-strengthened sections, the plastic hinges were formed more distant from the middle column than on the other specimens (Figure 3.37(a)-(d)) . At sections 1 and 4 (Figure 3.9), the total rotations recorded were identical among NSM_PR and NSM_TR, up to the development of the shear cracks in each side of the middle column. Whereas after that point, all the damage was concentrated at the major crack location (Figure 3.37d).

Specimen	CAA					P_{min}			TCA			
	Vertical		Horizontal			Vertical		$^{a4}d_{st}/d_{CON}$	$^{a5}d_{st}/d_{CON}$	Vertical	Horizontal	
	$^{a1}d_{st}/d_{CON}$	$^{b}P_{St}/P_{CON}$	$^{a2}d_{st}/d_{CON}$	$^{c}P_{St,b}/P_{CON,b}$	$^{d}P_{St,tc}/P_{CON,tc}$	$^{a3}d_{st}/d_{CON}$	$^{b}P_{St}/P_{CON}$			$^{b}P_{St}/P_{CON}$	$^{c}P_{St,b}/P_{CON,b}$	$^{d}P_{St,tc}/P_{CON,tc}$
CON	1	1	1	1	1	1	1	1	1	1	1	1
NSM_PR	1.13	1.47	1.89	1.85	1.45	-	-	-	0.99	0.72	0.38	0.91
TRM_TR	1.50	1.44	2.10	1.13	1.22	1.31	1.42	1.85	1.07	1.00	1.02	1.12
NSM_TR	1.77	1.42	2.44	1.41	1.15	1.48	1.35	1.97	1.04	0.81	0.89	1.02

a) Deflection ratio between strengthened and control specimens: 1 – Vertical at Pf; 2 – Horizontal at Pcaa; 3 – Vertical at Pmin; 4 – Vertical at transition between CAA and TCA; 5 – Vertical at Ptca

b) Strengthening Impact – Ratio between maximum strengthened and control specimens' vertical loads

c) Strengthening Impact considering the horizontal loads at the beam

d) Strengthening Impact considering the horizontal loads at the top columns

Table 3.8 – Comparison of measured loads and correspondent deflections.

Specimen	Beam Side Joints				Beam Middle Joints				Side Columns		
	CAA		P_{min}		CAA		P_{min}		CAA	P_{min}	TCA
	$^{a}F_{St}/F_{Con}$	$^{b}T_{St}/T_{Con}$	$^{a}F_{St}/F_{Con}$	$^{b}T_{St}/T_{Con}$	$^{a}F_{St}/F_{Con}$	$^{b}T_{St}/T_{Con}$	$^{a}F_{St}/F_{Con}$	$^{b}T_{St}/T_{Con}$	$^{c}C_{St}/C_{Con}$	$^{c}C_{St}/C_{Con}$	$^{c}C_{St}/C_{Con}$
CON	1	1	1	1	1	1	1	1	1	1	1
NSM_PR	1.95	2.91	-	-	0.22	0.58	-	-	3.47	-	4.45
TRM_TR	1.72	2.67	0.66	0.91	0.15	1.02	0.04	0.91	9.58	18.6	11.09
NSM_TR	1.16	2.48	0.58	0.86	0.24	1.26	0.04	1.79	2.37	3.62	0.93

a) Ratio of flexural rotation between strengthened and control specimens

b) Ratio of total rotation between strengthened and control specimens

c) Ratio of column rotation between strengthened and control specimens

Table 3.9 – Comparison of measured rotations.

The NSM_TR specimen did not present large side columns rotations (Figure 3.35). This is due the slippage and posterior rupture of the internal reinforcement in sections 1 and 4, as well as at the bottom of section 3 (Figure 3.9).

3.7 Robustness

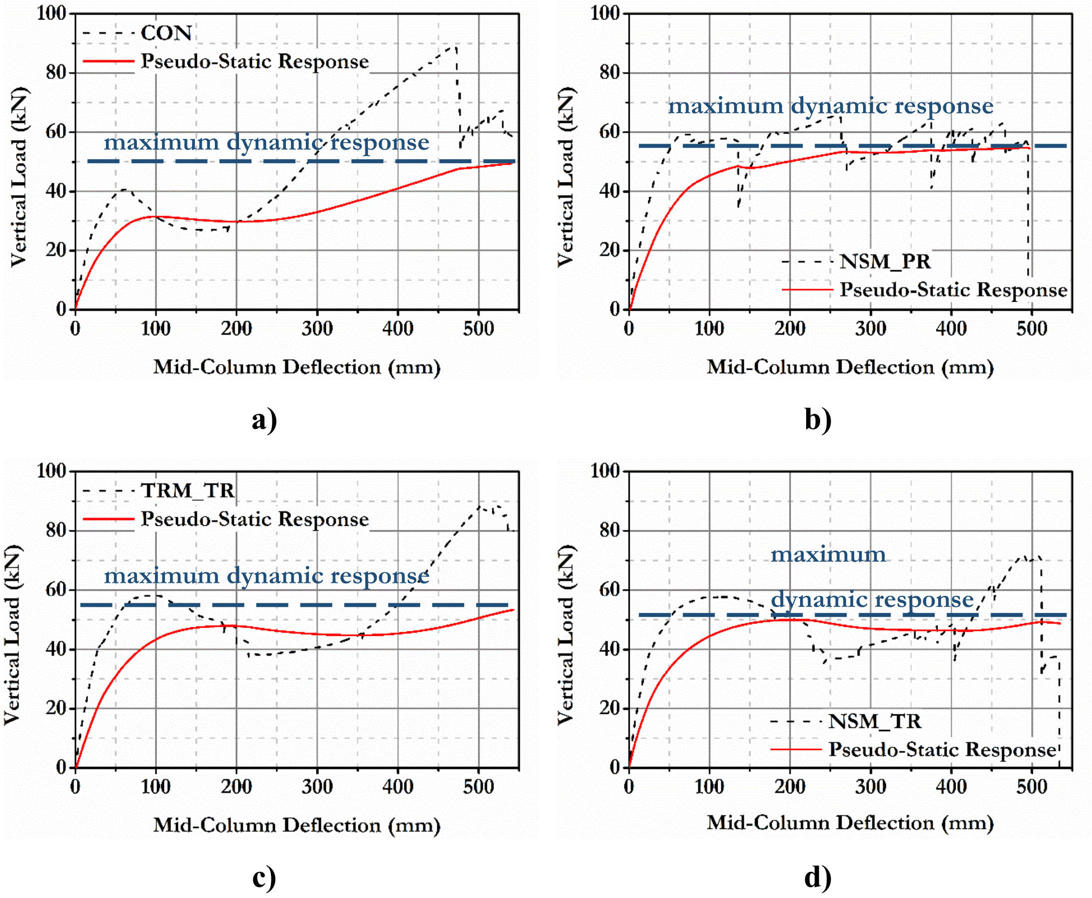

Figure 3.41 – Pseudo-static response of the specimens a) CON b) NSM_PR c) TRM_TR d) NSM_TR.

Following (Izzuddin et al., 2008), the pseudo-static response of the frame can be used as a reference to quantify its robustness when examined vis-à-vis the key indicators of the energy absorption capacity, the redundancy, and the ductility of the frame. According to the authors, when assessed separately, even if successful, the key indicators might provide wrong information. Therefore, to be considered that the frame robustness was increased, those must to be attended together, and the reference maximum dynamic response must to be surpassed. The redundancy of the frame depends on the topology of the actual structure. Hence, in the following we discuss the performance of the examined strengthening techniques with respect to energy absorption and ductility.

The resulting pseudo-static curves for all specimens are shown in Figure 3.41(a)-(d). In Figure 3.43, the pseudo-static curves are compared for all specimens. Moreover, in **Table 3.10** the maximum dynamic responses and correspondent deflections, as well as associated failure events, for both CAA and TCA phases are presented. Compared to the experimental results, the pseudo-static load corresponding to the fully developed CAA is significantly reduced. This fact agrees with the observations made by Yu and Tan (2013b). All specimens demonstrate a comparable maximum dynamic response and correspondent deflection at the CAA which is in accordance with the observations made from the static tests. The maximum dynamic responses at the TCA are also comparable for all specimens, contrary to the static tests where TRM_TR and NSM_TR resulted in higher ultimate loads than NSM_PR. The fact that the maximum dynamic responses of all strengthened specimens are higher than that of the control specimen fulfils the criteria of energy absorption (Izzuddin et al., 2008, Yu et al., 2014).

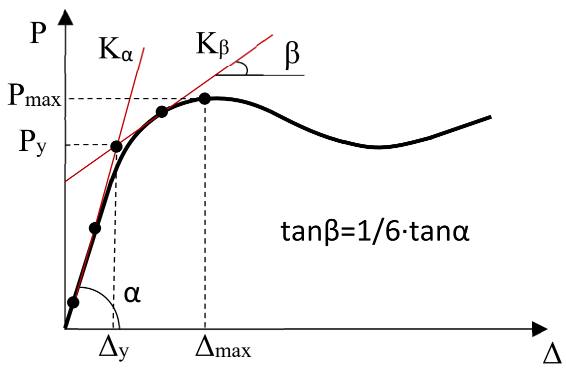

Figure 3.42 – Determination of the yield point.

The ductility ratios of all strengthened specimens were evaluated from their corresponding pseudo-static curves and are shown in Table 3.11. Herein, the ductility ratio is defined as the ratio between the displacements at failure and at the yield point; the latter is derived from an equivalent bilinear curve according to Muñoz et al. (2008). The point of failure considered for this assessment is the peak at the CAA. According to Muñoz et al. (2008), the yield point can be defined with two lines, the first represents the initial stiffness (K_α), usually calculated from 10% to 40% of the peak load. This secant line forms an angle α with the displacement axis. The second line (K_β) is built with a slope equals to one sixth of the secant line of the load. The yield point is found at the intersection of those two lines (K_α and K_β). Figure 3.42 shows the determination of this yield point on the Load x Deflection curve.

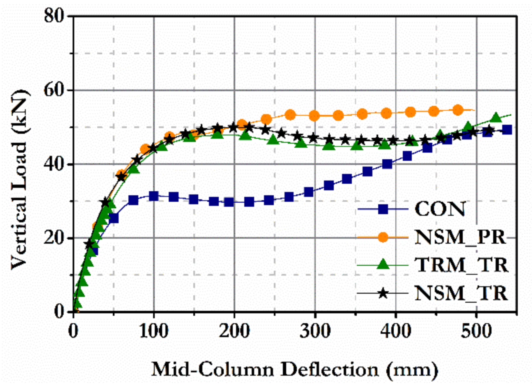

Figure 3.43 – Pseudo-static response of all specimens together.

Specimen	CAA			TCA		
	Maximum Dynamic Response (kN)	Deflection (mm)	Main Failure Event	Maximum Dynamic Response (kN)	Deflection (mm)	Main Failure Event
CON	31.5	99.8	[a] Concrete crushing	49.4	541.2	[d] Bar rupture
NSM_PR	48.5	135.4	[b] Shear crack	54.7	495.0	Test end
TRM_TR	48.5	195.3	[c] Concrete pull-off	53.6	542.9	Test end
NSM_TR	50.0	206.8	[d] Bar rupture	49.4	512.0	[e] Bar rupture

a) At the bottom of the beam at side joints

b) At unanchored region of TRM

c) Middle column

d) Longitudinal bar at the bottom of the beam at the middle joint

e) Longitudinal bar at the top of the beam at the side joint

Table 3.10 – Maximum dynamic responses and associated main failure event.

One can see that the ratio of the failure to the yield deflection is increased on strengthened specimens, where NSM_PR had the lowest improvement and NSM_TR the highest. Therefore, the recommendation of Izzuddin et al. (2008) were also fulfilled with the ductility. The improvement of ductility also attends the provisions of

Ellingwood et al. (2007) to provide structural robustness and reduce the risk of progressive collapse of a building.

	Ductility ratio ($\Delta_{failure}/\Delta_{yield}$)
CON	2.63
NSM_PR	2.75
TRM_TR	3.80
NSM_TR	5.12

Table 3.11 – Ductility ratios.

Finally, it is evaluated the Dynamic Increase Factors (DIFs) of the specimens based on the following expression

$$DIF|_{CAA,TCA} = \left.\frac{P_{max}^{experiment}}{P_{max}^{pseudo-static}}\right|_{CAA,TCA} \qquad \textbf{(3.7)}$$

where $P_{\max}^{experiment}$ corresponds to the experimentally measured loads reported in Table 3.6 and $P_{\max}^{pseudo-static}$ to the maximum loads reported in Table 3.10 during the CAA or TCA, respectively. The DIFs are 1.29, 1.23, 1.20, 1.16 during the CAA and 1.80, 1.18, 1.66 and 1.46 during the TCA, for the CON, NSM_PR, TRM_TR, and NSM_TR specimens, respectively. It is of interest to note that in all cases the values evaluated are smaller than 2, hence reaffirming the conservative nature of the GSA (2000) and DoD (2009) recommendations as also highlighted in the literature, see, e.g., Yu et al. (2014).

3.8 Experiments Findings

In this work the influence of strengthening the external frame of an old designed multi-storey building against progressive collapse was assessed. The additional reinforcement was composed by textile-reinforced mortar (TRM) and near-surface-mounted (NSM) reinforcement. The progressive collapse studied in this work is that generated by a removal of an internal column of an external frame. Internal column is referred here as not a corner or a penultimate column, but a column of which its beam has continuity in both sides. The focus of this study was on old buildings, i.e., those designed with standards in which progressive collapse was not addressed.

Four specimens were tested in laboratory: a control specimen, CON, with no strengthening, used as reference; a second one, NSM_PR, with the beam length partially strengthened for shear and stainless-steel NSM reinforcement for flexure; a third one, TRM_TR, with the beam strengthened in all its length for shear, and anchored TRM as flexural reinforcement; and the last specimen, NSM_TR, also strengthened in all its length for shear, but with stainless-steel NSM reinforcement for flexure.

The development of the resistant load was characterized by an increment of the load up to a peak P_f, after which the load dropped to a minimum P_{min}, and then a regain of load up to a second peak during TCA. Most of the specimens followed this pattern, with exception of the partially strengthened one. In this specimen the load increased up to the initial peak, then remained approximately around this value up to the end of the test.

The strengthening increased the resistant load during the CAA in up to 47%, however no significant increment in the load was observed at TCA. Instead, the maximum load achieved at this stage had the same magnitude of the CON but happening in a vertical deflection 7% higher. During the dropping-load phase, the strengthened specimens were able to sustain similar load to CON at P_f.

Furthermore, the strengthened specimens were able to transfer more load to the neighbour elements. The load cells at the beam level recorded an increment of 85% of the transferred load during the CAA and 2% during the TCA on the strengthened specimens. At the top of the columns those values were 27% and 12% respectively.

Additionally, the adopted strengthening techniques increased the rotations at the columns as well as the beam fixed-end rotations. The increased deformation at the joints associated with the higher load carrying capacity of the strengthened frames constituted an increased ductility. That could be later confirmed by the enhanced ductility ratios of the strengthened frames.

Other object of study in the present work was the influence of the type of flexural strengthening, NSM reinforcement and anchored TRM. Both techniques had pros and drawbacks, while the former could support and transfer more load during CAA, the later could dissipate more energy, and sustain and transfer higher loads at TCA. Nevertheless, both enhanced the progressive collapse resistance of the frame, being, therefore, suitable methods to improve the frame resistance to a column loss when associated to shear strengthening.

Furthermore, the length of shear strengthening was assessed in this study, partial or total. By varying the strengthening length, the peak of resistant load was maintained during CAA, but the vertical deflection in which this peak happened increased in 29% using full cover. During TCA, the fully strengthened specimen was able to sustain 12% more load than NSM_PR, yet 19% less than CON. NSM_PR had similar resistant capacity at the initial peak, was able to transfer more load during CAA, and less during TCA compared to NSM_TR. The latest better improved the frame ductility and presented no shear failure. Consequently, comparing both strengthening lengths for shear, the full cover is more adequate.

Furthermore, the robustness of the frame was assessed as proposed by Izzuddin et al. (2008). The dynamic response of the beam from its quasi-static test was achieved. Named pseudo-static response, with this curve it was possible to get the maximum dynamic response of the frame, as well as the energy absorption capacity of it. All the strengthened specimens improved the maximum dynamic responses, and consequently the energy absorption, compared to CON. The ductility of the frame was also enhanced, where the respective ductility ratios for CON, NSM_PR, TRM_TR and NSM_TR were 2.63, 2.75, 3.80 and 5.12.

With the pseudo-static curve achieved from the quasi-static tests it was possible to find the appropriate dynamic increase factor (DIF) of the specimens. For CON, NSM_PR, TRM_TR, NSM_PR the DIF found was respectively 1.80, 1.18, 1.66 and 1.44. Those results confirmed that the DIF used previously by GSA (2000) and DoD (2009) were conservative.

This page was left intentionally blank

CHAPTER 4 MICROMODELLING APROACH FOR THE SIMULATION OF PROGRESSIVE COLLAPSE

Due the complexity, size and time/resources demand of the experimental program, a numerical assessment emerges as an appropriate solution to enhance the research on progressive collapse due the loss of a column.

With the evolution of technology and methods of structural analysis, the prediction of a building's structural behaviour became gradually more representative. Finite Element Method (FEM) is a powerful tool that is constantly utilized in numerical simulations involving structural engineering studies (Ngo and Scordelis, 1967, Tedesco et al., 1994, Lowes, 1999, Kachlakev et al., 2001, Park et al., 2001, Hansbo and Hansbo, 2004, Li, 2007, Barbato, 2009, D'Amato et al., 2012, Lopez-Almansa et al., 2014, de Terán and Haach, 2017, Hajiloo and Green, 2019)

Currently, commercial software as Abaqus, DIANA, SAP2000 or Ansys (Hibbitt et al., 1997, Güntert et al., 1998, Wilson and Habibullah, 1998, Kohnke, 2001) have FEM inserted in their methods of analysis. Given the complexity of the mechanics of a frame under progressive collapse, the usage of those software allows the undertaking of a parametrical study in a faster and more reliable way, when compared to FEM-based self-made codes.

The usage of such programs is already well established in the structural engineering field to assess diverse problems, including progressive collapse. Birtel and Mark (2006), used the Abaqus` (Hibbitt et al., 1997) Concrete Damage Plasticity (CDP) model with embedded reinforcement. When varying material and geometrical properties, the authors observed the reliability of this tool in simulating load-bearing behaviour of reinforced concrete (RC) beams. Kwasniewski (2010) used LS-DYNA

(Hallquist, 2006) to perform a case study on the progressive collapse of an eight-story, steel-framed building. It was observed that on the large-scale global model, the mesh density is an important parameter on the modelling, and the representation of the structure must be simplified. Moreover, a realistic approximation of the structural response can be achieved with a detailed model when validated by experimental data.

Abaqus was also adopted in Su et al. (2010) to develop a FEM for simulating 3D crack propagation in quasi-brittle materials through the usage of cohesive elements. McKay et al. (2012) making use of SAP2000 (Wilson and Habibullah, 1998), found conservative values of the increase factors adopted by GSA (2003) and DoD (2009) on the analysis of the potential of a structure to progressive collapse. Lopez-Almansa et al. (2014) used a damage plasticity model with three different levels of simplification to assess its representativeness on reproducing results of non-linear, monotonic behaviour of RC-framed structures. A comparison of different program outcomes (SAP2000, SeismoStruct (Antoniou and Pinho, 2003), Abaqus) showed that the CDP model, used in Abaqus, provides the closest representation when compared to experimental results. Furthermore, Genikomsou and Polak (2015) observed that the dilation angle, damage criteria, and mesh size play an important role on the accuracy of simulations performed with the CDP model of Abaqus. Hajiloo and Green (2019) used the same CDP model to simulate the effects of fire on RC slabs strengthened with Glass Fibre-Reinforced Polymer (GFRP). Findings included the reliability of the model to conduct parametric studies on RC structures.

In this chapter a 3D finite element model is used to assess the structure more detailed, get local and global nonlinear behavior, and compare results with experimental outcomes. Here, all the tests performed along the experimental program, and the scenarios which were not possible to be reproduced in laboratory, were simulated with the commercial software Abaqus (Hibbitt et al., 1997).

Following, the background theory used in Abaqus is presented in conjunction with the material characterization to shed light over the decisions assumed in this work. Moreover, the description of the model, the results, parametrical analysis and the discussion over those subjects are presented in the following sections.

4.1 Background Theory

Abaqus has three types of models suitable for concrete: Brittle Cracking, Concrete Smeared Cracking, and Concrete Damage Plasticity (CDP). In resume, the model 'Brittle Cracking' is used for situations in which the concrete is over tension. For any compression load acting on the element, this model considers the behaviour as linear elastic. The 'Concrete Smeared Cracking' model is used in situations of monotonic load at low confining pressures. The Concrete Damage Plasticity (CDP) model is used when the element is subjected to cyclic loads. On CDP model it is considered the damage of the elastic modulus during the load/unloading process. For the present work, this model was chosen to characterize the material behaviour.

4.1.1 Concrete Damage Plasticity

All the following information regard to CDP model was extracted from the Abaqus manual (Hibbitt et al., 1997). The theory from which this model takes support can be found in Lubliner et al. (1989) and Lee and Fenves (1998). This model assumes that the two basic failure modes for concrete are due tensile cracking and compressive crushing. Despite it can be used to simulate plain concrete, CPD is more appropriate to use in reinforced concrete elements.

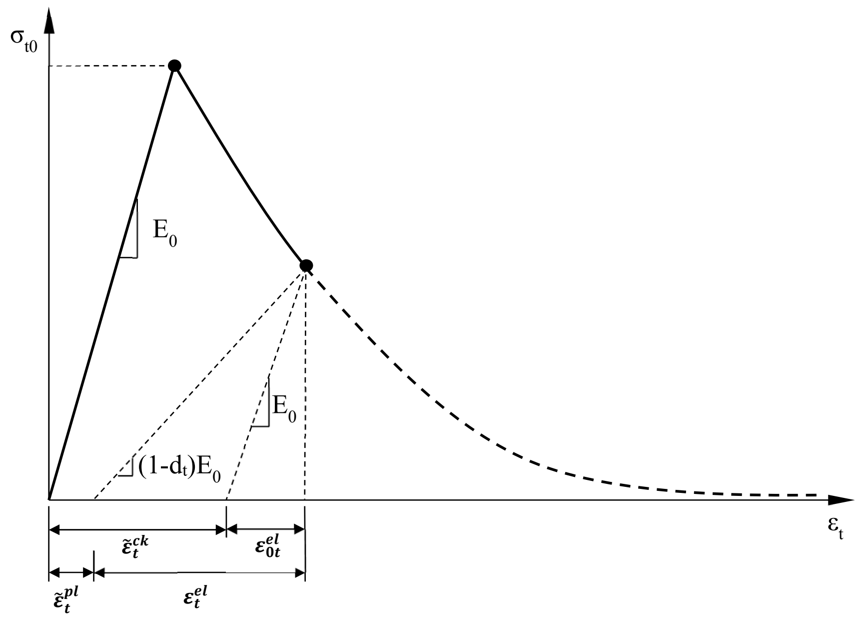

a)

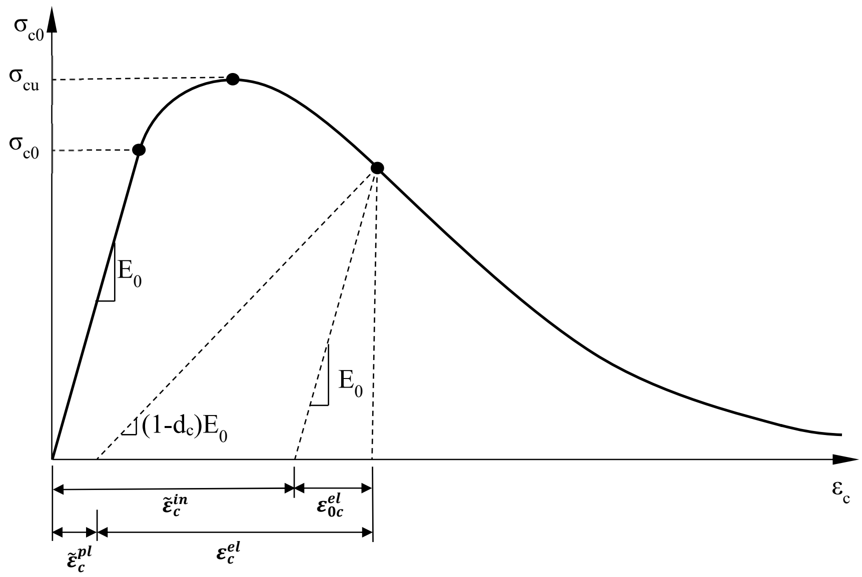

b)

Figure 4.1 – Concrete behaviour for Abaqus CDP a) Tension b) Compression (Hibbitt et al., 1997).

As mentioned before, CDP considers the degradation of the elastic modulus during the load/unload process. This degradation is accounted through a damage factor which applies directly to the elastic modulus. However, if it is intended, it is possible to simulate the behaviour of the concrete without damage. The uniaxial tensile and compressive behaviour of the concrete can be found in Figure 4.1(a)-(b) respectively.

Where:

$\boldsymbol{\sigma_{t0}}$ - Maximum tensile strength;

$\boldsymbol{E_0}$ - Elastic modulus;

$\boldsymbol{\varepsilon_{0t}^{el}}$ - Tensile elastic strain;

$\boldsymbol{\varepsilon_t^{el}}$ - Tensile strain in the concrete after unloading, considering the damage;

$\boldsymbol{\tilde{\varepsilon}_t^{ck}}$ - Tensile crack strain;

$\boldsymbol{\tilde{\varepsilon}_t^{pl}}$ - Tensile plastic strain;

$\boldsymbol{d_t}$ - Damage in tension;

$\boldsymbol{d_c}$ - Damage in compression;

$\boldsymbol{\sigma_{cu}}$ - Ultimate compressive strength;

$\boldsymbol{\sigma_{c0}}$ - Strength limit to the elastic behaviour;

$\boldsymbol{\varepsilon_{0c}^{el}}$ - Compressive elastic strain;

$\boldsymbol{\varepsilon_{c}^{el}}$ - Compressive strain in the concrete after unloading, considering the damage;

$\boldsymbol{\tilde{\varepsilon}_{c}^{in}}$ - Compressive inelastic strain;

$\boldsymbol{\tilde{\varepsilon}_{c}^{pl}}$ - Compressive plastic strain.

As shown in Figure 4.1a, after the peak stress the concrete is characterized by a softening in the stress-strain curve. This is to represent the formation of micro cracks in the concrete, which affects the response of stress with increment of strain. Moreover, in the compressive curve (Figure 4.1b) after the peak stress, it is possible to see the curve being softened, which accounts for main features of the reinforced concrete.

Both the tensile and compressive elastic strains can be achieved with the Hooke's law $\varepsilon_{0t}^{el} = \sigma_t/E_0$ and $\varepsilon_{0c}^{el} = \sigma_c/E_0$ respectively. The crack strain is the total tensile strain minus the elastic strain, as well as the inelastic strain, which is the total compressive strain minus the elastic strain, as following: $\tilde{\varepsilon}_t^{ck} = \varepsilon_t - \varepsilon_{0t}^{el}$, $\tilde{\varepsilon}_c^{in} = \varepsilon_c - \varepsilon_{0c}^{el}$. The plastic strain in tension and compression when the damage is considered are calculated by the software as per Equations 4.1 and 4.2 respectively:

$$\tilde{\varepsilon}_t^{pl} = \tilde{\varepsilon}_t^{ck} - \frac{d_t}{(1-d_t)}\frac{\sigma_t}{E_0} \quad \textbf{(4.1)}$$

$$\tilde{\varepsilon}_c^{pl} = \tilde{\varepsilon}_c^{in} - \frac{d_c}{(1-d_c)}\frac{\sigma_c}{E_0} \quad \textbf{(4.2)}$$

If the user does not want to input the tensile behaviour through the 'stress x strain' curve, the software provides the option to apply the yield stress and the associated displacement. Alternatively, the tensile behaviour can be defined through the fracture energy (G_f) and the tensile stress σ_t. The last method was the one considered in the present work, as presented in 4.2.1.2. In Abaqus, a linear loss of strength is assumed after cracking as it can be seen in Figure 4.2. In case the damage d_t is considered, Abaqus converts automatically the values of crack displacements (u_t^{ck}) in plastic displacements (u_t^{pl}) values as the following equation, considering the specimen length, l_0, as the unit, $l_0 = 1$. u_{t0} is the cracking displacement at complete loss of strength, and σ_{t0} the concrete maximum tensile strength.

$$u_t^{pl} = u_t^{ck} - \frac{d_t}{(1 - d_t)} \frac{\sigma_t l_0}{E_0} \tag{4.3}$$

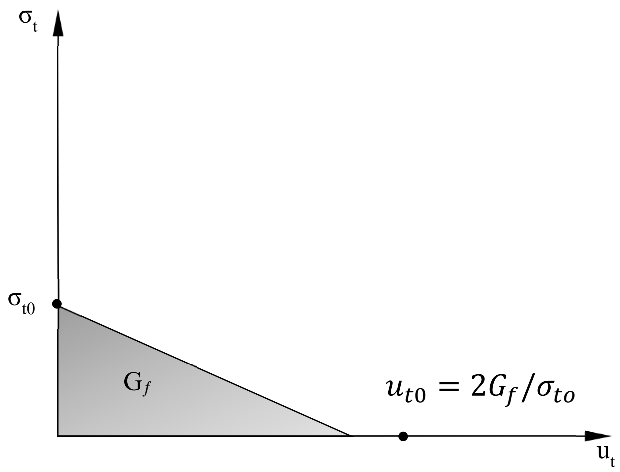

Figure 4.2 – Fracture energy assumption on Abaqus (Hibbitt et al., 1997).

The model proposed by Lubliner et al. (1989), base for the CDP model in Abaqus, used one scalar damage variable to represent the damage in compression (d_c) and tension (d_t). However, according to Lee and Fenves (1998), although the simulation of monotonic loads is possible with this assumption, it is not suitable to describe the concrete behaviour over cyclic load. So, Lee and Fenves (1998) modified the first model to account separately the damage in compression and tension, considering the stiffness recovery during the load/unload process. It was observed in quasi-brittle materials, as concrete, that the compressive stiffness is recovered when the cracks close due the change from tensile to compressive load. On the opposite way, the tensile stiffness is not recovered when load alternates from compression to tension. So, CDP model gives the option to the user to specify the tension and compression recovery parameter (w_t and w_c respectively). The default for the tension recovery is 0, what means no stiffness recovery after a crack is opened, and 1 for compression recovery, what means full recovery of the elastic stiffness after a crack is opened. Figure 4.3 presents one load cycle in the uniaxial behaviour for a quasi-brittle material.

In the CDP model some initial parameters are requested to describe the concrete behaviour: the dilation angle $\psi(\theta, f_i)$; the eccentricity ϵ; the ratio between the equibiaxial and uniaxial compressive yield stress σ_{b0}/σ_{c0}; the parameter Kc; and the viscosity parameter. Figure 4.4 presents the yield surface in the deviatoric plane (a) and in the plane stress (b) respectively adopted by Abaqus in the CDP model.

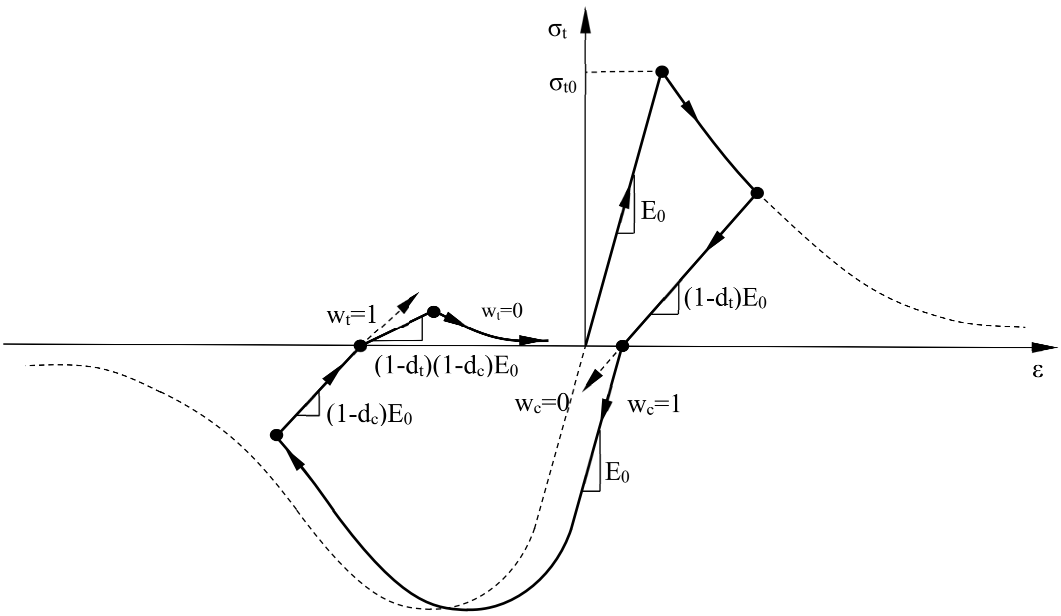

Figure 4.3 – Load cycle for a quasi-brittle material (Hibbitt et al., 1997).

The yield function of CDP model in Abaqus is presented in Equation (4.4). Where $\bar{q}$ is the Von Misses effective stress and $\bar{p}$ is the hydrostatic pressure, α and β are dimensionless constants (Equations (4.5) and (4.6)), $\hat{\bar{\sigma}}_{max}$ is the algebraically maximum principal stress. The notation ‹› represents the Macaulay bracket function, where ‹x› = (|x| + x)/2. The parameter γ (Equation (4.7)) is active only for stress states of triaxial compression, when $\hat{\bar{\sigma}}_{max}$ is negative. This parameter can be determined by comparing the yield conditions along the tensile and compressive meridians (T.M. and C.M. respectively). $\bar{\sigma}_c(\tilde{\varepsilon}_c^{pl})$ and $\bar{\sigma}_t(\tilde{\varepsilon}_t^{pl})$ are the effective compressive and tensile cohesion stresses respectively. If K_c = 1 the yield surface in the deviatoric plane takes the same shape as the Drucker-Prager criteria at high confining stresses. However, Abaqus uses a standard value of 2/3 to K_c (Figure 4.4a), which is adopted here. The ratio between the equibiaxial and the uniaxial compressive yield stress, σ_{b0}/σ_{c0}, is by default 1.16 in Abaqus, also adopted in the present work.

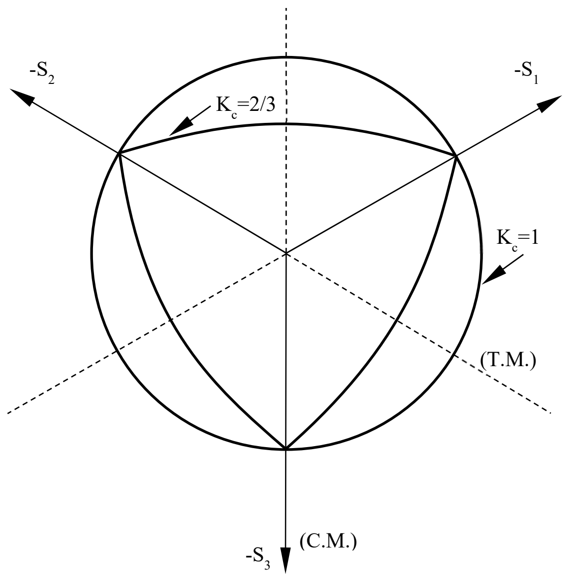

a)

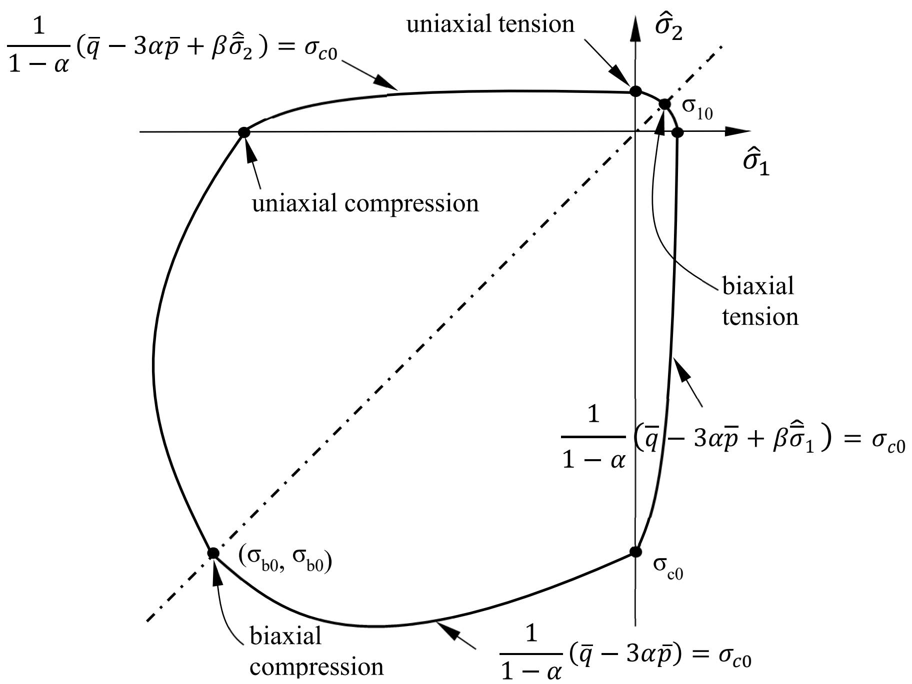

b)

Figure 4.4 – Yield surface on Abaqus a) deviatoric plane b) plane stress space (Hibbitt et al., 1997).

$$F = \frac{1}{1-\alpha}\left(\bar{q} - 3\alpha\bar{p} + \beta(\tilde{\varepsilon}^{pl})\langle\hat{\bar{\sigma}}_{max}\rangle - \gamma\langle-\hat{\bar{\sigma}}_{max}\rangle\right) - \bar{\sigma}_c\left(\tilde{\varepsilon}_c^{pl}\right) = 0 \quad \textbf{(4.4)}$$

$$\alpha = \frac{(\sigma_{b0}/\sigma_{c0}) - 1}{2(\sigma_{b0}/\sigma_{c0}) - 1};\ 0 \le \alpha \le 0.5 \quad \textbf{(4.5)}$$

$$\beta = \frac{\bar{\sigma}_c\left(\tilde{\varepsilon}_c^{pl}\right)}{\bar{\sigma}_t\left(\tilde{\varepsilon}_t^{pl}\right)}(1-\alpha) - (1+\alpha) \quad \textbf{(4.6)}$$

$$\gamma = \frac{3(1-K_c)}{2K_c - 1} \quad \textbf{(4.7)}$$

Other two parameters requested by CDP are the eccentricity and the dilation angle. Those are exposed in the flow potential (G) used by the CDP model:

$$G = \sqrt{(\epsilon\bar{\sigma}|_0 \tan\psi)^2 + q^2} - p\tan\psi \quad \textbf{(4.8)}$$

Where: $\psi(\theta, f_i)$ is the dilation angle, measured in the p-q plane at high confining pressure; $\bar{\sigma}|_0 = \bar{\sigma}|_{\bar{\varepsilon}^{pl}=0,\dot{\bar{\varepsilon}}^{pl}=0}$ is the initial yield stress; and ϵ is the eccentricity, which defines the rate at which the function approaches the asymptote. As it can be observed in Figure 4.5 the flow potential tends to become a straight line as ϵ approaches to zero. The default value for this parameter is $\epsilon = 0.1$, adopted for the simulations here.

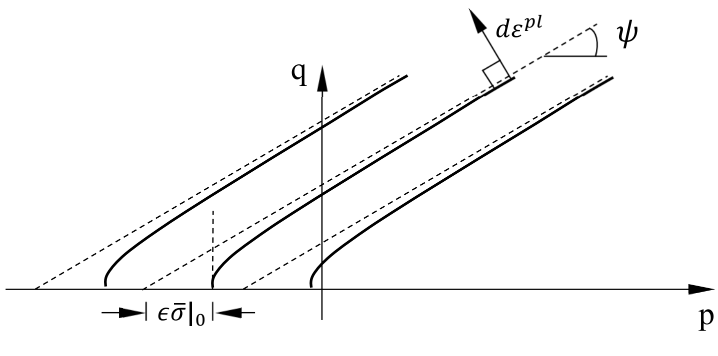

Figure 4.5 – Different flow potential curves (Hibbitt et al., 1997)

It is possible to find in the literature different values to the dilation angle, being used to match with each work need (Park et al., 2001, Jankowiak and Lodygowski, 2005, Birtel and Mark, 2006, Mercan et al., 2010, Kmiecik and Kamiński, 2011, Niza, 2012, López-Almansa et al., 2014, Genikomsou and Polak, 2015). For the present work the value assumed is 30º.

The viscosity parameter requested by CDP helps to improve the rate of convergence of the model by allowing stresses to be outside the yield surface. For this reason, if the user does not want to use the default, 0, very small positive values of viscosity might to be chosen, so the behaviour of the material will not be affected. For the present work the value of 10^{-4} was adopted. Table 4.1 summarizes all the parameters values adopted in the CDP models.

ψ	ϵ	σ_{b0}/σ_{c0}	k	Viscosity
30º	0.1	1.16	0.667	0.0001

Table 4.1 – CDP adopted parameters.

4.2 Material Characterization

4.2.1 Concrete Behaviour

4.2.1.1 Compression

The curves to describe the uniaxial stress-strain relation of the concrete were extracted from the literature and it is possible to find different criteria to define it (Hognestad, 1951, Hsu and Hsu, 1994, Nayal and Rasheed, 2006, Hordijk, 1992, Krätzig and Pölling, 2004, du Beton, 1993). To the present work, the compressive uniaxial behaviour of the concrete was the same as in Genikomsou and Polak (2015), where the authors used the Hognestad parabola (Hognestad, 1951) as presented in Figure 4.6. The numerical investigations conducted as part of this work demonstrated that this definition provides reliable and robust results similar to the findings of Genikomsou and Polak (2015). In this relation, f'_c is the maximum compressive strength of the concrete, which is being used here as the mean compressive strength of the concrete f_{cm}, defined in Eurocode 2 (Institution, 2004) as $f_{cm} = f_{ck} + 8$, in MPa. E_0 is the elastic modulus of concrete, defined by Genikomsou and Polak (2015) as $E_0 = 5500(f'c)1/2$. The concrete remains elastic with f_{cm} varying from 0 to $0{,}4f_{cm}$. E_{sec} can be achieved with $E_{sec} = 5000(f'_c)1/2$, and the strain at the maximum strength $\varepsilon_0 = f'_c/E_{sec}$. The development of σ_c is obtained as presented in Figure 4.6.

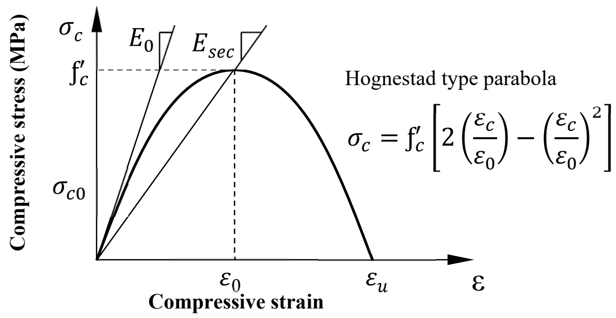

Figure 4.6 – Compressive behaviour (Hognestad, 1951).

The concrete compressive strength f'_c was assumed to be equal to the strength established by the cubic tests described in Chapter 3, which actually resulted in excellent predictions vis-à-vis the maximum attained load of the specimens at their CAA as shown in Section 4.4.1.

According to the Eurocode 2 (Institution, 2004) the elastic behaviour of the concrete depends also on the type of aggregate used. A 16 MPa concrete with quartzite aggregates has a secant value of the elastic modulus, E_{cm}, between $\sigma_c = 0$ to $0{,}4f_{cm}$, equal to 29 GPa. For concrete with limestone and sandstone the value must be reduced to 10% and 30%, respectively. For concrete with basalt aggregates this value must be increased by 30%.

4.2.1.2 Tension

For the tensile behaviour, the concrete is elastic up to the maximum tensile strength, f'_t. After that, a bilinear slope was used, as in Genikomsou and Polak (2015), according to the uniaxial tensile stress-crack width relation and the fracture energy of the concrete, G_f, as presented in Figure 4.7a. The crack strain is achieved with the elastic modulus $\varepsilon_{cr} = f'_t/E_0$. The other two key points of strains are defined as in Figure 4.7b, where l_c is related to the element of the mesh.

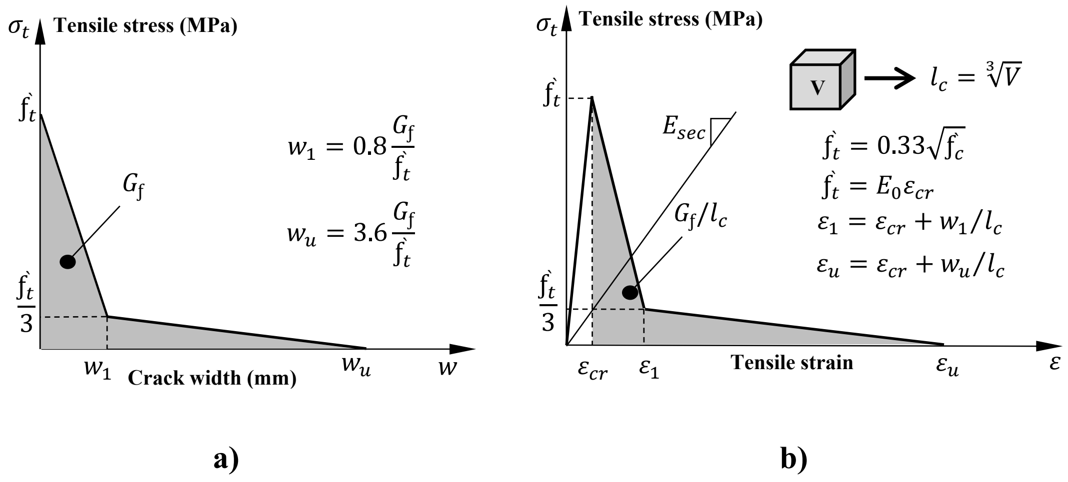

Figure 4.7 – Tensile behaviour of the concrete a) stress-crack width relation b) stress-strain relation (Genikomsou and Polak, 2015).

The fracture energy G_f is achieved with the area below the graph in Figure 4.7a, but alternatively, the Model Code (Code, 2010) defines it as $G_f = 73(f_{cm})1.8$.

4.2.2 Steel Behaviour

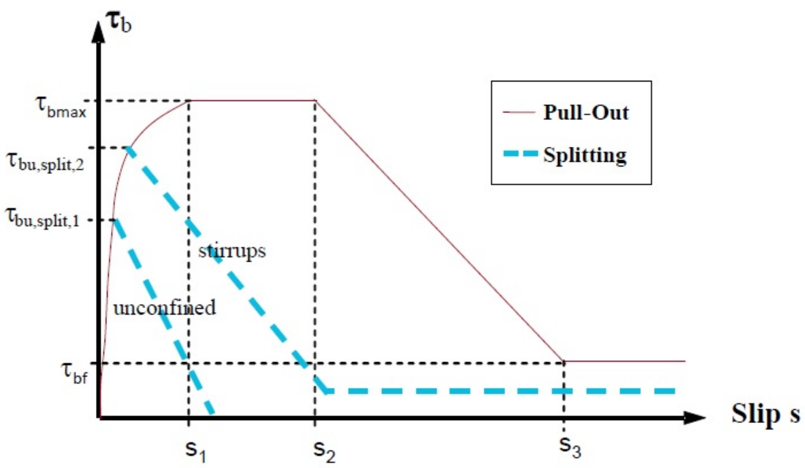

Figure 4.8 – Bond-Slip relationship between concrete and steel (Model Code, 2010).

The internal reinforcement was modelled with two different methods, one considering only the yield stress of steel as limit to plasticity, and the second considering the bond-slip interaction between concrete and steel. The stirrups were modelled with the former, and for that it was used the 'Plastic' model presented in Abaqus. In this model, it is necessary to define pairs of stress-plastic strain values starting from the yield stress and null plastic strain.

For the longitudinal reinforcement the bond-slip behaviour was considered. This interaction is crucial to better simulate large displacements such as this work does. In the present work that slippage was derived from the provided by the Model Code (Code, 2010), presented in Figure 4.8, where, considering the interaction between concrete and steel, τ_{b0} is the bond stress, τ_{bmax} is the maximum bond stress, τ_{bf} is the final bond stress, s is the relative displacement and s_1, s_2, s_3 are limit values of relative displacements as per Figure 4.8 and Table 4.2.

	Good bond conditions	**All other bond conditions**
τ_{bmax}	$2.5\sqrt{f_{cm}}$	$1.25\sqrt{f_{cm}}$
s_1	1.0 mm	1.8 mm
s_2	2.00 mm	3.6 mm
s_3	Cclear	Cclear
α	0.4	0.4
τ_{bmax}	$0.4\tau_{bmax}$	$0.4\tau_{bmax}$

*Cclear is the distance between ribs.

Table 4.2 – Parameters defining the mean bond-stress relationship of ribbed bars (Model Code (Code, 2010)).

The curve defined for this work considered the Pull-Out (PO) failure for all longitudinal bars and can be built according to the following equations (Model Code (Code, 2010)):

$$\tau_{b0} = \tau_{bmax}(\frac{s}{s1})^{\alpha} \qquad \text{for } 0 \leq s \leq s_1 \qquad \textbf{(4.9)}$$

$$\tau_{b0} = \tau_{bmax} \qquad \text{for } s_1 \leq s \leq s_2 \qquad \textbf{(4.10)}$$

$$\tau_{b0} = \tau_{bmax} - (\tau_{bmax} - \tau_{bf})\frac{(s - s_2)}{(s_3 - s_2)} \qquad \text{for } s_2 \leq s \leq s_3 \qquad \textbf{(4.11)}$$

$$\tau_{b0} = \tau_{bf} \qquad \text{for } s_3 \leq s \qquad \textbf{(4.12)}$$

de Terán and Haach (2017) modified the previous criteria in order to better calculate the crack opening with the following substitution:

$$\tau = \tau_1(A+1)\left(\frac{s}{s1}\right)[\left(\frac{s}{s1}\right)+A]^{-1} \qquad \text{for } 0 \leq s \leq s_1 \qquad \textbf{(4.13)}$$

Where the authors suggest A=0.3267, and τ_1 is the shear stress between 0 and s_1.

Taking as basis de Terán and Haach (2017) work, a ‘stress x strain’ curve is achieved for the steel considering the slippage between concrete and steel following these relations:

$$\sigma_s = \frac{\sigma_{s,max} + E_S(\varepsilon_{s,eq} + A\varepsilon_{s,eq1}) - R_1}{2} \leq f_y \qquad \text{if } 0 \leq \varepsilon_{s,eq} \leq \varepsilon_{s,eq1} \qquad \textbf{(4.14)}$$

$$\sigma_s = \sigma_{s,max} \leq f_y \qquad \text{if } \varepsilon_{s,eq1} \leq \varepsilon_{s,eq} \leq \varepsilon_{s,eq2} \qquad \textbf{(4.15)}$$

$$\sigma_s = \sigma_{s,max} - (\sigma_{s,max} - \sigma_{s,f})\left(\frac{\varepsilon_{s,eq} - \varepsilon_{s,eq2}}{\varepsilon_{s,eq3} - \varepsilon_{s,eq2}}\right) \qquad \text{if } \varepsilon_{s,eq2} \leq \varepsilon_{s,eq} \leq \varepsilon_{s,eq3} \qquad \textbf{(4.16)}$$

$$\sigma_s = \sigma_{s,f} \qquad \text{if } \varepsilon_{s,eq3} \leq \varepsilon_{s,eq} \qquad \textbf{(4.17)}$$

Where:

$$R_1 = \sqrt{\sigma_{s,1}^2 + E_s^2(\varepsilon_{s,eq} + A\varepsilon_{s,eq1})^2 - 4E_S\sigma_{s,max}[(\frac{A+1}{2})\varepsilon_{s,eq} - \frac{A\varepsilon_{s,eq1}}{2}]} \qquad \textbf{(4.18)}$$

$$\varepsilon_{s,eq1} = \frac{4l\tau_{bmax}}{d_bE_s} + \frac{s_1}{l} \qquad \textbf{(4.19)}$$

$$\varepsilon_{s,eq2} = \frac{4l\tau_{bmax}}{d_bE_s} + \frac{s_2}{l} \qquad \textbf{(4.20)}$$

$$\varepsilon_{s,eq3} = \frac{4l\tau_{bmax}}{d_bE_s} + \frac{s_3}{l} \qquad \textbf{(4.21)}$$

$$\sigma_{s,max} = \frac{4l\tau_{bmax}}{d_b} \quad \textbf{(4.22)}$$

$$\sigma_{s,f} = \frac{4l\tau_{bf}}{d_b} \quad \textbf{(4.23)}$$

Where, regard to the reinforcement steel: σ_s is the tensile stress; $\sigma_{s,max}$ is the maximum tensile stress; E_s is the elastic modulus; $\varepsilon_{s,eq}$ is the equivalent strain; $\varepsilon_{s,eq1}$, $\varepsilon_{s,eq2}$, $\varepsilon_{s,eq3}$ are limit values for the equivalent strain as per Figure 4.9; R_l is a factor applied to the tensile stress; f_y is the steel yield strength $\sigma_{s,f}$ is the final tensile stress; $\sigma_{s,1}$ is the stress between 0 and $\varepsilon_{s,eq1}$; and d_b is the diameter of the reinforcement.

The parameter 'l' is the transmission length. In the present work it was adjusted according to the experimental work. Following, the 'stress x strain' curve development is presented in Figure 4.9 for a S500 steel..

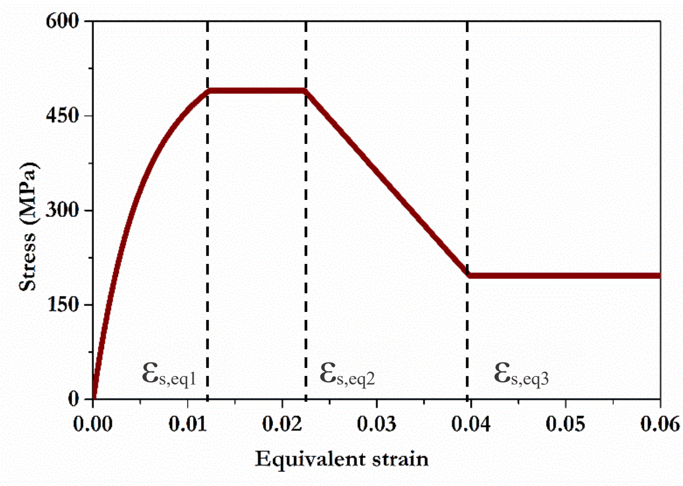

Figure 4.9 – Stress x Equivalent Strain curve for the steel.

4.2.3 Proposed Steel Behaviour After Slippage

During the experimental phase of this work the internal reinforcement was broken during the tests in most of the specimens. If the steel behaviour is built in the computational model only with the previously described 'stress x strain' curve, it would not be representative. The bond-slip relation as it is proposed by the Model Code (Figure 4.8) is adequate for situation where the steel inside the concrete keeps slipping during all the development of strain. Therefore, a curve which addresses the steel fracture after slippage is needed.

The reason for the bar fracture can be attributed to the topology of the frame, the configuration of the internal reinforcement inside it, and the evolution of the vertical deflection. With the evolution of the vertical displacement, depending on the size and location of the internal reinforcement, as well as the position of the appliance of the load, hooks are formed along the bar length (Figure 4.10). With this new configuration, the reinforcement gets mechanically constrained to the concrete. This new mechanism of anchorage of the reinforcement allows the steel to develop stress up to the fracture.

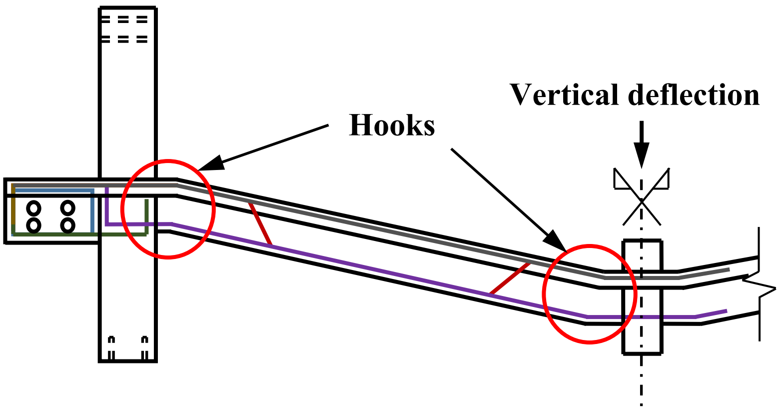

Figure 4.10 – Formation of hooks along the longitudinal reinforcement with the evolution of vertical deflection.

The curve presented in Figure 4.9 comprises both slippage and strains, therefore defining the point of the curve in which those hooks are activated will depend on, amongst other parameters, the geometry of the experiment. When the full model is taken in consideration the task become more complex, given that different bars will develop strains and slippage differently depending on the correspondent stress concentration as well. Therefore, a calibration process was conducted to establish to the model proposed the best point of activation of the hooks. It was achieved that defining the regain of load after $\varepsilon_{s,eq3}$ (Figure 4.11) provides faithful results to the full model (see section 4.6.2).

With the previously explained definition, all the longitudinal reinforcement can develop the slippage behaviour along its length before the load in any part of it starts increasing again. Dividing the reinforcement in element makes it easier to understand. For example: when the first element develops the strain up to $\varepsilon_{s,eq3}$, the neighbour elements will be yet decreasing the load with the increment of strain. Since the first element has an increment in its load capacity, the neighbour elements will be forced to deform up to the point where it supports the same load of the first element. This process repeats to the following adjacent elements and the first element is always the first to reach higher deformations and loads. This way, this element will reach the fracture criteria first.

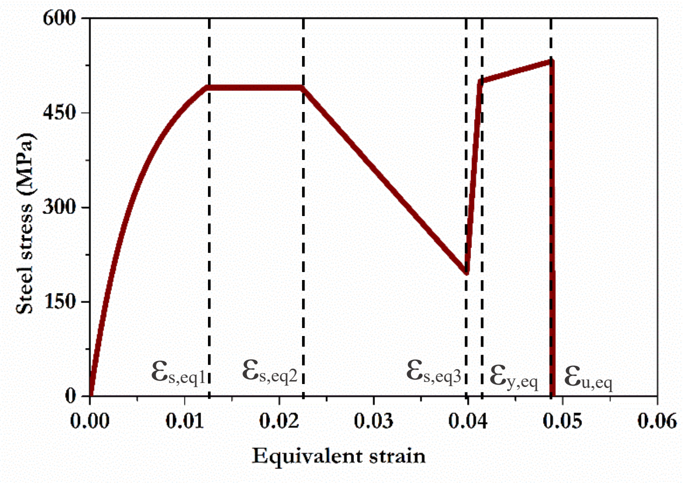

Figure 4.11 – Proposed Stress x Equivalent Strain relation for the steel.

On the development of equivalent strains in Figure 4.9 the reinforcement only reaches the yield strain, after that, only slippage occurs. Therefore, up to $\sigma_{s,f}$ it can be considered that there is no plastic deformation. So, in the suggested behaviour the load increases again with no plastic strain, only the elastic correspondent to the load where it starts growing back. Thus, the curve evolves up to the yield stress of the steel, and from this point onward it was considered hardening of the steel. To build the proposed curve after the deformation reaching $\varepsilon_{s,eq3}$ the following relations are needed:

$$\sigma_s = \sigma_{s,f} + E_s(\varepsilon_{s,eq} - \varepsilon_{s,eq3}) \quad \text{if } \varepsilon_{s,eq3} \leq \varepsilon_{s,eq} \leq \varepsilon_{y,eq} \qquad \textbf{(4.24)}$$

$$\sigma_s = f_y + E_{s,hard}(\varepsilon_{s,eq} - \varepsilon_{y,eq}) \quad \text{if } \varepsilon_{y,eq} \leq \varepsilon_{s,eq} \leq \varepsilon_{u,eq} \qquad \textbf{(4.25)}$$

$$\sigma_s = 0 \quad \text{if } \varepsilon_{u,eq} \leq \varepsilon_{s,eq} \qquad \textbf{(4.26)}$$

Where:

$$\varepsilon_{y,eq} = \varepsilon_{s,eq3} + \frac{f_y - \sigma_{s,f}}{E_s} \quad \textbf{(4.27)}$$

$$\varepsilon_{u,eq} = \varepsilon_{y,eq} + (\varepsilon_u - \varepsilon_y) \quad \textbf{(4.28)}$$

$$\varepsilon_y = \frac{f_y}{E_s} \quad \textbf{(4.29)}$$

$$E_{s,hard} = E_s \times \beta_s \quad \textbf{(4.30)}$$

Where, regard to the reinforcement steel: $E_{s,hard}$ is the steel stiffness at the hardening phase; ε_y is the yield strain; ε_u is the ultimate strain; $\varepsilon_{y,eq}$ is the equivalent yield strain; $\varepsilon_{u,eq}$ is the equivalent ultimate strain; and β_s is the hardening factor. The ultimate strain of the steel is considered here ε_u = 0.01, and the factor affecting the elastic modulus after the steel yields is β_s=0.02.

Figure 4.11 presents the final configuration of the 'stress x equivalent strain' curve for the steel adopted in the present work. In section 4.6.2 the good agreement between simulation and experimental curves can be witnessed.

4.2.4 NSM Stainless Steel Reinforcement

The same criteria adopted to the internal reinforcement was also used to simulate NSM. However, here the NSM reinforcement strength was 650 MPa.

4.2.5 TRM Behaviour

The behaviour of the TRM is derived from two components: the mortar, and the textile. The properties of both materials were obtained either through experimental tests or provider data sheet. Each batch of mortar used to compose the TRM was tested through flexural and compressive test. Therefore, for each experiment simulation the property of the mortar was inserted with the data from the experimental assessment. The mortar of the NSM_PR, TRM_TR and NSM_TR had respectively 30.1 MPa, 31.8 MPa and 36.8 MPa of compressive strength, while the Young's modulus was 2.1 GPa, 1.94 GPa and 2.15 GPa respectively. The textile follows the described in chapter 3.

4.3 Model Description

Initially, a complete model was built following the experiment set-up (Figure 4.12). However, the computational and time costs for this model would be against the efficiency of the development of this work. For that reason, simplifications were adopted in this model. The boundary conditions could not be simplified, therefore simulations of the attachments to the set-up presented more realistic results than with simplified boundary conditions. Hence, the model was reduced to the concrete element, internal reinforcement, strengthening scheme, load cells and some pieces of the test set-up (Figure 4.13).

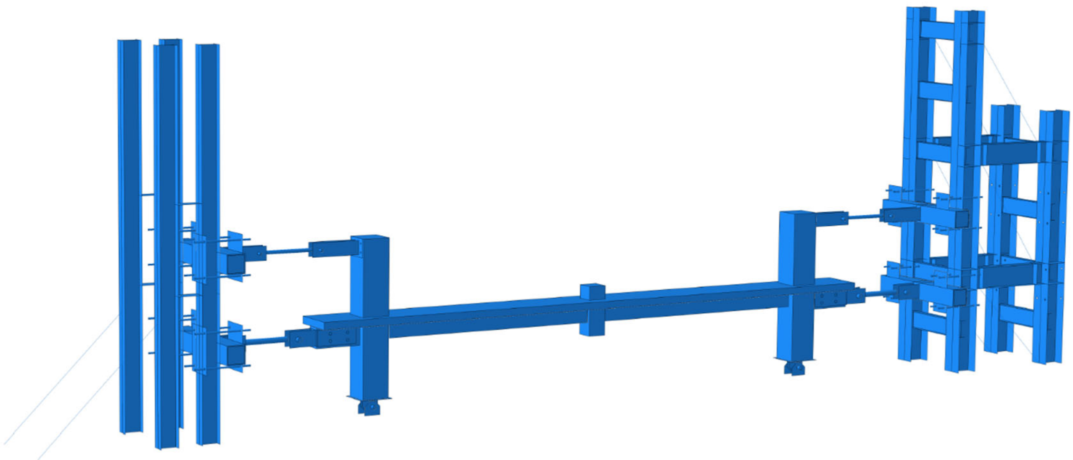

Figure 4.12 – Complete model.

Considering the failure modes of the specimens and the calibration process, two of the four models were kept in its full length (Figure 4.13), while other two were simulated in half (Figure 4.14). In section 3.5.3 the failure modes of the experiments are presented; one can see that the specimens with NSM have not had a symmetrical failure. On the other hand, the CON and TRM_TR specimens had. Therefore, NSM_PR and NSM_TR were simulated with the full length of the frame (Figure 4.13), while CON and TRM_TR with half of it (Figure 4.14). This decision also aimed to optimize the general time consumption of the numerical program without losing the representativity of the model.

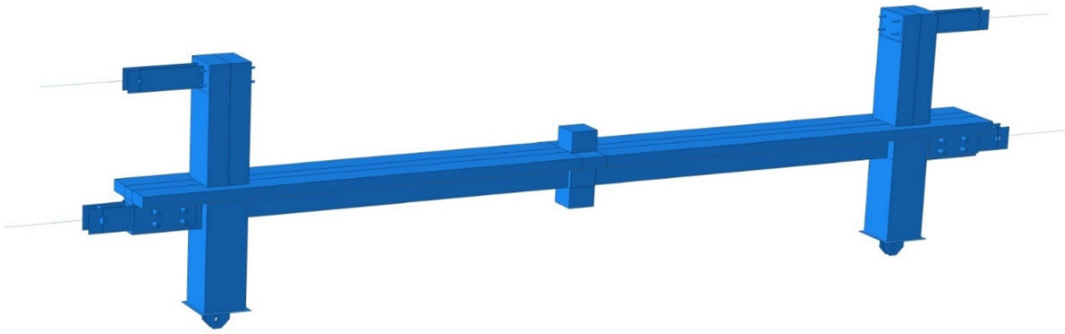

Figure 4.13 – Full frame.

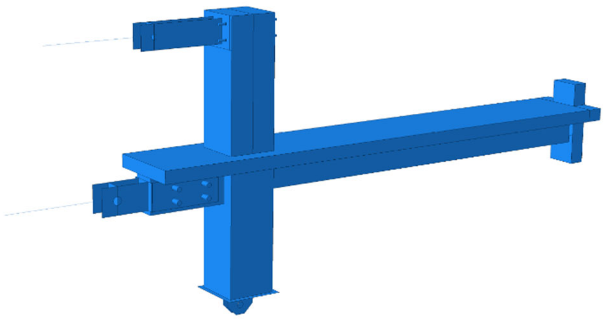

Figure 4.14 – Half frame.

The internal reinforcement was built considering that the beam reinforcement of both sides of the middle column had lap-splice around the middle column position as shown in Figure 4.15 in plan view. The distances between the reinforcement bars on the left and right side of the end column are shown in Table 4.3. As a result, the distribution of the reinforcement in plan view is slightly asymmetrical with respect to the midline of the beam. This asymmetry was expected to be reflected in the analysis results. The remaining reinforcement not shown in Figure 4.15 was symmetric and included in the model considering the layout shown in Figure 3.5 and Figure 3.7. The NSM reinforcement, TRM and flexural textile-based anchors were positioned as per Figure 3.18, Figure 3.19, Figure 3.23 and Figure 3.24, respectively.

Elements for each part were adopted as following. For the concrete and the bolts of the set-up it was chosen 3D solid deformable elements. For the internal reinforcement, NSM, flexure anchors, load cells and the pin of the bottom support it was chosen wire elements, being truss for the reinforcement, NSM, flexure anchors and load cells; and beam for the bottom pin. For the TRM and some pieces of the set-up, shell elements were used. Due the failure mode of the NSM_PR specimen, where part of the TRM remained attached to the concrete at the major crack location, cohesive elements were used to represent this region.

Side	Distances between bars (mm)			
	1-1'	2-2'	3-3'	4-4'
Right	27	65	252.5	440
Left	11	49	240.5	428

Table 4.3 – Computational model asymmetry regard to the longitudinal axis.

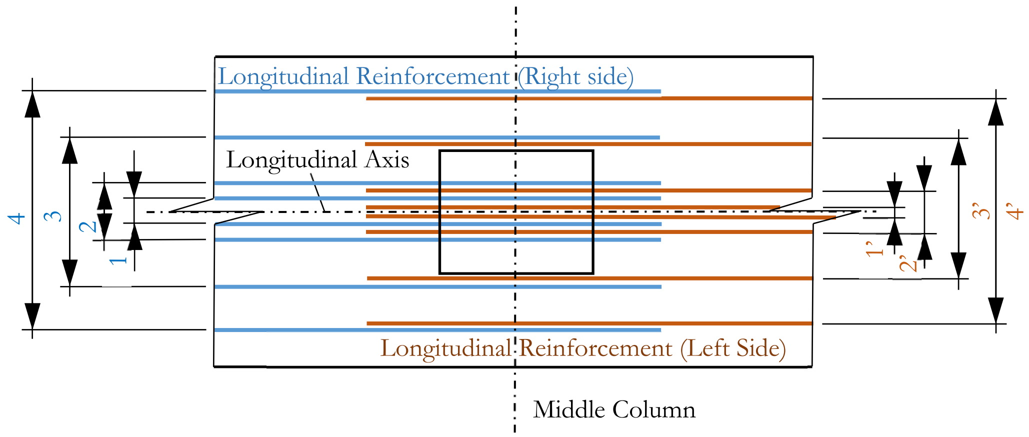

Figure 4.15 – Internal reinforcement position in the model.

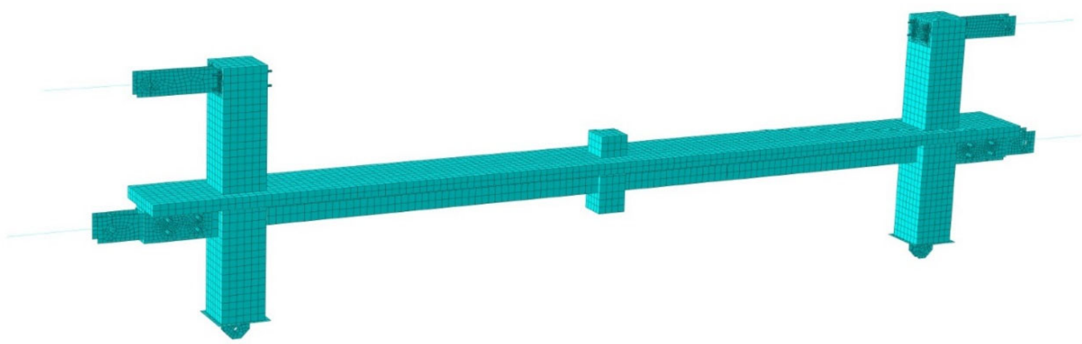

Figure 4.16 – Model general mesh.

The element chosen for the concrete mesh was the CD38R. 3D stress elements with linear geometric order, 8 nodes, and a length of 50 mm per side. Reduced integration was used to increase the computational efficiency. For the wires, T3D2 truss elements were used for the load cells, reinforcement, flexure anchors and NSM, while B31 beam element was used for the pin at the base. The former, a 2-node linear 3D truss, and the last, a 2-node linear element. For the set-up, the S4R, a doubly curved thin or thick shell, was used, while for the TRM the 4-node doubly curved general-purpose element S4 was considered. For the cohesive elements and 8-node-three-dimentional cohesive element, COH3D8, was considered. Figure 4.16 presents the model mesh.

The reinforcement was constrained to the beam through the ‘embedded region’ option. The TRM was constrained to the beam through the ‘tie constraint’ command, excluding in the second specimen, where, as mentioned previously, the region where there was no anchor was attached to the beam with cohesive elements. The properties of the cohesive elements were derived from curve fitting process. The cohesive stiffness was defined in proportion to the material stiffness in compression and in each direction of the plane (normal and shear directions) so as to not influence the analysis results; a factor equal 100000000 was assumed for this purpose. The value of the damage initiation stress along the normal direction was considered to be 1 MPa whereas a value of 10 Mpa was considered along the shear direction; finally, a fracture energy of 0.07 N/m was employed to define the damage evolution. The load was applied through a downward vertical displacement increment acting at the top of the middle column.

4.4 Calibration

A calibration process was conducted to validate the models with the experiments performed in laboratory. The parameters of the models were changed to achieve the curve which would best fit with the experimental results.

Apart of the representation of the boundary conditions, another influent factor for the complete processing of the model was its method of assessment – Explicit mode with mass scaling was presented to be crucial on the proper representation of the frame under large deflections. A small target increment time, i.e., 0.0001, was adopted to reduce the variation between increments’ responses. Furthermore, further to the mechanical paraemters shown in Table 4.4, a set of additional model parameters were assessed in the calibration process, with their optimal values shown in Table 4.6.

	Model	Conc.	Steel	Mortar	Textile	
	Type	**E_C**	**Es (GPa)**	**E_M**	**E_T**	**f_T**
CON	Half	$E_C/3$	210	-	-	-
NSM_PR	Full	$E_C/3$	210	E_M	E_T	f_T
TRM_TR	Half	$E_C/3$	210	E_M	$E_T/2$	$f_T/2$
NSM_TR	Full	$E_C/4$	150	$2E_M$	E_T	f_T

Table 4.4 – Parameters of calibrated models.

Some material parameters' values were represented as a fraction of each original value. The new values help to compensate for adaptations on the simulations, as a stiffer set-up and boundary conditions, bond-slip behaviour, for instance (see section 3.3). Moreover, as mentioned in Section 4.2, depending on the type of the aggregate, the stiffness of the concrete can be reduced in up to 30%. On NSM_TR the failue was characterized by localized cracks and bar fractures on non-strengthenes cross sections. Therefore, due to model limitations to simulate discrete failures the stiffness in this specimen had to be even more reduced than the other specimens.

Figure 4.17 presents the curves from the simulations which best fit the correspondent experimental curves during the calibration process. In all cases the the model predictions provide an excellemt match to the experimental results especially during the CAA regime of the response. For the case of the control specimen, the maximum load attained during the CAA depends solely on the compressive strength of concrete. This further reinforces the confidence in the validity of the assumptions with regards to the concrete constitutive modelling procedure, which is described in Section 4.2. The TCA is also closely reproduced although with higher discrepancies, which are discussed in Section 4.7. Following the final configuration of the models are compared to the correspondent experiments.

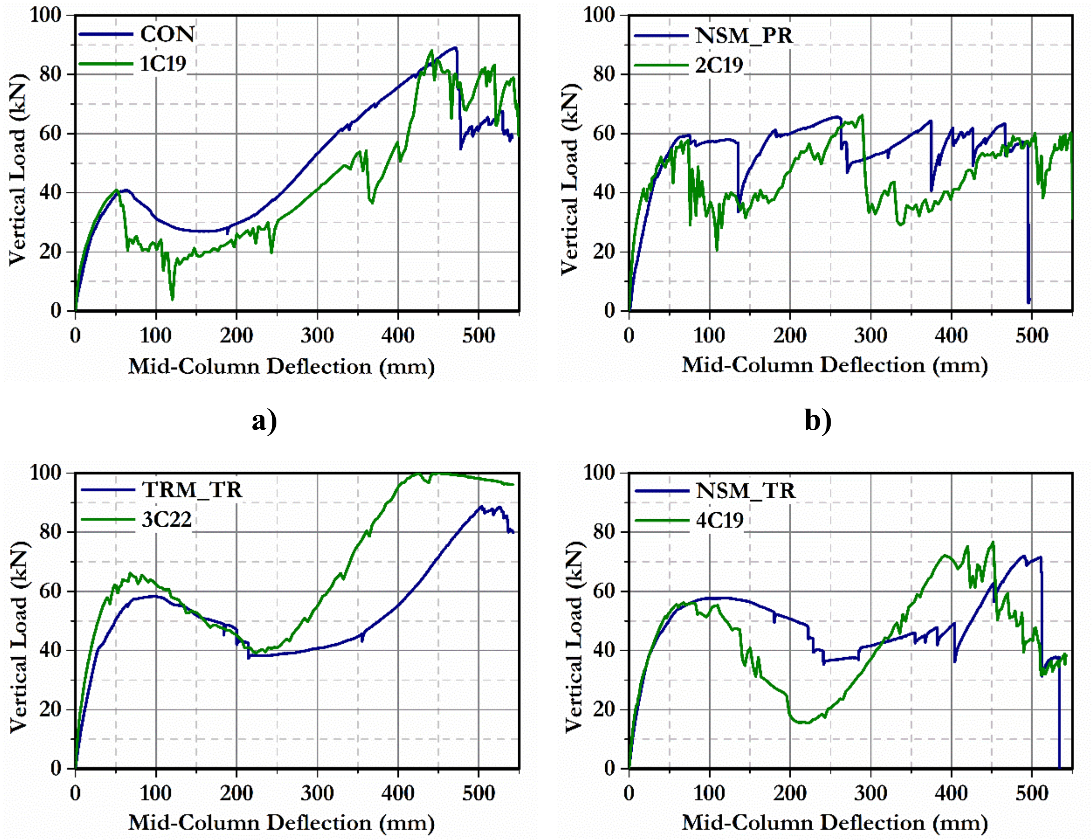

a) b)

c) d)

Figure 4.17 – Validation of the models a) CON b) NSM_PR c) TRM_TR d) NSM_TR.

4.4.1 CON

The failure modes of the models presented good representativity to each correspondent experiment. Figure 4.18a presents the final configuration of the model 1C19, highlighting the regions where plasticity was more intense in the concrete. The final configuration of CON is shown in Figure 4.18(b)-(c). One can see that concrete crushing at the side joints, the major cracks at the middle joint, as well as the beam detachment from the slab also at the middle joint could be reproduced in the simulation. Minor cracks are not being represented at Figure 4.18a because the major damages were disproportionally bigger than those minor cracks. Therefore, the differences on shades of colours are unperceptive to be shown.

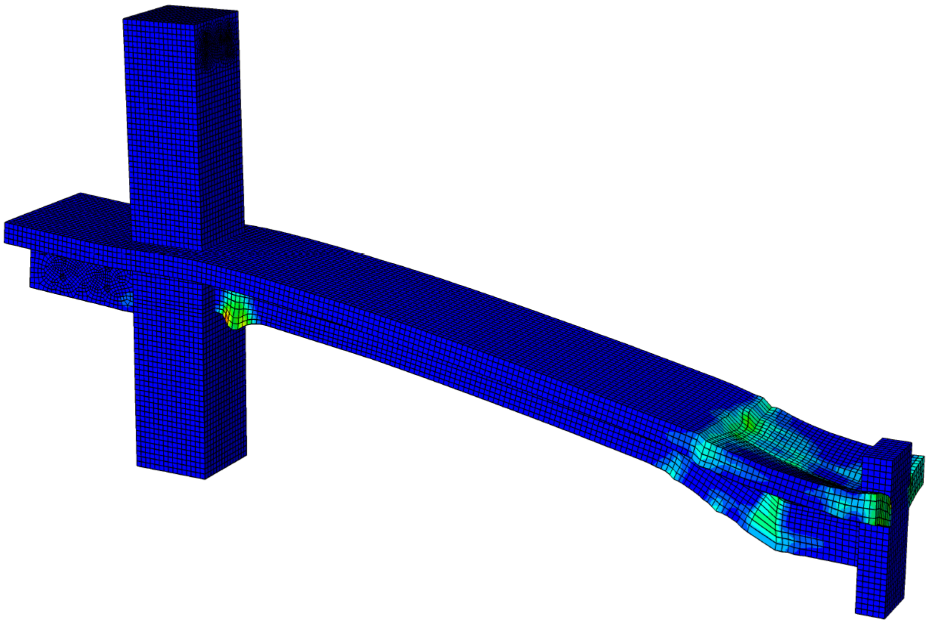

a)

b) c)

Figure 4.18 – Comparison of the failure modes of CON Model vs Experiment a) Simulation b) experiment side joint c) experiment middle joint.

4.4.2 NSM_PR

The comparison of the NSM_PR specimen can be visualized in Figure 4.19. The plasticity of the concrete is presented in (a), and in (b)-(c) the experiment final configuration at side and middle joints are presented. Since the failure was asymmetrical, at this time step the shear at the left side of the middle joint was already developed, reason why less plasticity can be visualized in this region. At the right side, the deformations due to shear were increasing, forcing the longitudinal reinforcement downwards, presenting therefore more plastic behaviour there. A crack was being opened at the top of the left side of the beam, being that the highest value of plastic deformation at this time step.

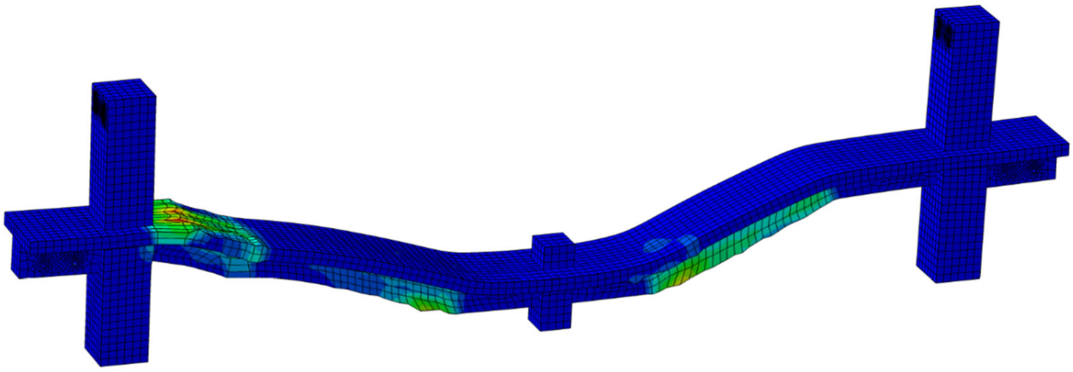

a)

b) c)

Figure 4.19 - Comparison of the failure modes of NSM_PR Model vs Experiment a) Simulation b) experiment side joint c) experiment middle joint.

4.4.3 TRM_TR

The third experiment, TRM_TR, is compared with the respective model in Figure 4.20, where the concrete plasticity in the model is presented in (a). Figure 4.20(b)-(c) show the side and middle joints failures respectively. As it is demonstrated, the major failure occurred at the middle column, where the concrete was pulled-off from it. At the side joint, the column presented plasticity in form of cracks. The top of the beam at this region failed by tension.

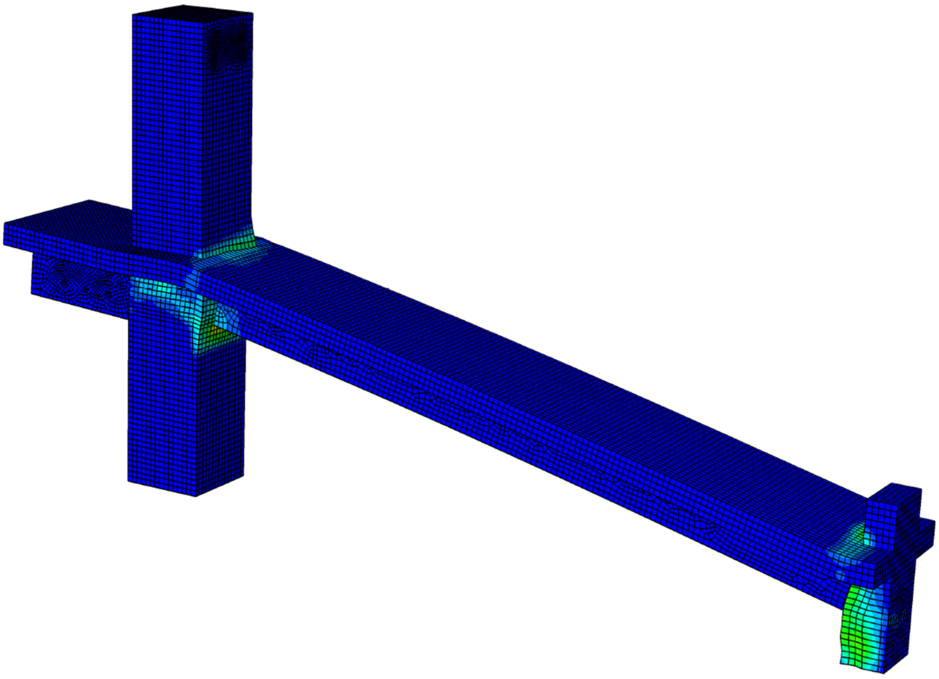

a)

b) c)

Figure 4.20 - Comparison of the failure modes of TRM_TR Model vs Experiment a) Simulation b) experiment side joint c) experiment middle joint.

4.4.4 NSM_TR

The comparison of the specimen NSM_TR model with its respective experiment is made in Figure 4.21. The plastic deformations on the concrete model are shown in Figure 4.21a. The experiment side and middle joints are shown respectively in Figure 4.21(b)-(c). Major damages were localized at the beam/column interfaces. At the end of the test the failure was asymmetrical, occurring majorly at the right side of the middle column. At the top of the beam in both sides, cracks were formed and increased up to the end.

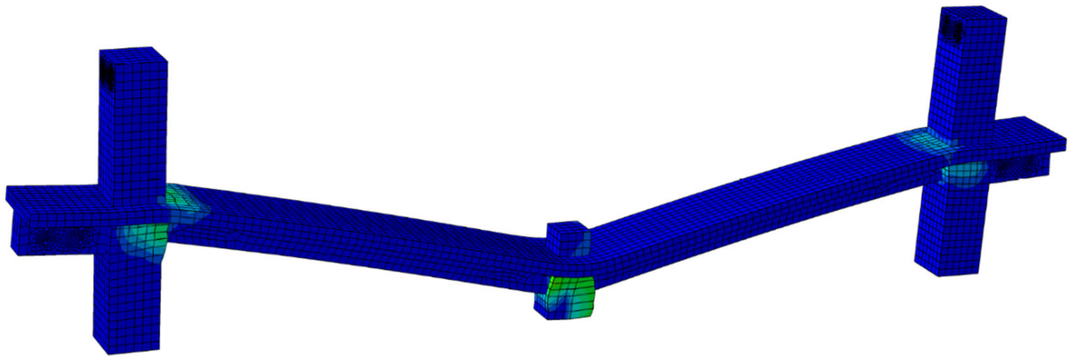

a)

b) c)

Figure 4.21 - Comparison of the failure modes of NSM_TR Model vs Experiment a) Simulation b) experiment side joint c) experiment middle joint.

Following, those key points adopted in Chapter 3, P_f (CAA), P_{min} (P_{med}) and P_{TCA} (TCA), were used here as point of comparison on the calibration process. Table 4.5 presents the values of vertical load and deflection for those points for each specimen test in conjunction with each respective original model. Given that in the specimen NSM_PR the load did not present the same development as in the other specimens, the second key point is called here as P_{med}.

At the first load peak, the maximum discrepancy between model and experiment was around 13%, at the TRM_TR, however in the other specimens the differences at the same key point reached less than 3%. The deflections in which that load peak occurred had a larger discrepancy, where the differences ranged between 1.5% and 71.6% on

CON and NSM_TR respectively. At P_{min} the opposite happened, the discrepancies were bigger in the load, where the maximum difference was 57% and the minimum was less than 1%, while the displacements had 22% and 10% respectively. During TCA, maximum and minimum differences between loads and deflections were 12% and 1%, and 18% and 6% respectively. Therefore, despite the differences in values between model and experiment, the models were considered to be satisfactory to proceed with the parametric study, however the study was focused on the CAA phase as it will be explained further.

Comparison	CAA (P_f)		P_{min} (P_{med})		TCA (P_{TCA})	
	Load (kN)	Deflection (mm)	Load (kN)	Deflection (mm)	Load (kN)	Deflection (mm)
CON	40.6	65.8	26.9	164.7	89.1	470.9
1C19	40.9	50.7	15.8	129.1	88.1	441.7
NSM_PR	59.5	74.7	65.6	257.9	64.3	464.7
2C19	57.8	73.6	66.2	289.3	60.3	548.0
TRM_TR	58.3	99.2	38.1	216.0	88.7	503.6
3C22	66.1	67.7	39.1	224.4	99.9	451.7
NSM_TR	57.7	116.2	36.4	244.1	72.0	490.5
4C19	56.2	67.7	15.6	220.7	76.8	451.7

Table 4.5 – Comparison of experiment and original model key points of each specimen.

4.5 Parametric Study

As presented in section 4.6, a calibration process was conducted to match the simulation and experimental curves. During this process some parameters were observed to be more influent on the vertical "Force vs Deflection" curve development and therefore were chosen to be studied more detailed. Additionally, the viscosity parameter of the Concrete Damage Plasticity (CDP) model was included in the parametric study to assess its influence on the convergence process.

The parameters chosen to the study were the following:

- Transmission length of the steel inside the concrete;

- Mesh size;
- Viscosity.

According to the Model Code (2010) the transmission length is one half of the medium spaciing between cracks. de Terán and Haach (2017) states that the higher the transmission length, the higher the equivalent stiffness of the reinforcement. Therefore, during the calibration process each specimen presented a different value of transmission length.

Parameter	CON	NSM_PR	TRM_TR	NSM_TR
Transmission Length (Serie L)	1L80	2L80	3L80	4L80
	1L100	2L100	3L100	4L100
	1L120	2L120	3L120	4L120
	1L140	2L140	3L140	4L140
	1L160	2L160	3L160	4L160
	1L180	2L180	3L180	4L180
	1L200	2L200	3L200	4L200
Mesh Size (Serie M)	1M20	2M20	3M20	4M20
	1M25	2M25	3M25	4M25
	1M30	2M30	3M30	4M30
	1M35	2M35	3M35	4M35
	1M40	2M40	3M40	4M40
	1M45	2M45	3M45	4M45
	1M50	2M50	3M50	4M50
Viscosity (Serie V)	1V1E-02	2V1E-02	3V1E-02	4V1E-02
	1V5E-03	2V5E-03	3V5E-03	4V5E-03
	1V1E-03	2V1E-03	3V1E-03	4V1E-03
	1V5E-04	2V5E-04	3V5E-04	4V5E-04
	1V1E-04	2V1E-04	3V1E-04	4V1E-04
	1V5E-05	2V5E-05	3V5E-05	4V5E-05
	1V1E-05	2V1E-05	3V1E-05	4V1E-05

Table 4.6 – Model parameter identification.

A total of 84 models were generated to perform the parametric study (Table 4.6), 21 of each specimen. Those parameters were divided in Series, named according to each parameter name: L, for the transmission length of the steel; M, to the mesh size; V, to the viscosity parameter of the CDP model. Each model was named following the same pattern - XYZ. Where X corresponds to a number representing each specimen: 1 –

CON; 2 – NSM_PR; 3 - TRM_TR; 4 – NSM_TR. The letter Y represents the correspondent Serie. The last letter, Z, refers to the correspondent value of each parameter. For example, 1M50, means the model where the mesh size was changed to 50 mm. Similarly, 1V5E-05 is the model where the viscosity was changed to 0.00005.

Table 4.6 summarizes all the models studied. For the transmission length and the mesh size, the dimensions are in millimetres, for the viscosity the values are dimensionless. The models identified in red are those where the parameter is the same of the 'original model'. The original model is that which provided the best outcome during the calibration process, used as basis to the parametric change.

4.6 Results

4.6.1 Energy Balance

When the explicit mode is adopted with mass scaling, one must consider that increasing the speed of the process means that the equilibrium that was static before becomes dynamic. For that reason, it is important implementing a time increment high enough to speed up the process, but low enough to keep the kinetic energy at low levels in the energy balance. All the models kept the kinetic energy significantly low during the simulations as it is represented in Figure 4.22, where the energy balance of 1M25 is depicted.

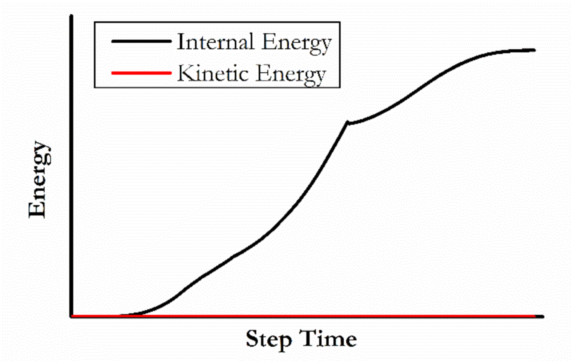

Figure 4.22 – General representation of the energy balance of the models.

4.6.2 Comparison of bond-slip relations

As part of the results, the influence of the usage of the proposed steel bond-slip relation, presented in this work in section 4.2.3, is shown here. As discussed in that section, adopting the usual bond-slip behaviour do not allow the steel to reach fracture, once all the reinforcement reached $\varepsilon_{s,eq3}$ there would be only slippage between steel and concrete.

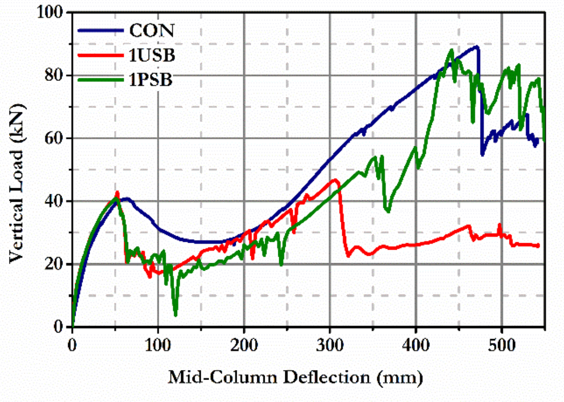

Figure 4.23 – Comparison between usual and proposed steel bond-slip behaviour.

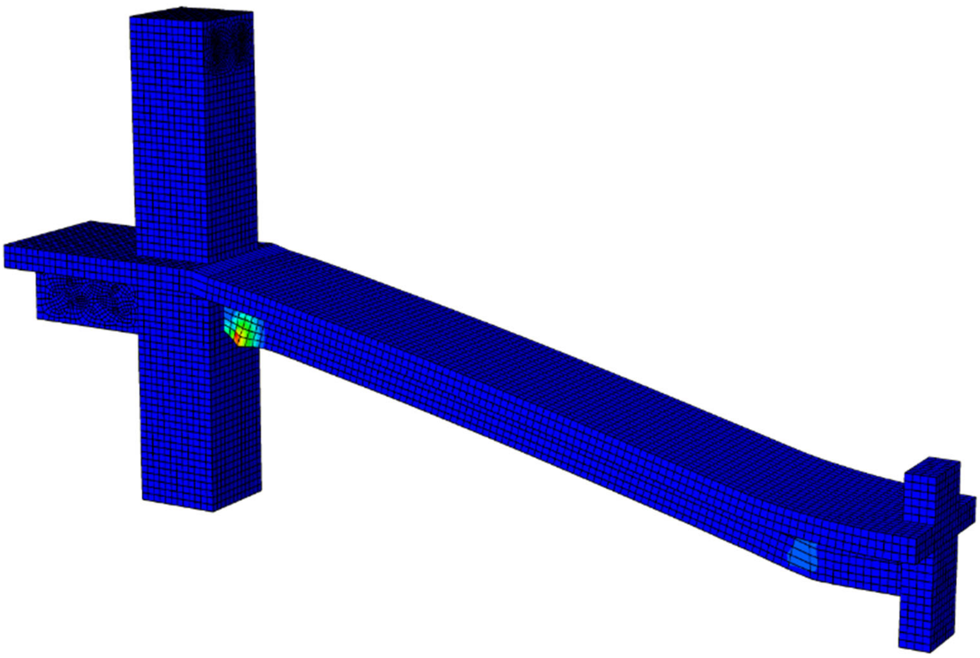

a)

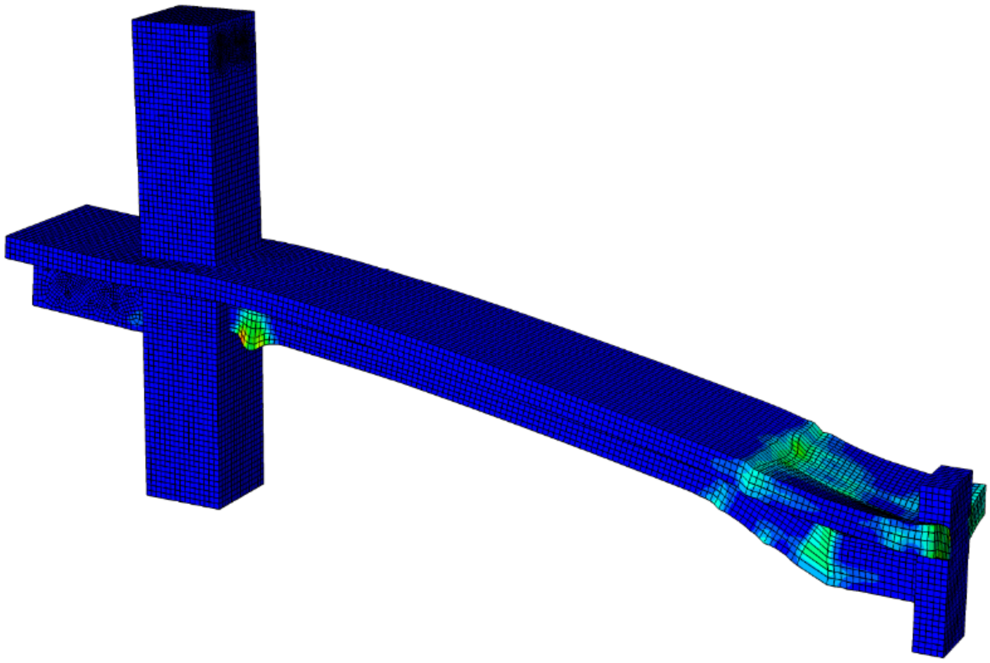

b)

Figure 4.24 – Comparison of failure modes of a) 1USB and b)1PSB.

Figure 4.23 shows the curves of the CON specimen with the usual (1USB) and the proposed (1PSB) steel bond-slip relation. Confirming the stated, in the 1USB simulation the curve decreases up to a certain load and remains around the same load up to the end. It means that the sections in which the stress is more intense, the reinforcement reaches $\varepsilon_{s,eq3}$ then remains at the same load, and all the deformations are concentrated in this region.

Moreover, in Figure 4.24 it can be seen the failure mode of both simulations with the two different bond-slip relations. In (a) 1USB is presented, while (b) shows 1PSB. Although the regions where major damages occurred in 1USB were the main sections of the overall failure, adopting the usual bond-slip behaviour do not result in the best representation of the total failure.

4.6.3 Parametric Study Results

Given the extension of the data assessed, the results of the parametric study will be initially presented separately (APPENDIX B), for each specimen, being subdivided by the parameter assessed, i.e., transmission length, mesh size and viscosity. Because the viscosity had no influence on the frame response, in Section 4.7 the discussion will be focused on the other two remaining parameters, namely Transmission Length and Mesh Size. Following, the discussion of the results is presented.

4.7 Discussion

4.7.1 Comparison between Models

With the results of all models presented in the previous section, the comparison between Series is performed here. To do so, the effect of each Serie on key indicators of performance of the frame in a column loss event is performed. The key indicators are those presented in Section B.1. First the effect of the parameters on the peak load (P_f) and its correspondent deflection. Following, the top columns and beam load cells responses will be evaluated facing different parameters. Sequentially, the maximum dynamic responses during CAA, and the correspondent deflections and DIF. Finally, the ductility ratios of the simulations.

In this section the parameters of all simulations are compared together, hence it is interesting using more realistic values than those achieved in the simulations. It means that the differences observed between the original model and the experiment shall be extinguished, even if those are small. For that, a ratio was achieved for each Serie between the value of the parameter from the model, P_{model} and that from the experiment, $P_{experiment}$. If the simulation had higher value than the experiment, then the ratio was P_{model} / $P_{experiment}$, and the values of the parameter from simulations were divided by that ratio. If the experiment had a higher value, then the ratio was $P_{experiment}$ / P_{model}, and the parameters values from simulations were multiplied by that ratio. With the factor applied to the parameters, the original models presented the same value of each parameter of the correspondent experiments. Those are highlighted in red in the tables in each correspondent following section. Therefore, the effect of the variation of the parameters can be compared between specimens.

4.7.1.1 First Load Peak (P_f)

Figure 4.25 presents graphically values of P_f for all simulations, where models of Serie L are shown in (a) and Serie M in (b). In all simulations of strengthened models, higher values of P_f were achieved when compared to CON. Confirming therefore, the effectiveness of the strengthening techniques adopted on increasing the load carrying capacity in a column loss scenario.

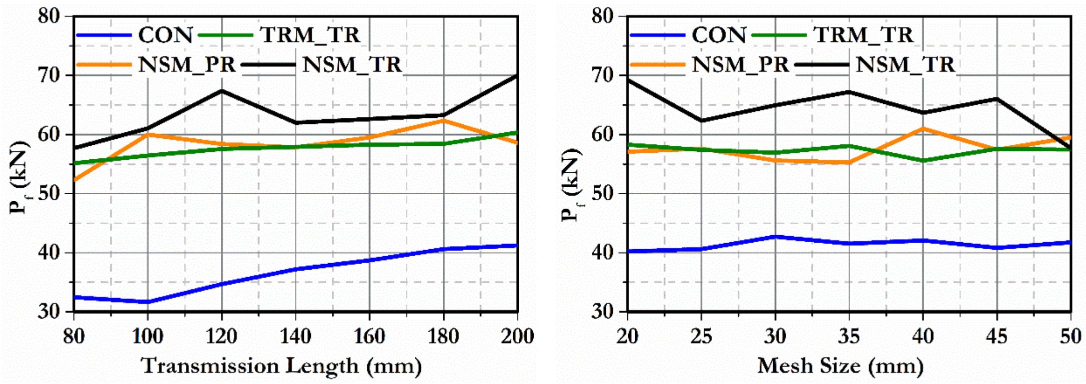

a) **b)**

Figure 4.25 – Parameters influence on P_f a) Transmission length b) Mesh size.

Param.	CON	NSM _PR	TRM _TR	NSM_ TR	Param.	CON	NSM _PR	TRM _TR	NSM _TR
L80	32.5	52.3	55.2	57.7	**M20**	40.2	57.1	58.3	69.2
L100	31.7	60.0	56.5	61.0	**M25**	40.6	57.6	57.4	62.3
L120	34.7	58.4	57.6	67.4	**M30**	42.7	55.6	56.9	65.0
L140	37.2	57.8	57.9	62.0	**M35**	41.5	55.3	58.1	67.2
L160	38.7	59.5	58.3	62.6	**M40**	42.1	61.0	55.6	63.7
L180	40.6	62.4	58.4	63.3	**M45**	40.8	57.4	57.6	66.0
L200	41.2	58.6	60.3	70.0	**M50**	41.8	59.5	57.5	57.7
MEAN	**36.6**	**58.4**	**57.7**	**63.4**	**MEAN**	**41.4**	**57.6**	**57.3**	**64.4**
%	**1.00**	**1.59**	**1.58**	**1.73**	**%**	**1.00**	**1.39**	**1.39**	**1.56**
S.D. (%)	**9.6**	**4.9**	**2.6**	**6.0**	**S.D. (%)**	**2.0**	**3.3**	**1.4**	**5.4**

Table 4.7 – Parameters influence on P_f.

In Table 4.7 it is possible to find the values of P_f for each simulation, as well as the mean value and the standard deviation for each specimen. The peak load is affected similarly for changes in both parameters.

Variations on P_f were small (less than 10%) when the transmission length was altered. The most sensitive specimen to such change was CON; amongst the strengthened, it was NSM_TR, which was the one with higher values of P_f as well. In NSM_TR the development of the resistance is more related to the reinforcement steel, given that in this specimen the shear failure, middle column concrete pull-off and concrete crushing were prevented. That specimen presented loads 73% higher than that from CON, followed by NSM_PR with 59% and TRM_TR with 58%. In those last two specimens the mean value of P_f was closely related to the correspondent experimental value, where in CON it was lower and in NSM_TR it was higher. It confirms the stated before, that in NSM_TR the resistance is more dependent on the conditions of the steel.

By changing the mesh size, the variation was even smaller than in the previous Serie. The differences between simulations in Series M occured due the relation between the tension softening and the elastic branch of the material in the CDP model, which varies with the element size. According to Lee and Fenves (1998): “Because the ratio of the softening bandwidth to the length of elastic unloading zone is different in each case, the global load-displacement response cannot be identical, even though the dissipated energy for all … cases is equal.”. Therefore, the responses of the simulations in this Series would present differences, even though those are small between models. It was more pronounced in NSM_TR, what can be associated to the discrete failure, varying the value of the peak load with the mesh size. The standard deviation in this specimen was 5.4% and the mean 64.4 kN. In the other specimens the mean value was kept similar to that from the experiments. TRM_TR was the most stable amongst strengthened specimens.

The dependency of the peak load on the transmission length is reduced by using the strengthening. Moreover, NSM_TR was the most affected amongst strengthened specimens in both Series due the dependency of this specimen on the steel properties and the localized failure.

4.7.2 Deflections at First Load Peak (P_f)

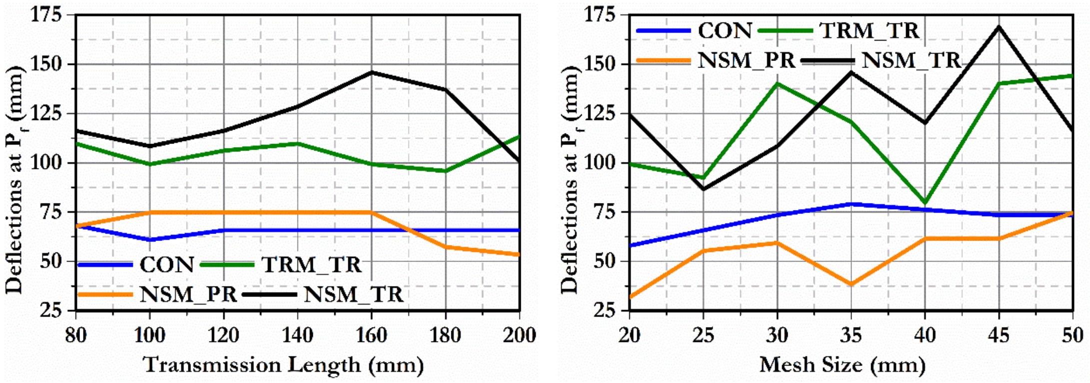

a) b)

Figure 4.26 – Parameters influence on the Deflections at P_f a) Transmission length b) Mesh size.

The displacements associated to P_f for each simulation are presented in charts in Figure 4.26, where (a) shows Serie L and (b) Serie M. The displacements of the peak load during CAA were, in general, higher on strengthened specimens, where NSM_PR at some points had lower values when compared to CON. It highlights the observed in the experiments, that the strengthening adopted sustained higher loads for more time on quasi-static tests.

Values of deflections at P_f for each parameter can be found in Table 4.8, as well as the mean and standard deviation for each specimen in each Serie. In general, the evolution of the deflections with changes in the parameters was not regular, presenting oscillation between values of the same parameter. That can be attributed to the oscillation in the load-deflection curve, product of the speed of convergence adopted.

The sensibility to changes in the transmission length was more pronounced in NSM_PR specimen, where the main failure event at this stage was shear crack opening. The transmission length parameter is directly related to the crack opening, therefore explaining the higher values of the deflection associated to P_f. Values of deflections reached more than 12% of standard deviation, while in TRM_TR it was 5.9%. What demonstrates that TRM_TR is less dependent on the characteristics of the steel. In NSM_TR, the mean value of deflections at P_f was 86% higher than that from CON.

TRM_TR presented a mean deflection 60% higher than CON, while this value for NSM_PR was 4%.

Param.	CON	NSM _PR	TRM _TR	NSM_ TR	Param.	CON	NSM _PR	TRM _TR	NSM _TR
L80	68.2	67.9	109.7	116.2	**M20**	57.9	31.8	99.2	124.3
L100	60.9	74.7	99.2	108.4	**M25**	65.8	55.3	92.5	86.6
L120	65.8	74.7	106.1	116.2	**M30**	73.5	59.4	140.1	108.4
L140	65.8	74.7	109.7	128.5	**M35**	79.1	38.4	120.7	145.8
L160	65.8	74.7	99.2	145.8	**M40**	76.2	61.4	79.9	120.2
L180	65.8	57.3	95.8	137.0	**M45**	73.5	61.4	140.1	168.8
L200	65.8	53.4	113.3	100.8	**M50**	73.5	74.7	144.1	116.2
MEAN	**65.4**	**68.2**	**104.7**	**121.8**	**MEAN**	**71.3**	**54.6**	**116.6**	**124.3**
%	**1.00**	**1.04**	**1.60**	**1.86**	%	**1.00**	**0.77**	**1.64**	**1.74**
S.D. (%)	**3.1**	**12.5**	**5.9**	**12.1**	**S.D. (%)**	**9.3**	**25.0**	**20.8**	**19.7**

Table 4.8 – Parameters influence on the deflections at P_f.

The variation of the deflections at P_f for different mesh sizes is considerably higher when compared to the transmission length, where the standard deviation reached up to 25% in NSM_PR, followed by 20.8% in TRM_TR, then 19.7% in NSM_TR. That can be associated to the speed of convergence and oscillation of the explicit method. However, the proportion of values of deflections compared to CON was maintained, where NSM_TR reached the highest values, then TRM_TR, and finally NSM_PR.

Therefore, the transmission length and mesh size changes affected more NSM strengthened specimens. Deflections in TRM_TR were the less affected by the changes in those Series.

4.7.3 Load Cells LC1-LC2 Responses

The responses of the load cells to the parametrical changes when the peak of CAA is achieved are shown in Figure 4.27. Following the previous sections, in (a) is Serie L and in (b) Serie M.

In most of the cases the load at those load cells was kept higher in strengthened specimens compared to CON. Therefore, in those cases a better load transference through the joint was achieved. That is directly associated to the prevented concrete crush at the bottom of the beam at the side joints, allowing the loads to reach the columns, hence rotating the joints. If failures do not happen in the column, those rotations mean more load at the top load cells.

Table 4.9 presents the values of each parameter change in each specimen. Moreover, the mean values, as well as the standard deviation of simulations per Serie can be found there. CON was the most affected specimen to changes in Series L and M.

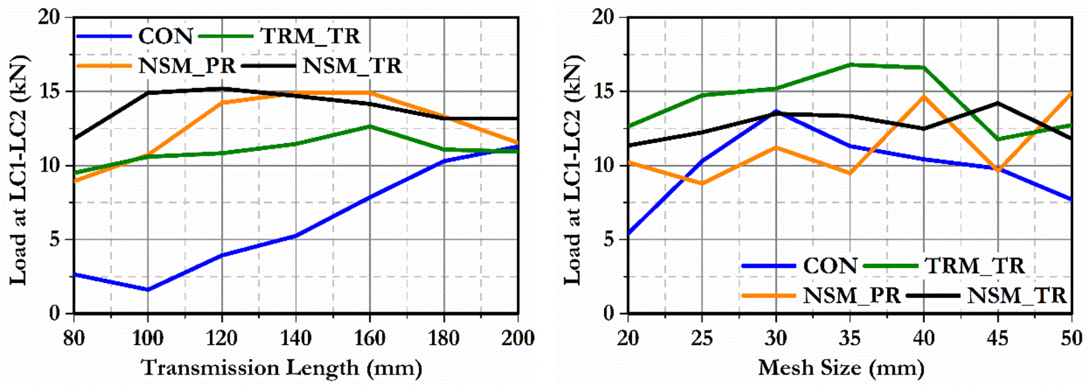

a) b)

Figure 4.27 – Parameters influence on LC1-LC2 response a) Transmission length b) Mesh size.

Param.	CON	NSM _PR	TRM _TR	NSM_ TR	Param.	CON	NSM _PR	TRM _TR	NSM _TR
L80	2.7	8.9	9.5	11.8	**M20**	5.4	10.2	12.6	11.3
L100	1.6	10.7	10.6	14.9	**M25**	10.3	8.8	14.7	12.2
L120	3.9	14.2	10.8	15.2	**M30**	13.7	11.2	15.2	13.5
L140	5.3	14.9	11.5	14.7	**M35**	11.3	9.5	16.8	13.3
L160	7.9	14.9	12.6	14.2	**M40**	10.4	14.7	16.6	12.5
L180	10.3	13.3	11.1	13.2	**M45**	9.8	9.6	11.8	14.2
L200	11.3	11.5	10.9	13.2	**M50**	7.7	14.9	12.7	11.8
MEAN	**6.1**	**12.6**	**11.0**	**13.9**	**MEAN**	**9.8**	**11.3**	**14.4**	**12.7**
%	**1.00**	**2.06**	**1.80**	**2.26**	**%**	**1.00**	**1.15**	**1.46**	**1.30**
S.D. (%).	**56.9**	**16.8**	**8.0**	**8.1**	**S.D. (%)**	**24.9**	**20.6**	**12.9**	**7.4**

Table 4.9 – Parameters influence on the LC1-LC2 load cells response.

The dependency of the load transference to the top columns on the transmission length is significantly reduced when strengthening is adopted. NSM strengthened specimens presented higher values than TRM_TR, and the most affected specimen is NSM_PR amongst the strengthened ones. It shows that the integrity of the beam and joints is crucial to the transference of loads. Fully strengthened specimens presented similar sensibility to changes on the transmission length, where the standard deviation was half of that in NSM_PR. The highest values of load at the top load cells were registered in NSM_TR, given that in this specimen the behaviour of the frame is related to the conditions of the steel inside the concrete.

Alterations in the mesh size emphasize the need of proper calibration of simulations. Here, for example, the standard deviation reaches up to 20.6% of the acting load, occurring in NSM_PR. The difference on results varying the mesh size is, as mentioned before, associated to material properties.

Here, the transmission length and mesh size had higher influence on NSM_PR. This is because the specimen with partial shear strengthening was more dependent on the concrete and steel performance to transfer the loads; therefore, being the most sensitive between strengthened specimens. Despite TRM_TR did not present the highest values in all Series, the transference of loads to the top columns was associated with the integrity on the beam, which in some cases was better than in NSM_PR but not more significant as in NSM_TR, where middle column integrity was also preserved.

4.7.4 Load Cells LC3-LC4 Responses

In this section, the load cells responses at the beam level for all simulations are presented in Figure 4.28, where (a) shows Serie L and (b) presents Serie M. Table 4.10 shows the value of horizontal loads for all simulations, as well as the mean and standard deviation of those values. Again, here the concrete strength was the most influent parameter.

As it can be witnessed in the graphs, the changes on the parameters revealed that TRM_TR had slightly higher response than CON, what will be explained in Section 4.7.7. Specimens strengthened via NSM technique presented higher values of transferred load at the beam load cells; therefore, reproducing the findings from the experiments.

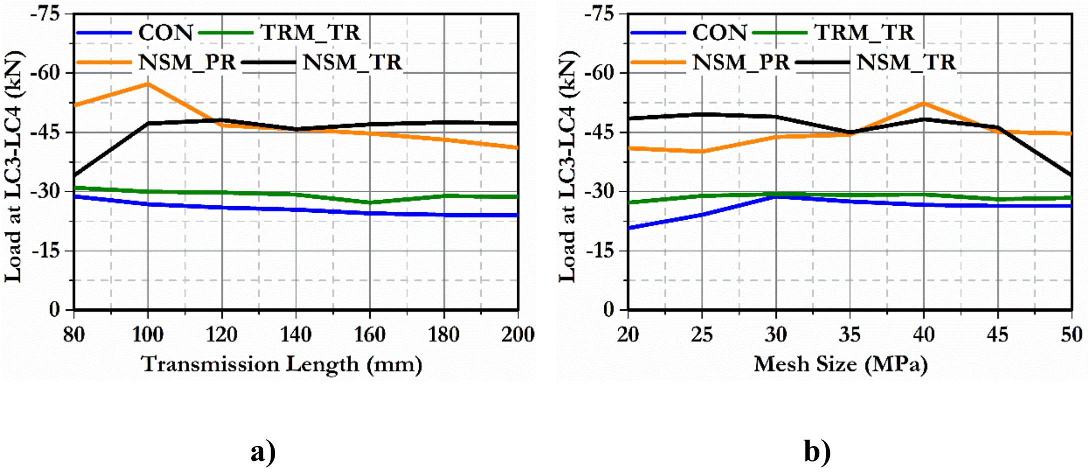

Figure 4.28 – Parameters influence on LC3-LC4 response a) Transmission length b) Mesh size.

Lower values of transmission length led to higher horizontal loads. That can be associated to the anchorage of the steel, which allowed more rotations of the side joints in higher values of L. Consequently, more load was transferred to the top columns when no damage occurred at the joints or beam/column interfaces (Table 4.9). With more slippage, less rotations occurred and the load that reached the joint during the CAA was transferred axially to the side structural elements. Each specimen however presented a limit value of L in which this behaviour was present. For example, in NSM_TR the maximum load was achieved in L120, then it decreases again. NSM reinforced specimens suffered higher influence with changes on the transmission length and presented highest values (in absolute values) of load transferred at the beam level. Specimen TRM_TR was the less affected with the changes on the transmission length and showed the lowest values (in absolute values) of transferred loads at CAA.

Changing mesh size affected more the specimens NSM_TR as in previous sections, where the standard deviation was at maximum 11%.

Those behaviours highlight the complexity of the mechanics of the frame when under a column loss, where a change in one parameter must be performed considering its effects in all indicators of progressive collapse resistance efficiency.

Param.	CON	NSM _PR	TRM _TR	NSM_ TR	Param.	CON	NSM _PR	TRM _TR	NSM _TR
L80	-28.8	-51.8	-31.0	-34.1	**M20**	-20.7	-41.0	-27.2	-48.5
L100	-26.8	-57.2	-30.0	-47.2	**M25**	-24.1	-40.1	-28.9	-49.6
L120	-26.0	-46.8	-29.7	-48.1	**M30**	-28.8	-43.8	-29.3	-48.9
L140	-25.4	-45.8	-29.2	-45.8	**M35**	-27.5	-44.4	-29.1	-45.0
L160	-24.5	-44.7	-27.2	-47.0	**M40**	-26.6	-52.3	-29.3	-48.3
L180	-24.1	-43.2	-28.9	-47.5	**M45**	-26.3	-45.1	-28.1	-46.3
L200	-24.0	-41.1	-28.7	-47.3	**M50**	-26.4	-44.7	-28.4	-34.1
MEAN	**-25.6**	**-47.2**	**-29.2**	**-45.3**	**MEAN**	**-25.8**	**-44.5**	**-28.6**	**-45.8**
%	**1.00**	**1.84**	**1.14**	**1.77**	**%**	**1.00**	**1.73**	**1.11**	**1.78**
S.D. (%)	**6.2**	**10.9**	**3.7**	**10.2**	**S.D. (%)**	**9.5**	**8.2**	**2.5**	**11.0**

Table 4.10 – Parameters influence on the LC3-LC4 load cells response.

Summarizing the effects of the parametric change on the transference of load at the beam level, changes on transmission length had more influence on NSM_PR, while mesh size alterations affected more NSM_TR. Once more, TRM_TR presented the lowest sensibility to changes in the parameters.

4.7.5 Maximum Dynamic Response (MDR)

Figure 4.29 presents the influence of the parametric change on the maximum dynamic responses of the specimens. As in the previous sections, (a) presents Serie L and (b) shows Serie M. As in the peak load P_f, the maximum dynamic responses were all larger than CON in strengthened specimens. Table 4.11 shows the parameters effect on the maximum dynamic response of the frame. Results in this section presented similar findings to section 4.7.1.1.

By increasing the transmission length, the maximum dynamic response is also increased. The most affected specimen was NSM_TR, showing the higher dependency of this specimen on the conditions of the reinforcement steel. As mentioned previously, the shear damage, concrete crush and the concrete pull-off in the middle column were prevented in that specimen; consequently, plastic hinges were formed at the beam/column interfaces. Therefore, the anchorage and bond condition in those areas affected more NSM_TR than the other specimens. The highest values of MDR for different transmission lengths was achieved in this specimen, where the mean value was 87% higher than that from CON. Sequentially, NSM_PR presented 69% more load than CON, then TRM_TR with 58%.

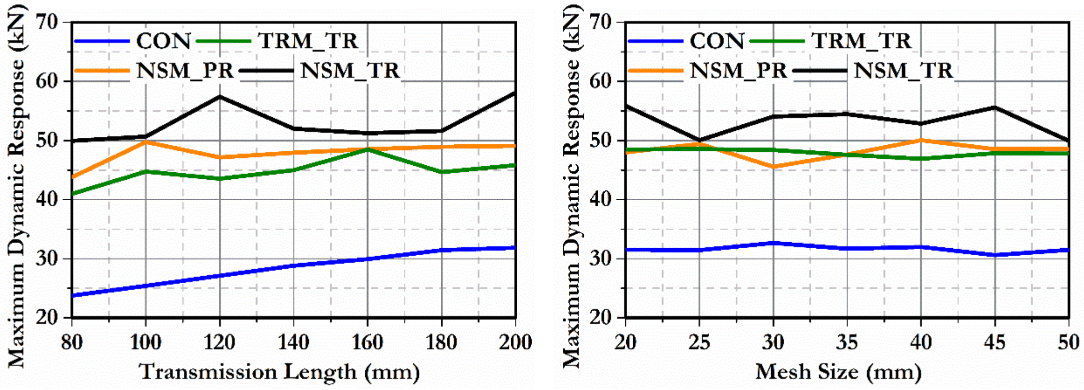

a) b)

Figure 4.29 – Parameters influence on the MDR a) Transmission length b) Mesh size.

Changes in the mesh size were more pronounced again in NSM_TR, as in previous sections, what indicates the sensibility of this specimen to alterations in the models due the localizeed failures. However, this variation reached at maximum 4.2%.

Param.	CON	NSM _PR	TRM _TR	NSM_ TR	Param.	CON	NSM _PR	TRM _TR	NSM _TR
L80	23.8	43.8	41.0	50.0	**M20**	31.5	48.0	48.5	55.9
L100	25.4	49.7	44.7	50.7	**M25**	31.5	49.4	48.6	50.1
L120	27.1	47.1	43.5	57.4	**M30**	32.7	45.5	48.4	54.1
L140	28.8	47.9	45.0	52.0	**M35**	31.7	47.6	47.6	54.5
L160	29.9	48.5	48.5	51.2	**M40**	32.0	50.0	46.9	52.9
L180	31.5	48.9	44.7	51.6	**M45**	30.6	48.5	47.9	55.6
L200	31.9	49.1	45.8	58.1	**M50**	31.5	48.5	47.8	50.0
MEAN	**28.3**	**47.9**	**44.7**	**53.0**	**MEAN**	**31.6**	**48.2**	**47.9**	**53.3**
%	**1.00**	**1.69**	**1.58**	**1.87**	**%**	**1.00**	**1.53**	**1.30**	**1.45**
S.D. (%)	**10.0**	**3.9**	**4.7**	**5.8**	**S.D. (%)**	**1.8**	**2.8**	**1.1**	**4.2**

Table 4.11 – Parameters influence on the maximum dynamic response.

Therefore, changes on the transmission length and mesh size were related to major changes in NSM_TR behaviour.

4.7.6 Deflections at MDR

Figure 4.29 presents the variation of the deflections at the maximum dynamic response of each simulation under different parameters. Following the previous sections, (a) presents Serie L and (b) shows Serie M. All the deflections were higher on strengthened specimens, regardless the variation on the parameter.

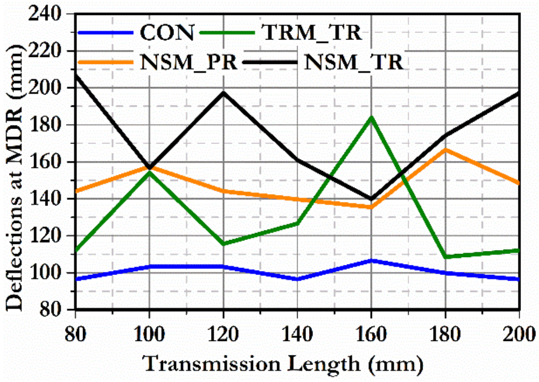

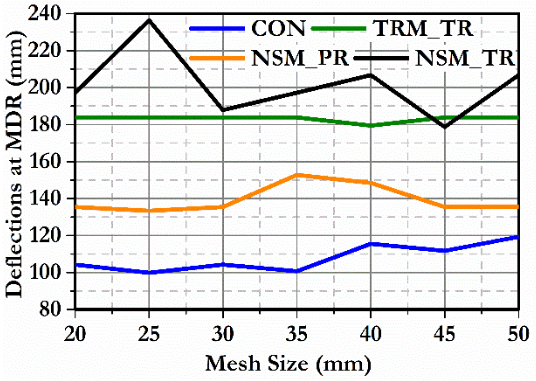

a) **b)**

Figure 4.30 – Parameters influence on the deflection at MDR a) Transmission length b) Mesh size.

Table 4.11 shows the parameters effect on those deflections for each specimen. The evolution of the deflections at MDR, as in section 4.7.2, was irregular considering different values of the same parameter in the same specimen, what is again addressed to the oscillation on the load-deflection curves associated to the explicit method.

When the transmission length is changed, NSM_TR has the highest value, followed by NSM_PR, then TRM_TR. However, in the later the variation of this deflection with changes in the transmission length was higher than in the other specimens. It is attributed to the variation of the peak load P_f and its associated deflections, observed in TRM_TR simulations, and explained in the following section. However, TRM_TR still showed higher deflections than CON for the MDR.

The variation of the mesh size affected more the specimen NSM_TR again, where the standard deviation was 8.4% of 201.6 mm. That was the highest value of deflections amongst specimens, followed by TRM_TR then NSM_PR, what is in accordance with the experiments.

Param.	CON	NSM _PR	TRM _TR	NSM_ TR	Param.	CON	NSM _PR	TRM _TR	NSM _TR
L80	96.5	144.1	112.0	206.8	**M20**	104.3	135.4	183.9	197.2
L100	103.2	157.4	154.1	156.6	**M25**	99.8	133.3	183.9	236.4
L120	103.2	144.1	115.6	197.2	**M30**	104.3	135.4	183.9	187.9
L140	96.5	139.7	126.6	160.9	**M35**	100.7	152.8	183.9	197.2
L160	106.6	135.4	183.9	139.9	**M40**	115.5	148.5	179.5	206.8
L180	99.8	166.6	108.5	174.2	**M45**	111.7	135.4	183.9	178.7
L200	96.5	148.4	112.0	197.2	**M50**	119.3	135.4	183.9	206.8
MEAN	**100.3**	**147.9**	**130.4**	**176.1**	**MEAN**	**107.9**	**139.5**	**183.2**	**201.6**
%	**1.00**	**1.47**	**1.30**	**1.76**	**%**	**1.00**	**1.29**	**1.70**	**1.87**
S.D. (%)	**3.8**	**6.7**	**20.1**	**13.2**	**S.D. (%)**	**6.5**	**5.1**	**0.8**	**8.4**

Table 4.12 – Parameters influence on the deflection at MDR.

Summarizing, regard to the deflections associated to the MDR the fully covered presented higher sensibility with changes on the transmission length. The mesh size variation affected NSM_TR more than the other specimens.

4.7.7 Ductility Ratio

The influence of the parametric change on the ductility ratio of each specimen is presented in Figure 4.31, where (a) presents Serie L and (b) shows Serie M. Furthermore, values of ductility ratios, for all simulations, as well as the mean and standard deviation are presented in Table 4.13.

NSM_TR presented the best ductility ratios amongst strengthened specimens. The specimen NSM_PR presented values of ductility similar to those from CON. The parameter with higher influence on the values of ductility ratios was the transmission length of the steel, due its modified slippage level, which resulted in different stiffness.

From the experiments the differences on the ductility ratios between the NSM strengthened specimens was already significant. The different rotational capacity of those specimens, while sustaining high loads, additional to the shear prevention led the fully strengthened specimen to reach a higher value. This behaviour was highlighted here in the parametric study.

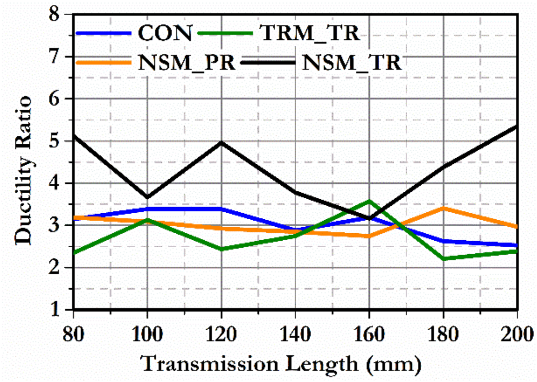

a)

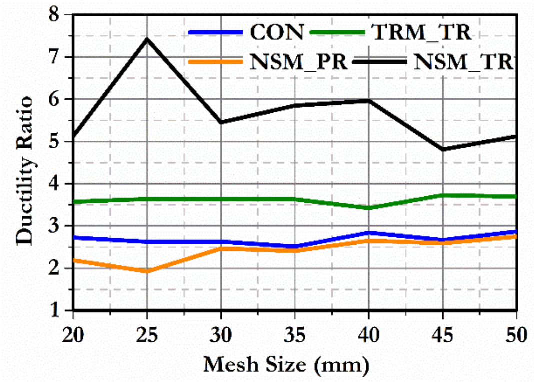

b)

Figure 4.31 – Parameters influence on the ductility ratio a) Transmission length b) Mesh size.

Param.	CON	NSM _PR	TRM _TR	NSM_ TR	Param.	CON	NSM _PR	TRM _TR	NSM _TR
L80	3.15	3.19	2.35	5.12	**M20**	2.72	2.19	3.57	5.12
L100	3.39	3.09	3.13	3.66	**M25**	2.63	1.92	3.64	7.42
L120	3.39	2.93	2.44	4.96	**M30**	2.63	2.46	3.64	5.45
L140	2.88	2.85	2.75	3.78	**M35**	2.51	2.41	3.63	5.85
L160	3.19	2.75	3.57	3.16	**M40**	2.84	2.65	3.42	5.96
L180	2.63	3.41	2.21	4.38	**M45**	2.67	2.59	3.73	4.81
L200	2.53	2.97	2.39	5.35	**M50**	2.87	2.75	3.70	5.12
MEAN	**3.02**	**3.02**	**2.69**	**4.34**	**MEAN**	**2.70**	**2.43**	**3.62**	**5.68**
%	**1.00**	**1.00**	**0.89**	**1.44**	**%**	**1.00**	**0.90**	**1.34**	**2.11**
S.D. (%)	**10.7**	**6.8**	**17.1**	**17.8**	**S.D. (%)**	**4.3**	**10.9**	**2.5**	**14.2**

Table 4.13 – Parameters influence on the ductility ratio.

Ductility ratios of specimen TRM_TR presented inconsistent behaviour with the variation of the transmission length. In this specimen load-deflection curves (section B.4), one can observe sudden drops in the load after the peak load P_f. Considering that in this specimen, the evolutions of the damages were coherent to the strengthening configuration adopted, added to the comparable results in previous sections, and that the failure mode was representative in all simulations, it can be inferred that a premature failure occurred in the models, preventing the frame to achieve higher loads during

CAA. Therefore, even that the previous evaluations were correct, those were not performed to the highest potential of the frame. Consequently, the outcome of the ductility ratio investigation was correct only for the original model and the models of Serie M, where the premature failure did not happen. The method adopted to achieve the ductility ratio takes as basis the peak load, which here was P_f, the tangent to the curve up to P_f and the deflection at P_f. Hence, the ductility ratio of TRM_TR could not be assessed here. However, the effectiveness of this strengthening method on improving the ductility ratio of the frame is attested on the experimental phase.

High values of ductility ratio can be observed in NSM_TR in Series L and M, where compared to CON NSM_TR had ratios 44% and 111% higher respectively. Additionally, the sensibility of the ductility in NSM_TR is also the highest in those Series. This is attributed to the fact that the damages in NSM_TR occured in localized sections, any alteration in the material properties is reflected in the ductility of the frame. NSM_PR did not present higher values of ductility ratio than CON in all simulations, what is attributed to the shear cracks affecting the peak loads and rotations at the beam ends.

4.7.8 Dynamic Increase Factor (DIF)

Figure 4.32 presents the alteration of the dynamic increase factors facing a parametric change, where in (a) Serie L is presented and (b) shows Serie M. In general, the values of DIF were reduced on strengthened specimens, indicating a smaller difference between quasi-static and pseudo-static results. Only in specimen TRM_TR, at some points, values of DIF were higher than in CON. It means that the difference between P_f and maximum dynamic response was higher in those simulations. The maximum dynamic response was higher in strengthened specimens. So, the energy absorption capacity was yet higher in those. It is worth remembering that the results assessed here are those regard to the peak of load during CAA.

Table 4.14 presents the values of DIF achieved for different parameters in each Serie. Additionally, mean values and standard deviations of each Serie for each specimen are presented.

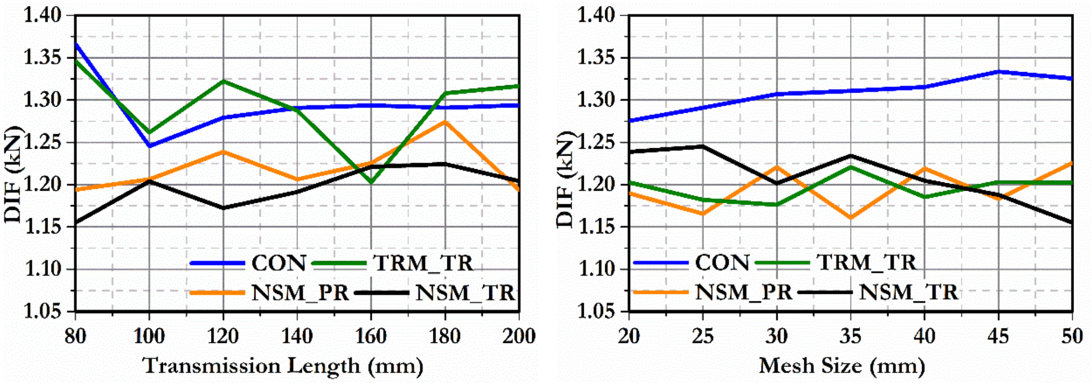

a) **b)**

Figure 4.32 – Parameters influence on the DIF a) Transmission length b) Mesh size.

Param.	CON	NSM _PR	TRM _TR	NSM_ TR	Param.	CON	NSM _PR	TRM _TR	NSM _TR
L80	1.37	1.19	1.35	1.16	**M20**	1.28	1.19	1.20	1.24
L100	1.25	1.21	1.26	1.20	**M25**	1.29	1.17	1.18	1.24
L120	1.28	1.24	1.32	1.17	**M30**	1.31	1.22	1.18	1.20
L140	1.29	1.21	1.29	1.19	**M35**	1.31	1.16	1.22	1.23
L160	1.29	1.23	1.20	1.22	**M40**	1.32	1.22	1.19	1.20
L180	1.29	1.27	1.31	1.22	**M45**	1.33	1.18	1.20	1.19
L200	1.29	1.19	1.32	1.20	**M50**	1.33	1.23	1.20	1.16
MEAN	**1.29**	**1.22**	**1.29**	**1.20**	**MEAN**	**1.31**	**1.20**	**1.20**	**1.21**
%	**1.00**	**0.94**	**1.00**	**0.92**	**%**	**1.00**	**0.91**	**0.91**	**0.92**
S.D. (%)	**2.6**	**2.2**	**3.4**	**1.9**	**S.D. (%)**	**1.4**	**2.1**	**1.2**	**2.5**

Table 4.14 – Parameters influence on the DIF.

Considering the variations of P_f and maximum dynamic responses together, the behaviour of each one combined determines the values of DIF. However, despite each specimen responded differently to variations on the parameters, the standard deviations were small, reaching at maximum 3.4%. TRM_TR presented similar values to CON, yet one must to consider that the vertical 'Load vs Deflection' curves in this specimen did not evolved up to its maximum potential due to premature failures in the frame. The evolution of this curve will provide information on the energy absorption capacity of the frame. Therefore, even that the curves did not evolve up to its maximum, TRM_TR still presented similar DIF to CON, what highlights the capacity of this strengthening technique facing a column loss.

The alteration on the mesh size did not affect values of DIF so significantly, where the maximum standard deviation was 2.5%, highlighting the stated by Lee and Fenves (1998), who says that, despite the differences on values of loads, the energy dissipation remains the same. Moreover, the Serie M was useful to expose the real behaviour of TRM_TR where the DIF was smaller than that from CON. Furthermore, all strengthened specimens in this Serie presented similar mean value of DIF: nearly 1.2.

From the assessment of each parameter, considering mean values and standard deviations, it was observed that the DIF values achieved from the experiments can be considered as reference values for each kind of strengthening approach. For non-strengthened specimens, the value of 1.30 is suitable, while for partially strengthened specimens, a DIF of 1.21 can be assumed; for fully covered specimens, 1.20.

4.8 Micromodelling Findings

In this chapter, a parametrical study was conducted on the frames tested in Chapter 3 through computational simulations with the commercial software for structural analysis Abaqus (Hibbitt et al., 1997). Three-dimensional finite element models were used to assess the frames behaviour under different conditions, which could not be performed in laboratory. The outcome helped to better understand the mechanics of progressive collapse due a column removal in both non-strengthened and strengthened frames. Moreover, the investigation highlighted the efficiency of the strengthening method adopted on mitigating the effects of a column loss in a portal frame.

The parameters investigated here were the transmission length of the steel, which is one half of the medium space between cracks; the size of the mesh; and the viscosity, which is an internal parameter of Concrete Damage Plasticity model in Abaqus.

In total, 84 models were generated, separated in Series per each specimen. Each Serie comprised a different parameter assessed. Serie L for transmission length, varied from 80 to 200 mm in each 20 mm. Serie M, for mesh size, varied from 20 to 50 mm in each

10 mm; Serie V, for viscosity, varied from 0.00001 to 0.01 in each half of the value of the next decimal.

Proposed Stress-Equivalent Strain Relation

The models were calibrated with the experimental results, and those with the best fit were called original models. To allow the original model to achieve the proper representativity of the experimental curve, a modification of the stress-equivalent strain relation of the steel present in the literature to address bond-slip behaviour was proposed to include also the steel fracture.

With this new relation, the vertical 'Load vs Deflection' curves off all specimens were reproduced successfully in the simulations. Moreover, the damages evolution through the beam as well as the final failure configuration was more realistic when the proposed steel behaviour was adopted. Furthermore, the consistency on the outcome from the parametric study remarked the representativity and validity of the proposed relation.

Parametric Study

The study focused on the CAA phase due the advanced stage of the damages along the beam at TCA; the dependency of the frame resistance on the conditions of the internal reinforcement at the TCA phase; the better performance of the strengthening method during CAA; and the sensibility of the models to changes in the parameters expressed at the TCA phase. Similar conclusion can be found in the literature, e.g., in Stathas et al. (2017b) it was found that the CAA is more important to the enhancement of the frame load carrying capacity than the TCA.

The simulations presented good representativity to the experiments, and the prediction of the behaviour facing different parameters showed coherent outcome. Moreover, the failure modes of the specimens demonstrated to be in accordance with the alteration of the parameters.

The results of the parametric study highlighted key indicators to assess the progressive collapse resistance of the frame. The first of those is the first peak load, here called P_f, which is a direct indicator of the frame robustness. Following, the P_f associated deflection, which demonstrates up to which deflection the frame is able to sustain P_f.

The next indicators are the load cells responses at the top of the side columns and at the beam level. The former shows the joint capacity to transfer moment through the columns, and the second shows the capacity of the frame to transfer axial loads to the adjacent elements. The following indicators were the maximum dynamic response and the associated deflection, which reveals the energy absorption capacity of the frame and up to which deflection it can be sustained, and further allow the achievement of the dynamic increase factor (DIF). Following, the ductility ratio, which shows the capacity of the frame to deform and, in conjunction with the maximum dynamic response, provides direct information of the efficiency of the frame facing a progressive collapse due to a column removal. Furthermore, the DIF was achieved for each Serie, which allows to find dynamic responses from the quasi-static tests.

The investigation of changes in the parameters revealed that all strengthened specimens were, in general, able to sustain higher loads than CON, in higher deflections, even with changes in the parameters. Moreover, the energy absorption capacity and the ductility were improved on strengthened specimens, even facing different steel conditions, for example. Therefore, the effectiveness of the strengthening methods adopted here on improving the progressive collapse resistance of the frame was attested.

TRM_TR could not develop the load-deflection curve up to its maximum in most of the specimens due to a premature failure occurring at the middle column. This was attributed to the embedment method of the steel inside the concrete, adopted in Abaqus. Even though TRM_TR did not reach its full potential in the simulations and the ductility ratio could not be assessed properly in the parametric study, this specimen demonstrated enhanced robustness and energy absorption capacity compared to CON.

Regard to changes on the transmission lengths, NSM_TR presented the highest values of loads and deflections both in P_f and maximum dynamic responses. Between the other two specimens, assessing P_f, TRM_TR and NSM_PR had similar loads, while at the maximum dynamic response NSM_PR reached the highest, because the load in TRM_TR was not developed to its maximum, as explained before. Deflections between those two specimens were higher in TRM_TR at P_f and the opposite at the maximum dynamic response. The variation on the deflections results was associated to the method of convergence and its parameters.

The increment of the transmission length caused an increment of the first peak load and the associated deflections. Similarly, the maximum dynamic response of the frame was increased as well; however, the correspondent deflection did not have a clear evolution, oscillating with the variation of the parameters. Since the maximum dynamic response is more related to the deflection in which the failure occurs at the beam, the correspondent deflection depends on the internal stress distribution and the limits of the materials. Therefore, higher deflections were achieved in fully strengthened specimens.

The viscosity parameter was revealed to have no influence on the behaviour of the frame under progressive collapse due to a column loss. Moreover, changes in the viscosity did not affected significantly time spent on simulations

The transference of loads was better in all strengthened specimens when compared to CON, facing changes in the parameters. The transference of loads to the neighbor elements was observed to be dependent on the integrity of the frame. Therefore, with the prevention of the concrete crush at the bottom of the beam at the side joints, the compression from CAA reached the side columns. Depending on the damage at the column, this load is transferred to the top of the column. When transmission lengths were evaluated, NSM_TR had the best transference of loads at the top load cells, while NSM_PR assumed the position on the transference of loads at the beam load cells.

The ductility ratio is related to the rotational capacity of the beam as well as to its capacity to deform while sustain the loads, and was found to be higher on strengthened specimens when compared to CON. NSM_TR presented the highest values of ductility ratio with the variation of the parameters. Fully strengthened specimens presented a beter performance on the assessment of this parameter, because concrete crush at the bottom of the beam at the side joints and shear failure were prevented. The evolution of the ductility ratio with changes in the parameters was not regular given that deflections and the evolution of the curve up to the maximum dynamic response are involved on the achievement of this ratio.

The DIF was assessed for each simulation, in order to find a proper increase factor for the strengthened specimens, and it was found to be smaller than CON on those specimens, where full covered specimens had a slightly better performance. It shows that in a dynamic event the kinetic energy is reduced with the usage of the proposed strengthening technique, what is beneficial considering the progressive collapse resistance. Variations on the parameters affected similarly the DIF in all specimens, and its evolution is not regular with the increment of the values of each parameter. The outcome from the parametric study revealed that during CAA the DIFs of 1.30, 1.21 and 1.20 can be considered for the case of non-strengthened frames, partially and fully strengthened respectively.

The assessment of the mesh size revealed the weakness of the CDP model on simulating discrete failures. Moreover, it was emphasized that the proper calibration of the model is fundamental to the accuracy of it. Regard to P_f and maximum dynamic response, changes in the mesh size caused a variation up to 5.4 % around the mean. When deflections were assesses, this value reached up to 25%. Similar number was found when the horizontal loads were investigated. The influence of the mesh size on the ductility ratio led to a variation of 14.2% around the mean, while the DIF varied only 2.5%. In general NSM_TR was the most affected to changes in the mesh size due to the localized damaged in this specimen.

This page was left intentionally blank

CHAPTER 5 MACROMODELLING APROACH FOR THE SIMULATION OF PROGRESSIVE COLLAPSE

Alternative to complex 3D FE models, a simplified approach can be used on the assessment of RC structures, including that regard to the progressive collapse of a frame due a sudden column removal. With respect to that, Izzuddin et al. (2008) proposed an analytical method that characterizes the structure in different levels of representativity, from where the nonlinear static and the dynamic responses of the building can be achieved. Furthermore, the method allows a ductility and a simplified dynamic assessment of the structure. Valipour and Foster (2010) adopted 1D elements to develop a new formulation which includes catenary action effects, physical and geometrical nonlinearities, and large deflections features. Yu and Tan (2010) proposed a component-based model, latter used by Yu and Tan (2013a), where effects of bond-slippage and rupture of longitudinal bars were accounted. Fascetti et al. (2015) introduced the Local Robustness Evaluation (LRE) method to assess the robustness, and therefore the potential of a building to resist progressive collapse due a sudden column removal. Moreover, comparisons between 2D and 3D modelling highlighted the importance of the slab in the internal mechanism of resistance of the structure. Dat et al. (2015) studied the removal of penultimate column of a building with a Single Degree of Freedom (SDOF) model. Amongst the observations, it was found that the vertical displacement is mainly governed by rotational deformations of various beam plastic hinges. Consequently, the displacement ductility is calculated and related to the curvature ductility ratio of the critical hinge component of the system. Chen et al. (2016) adopted numerical examples of idealized RC structures to propose a robustness index of a building based in its vulnerability.

In this chapter an analytical model was adopted to present a faster and reliable way to simulate frames under progressive collapse in a column removal scenario, compared to the 3D FEM simulations. To perform such study, the open source software OpenSees (Mazzoni et al., 2004) associated with the high performance interactive software for numerical calculation Matlab (Manual, 2000) is utilized.

5.1 Model description

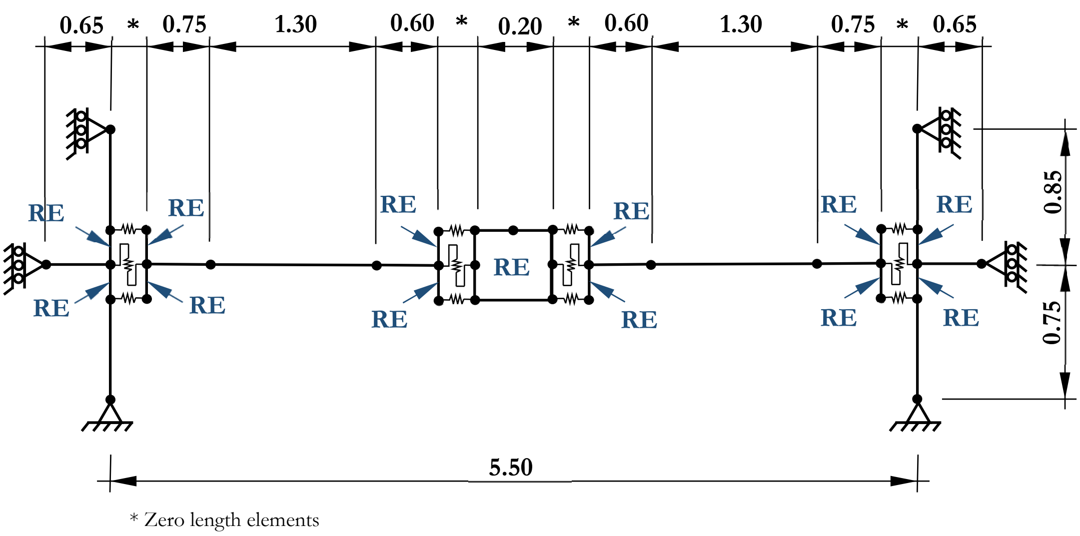

Figure 5.1 – OpenSees CON, TRM_TR and NSM_TR models.

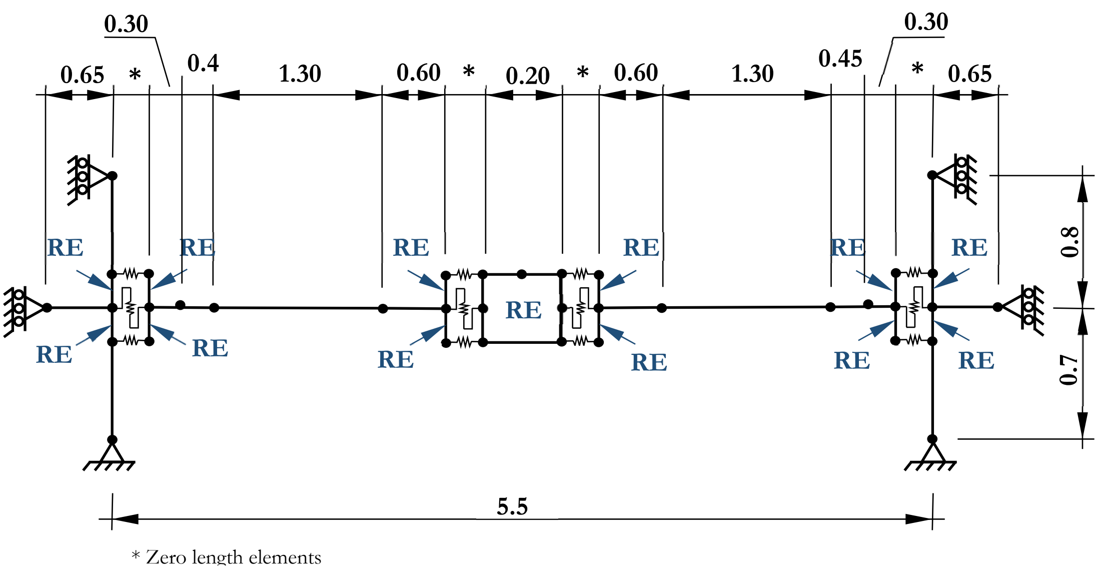

Figure 5.2 – OpenSees NSM_PR model.

andre.vieira@nottingham.ac.uk / andre.engc@gmail.com

Based on the work of Yu and Tan (2010) and Yu and Tan (2013a), the component-based RC joint model aimed to simulate the same frames tested in the experimental program. The macromodelling was built with 2 nodes elements connected in key positions of the frame, and a set of springs at each joint. This set comprised two axial springs, located at the position of the longitudinal reinforcement in the cross-section, and a vertical spring to account for shear, connected by two adjacent beam nodes.

Nodes were also positioned where arrangement of the longitudinal reinforcement inside the beam is changed (Figure 3.7), as well as at the position of appliance of the load. Rigid elements were used at the positions of transference of loads from the beam to the joints, these are signalized in Figure 5.1 as ‘RE. Furthermore, the beam was restrained at the bottom and the top of the side columns, and at the end of the beam, beyond side columns.

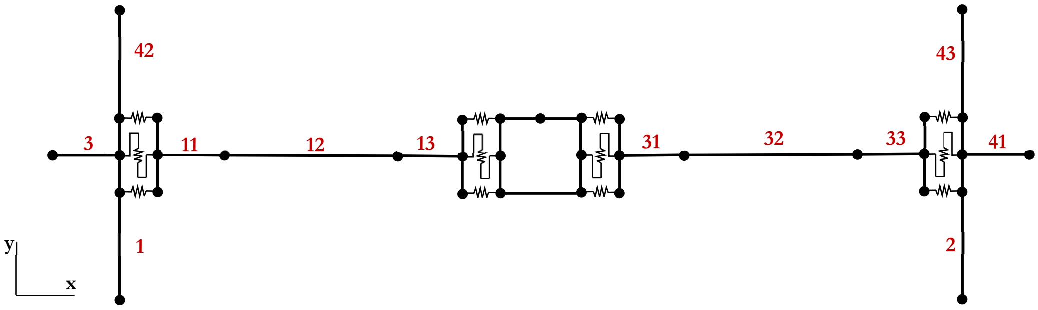

a)

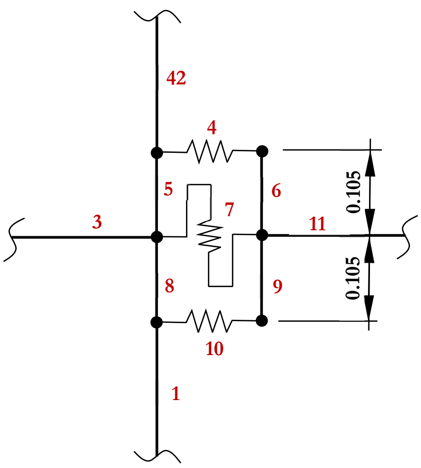

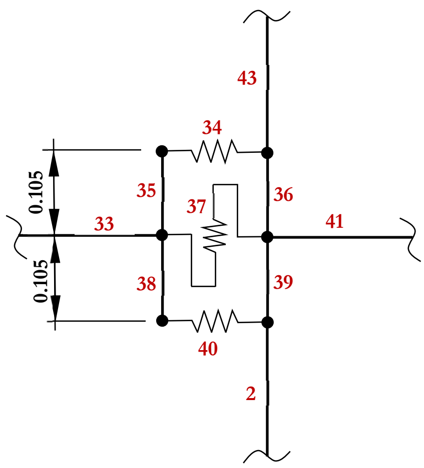

b) **c)**

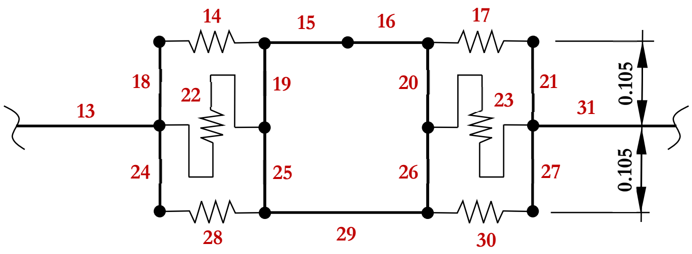

d)

Figure 5.3 –Elements identification of CON, TRM_TR and NSM_PR OpenSees model a) frontal view b) left joint c) right joint d) middle joints.

Element	Material	Cross-Section	Element	Material	Cross-Section
1	Reinforced Concrete	A	**23**	Vertical Spring	-
2	Reinforced Concrete	A	**24**	Rigid Element	E
3	Reinforced Concrete	B	**25**	Rigid Element	E
4	Longitudinal Spring	-	**26**	Rigid Element	E
5	Reinforced Concrete	A	**27**	Rigid Element	E
6	Rigid Element	E	**28**	Longitudinal Spring	-
7	Vertical Spring	-	**29**	Rigid Element	E
8	Reinforced Concrete	A	**30**	Longitudinal Spring	-
9	Rigid Element	E	**31**	Reinforced Concrete	C
10	Longitudinal Spring	-	**32**	Reinforced Concrete	D
11	Reinforced Concrete	C	**33**	Reinforced Concrete	C
12	Reinforced Concrete	D	**34**	Longitudinal Spring	-
13	Reinforced Concrete	C	**35**	Rigid Element	E
14	Longitudinal Spring	-	**36**	Reinforced Concrete	A
15	Rigid Element	E	**37**	Vertical Spring	-
16	Rigid Element	E	**38**	Rigid Element	E
17	Longitudinal Spring	-	**39**	Reinforced Concrete	A
18	Rigid Element	E	**40**	Longitudinal Spring	-
19	Rigid Element	E	**41**	Reinforced Concrete	B
20	Rigid Element	E	**42**	Reinforced Concrete	A
21	Rigid Element	E	**43**	Reinforced Concrete	A
22	Vertical Spring	-			

Table 5.1 - Elements' characteristics.

From the beam level to above, constraints restricted movements in x, while vertical displacements and rotations were allowed. The ground constraints prevented displacements in x and y, while rotations were allowed. The representation of the specimens – CON, NSM_PR, TRM_TR and NSM_TR – are presented in Figure 5.1 and Figure 5.2.

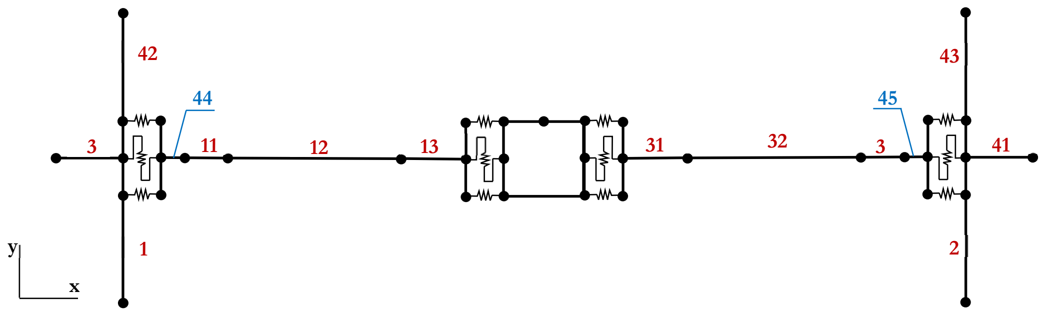

Figure 5.4 – Additional elements for specimen NSM_PR.

The elements were numbered according to Figure 5.3. Figure 5.4 shows the additional elements and nodes inserted in NSM_PR mode. All the other elements are numbered similarly for all specimens' models.

Specimen	Element	Material	Cross-Section
NSM_PR	13	Strengthened RC	F
	31		F
	44		G
	45		G
TRM_TR	11	Strengthened RC	G
	12		H
	13		I
	31		I
	32		H
	33		G
NSM_TR	11	Strengthened RC	G
	12		H
	13		F
	31		F
	32		H
	33		G

Table 5.2 – Modified elements` characteristics.

Because the characteristics of the elements are different in each specimen model, the identification of each one is presented separately. Table 5.1 shows the elements of CON, while Table 5.2 shows the characteristics of the additional elements as well as those which were modified due the strengthening. The description of each material property and the cross-sections adopted are further presented in section 5.2 and 5.3.

5.2 Material Properties

5.2.1 Concrete

OpenSees has different models do characterize the uniaxial behaviour of concrete. The pre-established models differ from each other on the concrete tensile strength, tension softening behaviour, degradation of stiffness through cycles of load/unload process, presence of Fibre-Reinforced Polymer (FRP), as well as the theoretical work from which the model is based.

To the present work, the model Concrete02 was chosen to represent the concrete in the simulations. In this model, the cross section of the beam is divided in a mesh of fibres, in which the reinforcement steel is positioned. That mesh also delimitates the core of confined concrete, and the cover of unconfined concrete. Moreover, the damage of the elastic modulus is considered for the case of cyclic loads.

In Concrete02 the confined concrete behaviour is based on Chang and Mander (1994) work, while in the unconfined concrete behaviour Todeschini et al. (1964) parabolic model is considered. The concrete tensile behaviour during the softening phase is linear in Concrete02. Figure 5.5 shows the concrete uniaxial behaviour for the confined concrete.

The required input to characterize the concrete is the following: concrete strength, $f`_c$; elastic modulus, E_0; ratio of confined (core) to unconfined (cover) concrete strength, k_{fc}; ratio of residual/ ultimate to maximum stress, k_{res}; strain at maximum strength, ε_{c0} (epsc0); strain at ultimate stress, ε_{cU} (epscU); ratio between unloading slope at ε_{cU} and initial slope E_0, λ (lambda); Poisson's ratio, ν, assumed here as 0.2. Additionally, a tension softening factor was inserted in the code to achieve the softening stiffness Ets, named Tensoft. The concrete strength f_c and the elastic modulus E_0 were adopted with the same values of those found in the calibration phase in Chapter 4 for each original models of each correspondent specimen (see Section 4.4).

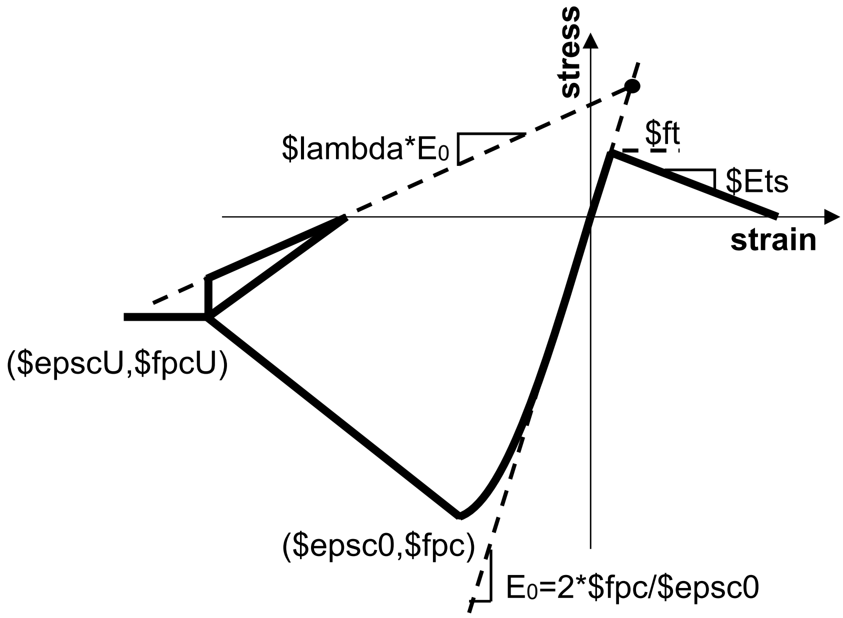

Figure 5.5 – OpenSees confined concrete uniaxial behaviour (Mazzoni et al., 2004).

With those values defined, the software calculates fpc = $f`_c.k_{fc}$, which helps to find ε_{c0} = $2.E_0$.fpc, from where it is possible to reach $\varepsilon_{cU} = 20.\varepsilon_{c0}$. Moreover, the concrete crush strength is achieved with fpcU = k_{res}.fpc, and the concrete tensile strength is achieved with the relation fts = -0.105.fpc. The concrete strength is inserted with negative value to represent compression. The parameter λ was kept constant in all models as 0.1. In the unconfined concrete, $fpc_{un} = 0.77.f`_c.k_{fc}$, and $fpcU_{un} = k_{res}.fpc_{un}$, and the respective correspondent strains ε_{c0un} and ε_{cUun} were achieved with the optimization process described in section 5.4. The tensile strength of the unconfined concrete was obtained as in the confined core, with $fts_{un} = -0.105.fpc_{un}$. To build the tension softening slope, Ets = $fpcU_{un}$/Tensoft was adopted.

5.2.2 Steel

Similar to concrete, the steel behavior can be characterized through one of the pre-existing models in the software. Those models vary according to the type of steel adopted, consideration of stiffness degradation, as well as the steel hardening phase.

The model adopted in the present work is the Steel02. It represents the steel through an uniaxial behaviour based on the work of Giuffrè (1970), enhanced later by Menegotto and Pinto (1973) where kinematic hardening of the steel is accounted. The input to this model is the following: yield stress, f_y; elastic modulus, E_s; strain-hardening ratio, β_s; and three factors controlling the transition between elastic and plastic branches, R_0, C_{R1}, C_{R2}. The software manual (Mazzoni et al., 2004) defines C_{R1} = 0.925 and C_{R2} = 0.15, in the present work those values were adopted with 0.99 and 0.1 respectively. The strain-hardening ratio and the parameter R_0 were kept with the same value in all simulations, where β_s = 0.002 and R_0 = 0.62. Moreover, the yield stress of the steel was maintained with 500 MPa and the correspondent Young's Modulus with 210 GPa. Figure 5.6 presents the uniaxial stress-strain curve for the steel according to Mazzoni et al. (2004).

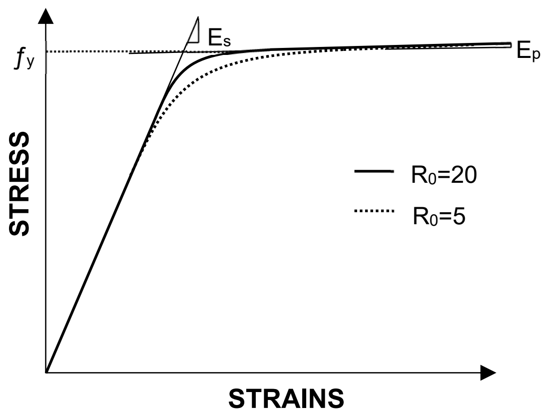

Figure 5.6 – OpenSees steel behaviour.

5.2.3 Rigid Elements

Rigid elements (REs) were built in a simplified way to ensure that no deformations would happen in it. Therefore, the strength of the RE was defined with an extremely high value as well as its elastic modulus. The behaviour of the material was kept in the elastic range, though the pre-existing material model 'Elastic', where only the elastic modulus, the material strength and the moment of inertia are required as input. The identification of the elements which had rigid elements assigned can be seen in Table 5.1. Moreover, the cross-sections of those elements are presented in section 5.3.

5.2.4 Springs

As mentioned before, each beam/column connection is simulated with a set of three springs - two longitudinal, at the positions of longitudinal reinforcement, and a vertical one to account for shear. The longitudinal springs combined can simulate the effect of bending moment through the axial compressive and tensile behaviour, as well as the effects of axial forces.

OpenSees has an existing model to define the uniaxial behaviour of a material when it is over tension and compression in the same event. This model accounts for the degradation of the stiffness due unloading process and can be found as `Hysteretic Material` in the software documentation. In this pre-defined model, the stress-strain relations of the material in compression, as well as in tension, are built with up to three points of the stress-strain (or force-displacement) uniaxial behaviour. When in compression those springs should consider both steel and concrete contribution. However, in tension only the reinforcement resistance is accounted.

To reproduce the combined steel and concrete responses in compression, the relation presented in Lowes and Altoontash (2003) is adopted here as point of departure:

$$C = C_S^{`} + C_C = f_s^{`} A_S^{`} \left( 1 + \frac{0.85 f_C^{`} dw}{E_S - A_S^{`}} \frac{2(1-j)}{0.003\beta_u \left(1 - \frac{d^{`}}{d} \frac{\beta_u}{2(1-j)}\right)} \right) \tag{5.1}$$

Where:

$\boldsymbol{C_S^{`}}$ - steel compression resultant;

$\boldsymbol{C_C}$ - concrete compression resultant;

$f_C^{`}$ - nominal concrete compressive strength;

$\boldsymbol{A_S^{`}}$ - area of reinforcing steel carrying compression;

$\boldsymbol{E_S}$ – reinforcing steel elastic modulus;

$\boldsymbol{d}$ – depth to the tension reinforcement;

$\boldsymbol{w}$ **–** width of the frame member;

$\boldsymbol{d}^{`}$ - depth to centroid of compression reinforcement;

$\boldsymbol{\beta_u}$ – scale factor to account for the use of a uniform concrete compressive stress distribution in place of the true stress distribution;

The relation $j * d$ is the distance between tension and compression resultants acting on the cross section, where, as in the mentioned work, j=0.85 for beams and j=0.75 for columns. Initially the factor β was assumed to be 0.5. Additionally, the assumptions adopted by Yu and Tan (2013a) were followed at the start point. Tensions on the springs were resisted only by the reinforcement; hence, the steel bond-slip criteria, adopted in Chapter 4, was used here.

Vertical springs address the transference of shear force between the beam and the column due "the dowel action of reinforcing steel and aggregate interlock on cracked concrete surfaces" Yu and Tan (2013a). The same assumption of Lowes and Altoontash (2003) is adopted here, where the shear spring is considered to have a stiff elastic load-deformation response. Elements with the vertical spring can be found in Table 5.1.

5.3 Cross-Sections

The correspondence of element and cross-sections can be visualized in Table 5.1 and Table 5.2. In place of the T-beam used in the experiment and in the micromodelling section, an equivalent cross-section, with the same moment of inertia, was adopted here. Figure 5.7a presents the cross-section of the T-beam between side columns (within parenthesis are the information regard to the beam beyond side columns). Figure 5.7b presents the equivalent cross-section.

Instead of using the original configuration of the internal reinforcement on the top of the beam, where there was 4Ø6 + 4Ø8 or 4Ø6 + 2Ø8, an equivalent tensile capacity with different bars was adopted here. For the combination 4Ø6 + 4Ø8, with an area of steel $A_s = 3.14 \times 10^{-4}$ m^2, it was used 4Ø10, where the $A_{s,eq} = 3.14 \times 10^{-4}$ m^2. For 4Ø6 + 2Ø8, where $A_s = 2.14 \times 10^{-4}$ m^2, the equivalent number of bars was 3Ø10, with $A_{s,eq}$ = 2.36 x10^{-4} m^2. These replacements can be visualized in Figure 5.8.

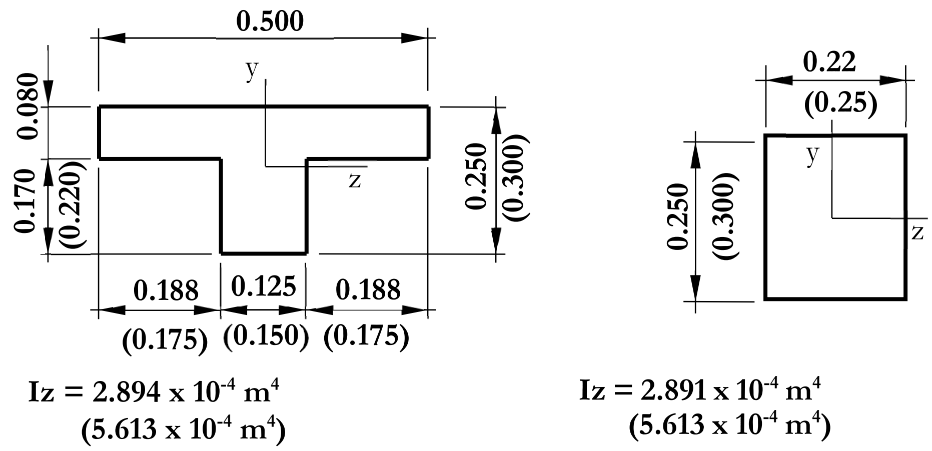

a) b)

Figure 5.7 – Cross-sections` inertia a) T-beam b) equivalent beam.

There are nine different types of cross-sections adopted in the models, labeled from A to I, differing on the dimensions of the section, the configuration of the internal reinforcement and contribution of the strengthening to the reinforcement steel. Figure 5.8 shows the cross-sections of the frame without strengthening. A is the column cross-section; B is the cross-section of the beam beyond side columns (elements 3 and 41 – see Figure 5.3); C is the cross-section of the non-strengthened beam between side columns , at the vicinity of the columns (elements 11, 13, 31, and 33 – see Figure 5.3); D is the cross-section of the mid-span of the non-strengthened beam between columns (elements 12 and 32 – see Figure 5.3); E is the rigid elements cross-section.

The contribution of the strengthening in the cross section was accounted on the reinforcement steel area. Given that the strengthening in the original cross-section reached up to nearly 2/3 of the beam high, the OpenSees` reinforcement enhanced with the area of the TRM were the intermediary, $A_{s,int}$, and bottom ones, $A_{s,bot}$, (Figure 5.9).

The area of strengthening was converted in an equivalent area of steel by considering the position of the bar inside the original section (Figure 5.9), the nominal thickness of the light carbon textile, 0.062 mm (Table 3.3), and the three layers of TRM (Figure 3.23). The portion of TRM which contributed to the equivalent intermediary area of reinforcement ($A^{`}_{s,int}$), had 55 mm high per bar (Figure 5.9). For the bottom bars, this value was 60 mm (Figure 5.9). The tensile strength of the light carbon was adopted as 1434 MPa (Raoof and Bournas, 2017) . Consequently, for each intermediary bar, the equivalent area of steel was $A`_{s,int} = (0.062 \times 55 \times 3 \times 1434) / 500 = 29.34$ mm^2 per bar, and the equivalent diameter of this bar is $Ø_{eq} = 6.1$ mm. For the bottom bars, the contribution of the lateral portion of the TRM was $A`_{s,TRM,lat} = (0.062 \times 60 \times 3 \times 1434) / 500 = 32.01$ mm^2 per bar.

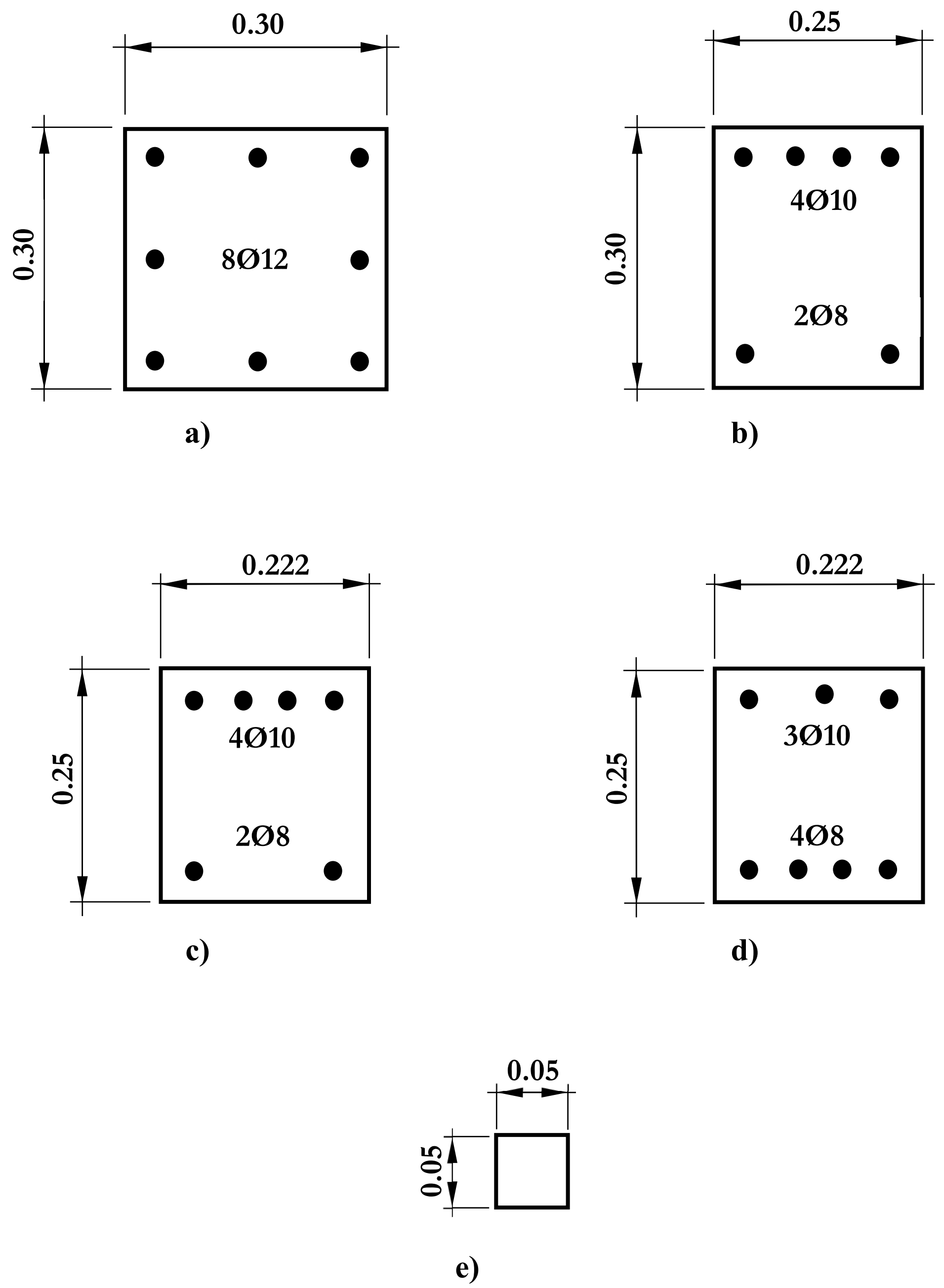

Figure 5.8 – Cross-sections of CON a) A b) B c) C d) D e) E (dimensions in m).

The bars at the bottom had yet the contribution of the portion of the TRM below the beam. This parcel of the TRM is, however, in a depth lower than the internal reinforcement considering the neutral line. Therefore, the converted area of TRM was enhanced by a factor to account for this difference in the depth. This factor was achieved by considering different locations of the neutral line and the mean value reached was 1.2. Hence, considering the beam width of 125 mm, the contribution of the lower part of the TRM was $A`_{s,TRM,bot}$ = (0.062 x 125 x 3 x 1434 x 1.2) / 500 = 80.02 mm^2.

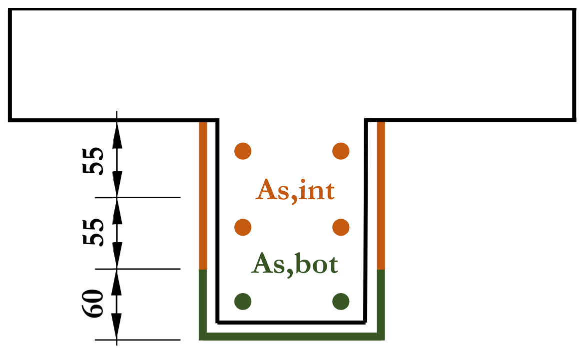

Figure 5.9 – Enhanced reinforcement (dimensions in mm).

Therefore, considering the TRM shear strengthening, the equivalent area of the bottom reinforcement, $A`_{s,\ bot}$, was composed by the area of the steel already present in the section, $A_{s,bot}$; two times the equivalent area of the lateral portion of the TRM, $A`_{s,TRM,lat}$, and the equivalent area of the inferior part of the TRM, $A`_{s,TRM,bot}$. Hence, for the sections of the beam with two longitudinal bars of 8 mm at the bottom of the beam (see Figure 3.7), the total equivalent area of the bottom reinforcement is $A`_{s,bot} = A_{s,bot} + 2A`_{s,TRM,lat} + A`_{s,TRM,bot}$ = 2 x 50.27 + 2 x 32.01 + 80.02 = 244.57 mm^2. Dividing this area per two bars, $A`_{s,bot}$ = 122.29 mm^2 per bar, where the equivalent diameter of this bar is $Ø_{eq}$ = 12.5 mm. For the sections where four longitudinal bars of 8 mm were present at the bottom of the beam (see Figure 3.7), $A_{s,bot}$ = 4 x 50.27 + 2 x 32.01 + 80.02 = 345.10 mm^2. Dividing this area for four bars, $A`_{s,bot}$ = 86.28 mm^2 per bar. The equivalent diameter of this bar is $Ø_{eq}$ = 10.4 mm.

For the case of the specimen TRM_TR, where the flexural strengthening was complemented by one additional layer of textile, the equivalent area of steel per bar at the bottom of the beam becomes $A`_{s,bot}$ = 135.78 mm^2. The equivalent diameter of this bar is $Ø_{eq}$ = 13.2 mm.

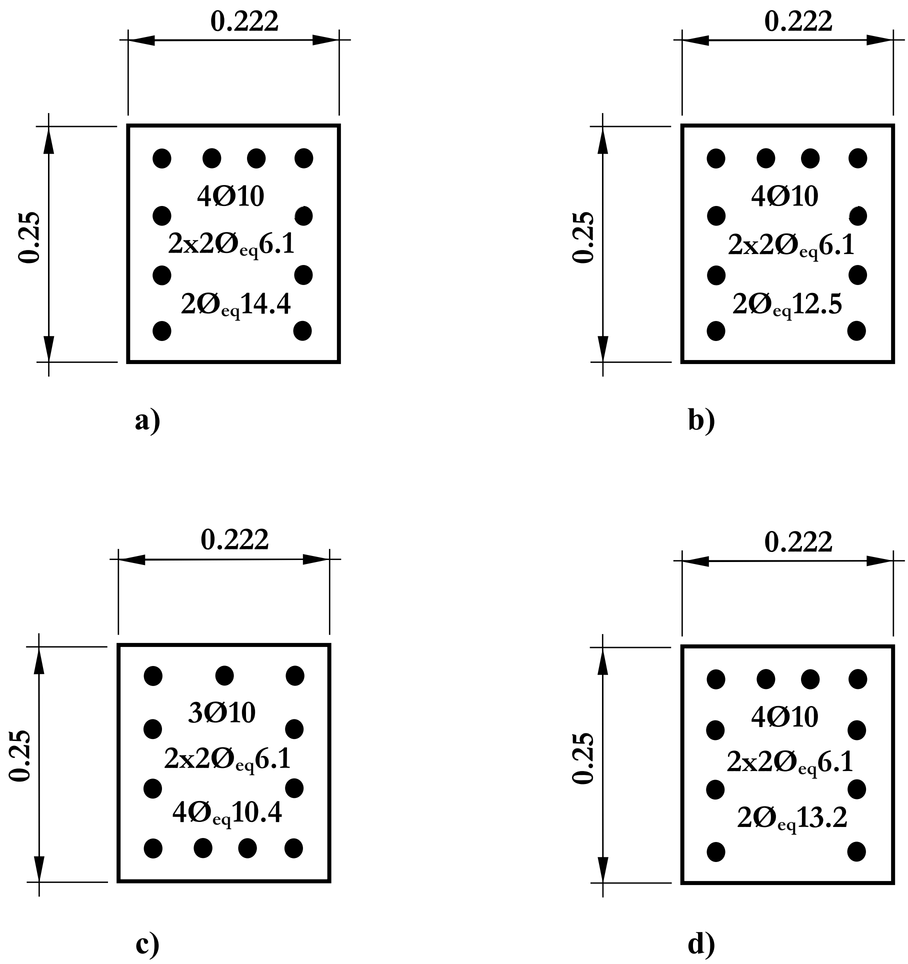

Figure 5.10 – Modified cross-sections for strengthened specimens a) F b) G c) H d) I (dimensions in m).

Strengthening characteristics	$A^{`}_{s,bot}$/bar (mm^2)	$Ø_{eq}$ (mm)
3 layers of TRM (lateral)	29.34	6.1
2 bars + 3 layers of TRM	122.29	12.5
4 bars + 3 layers of TRM	86.28	10.4
2 bars + 4 layers of TRM	135.78	13.2
2 bars + 3 layers of TRM	162.74	14.4

Table 5.3 – Equivalent diameter of steel for strengthened specimens.

For NSM strengthened specimens, instead of one additional layer of TRM, the NSM reinforcement was adopted. Hence the equivalent area of steel per bar at the bottom of the beam becomes $A`_{s,bot}$ = 162.74 mm^2. The equivalent diameter of this bar is $Ø_{eq}$ = 14.4 mm. Table 5.3 summarizes the equivalent areas pear bar and diameter for each previously described situation.

Therefore, with the equivalent steel defined, the cross-sections of the elements of strengthened specimens are presented in Figure 5.10.

5.4 Results

5.4.1 Concrete

A calibration process was necessary to adequate the parameters. Additionally, this process was useful to find correlated values of transmission length of steel and its properties, as well as to find the best force-displacement values for the springs. Therefore, Matlab (Manual, 2000) was adopted to conduct an optimization process via genetic algorithm technique to find values for the parameters with respect to the experimental results. Results of the calibrated concrete properties for each specimen can be found in Table 5.4.

Specimen	$f`_c$ (MPa)	E_c (MPa)	k_{fc}	k_{Res}	ε_{c0un}	ε_{cUun}	Tensoft
CON	-19	7991.3	1.30	0.2	-0.004	-0.01	0.001
NSM_PR	-19	7991.3	1.30	0.2	-0.004	-0.01	0.001
			2	0.6	-0.03	-0.10	0.050
TRM_TR	-22	8599.1	2	0.6	-0.03	-0.10	0.050
NSM_TR	-19	7991.3	2	0.6	-0.03	-0.10	0.050

Table 5.4 – Values of the parameters of the concrete.

As mentioned previously, the concrete strength and the elastic modulus of the concrete were maintained with the same values achieved in the calibration process for the original models in Chapter 4 (explained at the end of this Section). Therefore, the differences between 3D and 2D models were expressed on the other parameters of the concrete. In the non-strengthened specimen, the ratio between the concrete in the core of the section to the concrete in the cover was 1.3. The strain at the maximum tensile strength of the concrete cover achieved was -0.004, while the strain at ultimate strength was -0.01. The factor affecting the tension softening stiffness had the value of 0.001. Those values are comparable to values adopted by the software (Mazzoni et al., 2004). Strengthened specimens presented higher values of k_{fc} compared to CON, because in those specimens the concrete is confined by the TRM.

Additionally, values of the strains of the concrete cover at the maximum and ultimate strengths of the concrete, as well as the tension softening factor, were considerably higher in strengthened specimens compared to CON. This occurs because on those specimens the concrete of the cover is attached to the TRM, what modifies significatively the stiffness of this region. This is expressed on the analytical model through the values of ε_{c0un}, ε_{cUun} and Tensoft.

Finally, one can see that specimen NSM_PR presented two values of the parameters. In this specimen there were two types of sections at the beam, those with and those without strengthening. Elements 11, 12, 32 and 33 were non-strenghned, while elements 13, 31, 44 and 45 were (see Figure 5.4). Therefore, the uncovered elements had the same characteristics of CON, while the others had the same parameters of the strengthened specimens.

Considering the properties of the concrete achieved with the calibration process, as well as those of steel and springs, presented following, the ‘Load x Deflection’ curve was compared considering the experiment, the analytical model with concrete with $E_c = E_c/3$ (value also reached in Chapter 4), and the analytical model with $E_c = E_c$. This comparison shows the consistency of the models on simulating the studied frame up to the CAA peak load. One can see that, in all specimens, to reach a comparable curve between models and experiments, the Young’s modulus of the concrete had to be reduced, being divided by three ($E_c = E_c/3$). This can also be attributed here to the stiffness of the boundary conditions, and/or the kind of aggregate used on the tests, and slippage of the internal reinforcement, for instance. Figure 5.11 presents the vertical ‘Load vs Deflection’ curves of all specimens, with simulations considering both stiffness $E_c/3$ and E_c, as well as the experiment.

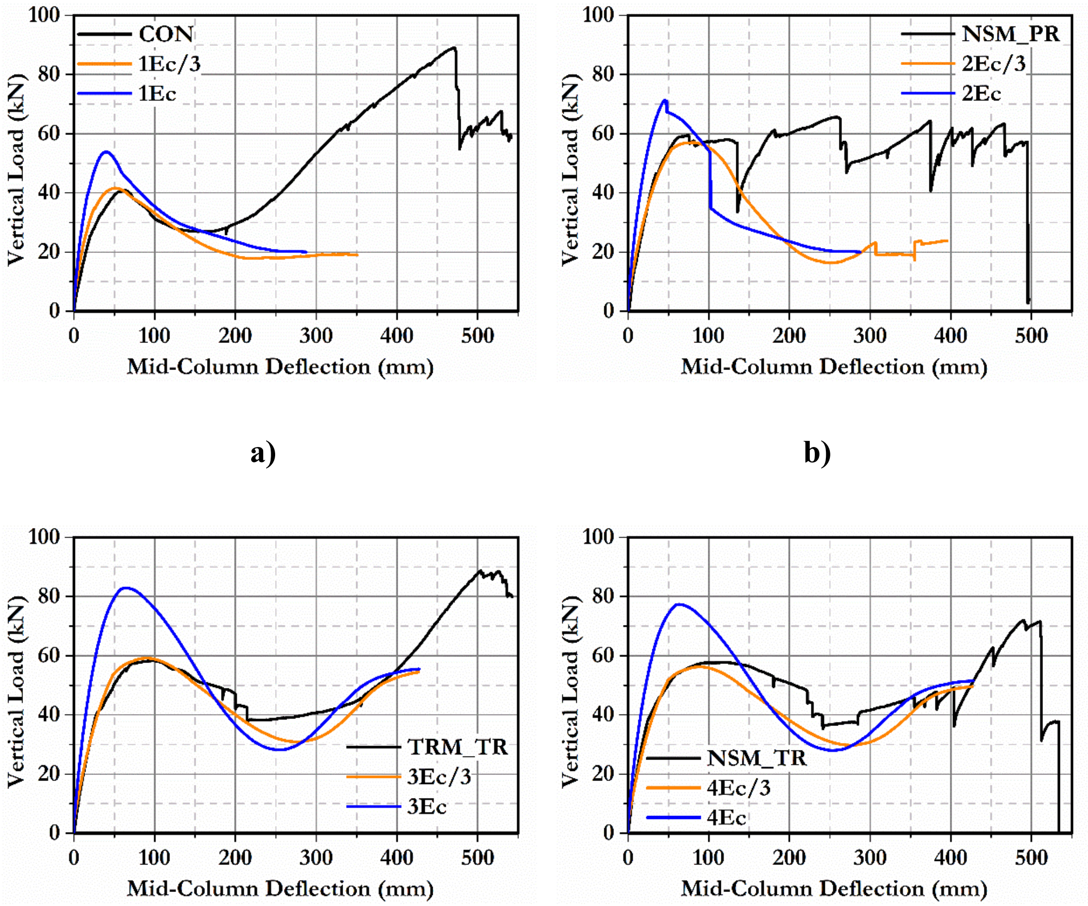

a) b)

c) d)

Figure 5.11 – Concrete stiffness comparison on vertical 'Load vs Deflection' curves a) CON b) NSM_PR c) TRM_TR d) NSM_TR.

5.4.2 Steel

The optimization process, conducted for the concrete parameters, was performed in conjunction with the information of the steel. The outcome provided the values of those parameters which were fixed in section 5.2.2.

5.4.2.1 Springs

The hysteretic material representing the longitudinal springs was also part of the optimization process, having as initial values those achieved with the relations presented previously. Two types of springs were used in the present work, one representing the top longitudinal reinforcement of the beam at the beam/column interfaces with four bars (Spring K_1); and the other representing the bottom longitudinal reinforcement of the beam at the same region, with two bars (Spring K_2). The outcome of the optimization can be seen in Table 5.5, where the longitudinal spring behaviour is defined through three force-displacement points.

Spring		Compression		Tension		Spring		Compression		Tension	
		F (kN)	δ (mm)	F (kN)	δ (mm)			F (kN)	δ (mm)	F (kN)	δ (mm)
	1	319.5	0.0011	-411.6	-0.00008		1	53.0	0.0028	-404.8	-0.00011
K_1	2	249.5	0.0026	-961.6	-0.00013	K_2	2	38.6	0.0048	-441.4	-0.00012
	3	31.8	0.0046	-780.1	-0.00508		3	19.2	0.0115	-577.6	-0.00221

Table 5.5 – Longitudinal springs characterization.

Element	Spring type			
	CON	NSM_PR	TRM_TR	NSM_TR
4	K_1	K_1	K_1	K_1
10	K_2	K_2	K_2	K_2
14	K_1	K_1	K_1	K_1
17	K_1	K_1	K_1	K_1
28	K_2	K_1	K_1	K_1
30	K_2	K_1	K_1	K_1
34	K_1	K_1	K_1	K_1
40	K_2	K_2	K_2	K_2

Table 5.6 – Identification of longitudinal springs per element for each specimen.

Table 5.6 shows the correspondence between longitudinal spring and element for each specimen. For strengthened specimens the spring capacity of elements 28 and 30 were changed to be similar to elements 4 and 34, thus characterizing the flexural reinforcement, i.e., NSM stainless-steel bars or textile-based anchors.

5.4.3 Original models comparisons

As in the previous chapter, here the model with the best fit on the vertical 'Load vs Deflection' curve is also named as original model. Figure 5.12 presents the vertical 'Load vs Deflection' curves for all specimens, where the experiment, micromodelling and macromodelling original models' outcomes are plotted. In (a) it is presented CON, in (b) is NSM_PR, in (c) is TRM_TR and in (d) is NSM_TR. One can see that the specimens where shear was one of the main damages at the beam (CON and NSM_PR), the development of the curve could not be as fit as in the other specimens. However, all the analytical models presented good agreement with the correspondent experimental curves during the CAA phase. As in the previous chapter, the focus of the study of the progressive collapse resistance of the frame is kept on the CAA phase.

	CON		NSM_PR		TRM_TR		NSM_TR	
	Load (kN)	Def.* (mm)	Load (kN)	Def.* (mm)	Load (kN)	Def.* (mm)	Load (kN)	Def.* (mm)
Experiment	40.6	65.8	59.5	74.7	58.3	99.2	57.7	116.2
OpenSees	41.6	51.3	57.0	80.8	59.1	89.7	56.2	88.4
Abaqus	40.9	50.7	57.8	73.6	66.1	67.7	56.2	67.7

*Deflections

Table 5.7 – Comparison of the first peak load and the correspondent vertical deflection.

Table 5.7 presents the comparison between values of the first peak load and the correspondent deflections. The difference between loads of the experiments and OpenSees simulations reached a maximum of 2.5 kN, while between Abaqus and the experiments the maximum difference was 7.8 kN. On the displacements Those differences were 27.8 mm and 48.5 mm respectively.

The pseudo-static responses of the original models from OpenSees and Abaqus, as well as those from the experiments are presented in Figure 5.13. In (a) specimen CON is presented, in (b) NSM_PR, in (c) TRM_TR is shown, and in (d) NSM_TR. The curves from OpenSees presented a better fit with the experimental ones than the curves from Abaqus.

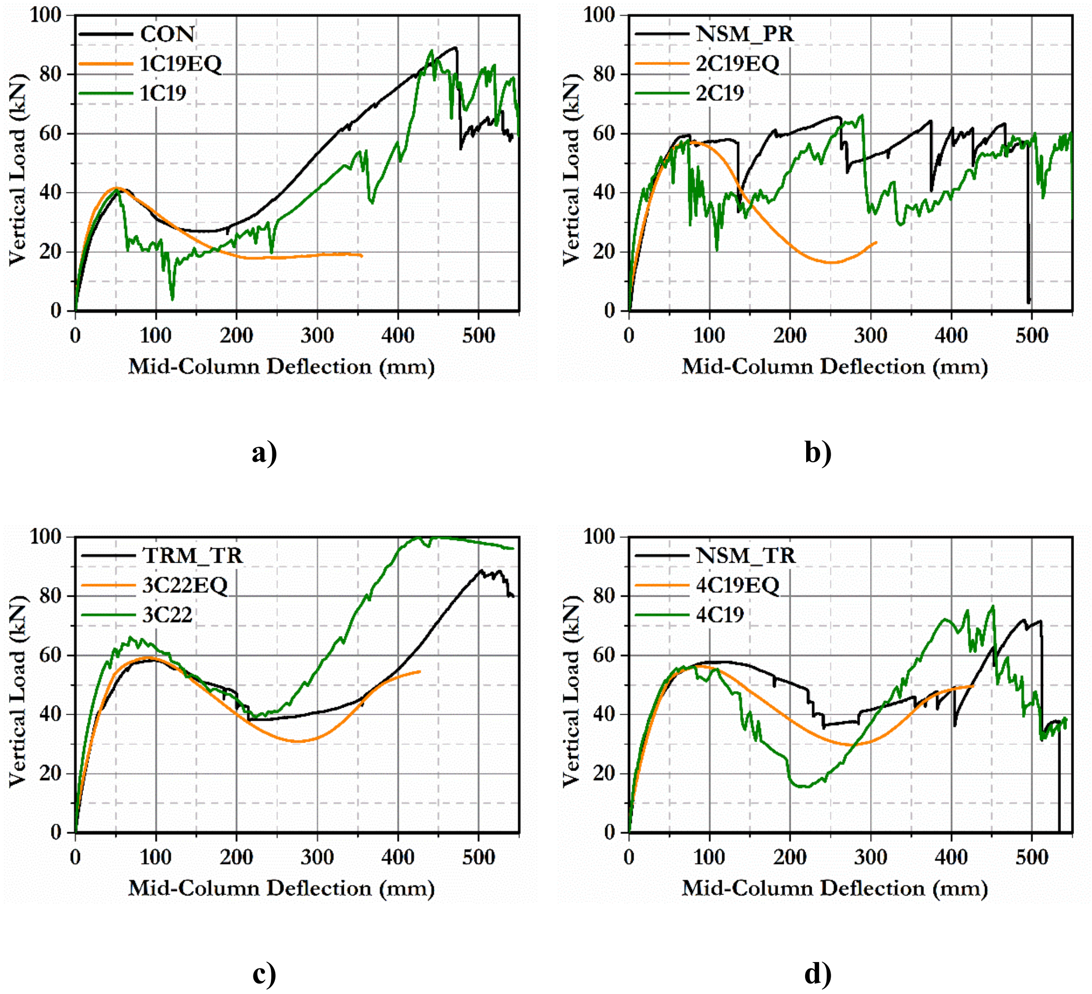

Figure 5.12 – Comparison of vertical 'Load vs Deflection' curves a) CON b) NSM_PR c) TRM_TR d) NSM_TR.

Table 5.8 presents the values of maximum dynamic responses and the associated deflections for the original models of all simulations during the CAA. The maximum dynamic responses of the models from OpenSees were at maximum 3.3 kN distant from the experimental results, while Abaqus` maximum dynamic responses reached up to 6 kN. When the correspondent deflections are assessed, the difference between OpenSees and experiment reached 50.6 mm, while between Abaqus and experiment this difference was up to 75.7 mm. Considering CAA up to its peak, the evolution of the pseudo-static curves was more representative using the analytical model.

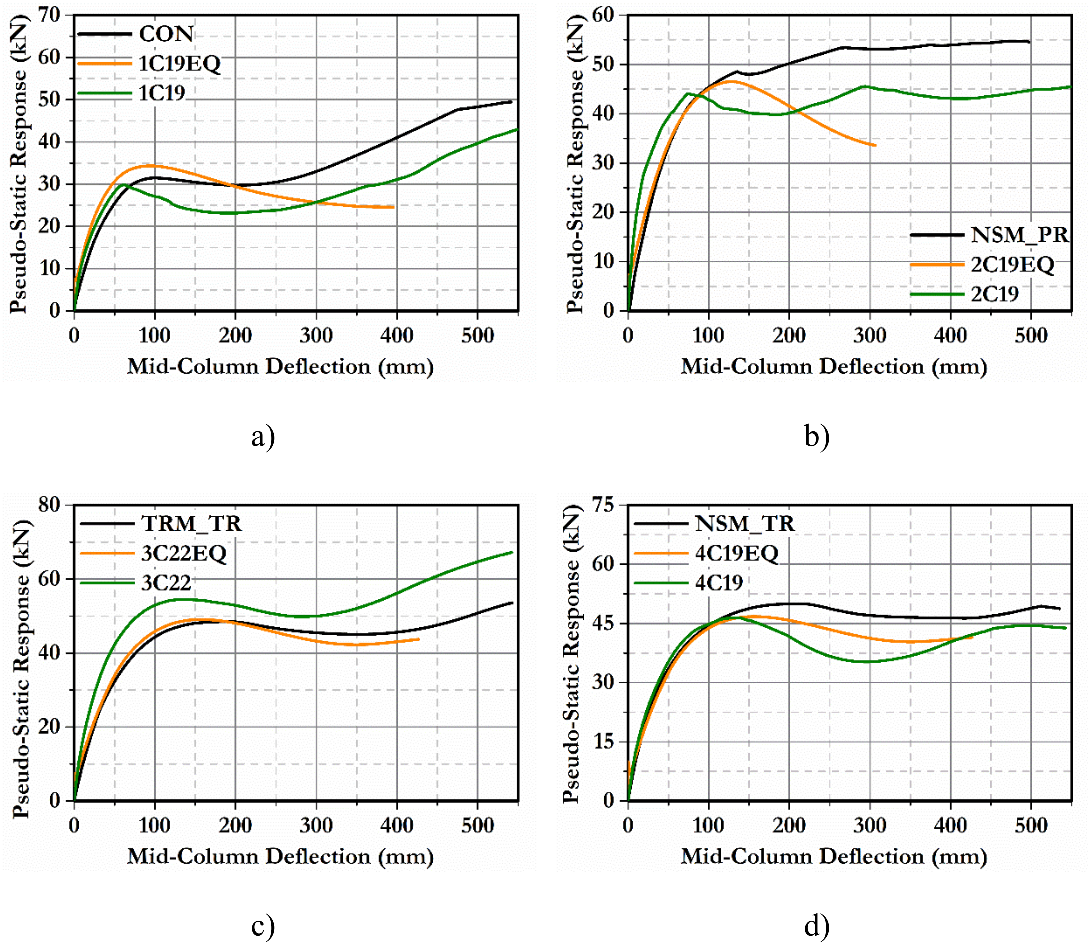

Figure 5.13 – Comparison of pseudo-static responses a) CON b) NSM_PR c) TRM_TR d) NSM_TR.

	CON		NSM_PR		TRM_TR		NSM_TR	
	Load (kN)	Def.* (mm)	Load (kN)	Def.* (mm)	Load (kN)	Def.* (mm)	Load (kN)	Def.* (mm)
Experiment	31.5	99.8	48.5	135.4	48.5	183.9	50.0	206.8
OpenSees	34.3	94.6	46.5	128.8	49.0	157.1	46.7	156.2
Abaqus	29.9	62.6	44.1	73.6	54.5	131.1	46.4	131.1

*Deflections

Table 5.8 – Comparison of the maximum dynamic responses and the correspondent vertical deflections.

Further comparisons are performed with the ductility ratios achieved from the pseudo-static curves of each specimen (see section 3.7). Table 5.9 presents the original models and the experiments values of ductility ratio. In this topic, the proximity between model and experimental values was equilibrated between Abaqus and OpenSees simulations. The maximum difference between experiment and OpenSees models was 1.84, while between experiment and Abaqus simulations was 2.75.

	CON	NSM_PR	TRM_TR	NSM_TR
Experiment	2.63	2.75	3.57	5.12
OpenSees	4.03	2.89	3.60	3.28
Abaqus	2.90	5.54	4.30	4.61

Table 5.9 – Comparison of the ductility ratios.

5.5 Discussion

Abaqus simulations are far more complex than those from the analytical models, in which the characteristics of the frame were simplified, and the development of the damage through the structure is poorly represented on the reductions of the elements' properties. Therefore, despite good agreement of the simulations with the experiments, differences were more expressed when Abaqus was adopted. Figure 5.14 presents the comparison performed for indicators of the progressive collapse resistance of the frame, where the experiment outcomes were taken as reference. Figure 5.14(a)-(b) presented the comparison for the first peak loads and the correspondent deflections respectively. Figure 5.14(c)-(d) shows the same for the dynamic response, and Figure 5.14e presents the comparisons between ductility ratios.

Analysing the first peak load, values from both OpenSees and Abaqus differed from Experiments in less than 5 %, apart from Abaqus' TRM_TR which was the most distant value of the calibraitons, presenting 13.4%. Comparing the deflections at P_f, those numbers go to 23.9% and 41.7% respectively when OpenSees and Abaqus are compared with the experiments. Those number highlight the representativity of the analytical model on simulating the pregressive collapse scenario studied here. In parallel, it remarks the difficulty of both models on predicting with accuracy the peak load associated vertical deflection.

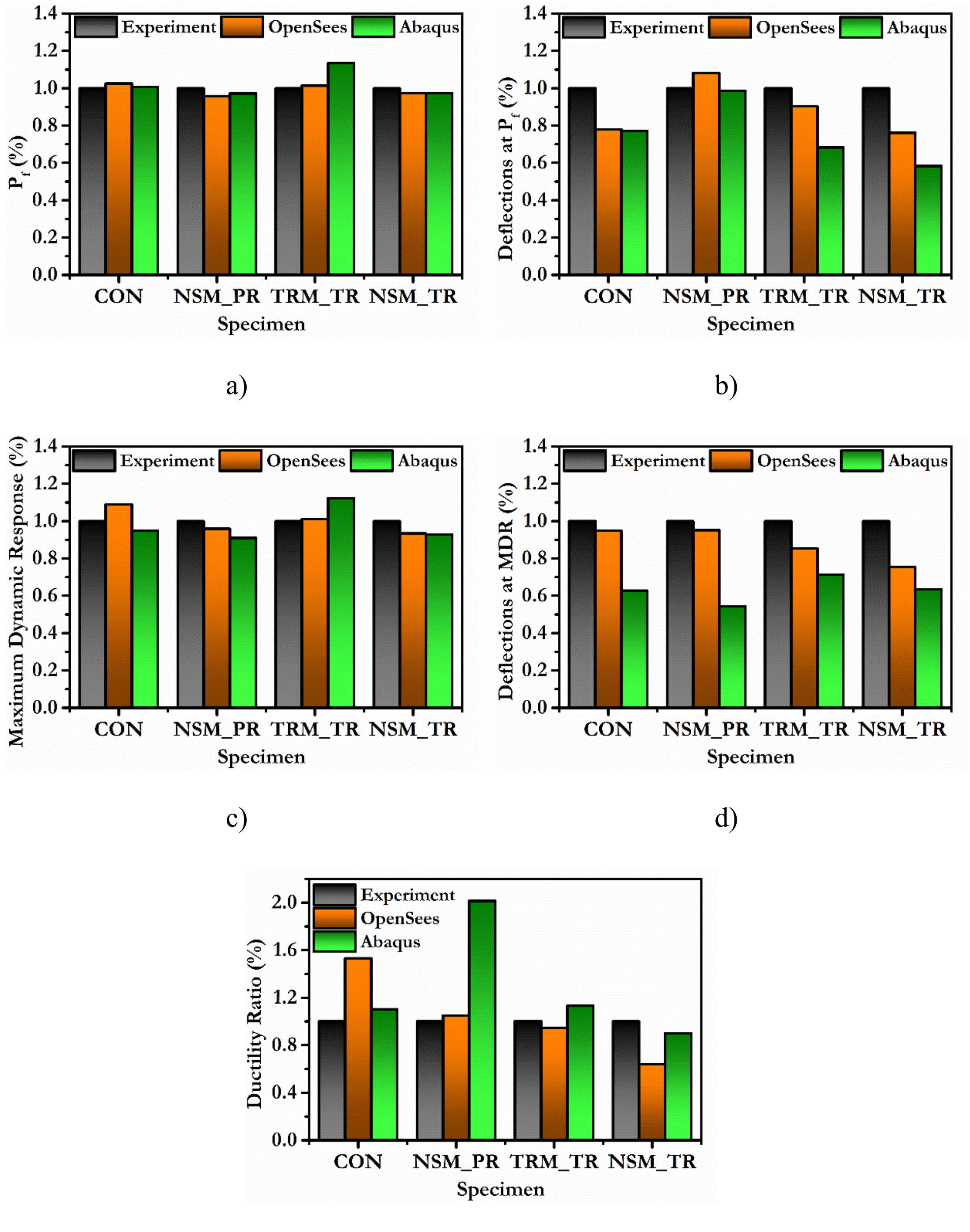

a) b)

c) d)

e)

Figure 5.14 – Modelling techniques comparisons.

The relation between results was further examined comparing the maximum dynamic responses, and the correspondent deflections. OpenSees simulations showed again better agreement when representing that, differing in up to 8.9% from the experiments when peak loads were compared, and in up to 24.5% regard to the deflections. Correspondent values from Abaqus simulations were 12.4% and 45.6%.

The ductility ratios from each specimen was also assessed. The tangent to the pseudo-static curve is used to achieve the ductility ratios, as well as the deflections at the maximum dynamic response. Moreover, the dynamic responses of the frames vary according to the area below the graph, i.e., the energy absorption capacity. Damages during the evolution of the curve could be better expressed on 3D simulations, what altered the development of the pseudo-static curve. Hence, differences in the ductility ratios can be addressed to the differences in stiffness in early stages of the development of the pseudo-static curves. Moreover, the different vertical deflections associated to the maximum dynamic responses achieved with simulations also had influence on the ductility ratio values. Therefore, to reach the best representativity of the model, the proper stiffness of the frame must be used on the simulations. Furthermore, the closer the model gets to the experiments the better.

5.6 Macromodelling Findings

The adoption of a simplified model to assess the behaviour of a portal frame under progressive collapse due to a sudden column removal can be used as an alternative feasible solution. The component-based RC joint model adopted in the present work demonstrated to attend the demands of such assessment.

The simulations with the component-based RC joint model presented good agreement with the experiments outcomes as well as with those from micromodelling approach. Moreover, it highlighted how the representation of the boundary conditions affects the frame response to a column loss. Additionally, the analytical model consumed significantly less time and computational resources than the complex 3D model. Furthermore, the adaptations of the parameters on the analytical simulations inputs were realistic and showed to be reliable and representative, given the results reached.

To achieve those results, the component-based model had modifications in the material properties. Material information showed that the strengthening scheme adopted was represented in the model by enhancing the concrete strength of the beam, augmenting the stiffness of the cover of the concrete, the concrete strength of the core, and increasing the steel area in the cross-section. Furthermore, the reproduction of the steel behaviour was possible with a reduction of the parameters controlling the transition between elastic and plastic branches of the steel.

Comparisons with key indicators of progressive collapse resistance of the frame showed that the analytical model presented closer response to the experimental ones than those from the 3D finite element models up to the CAA peak. After that, the post-peak behaviour of the frame in some simulations did not allow the full development of the pseudo-static curves.

Finally, given the good response of the analytical model, the results confirmed that the strengthening techniques addressed here were beneficial to the progressive collapse resistance of the frame under a sudden loss of a column.

This page was left intentionally blank

CHAPTER 6 CONCLUSIONS AND RECOMMENDATIONS FOR FUTURE WORKS

6.1 Conclusions

In the present work, the progressive collapse resistance of a pre-1968 designed portal frame in a multi-storey building under a loss of an internal column was investigated. For the first time two specific strengthening techniques were adopted in such study namely TRM and NSM reinforcement. The first is a mesh of advanced fibres immersed in a binder material, applied externally to the beam. A further innovation of this work lays on the utilization of textile-based anchors associated to the TRM technique. Furthermore, high-strength reinforcement, applied at the concrete cover, i.e., NSM using stainless steel bars is investigated as means to prevent progressive collapse for the first time.

In this work, key essential parameters to assess the progressive collapse response of a frame in such collapse scenario with the techniques adopted are identified and presented for the first time. Moreover a numerical procedure to simulate the studied case was stablished with the insertion of NSM reinforcement and TRM in the models. Additionally, the energy absorption capacity and the dynamic factor of the strengthened frames were assessed and insights were provided on the topic.

The work was composed by an experimental and a numerical investigation to observe the influence of the external strengthening in the studied frame. For the experimental phase, four specimens were cast and tested in laboratory: CON, as a reference, with no strengthening; NSM_PR, with partial cover of the beam against shear, and NSM reinforcement as flexural strengthening; TRM_TR, with full cover of the beam against shear, and textile-based anchors as flexural strengthening; and NSM_TR, with full cover and NSM as flexural strengthening.

The outcome of the tests demonstrated the effectiveness of the strengthening technique adopted on improving the progressive collapse resistance of the frame by enhancing its robustness, resilience, energy absorption capacity, ductility and transference of load.

By comparing different flexural strengthening methods, it was observed that the NSM technique favoured a better performance during CAA, while in TRM_TR a better response was achieved at TCA. In the former, the frame sustained loads for higher deflections, as well as transferred more loads axially through the beam. In the later, a more spread and released internal stored energy through deformations avoided reinforcement rupture and allowed the frame to reach higher load than P_f at the fully development of TCA.

By comparing shear covering lengths, it was observed that in the partially strengthened frame, shear damage was not avoided, but transferred to weaker sections. Similarly, concrete crush at the vicinity of the side columns was also transferred to weaker sections. Moreover, in this specimen, the load drop phase, well defined in other specimens, was not observed. Instead, sudden drops in the load occurred, yet the resistant load kept increasing back to values around the first peak load. The full covered specimen was able to avoid the shear failure and the concrete crush; therefore, CAA in this specimen lasted for longer. For that reasons, the ductility ratio of fully strengthened specimens reached higher values.

The numerical investigation comprised two methods, one involving a 3D finite element commercial software (Hibbitt et al., 1997), and the other using a component-based model inspired in the literature (Yu and Tan, 2013a). In the former, a parametric study was conducted to evaluate the frame response facing changes in numerical parameters, transmission length, mesh size and CDP parameter viscosity. In the later, an alternative solution to the high time and computational resources demand of the previous modelling technique was assessed.

In the micromodelling approach, in order to achieve more representative results, an adapted stress-equivalent strain relation for the steel, addressing the slippage of the internal reinforcement and the steel fracture, was proposed. When this new relation was implemented, the simulations presented good agreement with experimental results, and further coherent representativity when parameters were changed.

Key indicators of the progressive collapse resistance of the frame were recognized in the parametrical study; the first peak load, and its deflections; the maximum dynamic response and the correspondent deflection; the transferred loads at the beam and the top of the side columns; the ductility ratio; and the dynamic increase factor (DIF).

The outcome from the parametric study presented consistency on showing the improvement provided by the strengthening techniques on increasing the progressive collapse resistance of the frame under a column loss. Despite expressed differently in each specimen, the robustness, energy absorption capacity, ductility and load transference on strengthened specimens were improved when compared to CON with different parameters adopted. The CDP viscosity parameter was found to have no significant influence on the computational time to run the simulations, as well as no influence on the frame behaviour. Thus, the parameters assessed were transmissionlength and mesh size.

Amongst strengthened specimens, NSM_TR presented the higher variation to changes in the steel anchorage. Changes in the mesh size highlighted the importance of the proper calibration of the models, because localized damdages can lead to considerable differences on the frame response. Moreover, the adequate DIF found to be applied to strengthened specimens during the CAA was achieved: 1.3 for non-strengthened specimen; 1.21 for partially strengthened one; and 1.20 for fully covered specimens.

In the macromodelling approach, the adapted analytical model presented good agreement with the experimental and micromodelling outcomes. To achieve that, adaptations on the material properties of the concrete and the steel were necessary. The analytical models showed less oscillation with the evolution of the vertical deflections when compared to the 3D models.

6.2 Suggestions for Future Work

The present work can be further enriched with the following studies:

- Given that in the present work old design practices were assessed, and one specific practice was chosen to the design of the internal reinforcement, it would be interesting conducting an investigation considering different old practices;
- The utilization of the chosen strengthening technique on structures designed based on current versions of standards, where progressive collapse prevention is addressed, would be of great contribution to the field;
- To avoid the pull-off failure at the middle column, a study with continuous textile-based anchors passing through the middle column would contribute to closer comparisons between this flexural strengthening and the NSM one;
- Given the different deformability of different textile materials, and the importance of the energy balance without losing load carrying capacity, a study addressing a larger range of materials for the strengthening would enlarge the knowledge of the subject;
- The utilization of TRM and NSM strengthening techniques on frames under different boundary conditions, and different continuities with adjacent members, would provide information over different scenarios of column loss;
- The study of frames with the presence of redundancy with transversal beams, as well as the presence of the slab, considering strengthening with different configurations, would certainly be a good contribution to the area;
- The study of the strengthening method adopted here applied to precast concrete considering different connections configurations, would shed light over the behaviour of such frames;
- A study involving simulations of the frames studied in this work under cyclic loads with the consideration of the degradation of the elastic modulus would enhance the understanding of the mechanics of the damage in this situation;
- Moreover, the examination of the frames of the present work under blast loads, as well as under the event of fire, would show the responses of the frame and the strengthening techniques in extreme events;
- A study providing a deeper understanding and a mathematical support to the mechanics of the damage of the internal reinforcement, better characterizing the steel bond-slip behaviour and posterior fracture in events involving large deflections would be a great contribution to this subject.

REFERENCES

AMERICAN SOCIETY OF CIVIL ENGINEERS (ASCE) 2005. *Minimum design loads for buildings and other structures,* SEI/ASCE 7-05. Reston (VA, USA).

ANTONIOU, S. & PINHO, R. 2003. Seismostruct–Seismic Analysis program by Seismosoft. *Technical manual and User manual*.

AVESTON, J., COOPER, G. & KELLY, A. The properties of fiber composites. Conference proceedings, 1971. IPC Science and Technology Press Hellertown, PA.

BARBATO, M. 2009. Efficient finite element modelling of reinforced concrete beams retrofitted with fibre reinforced polymers. *Computers & Structures,* 87**,** 167-176.

BIRTEL, V. & MARK, P. Parameterised finite element modelling of RC beam shear failure. ABAQUS Users' Conference, 2006. 95-108.

BOURNAS, D. & TRIANTAFILLOU, T. 2011. Bond strength of lap-spliced bars in concrete confined with composite jackets. *Journal of Composites for Construction,* 15**,** 156-167.

BOURNAS, D. A., LONTOU, P. V., PAPANICOLAOU, C. G. & TRIANTAFILLOU, T. C. 2007. Textile-reinforced mortar versus fiber-reinforced polymer confinement in reinforced concrete columns. *ACI Structural Journal,* 104**,** 740.

BOURNAS, D. A., PAVESE, A. & TIZANI, W. 2015. Tensile capacity of FRP anchors in connecting FRP and TRM sheets to concrete. *Engineering Structures,* 82**,** 72-81.

BOURNAS, D. A. & TRIANTAFILLOU, T. C. 2009. Flexural strengthening of reinforced concrete columns with near-surface-mounted FRP or stainless steel. *ACI Structural Journal,* 106**,** 495.

BOURNAS, D. A., TRIANTAFILLOU, T. C., ZYGOURIS, K. & STAVROPOULOS, F. 2009. Textile-reinforced mortar versus FRP jacketing in seismic retrofitting of RC columns with continuous or lap-spliced deformed bars. *Journal of Composites for Construction,* 13**,** 360-371.

CHANG, G. & MANDER, J. B. 1994. Seismic energy based fatigue damage analysis of bridge columns: part 1-evaluation of seismic capacity.

CHEN, Y.-L., HUANG, L., LU, Y.-Q., DENG, L. & TAN, H.-Z. 2016. Assessment of Structural Robustness under Different Events according to Vulnerability. *Journal of Performance of Constructed Facilities***,** 04016004.

CODE, M. 2010. Model Code 2010–Final draft, Volume 1, bulletin no. 65. *International Federation for Structural Concrete (fib), Lausanne, Switzerland.*

COMMITTEE, A. & STANDARDIZATION, I. O. F. Building code requirements for structural concrete (ACI 318-08) and commentary. 2008. American Concrete Institute.

D'AMATO, M., BRAGA, F., GIGLIOTTI, R., KUNNATH, S. & LATERZA, M. 2012. Validation of a modified steel bar model incorporating bond-slip for seismic assessment of concrete structures. *Journal of Structural Engineering,* 138**,** 1351-1360.

DAT, P. X., HAI, T. K. & JUN, Y. 2015. A simplified approach to assess progressive collapse resistance of reinforced concrete framed structures. *Engineering Structures,* 101**,** 45-57.

DAT, P. X. & TAN, K. H. 2014. Experimental Response of Beam-Slab Substructures Subject to Penultimate-External Column Removal. *Journal of Structural Engineering,* 141**,** 04014170.

DE TERÁN, J. R. D. & HAACH, V. G. 2017. Crack opening prediction at casting joints with a new modified stress-strain law for embedded reinforcement. *Construction and Building Materials,* 157**,** 668-675.

DOD, U. 2009. Unified facilities criteria: design of buildings to resist progressive collapse. UFC 4-023-03. United States Department of Defense.

DU BETON, C. E.-I. 1993. CEB-FIP model code 1990. *Bulletin d'Information,* 213**,** 214.

ELKOLY, S. & EL-ARISS, B. 2014. Progressive collapse evaluation of externally mitigated reinforced concrete beams. *Engineering Failure Analysis,* 40**,** 33-47.

ELLINGWOOD, B. R., SMILOWITZ, R., DUSENBERRY, D. O., DUTHINH, D., LEW, H. & CARINO, N. J. 2007. *Best practices for reducing the potential for progressive collapse in buildings*, US Department of Commerce, National Institute of Standards and Technology.

ELNASHAI, A., PAPANIKOLAOU, V. & LEE, D. 2010. Zeus-NL-A System for Inelastic Analysis of Structures-User Manual. *Mid-America Earthquake Center, Department of Civil and Environmental Engineeering, University of Illinois at Urbana-Champaign, Urbana, IL*.

EN, B. 1999. 1015-11, Methods of test for mortar for masonry–Part 11: Determination of flexural and compressive strength of hardened mortar. *European Committee for Standardization, Brussels*.

EN, B. 2009. 12390-3. Testing hardened concrete–Part 3: Compressive strength of test specimens. *Brussels, Belgium: European Committee for Standardization*.

EUROCODE, B. 2006. 1. Actions on structures-Part 1-7: General actions-Accidental actions. *British Standard: London*.

FASCETTI, A., KUNNATH, S. K. & NISTICÒ, N. 2015. Robustness evaluation of RC frame buildings to progressive collapse. *Engineering Structures,* 86**,** 242-249.

GENIKOMSOU, A. S. & POLAK, M. A. 2015. Finite element analysis of punching shear of concrete slabs using damaged plasticity model in ABAQUS. *Engineering Structures,* 98**,** 38-48.

GIUFFRÈ, A. 1970. Il comportamento del cemento armato per sollecitazioni cicliche di forte intensità. *Giornale del Genio Civile*.

GSA, G. S. A. 2003. *Progressive collapse analysis and design guidelines for new federal office buildings and major modernization projects*. *Washington, DC*.

GSA, U. 2000. Progressive collapse analysis and design guidelines for new federal office buildings and major modernization projects. *Washington, DC*.

GÜNTERT, P., MUMENTHALER, C. & HERRMANN, T. 1998. DYANA 1.5 User's manual.
HADI, M. N. & SAEED ALRUDAINI, T. M. 2012. New building scheme to resist progressive collapse. *Journal of Architectural Engineering,* 18**,** 324-331.
HAJILOO, H. & GREEN, M. F. 2019. GFRP reinforced concrete slabs in fire: Finite element modelling. *Engineering Structures,* 183**,** 1109-1120.
HALLQUIST, J. O. 2006. LS-DYNA theory manual. *Livermore software Technology corporation,* 3**,** 25-31.
HANSBO, A. & HANSBO, P. 2004. A finite element method for the simulation of strong and weak discontinuities in solid mechanics. *Computer methods in applied mechanics and engineering,* 193**,** 3523-3540.
HAO, H., LI, Z.-X. & SHI, Y. 2015. Reliability Analysis of RC Columns and Frame with FRP Strengthening Subjected to Explosive Loads. *Journal of Performance of Constructed Facilities***,** 04015017.
HIBBITT, KARLSSON & SORENSEN 1997. *ABAQUS: Theory Manual*, Hibbitt, Karlsson & Sorensen.
HOFFMANN, K. 1974. *Applying the wheatstone bridge circuit*, HBM.
HOGNESTAD, E. 1951. Study of combined bending and axial load in reinforced concrete members. University of Illinois at Urbana Champaign, College of Engineering. Engineering Experiment Station.
HORDIJK, D. A. 1992. Tensile and tensile fatigue behaviour of concrete; experiments, modelling and analyses. *Heron,* 37.
HSU, L. & HSU, C.-T. 1994. Complete stress—strain behaviour of high-strength concrete under compression. *Magazine of Concrete Research,* 46**,** 301-312.
HUSAIN, M. & TSOPELAS, P. 2004. Measures of structural redundancy in reinforced concrete buildings. I: redundancy indices. *Journal of Structural Engineering,* 130**,** 1651-1658.
INSTITUTION, B. S. 2004. *Eurocode 2: Design of Concrete Structures: Part 1-1: General Rules and Rules for Buildings*, British Standards Institution.
IZZUDDIN, B., VLASSIS, A., ELGHAZOULI, A. & NETHERCOT, D. 2008. Progressive collapse of multi-storey buildings due to sudden column loss—Part I: Simplified assessment framework. *Engineering Structures,* 30**,** 1308-1318.
JANKOWIAK, T. & LODYGOWSKI, T. 2005. Identification of parameters of concrete damage plasticity constitutive model. *Foundations of civil and environmental engineering,* 6**,** 53-69.
KACHLAKEV, D., MILLER, T. R., YIM, S., CHANSAWAT, K. & POTISUK, T. 2001. Finite element modeling of concrete structures strengthened with FRP laminates. Oregon. Dept. of Transportation. Research Section.
KANG, S.-B., TAN, K. H. & YANG, E.-H. 2015. Progressive collapse resistance of precast beam–column sub-assemblages with engineered cementitious composites. *Engineering Structures,* 98**,** 186-200.
KAZEMI-MOGHADDAM, A. & SASANI, M. 2015. Progressive collapse evaluation of Murrah Federal Building following sudden loss of column G20. *Engineering Structures,* 89**,** 162-171.
KIAKOJOURI, F., DE BIAGI, V., CHIAIA, B. & SHEIDAII, M. R. 2020. Progressive collapse of framed building structures: Current knowledge and future prospects. *Engineering Structures,* 206**,** 110061.

KIM, J. & SHIN, W. S. 2013. Retrofit of RC frames against progressive collapse using prestressing tendons. *The Structural Design of Tall and Special Buildings,* 22**,** 349-361.
KIM, Y. J., KANG, J.-Y. & PARK, J.-S. 2015. Post-tensioned NSM CFRP strips for strengthening PC beams: A numerical investigation. *Engineering Structures,* 105**,** 37-47.
KMIECIK, P. & KAMIŃSKI, M. 2011. Modelling of reinforced concrete structures and composite structures with concrete strength degradation taken into consideration. *Archives of civil and mechanical engineering,* 11**,** 623-636.
KOHNKE, P. 2001. ANSYS theory manual. *ANSYS Inc***,** 40.
KOUTAS, L., PITYTZOGIA, A., TRIANTAFILLOU, T. & BOUSIAS, S. 2013. Strengthening of infilled reinforced concrete frames with TRM: Study on the development and testing of textile-based anchors. *Journal of Composites for Construction,* 18**,** A4013015.
KRÄTZIG, W. B. & PÖLLING, R. 2004. An elasto-plastic damage model for reinforced concrete with minimum number of material parameters. *Computers & structures,* 82**,** 1201-1215.
KWASNIEWSKI, L. 2010. Nonlinear dynamic simulations of progressive collapse for a multistory building. *Engineering Structures,* 32**,** 1223-1235.
LARANJEIRAS, A. C. R. 2013. Colapso Progressivo dos Edifícios. São Paulo: ABECE Informa
LARRINAGA, P., CHASTRE, C., BISCAIA, H. C. & SAN-JOSÉ, J. T. 2014. Experimental and numerical modeling of basalt textile reinforced mortar behavior under uniaxial tensile stress. *Materials & Design,* 55**,** 66-74.
LE, J.-L. & XUE, B. 2014. Probabilistic analysis of reinforced concrete frame structures against progressive collapse. *Engineering Structures,* 76**,** 313-323.
LEE, J. & FENVES, G. L. 1998. Plastic-damage model for cyclic loading of concrete structures. *Journal of engineering mechanics,* 124**,** 892-900.
LI, X. 2007. *Finite Element Modeling of Skewed Reinforced Concrete Bridges and the Bond-slip Relationship Between Concrete and Reinforcement.*
LIU, M. 2013. Pulldown Analysis for Progressive Collapse Assessment. *Journal of Performance of Constructed Facilities,* 29**,** 04014027.
LIU, P.-L., LIN, H.-Z. & DER KIUREGHIAN, A. 1989. *CALREL user manual*, Department of Civil Engineering, University of California at Berkeley.
LIVINGSTON, E., SASANI, M., BAZAN, M. & SAGIROGLU, S. 2015. Progressive collapse resistance of RC beams. *Engineering Structures,* 95**,** 61-70.
LOPEZ-ALMANSA, F., ALFARAH, B. & OLLER, S. Numerical simulation of RC frame testing with damaged plasticity model. Comparison with simplified models. Second European conference on Earthquake Engineering and Seismology, Istanbul, Turkey, 2014.
LÓPEZ-ALMANSA, F., ALFARAH, B. & OLLER, S. Numerical simulation of RC frame testing with damaged plasticity model. Comparison with simplified models. Second European Conference on Earthquake Engineering and Seismology, Istanbul, Turkey, 2014.
LOWES, L. N. 1999. *Finite element modeling of reinforced concrete beam-column bridge connections*, University of California, Berkeley.
LOWES, L. N. & ALTOONTASH, A. 2003. Modeling reinforced-concrete beam-column joints subjected to cyclic loading. *Journal of Structural Engineering,* 129**,** 1686-1697.

LUBLINER, J., OLIVER, J., OLLER, S. & ONATE, E. 1989. A plastic-damage model for concrete. *International Journal of solids and structures,* 25**,** 299-326.
MANUAL, M. U. S. 2000. The MathWorks Inc. *MATLAB Version,* 7.
MAZZONI, S., MCKENNA, F., SCOTT, M. H. & FENVES, G. 2004. OpenSees users manual. *PEER, University of California, Berkeley*.
MCKAY, A., MARCHAND, K. & DIAZ, M. 2012. Alternate path method in progressive collapse analysis: Variation of dynamic and nonlinear load increase factors. *Practice Periodical on Structural Design and Construction,* 17**,** 152-160.
MENEGOTTO, M. & PINTO, P. 1973. Method of Analysis for Cyclically Loaded Reinforced Concrete Plane Frames Including Changes in Geometryand Non-elastic Behavior of Elements Under Combined Normal Force and Bending. *Proceedings. IABSE Sympoium on Resistance and Ultimate Deformability of Structures Acted on by Well-Defined Repeated Loads*.
MERCAN, B., SCHULTZ, A. E. & STOLARSKI, H. K. 2010. Finite element modeling of prestressed concrete spandrel beams. *Engineering Structures,* 32**,** 2804-2813.
MOAVENI, S. 2003. *Finite element analysis: theory and application with ANSYS*, Pearson Education India.
MOFIDI, A., CHAALLAL, O., CHENG, L. & SHAO, Y. 2015. Investigation of Near Surface–Mounted Method for Shear Rehabilitation of Reinforced Concrete Beams Using Fiber Reinforced–Polymer Composites. *Journal of Composites for Construction***,** 04015048.
MUÑOZ, W., MOHAMMAD, M., SALENIKOVICH, A. & QUENNEVILLE, P. 2008. Determination of yield point and ductility of timber assemblies: in search for a harmonised approach. *Engineered Wood Products Association*.
MUTALIB, A. A. & HAO, H. 2011. Development of PI diagrams for FRP strengthened RC columns. *International Journal of Impact Engineering,* 38**,** 290-304.
NAIR, R. S. 2006. Preventing disproportionate collapse. *Journal of Performance of Constructed Facilities,* 20**,** 309-314.
NAYAL, R. & RASHEED, H. A. 2006. Tension stiffening model for concrete beams reinforced with steel and FRP bars. *Journal of Materials in Civil Engineering,* 18**,** 831-841.
NGO, D. & SCORDELIS, A. C. Finite element analysis of reinforced concrete beams. Journal Proceedings, 1967. 152-163.
NIZA, M. S. 2012. Computational analysis of reinforced concrete slabs subjected to impact loads. *International journal of integrated engineering,* 4.
ORTON, S. L. & KIRBY, J. E. 2013. Dynamic response of a RC frame under column removal. *Journal of Performance of Constructed Facilities,* 28**,** 04014010.
PARK, S., XIA, Q. & ZHOU, M. 2001. Dynamic behavior of concrete at high strain rates and pressures: II. Numerical simulation. *International journal of impact engineering,* 25**,** 887-910.
PEARSON, C. & DELATTE, N. 2005. Ronan point apartment tower collapse and its effect on building codes. *Journal of Performance of Constructed Facilities,* 19**,** 172-177.
PHAM, A. T., LIM, N. S. & TAN, K. H. 2017. Investigations of tensile membrane action in beam-slab systems under progressive collapse subject to different loading configurations and boundary conditions. *Engineering Structures,* 150**,** 520-536.

QIAN, K. & LI, B. 2012. Strengthening and retrofitting of RC flat slabs to mitigate progressive collapse by externally bonded CFRP laminates. *Journal of Composites for Construction,* 17**,** 554-565.

QIAN, K., LI, B. & MA, J.-X. 2014. Load-carrying mechanism to resist progressive collapse of RC buildings. *Journal of Structural Engineering,* 141**,** 04014107.

RAOOF, S. M. & BOURNAS, D. A. 2017. TRM versus FRP in flexural strengthening of RC beams: behaviour at high temperatures. *Construction and Building Materials,* 154**,** 424-437.

REDA, R., SHARAKY, I., GHANEM, M., SELEEM, M. & SALLAM, H. 2016. Flexural behavior of RC beams strengthened by NSM GFRP Bars having different end conditions. *Composite Structures,* 147**,** 131-142.

SASANI, M. & SAGIROGLU, S. 2008. Progressive collapse resistance of hotel San Diego. *Journal of Structural Engineering,* 134**,** 478-488.

STATHAS, N., BOUSIAS, S., PALIOS, X., STREPELIAS, E. & FARDIS, M. 2017a. Continuous one-way RC slabs with sinking outer support: tests and simple model. *Journal of Structural Engineering,* 144**,** 04017194.

STATHAS, N., BOUSIAS, S., PALIOS, X., STREPELIAS, E. & FARDIS, M. 2017b. Tests and Simple Models of RC Frame Subassemblies for Postulated Loss of Column. *Journal of Structural Engineering,* 144**,** 04017195.

SU, X., YANG, Z. & LIU, G. 2010. Finite element modelling of complex 3D static and dynamic crack propagation by embedding cohesive elements in Abaqus. *Acta Mechanica Solida Sinica,* 23**,** 271-282.

TEDESCO, J., HUGHES, M. & ROSS, C. 1994. Numerical simulation of high strain rate concrete compression tests. *Computers & structures,* 51**,** 65-77.

TETTA, Z. C., KOUTAS, L. N. & BOURNAS, D. A. 2015. Textile-reinforced mortar (TRM) versus fiber-reinforced polymers (FRP) in shear strengthening of concrete beams. *Composites Part B: Engineering,* 77**,** 338-348.

TETTA, Z. C., KOUTAS, L. N. & BOURNAS, D. A. 2016. Shear strengthening of full-scale RC T-beams using textile-reinforced mortar and textile-based anchors. *Composites Part B: Engineering,* 95**,** 225-239.

TODESCHINI, C. E., BIANCHINI, A. C. & KESLER, C. E. Behavior of concrete columns reinforced with high strength steels. Journal Proceedings, 1964. 701-716.

TSAI, M.-H. 2012. A performance-based design approach for retrofitting regular building frames with steel braces against sudden column loss. *Journal of Constructional Steel Research,* 77**,** 1-11.

TSAI, M. H. & CHANG, Y. T. 2015. Collapse-resistant performance of RC beam–column sub-assemblages with varied section depth and stirrup spacing. *The Structural Design of Tall and Special Buildings,* 24**,** 555-570.

VALIPOUR, H. R. & FOSTER, S. J. 2010. Finite element modelling of reinforced concrete framed structures including catenary action. *Computers & structures,* 88**,** 529-538.

WILSON, E. & HABIBULLAH, A. 1998. SAP2000-structural analysis users manual. *Computers and Structures, Inc*.

WILSON, E. L. 1997. *SAP2000: integrated finite element analysis and desing of structures. Analysis reference*, Computers and Structures.

YU, J., RINDER, T., STOLZ, A., TAN, K.-H. & RIEDEL, W. 2014. Dynamic progressive collapse of an RC assemblage induced by contact detonation. *Journal of Structural Engineering,* 140**,** 04014014.

YU, J. & TAN, K.-H. 2013a. Experimental and numerical investigation on progressive collapse resistance of reinforced concrete beam column sub-assemblages. *Engineering Structures,* 55**,** 90-106.

YU, J. & TAN, K. Macromodel-based simulation of catenary action of RC beamcolumn sub-assemblages. Proceedings of the 3rd fib International Congress 2010, Washington, DC, 2010.

YU, J. & TAN, K. H. 2012. Structural behavior of RC beam-column subassemblages under a middle column removal scenario. *Journal of Structural Engineering,* 139**,** 233-250.

YU, J. & TAN, K. H. 2013b. Special detailing techniques to improve structural resistance against progressive collapse. *Journal of Structural Engineering,* 140**,** 04013077.

This page was left intentionally blank

APPENDIX A

A.1 Construction of Pseudo-Static curve

Since a column removal scenario is a dynamic phenomenon, any ductility demands have to consider the maximum dynamic response of the structure, for a given gravity load, rather than the quasi-static one (derived either from a nonlinear static analysis or a quasi-static experiment).

Under the assumption of a SDOF system, Izzudin et al. (2008) proposed a method to derive such estimates given the nonlinear static response of the system. In that work the nonlinear static response is derived from simulation. In the present work, this is the measured response of the system.

In the pseudo-statiic curves introduced in Izzudin et al. (2008) and shown in Figure 3.41, the equivalent levels of gravity load are evaluated for increments of maximum dynamic displacement. The gravity loads are evaluated under the observation that the maximum dynamic response of the SDOF system arises when its kinetic energy reduces to zero. Hence, for a specific level of dynamic displacement u_d the potential energy of the system as evaluated from a static analysis will have to be equal to the work done by an external force P_{eq} (corresponding to the gravity loads) over the same displacement. Hence, the external force corresponding to the level of dynamic displacement u_d (see also Figure A. 1) can be established through the following equation, i.e.,

$$P_{eq} u_d = \int_{u=0}^{u=u_d} P(u_d)\, du \qquad \textbf{(A.1)}$$

here the integral expression corresponds to the area highlighted in Figure A. 1.

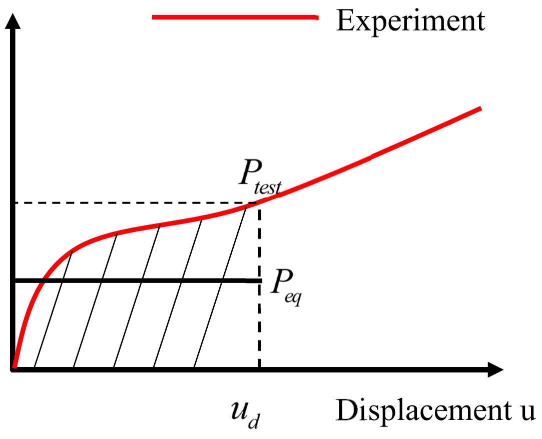

Figure A. 1 - Construction of the Pseudo-Static curve.

APPENDIX B

B.1 Parametric Study Results

Due the complexity and quantity of parameters affecting the behaviour of the models, the simulations were, in general, sensitive to changes. This sensitivity can be visualized from the CAA peak forward, where abnormal behaviour can be observed in the vertical "Force vs Deflection" curves. For instance, in some of those curves the load is decreased up to negative values, what is not normal

Although the simulations reproduced the experiments outcomes, it is prudent to focus the progressive collapse prevention in the CAA stage. The advanced stage of the failure of the frame during TCA makes the success of regain of load be dependent majorly on the reinforcement steel conditions. Whether the steel is well anchored inside the concrete, if it is close to rupture, if any out-of-plane deflections occur, or whether it slipped inside the concrete will determine the development of the resistant load. As presented, changing the parameters resulted in stress concentrations in different regions along the beam. Moreover, results of the experimental program (Chapter 3) have shown that the influence of external strengthening was more significant in early vertical deflections. Furthermore, values of the maximum dynamic responses of the strengthened specimens during CAA and TCA were similar in the experiments. Finally, as mentioned, the simulations were sensitive to changes in the parameters, what can be seen after the first load peak. Therefore, the assessment of the influence of parameters changing will be performed considering mainly the CAA phase. This finding is confirmed by Stathas et al. (2017b), where it was concluded that the CAA is more important to the enhancement of the frame load carrying capacity than the TCA.

As mentioned in Chapter 3, the success of the progressive collapse resistance of the frame is associated to three factors which must to be considered together to a correct evaluation: energy absorption capacity, redundancy and ductility (Izzuddin et al., 2008). Therefore, beyond the influence of each parameter on the structure behaviour, it is investigated here the progressive collapse resistance of the models. Hence, points of interest of the assessment are the frame capacity to resist the increased load, what can be seen on the load-deflection curve, as well as in it pseudo-static response, where the energy absorption capacity can be evaluated. Moreover, the capacity of transference of load of the frames are investigated too, through the load cells responses. Furthermore, the ductility ratio of each model from its pseudo-static response is presented. Additionally, the failure modes of the simulations are compared.

B.2 CON

B.2.1 Transmission Length (Serie L)

Vertical 'Force vs Deflection' Response

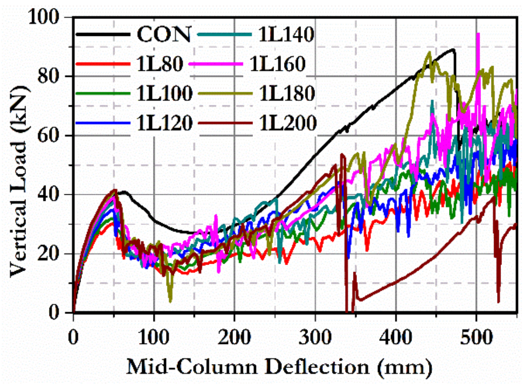

Figure B. 1 - CON 'Mid-Column Deflection vs Vertical Load' curves of Serie L.

The transmission length has influence in both resistant mechanisms CAA and TCA, and so its interaction with concrete. Changing the transmission length affects the magnitude of P_f as well as the overall stiffness of the beam, therefore changing the evolution of the resistant load with the vertical deflection. The later can be visualized in Figure B. 1, where the inclination of the curve after P_{min} is changed.

By doubling the transmission length of the steel from 80 mm to 160 mm the first peak Pf is increased in 19%. With the maximum transmission length studied here, 1L200, the increment from 80 mm to 160 mm is 27%. The vertical deflection at which those load peaks occurred remained around the same value in the great majority of the specimens assessed, 50.7 mm. Values of Pmin when compared with each respective Pf reached its lowest in 1L200, where it was reduced to 30% of Pf, and the highest in 1L140, where it reached 49% of P_f. After Pmin, the resistant load is increased with the increment of the transmission length, considering the same vertical deflection. Table B. 1 shows the values of loads and deflections for the three key points.

Transm. Length	CAA		P_{min}		TCA	
	Load (kN)	Deflection (mm)	Load (kN)	Deflection (mm)	Load (kN)	Deflection (mm)
1L80	32.7	52.6	13.1	111.9	52.9	552.3
1L100	31.9	46.9	13.4	114.6	49.4	557.6
1L120	35.0	50.7	15.9	98.3	60.0	549.7
1L140	37.5	50.7	18.3	98.3	71.7	445.0
1L160	39.0	50.7	13.8	180.0	94.5	502.0
1L180	40.9	50.7	15.8	129.1	88.1	441.7
1L200	41.6	50.7	12.5	111.9	53.6	332.9

Table B. 1 - CON key points of Serie L.

Load Cells Responses

Figure B. 2 shows the load cells responses of the Serie L, where LC1 and LC2 are represented in (a), while (b) presents the load cells at the beam level, LC3 and LC4. In early vertical deflections the similarity of the top load cells responses was maintained and the development of the rest of the curve is changed with different transmission lengths. At the load cells LC3 and LC4, the load development showed differences since CAA, where the peak load is decreased with the increment of transmission length. Here, the transition between CAA and TCA decreased with the increment of the transmission length. A better anchored steel reduces the slippage and the transference of loads up to the top of the side columns is increased, then the load transferred at the beam level is reduced.

Table B. 2 present the readings of the load cells during the CAA. At the top load cells the transference of load increased in 675% considering the minimum value in 1L100, and the maximum in 1L200. However, in general, the load recorded by those load cells tended to increase with L. At load cells LC3 and LC4 the load decreased in 17% with the increment of the transmission length when the extreme values are considered.

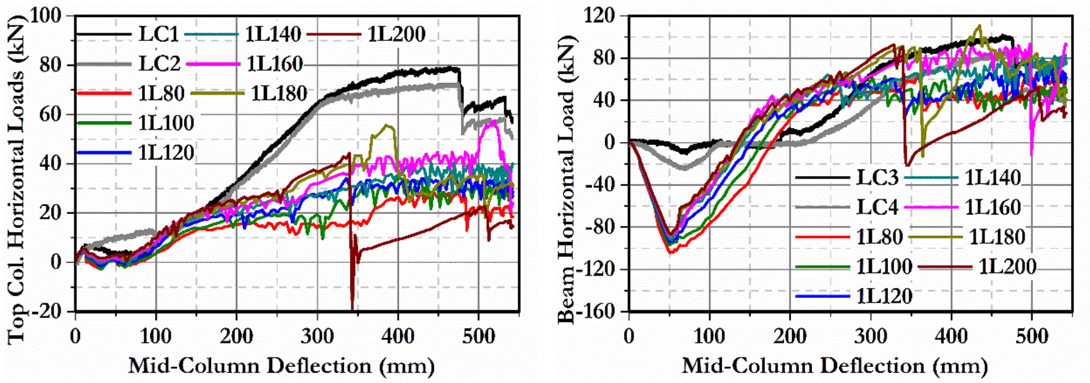

a) b)

Figure B. 2 - CON load cells responses on Serie L a) LC1 and LC2 b) LC3 and LC4.

Specimen	LC1 - LC2 (kN)	LC3 - LC4 (kN)
CON	10.3	-24.1
1L80	0.7	-104.2
1L100	0.4	-97.0
1L120	1.1	-93.9
1L140	1.4	-91.9
1L160	2.2	-88.5
1L180	2.8	-87.2
1L200	3.1	-86.8

Table B. 2 – CON load cells responses of Serie L during CAA.

Maximum dynamic response and DIF

The maximum dynamic responses and the correspondent vertical deflections (Figure B. 3), as well as the DIFs were achieved for different transmission lengths. In all Series of all specimens the pseudo-static curves and the DIFs were calculated as per presented in

APPENDIX A and Section 3.7 respectively. Despite the simulations of Serie L presented the full development of the TCA, the information regard to the dynamic behaviour to be presented here will be the same as in all other parameters assessed, which is that correspondent to the CAA.

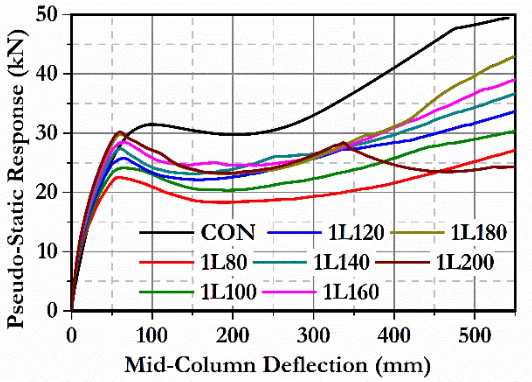

Figure B. 3 – CON Progressive collapse resistance of Serie L.

Specimen	Maximum Dynamic Response (kN)		Dynamic Increase Factor (DIF)
	Load (kN)	Deflection (mm)	
CON	31.5	99.8	1.29
1L80	22.6	60.5	1.45
1L100	24.1	64.8	1.32
1L120	25.7	64.8	1.36
1L140	27.4	60.5	1.37
1L160	28.4	66.9	1.37
1L180	29.9	62.6	1.37
1L200	30.2	60.5	1.37

Table B. 3 - CON Dynamic response of Serie L.

Values of maximum dynamic response and DIF for the Serie L are presented in Table B. 3. Since P_f is increased with the increment of L, the maximum dynamic response of this Serie followed the same behaviour. The difference between maximum (1L200) and minimum (1L80) values of maximum dynamic responses was approximately 34%, while the DIF remained around the same value on most of the specimens, 1.37, with

2.6% as standard deviation. The deflections at MDR presented low variation, showing values distant at maximum in 11%.

Ductility ratio

Specimen	Ductility ratio ($\Delta_{failure}/\Delta_{yield}$)
CON	2.63
1L80	3.47
1L100	3.73
1L120	3.74
1L140	3.18
1L160	3.51
1L180	2.90
1L200	2.78

Table B. 4 – CON Ductility ratios of Serie L.

The ductility ratios of the simulations in Serie L are presented in Table B. 4. The specimen with highest transmission length presented smaller ductility ratio compared with the original model 1L180, and this ratio is increased in general to lower transmission lengths. A better adherence between concrete and steel retards the slippage, consequently reduces the ductility of the frame. The difference between models 1L180 and 1L200 was not significative, 4%. The difference between minimum and maximum values was nearly 35%.

Failure modes

The failure modes of the specimens with both extreme transmission lengths studied here presented different configurations. The plasticity of the concrete is depicted in Figure B. 4 - CON Failure modes of Serie L a) 1L80 b) 1L200.

to emphasize the regions where the failure was more severe. On both specimens the concrete crushing at the bottom of the beam at the side joint, original from CAA, happened regardless the transmission length. With less length to transfer the loads to the concrete, the reinforcement steel of model 1L80 (Figure B. 4a) had more slippage inside the concrete. Consequently, the yield and posterior failure of the steel occurred in sections where the steel could not slip more, and tensions were not spread.

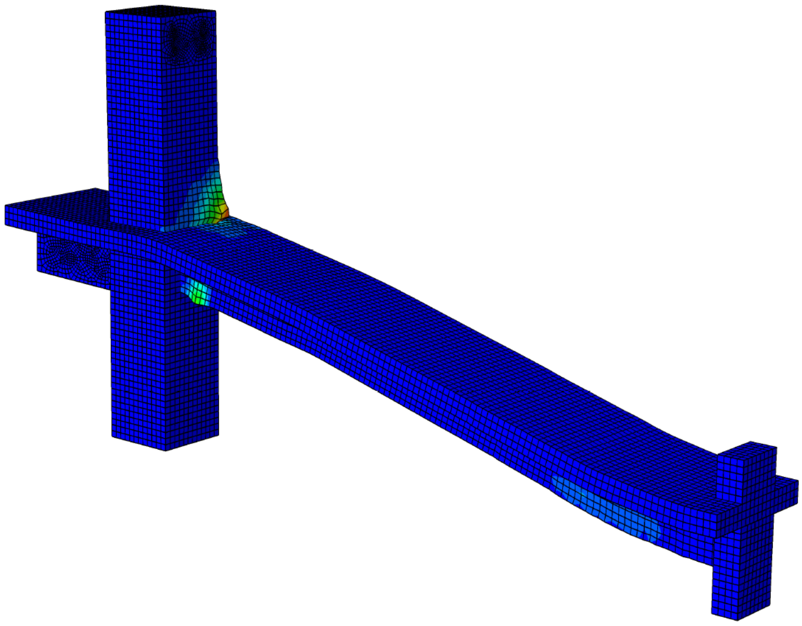

a)

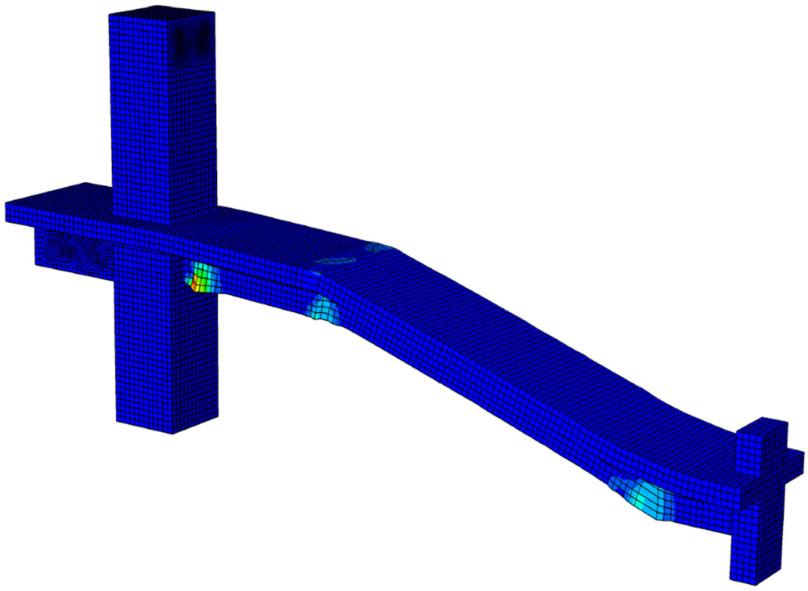

b)

Figure B. 4 - CON Failure modes of Serie L a) 1L80 b) 1L200.

The failure at the TCA stage on 1L80 (Figure B. 4a) was more present in the side column, indicating that no slippage occurred more, leading to the fracture of the steel in this region. Less severe damage was showed at the bottom of the beam, at the vicinity of the middle column. That indicates that slippage between steel and concrete was more present in this region. Figure B. 4b shows the failure mode of the specimens with 200 mm of L. It is evident at least three different sections with major failures. The larger quantity of cracks opened on the beam in this specimen can not be visualized because the color system follows the larger values. However, the failure of 1L200 demonstrates that the better adherence between steel and concrete leads to rupture of the steel at the mid-sections, as well as a plastic hinge formation where part of the internal reinforcement changes its position inside the beam.

B.2.2 Mesh Size (Serie M)

The differences of the first load peak were not significant as in the previous parameter variation, however, here the failure of the simulations occurred at different vertical deflections during the TCA stage. Figure B. 5 presents the outcome of the simulations with different mesh sizes.

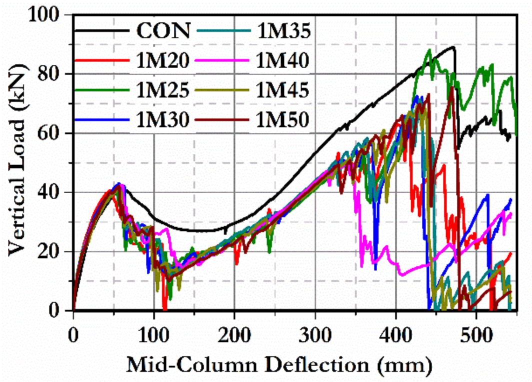

Figure B. 5 - CON ‘Mid-Column Deflection vs Vertical Load’ curves of Serie M.

As previously mentioned in Section 4.7.1.1, the differences between simulation in this Serie occur due the relation between the tension softening and the elastic branch of the material in the CDP model, which is dependent on the element size. Hence, changes can be observed from model to model in this Serie, even thought those are small. Apart of that, by modifying the mesh size another affected factor was the time demanded to conclude the runs. The time necessary to finish the simulation was around 8 times bigger on 1M20 compared to 1M50.

Mesh Size	CAA		P_{min}		TCA	
	Load (kN)	Deflection (mm)	Load (kN)	Deflection (mm)	Load (kN)	Deflection (mm)
1M20	40.5	44.7	13.5	128.0	63.0	401.4
1M25	40.9	50.7	15.8	129.1	88.1	441.7
1M30	43.1	56.6	12.9	112.8	72.4	426.3
1M35	41.9	61.0	12.2	124.8	71.4	429.2
1M40	42.4	58.8	14.6	137.4	50.7	339.5
1M45	41.2	56.6	13.0	118.7	69.4	426.3
1M50	42.1	56.6	11.2	121.8	75.5	469.5

Table B. 5 - CON key points of Serie M.

Table B. 5 presents the values of the Serie M for the three key points. During CAA the major difference in the load between simulations was 2.6 kN, or approximately 6%. Comparing deflections, this value goes up to 36%, however most of the runs had P_f happening around 57 mm. The minimum load after P_f had a mean of 13.3 kN with the most distant value being 2.1 kN lower, on 1M50. After P_{min}, the development of the resistant load with the evolution of the vertical deflection was similar in all specimens, however presenting different P_{TCA} at different deflections.

Load Cells Responses

The load cells responses for Serie M can be visualized in Figure B. 6. In (a) are the responses of LC1 and LC2, while in (b) are the LC3 and LC4 readings. One can see that changes between CAA and TCA phase (Figure B. 6b) are low compared with the previous Series. Complementing the information presented in Figure B. 6, the load cells readings at the peak load during the CAA can be seen in Table B. 6. The specimen with larger values was the intermediary 1M30, being 36% higher than the original model 1M25 and 153% higher than the minimum value of the top load cells, recorded in 1M20. Considering the larger mesh size, 50 mm, the value presented for LC1 and LC2 in 1M30 was 81% higher. Comparing 1M30 with the original model, 1M25, and with the minimum and maximum mesh sizes studied, 1M20 and 1M50, the reading of LC3 and LC4 was 19%, 39% and 9% higher respectively. The load is reduced as the mesh size gets distant from 30 mm.

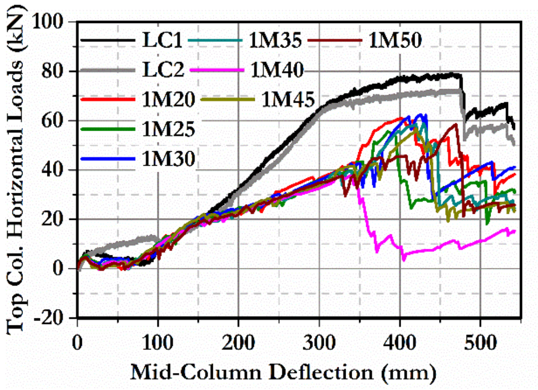

a)

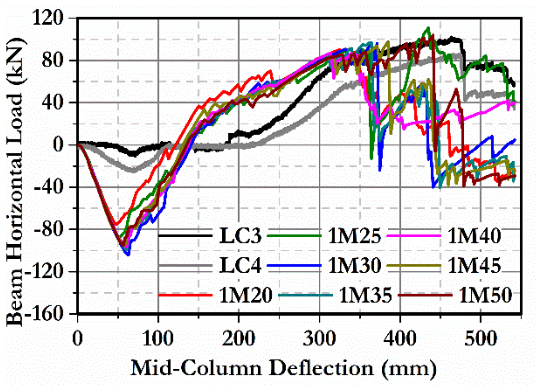

b)

Figure B. 6 – CON load cells responses on Serie M a) LC1 and LC2 b) LC3 and LC4.

Specimen	LC1 - LC2 (kN)	LC3 - LC4 (kN)
CON	10.3	-24.1
1M20	1.5	-75.0
1M25	2.8	-87.2
1M30	3.8	-104.2
1M35	3.1	-99.4
1M40	2.9	-96.3
1M45	2.7	-95.3
1M50	2.1	-95.3

Table B. 6 – CON load cells responses of Serie M during CAA.

Maximum dynamic response and DIF

Although the mesh size is not a material property it is interesting observing the influence of changing this parameter on the dynamic behaviour of the original model.

The dynamic response of the Serie M is depicted in Figure B. 7, which were similar during CAA, presenting the biggest divergence during TCA.

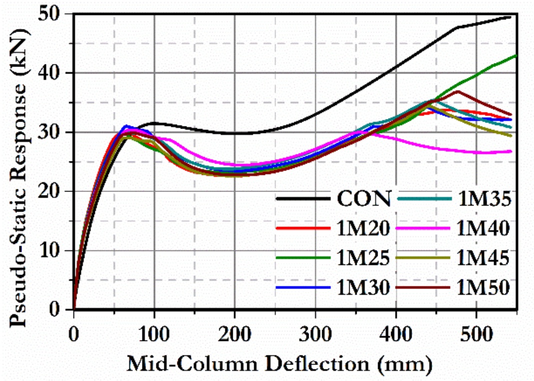

Figure B. 7 – CON Progressive collapse resistance of Serie M.

Specimen	Maximum Dynamic Response (kN)		Dynamic Increase Factor (DIF)
	Load (kN)	Deflection (mm)	
CON	31.5	99.8	1.29
1M20	29.9	65.4	1.35
1M25	29.9	62.6	1.37
1M30	31.0	65.4	1.39
1M35	30.1	63.2	1.39
1M40	30.4	72.5	1.40
1M45	29.1	70.1	1.42
1M50	29.9	74.9	1.41

Table B. 7 – CON Dynamic response of Serie M.

Table B. 7 presents the values of maximum dynamic response, correspondent deflections and DIF for all the runs in this Serie. The maximum dynamic response remained around the same value, 30 kN, while the deflections had high variation, 20% between extreme values. That highlights the need of a proper calibration of the mesh size. DIF had a mean of 1.39 presenting low variation between simulations.

Ductility ratio

Specimen	**Ductility ratio ($\Delta_{failure}/\Delta_{yield}$)**
CON	2.63
1M20	3.00
1M25	2.90
1M30	2.90
1M35	2.77
1M40	3.13
1M45	2.94
1M50	3.16

Table B. 8 – CON Ductility ratios of Serie M.

Here the values of ductility ratios (Table B. 8) were closer, around 2.97. Again, only one specimen presented lower ratio than the original model 1M25, which can be product of the variation of results between specimens, expected when different mesh sizes are used due its relationship with material properties.

Failure modes

The failure modes presented in Figure B. 8 shows considerable differences between 1M20 (Figure B. 8a) and 1M50 (Figure B. 8b). The fine mesh allows the capture of failure events that are not represented in 1M50, for example, the punching at the vicinity of the middle column. This is regard to the relation between tension behaviour of the material and the element size, as mentioned previously. When an element reaches the failure and posterior softening, the tension in other elements is attenuated, consequently the distance between nodes will affect how this attenuation and the softening occurs. Therefore, events occurring in one element are differently represented when a larger mesh is adopted. On the other hand, choosing a small mesh size results in a high computational and time demand. For that reason, it is recommended a calibration process to choose the proper mesh size.

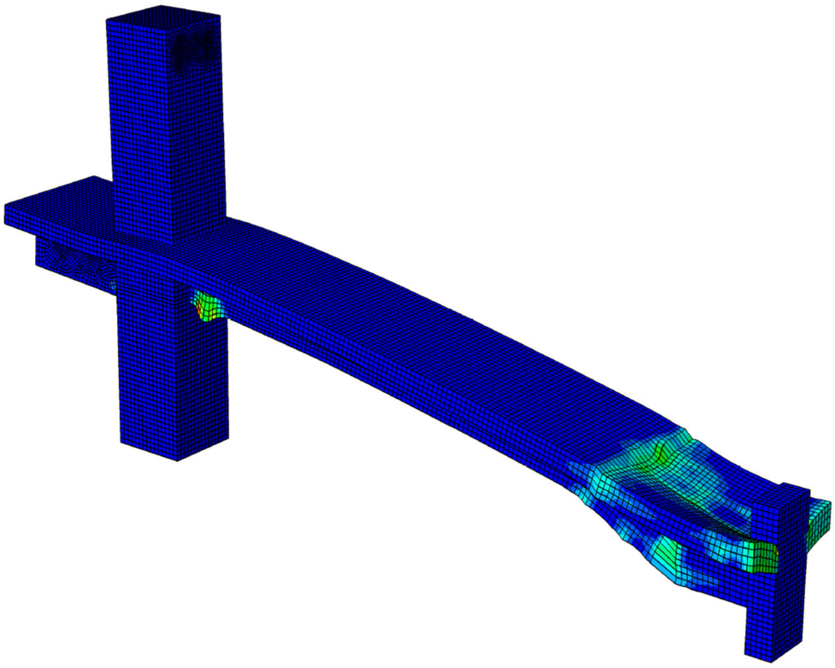

a)

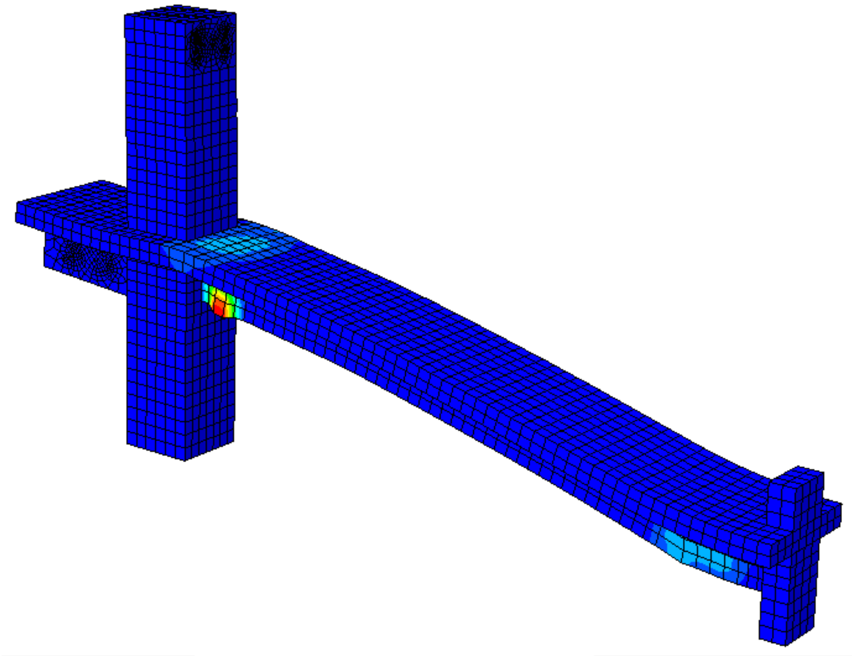

b)

Figure B. 8 - CON Failure modes of Serie M a) 1M20 b) 1M50.

B.2.3 Viscosity (Serie V)

The viscosity is a parameter to help the convergence process, changing the value of this parameter seek to study if a faster convergence would result in changes on the frame behaviour.

From the simulations, no significant computational time difference was observed for different viscosity parameter. Furthermore, Figure B. 9a with the vertical 'Load vs Deflection' curve and Figure B. 9(b)-(c) with the load cells readings demonstrate that no change occurred in any form when different values of viscosity are adopted. For that reason, no further discussion is necessary in this topic.

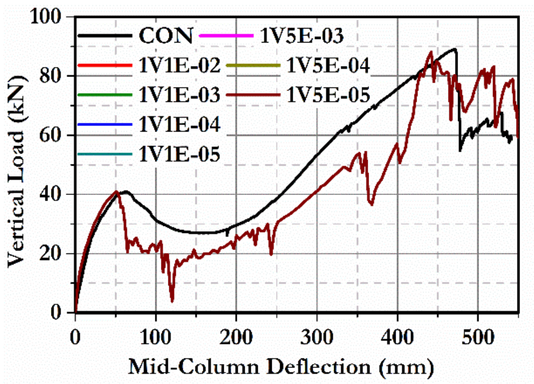

a)

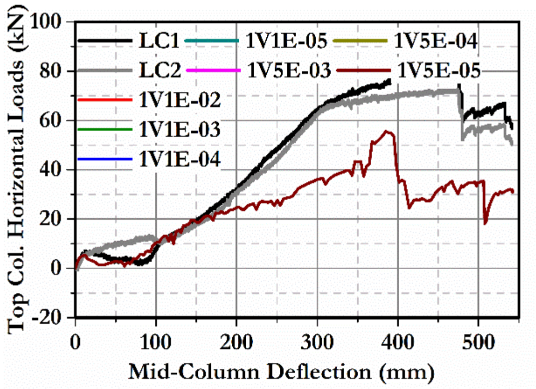

b)

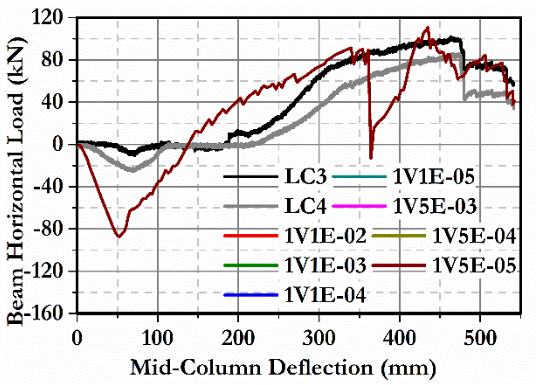

c)

Figure B. 9 – CON curves of Serie V a)'Mid-Column Deflection vs Vertical Load' b) LC1 and LC2 c) LC3 and LC4.

B.3 NSM_PR

B.3.1 Transmission Length (Serie L)

Vertical 'Force vs Deflection' Response

Figure B. 10 presents the influence of the transmission length on the vertical `Load vs Deflection` response of the frame. The major difference is observed during the initiation of the TCA. As mentioned before, the development of TCA is basically function of the internal reinforcement condition. Consequently, a bigger transmission length will better develop the TCA. However, major shear cracks formation in this specimen did not allow the full development of it. Therefore, sudden drop in the load can be observed.

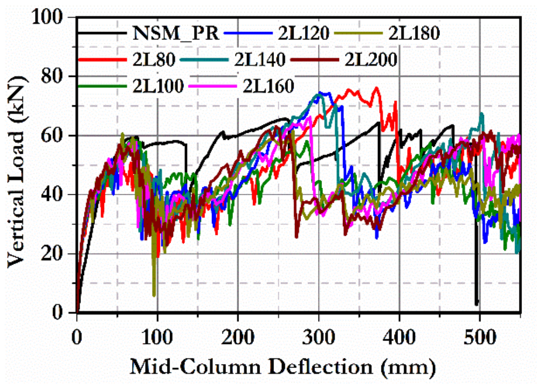

Figure B. 10 – NSM_PR 'Mid-Column Deflection vs Vertical Load' curves of Serie L.

Table B. 9 shows the values of loads and deflections for the three main points of the vertical `Load vs Deflection` curve. The minimum load achieved during CAA was in 2L80, where 50.8 kN was registered at 66.9 mm. The maximum load recorded at this stage was 60.6 kN in 2L180, at 56.5 mm. Those values in the original model (2L160) were 57.8 kN and 73.6 mm respectively. Comparing the loads in 2L80 with those from 2L160 and 2L180, the increment was of 14% and 19% respectively. Conversely, when the deflections at P_f in those specimens are compared, 2L180 presents the minimum value, while 2L160 presents the maximum. The mean value of P_{min} in this Serie was 67.6 kN, while during TCA was 58.2 kN.

Transm. Length	CAA		P_{MED}		TCA	
	Load (kN)	Deflection (mm)	Load (kN)	Deflection (mm)	Load (kN)	Deflection (mm)
2L80	50.8	66.9	76.2	371.7	60.1	513.4
2L100	58.3	73.6	58.1	285.1	57.4	438.2
2L120	56.7	73.6	74.4	301.4	51.9	463.4
2L140	56.2	73.6	73.8	301.4	67.5	501.6
2L160	57.8	73.6	66.2	289.3	60.3	548.0
2L180	60.6	56.5	61.6	268.1	48.7	457.7
2L200	56.9	52.6	63.1	247.0	61.6	513.4

Table B. 9 – NSM_PR key points of Serie L.

Load Cells Responses

As in all Series of NSM_PR the graphical presentation of the load cells readings shows only one side of the frame due the similarity of results. Figure B. 11 presents the load cells reading of Serie L. In (a) the top columns load cells responses are shown, and in (b) the responses of the beam load cells are depicted.

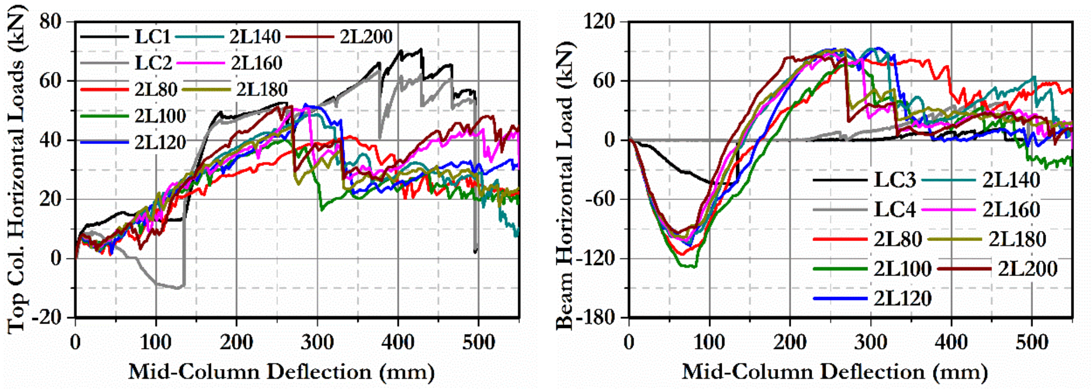

a) b)

Figure B. 11 – NSM_PR load cells responses on Serie L a) LC1 and LC2 b) LC3 and LC4.

Again, despite the difference of stiffness of the set-up between simulations and experiments, the response of vertical load with the deflection were increased. In Figure

B. 11 one can see that the load peaks on LC3 and LC4 at CAA are considerably higher than the experimental ones, what did not affect the values of P_f. Here, the influence of changes in the transmission length on the alternation between CAA and TCA is not clear (Figure B. 11b). However, models where the deflection correspondent to that change assume extreme values, demonstrate a higher difference, at least 60 mm.

Table B. 10 presents the values of the load cells readings during the CAA, where positive values represent tension acting on the load cell, while negative values mean compression. In early vertical deflections, the responses of LC1 and LC2 presented good agreement with the experimental correspondent outcome. As explained in the previous section, the comparison between values must to be performed with bigger values in a pair of load cells. Minimum value of load registered at the top load cells was 7.7 kN, in 2L80, while the maximum was 12.8 kN at 2L140 and 2L160. The maximum readings at the top load cells occurred in specimens with intermediary lengths of transmission. At LC3 and LC4 with the increment of L, the load transferred decreased. The maximum load recorded was 118.2 kN, in 2L80, being nearly 26% higher of the minimum, recorded in 2L200.

Specimen	**LC1 (kN)**	**LC2 (kN)**	**LC3 (kN)**	**LC4 (kN)**
NSM_PR	14.9	-10.1	-44.7	-1.0
2L80	7.7	5.1	-115.8	-118.2
2L100	8.7	9.2	-128.8	-130.6
2L120	12.3	10.3	-106.7	-106.2
2L140	12.8	-5.2	-104.5	-103.8
2L160	12.8	9.1	-102.0	-100.8
2L180	11.5	9.6	-98.5	-96.2
2L200	9.9	9.5	-93.7	-92.6

Table B. 10 – NSM_PR load cells responses of Serie L during CAA.

Maximum dynamic response and DIF

The pseudo-static curves of the frame for Serie L can be found in Figure B. 12. The development of those curves presents more variation during TCA. During CAA the curves evolved similarly in all specimens.

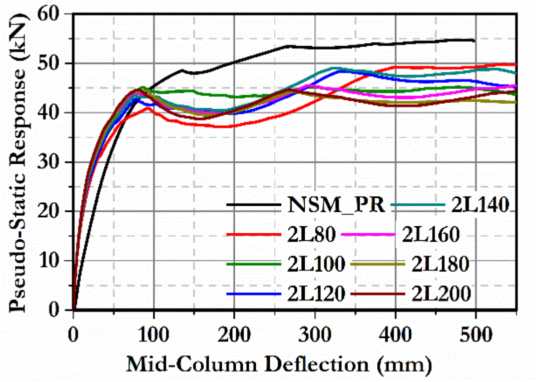

Figure B. 12 – NSM_PR Progressive collapse resistance of Serie L.

Values of maximum dynamic response and its deflections, as well as the DIF for the Serie L are presented in Table B. 11. The minimum value of maximum dynamic response is achieved in 2L80, while the other models presented similar results, around 44 kN. As in the previous Serie, the deflections presented irregular variation with different transmission lengths, going from 73.6 mm in 2L160 to 90.5 mm in 2L180. That is attributed to the oscillation in the load-deflection curves associated to the explicit method. For the same reason, the values of DIF oscillated from one model to the other around the mean 1.30, with a standard deviation of 0.03. Extreme models presented the same DIF, 1,28.

Specimen	Maximum Dynamic Response (kN)		Dynamic Increase Factor (DIF)
	Load (kN)	Deflection (mm)	
NSM_PR	48.5	135.4	1.23
2L80	39.8	78.3	1.28
2L100	45.2	85.5	1.29
2L120	42.8	78.3	1.33
2L140	43.5	75.9	1.29
2L160	44.1	73.6	1.31
2L180	44.4	90.5	1.36
2L200	44.6	80.7	1.28

Table B. 11 – NSM_PR Dynamic response of Serie L.

Ductility ratio

All simulations presented ductility ratios above the achieved in the original model (Table B. 12), 2L160. Apart from 2L180, lower values of ductility were achieved in models with larger transmission lengths. The highest difference between ratios was 24%. The mean value and standard deviation for the ductility ratios are 6.10 and 0.41 respectively.

Specimen	Ductility ratio ($\Delta_{failure}/\Delta_{yield}$)
NSM_PR	2.75
2L80	6.43
2L100	6.22
2L120	5.90
2L140	5.74
2L160	5.54
2L180	6.87
2L200	5.98

Table B. 12 – NSM_PR Ductility ratios of Serie L.

Failure modes

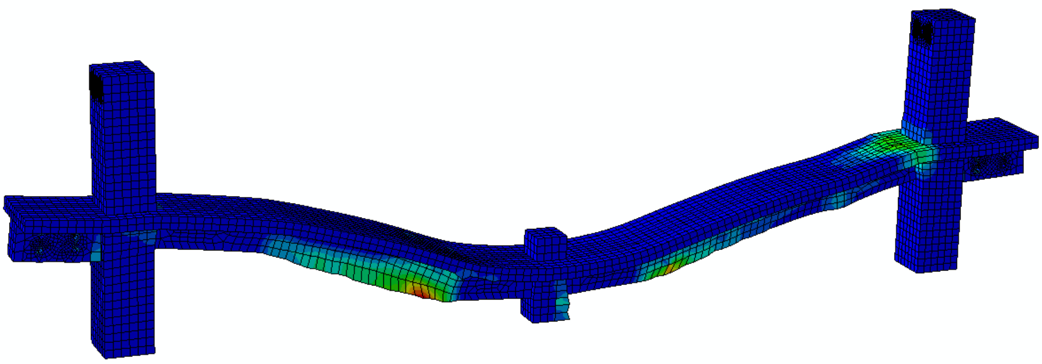

a)

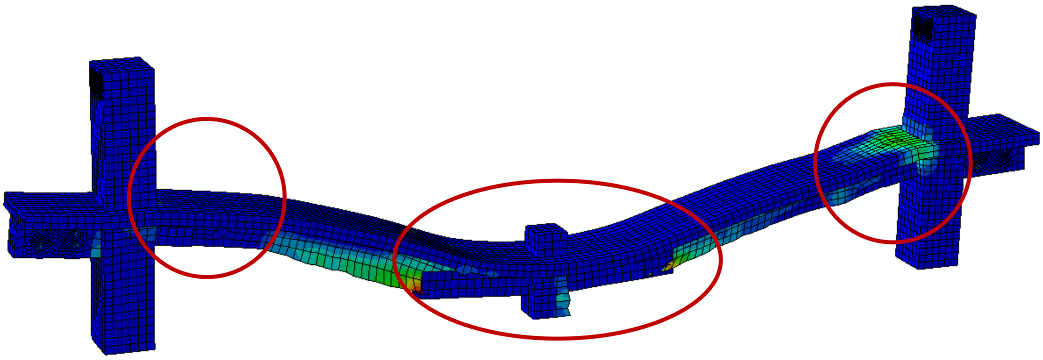

b)

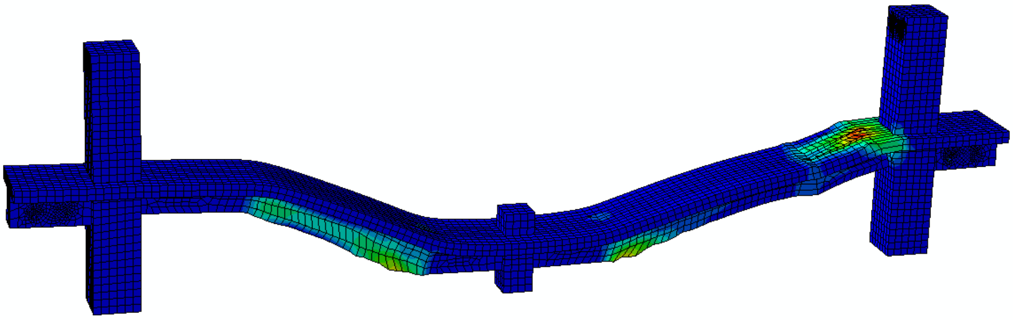

c)

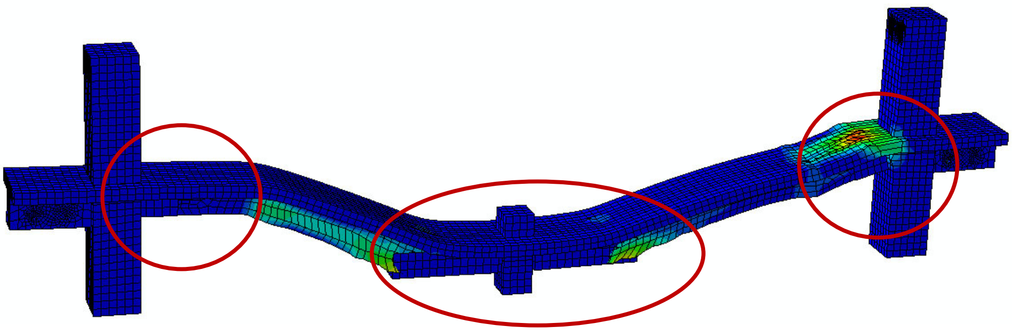

d)

Figure B. 13 – NSM_PR Failure modes of Serie L a) 2L80 b) 2L200.

Figure B. 13 shows the failure modes of the two extreme specimens of Serie L, 2L80 and 2L200. In Figure B. 13a one can find the representation of the plasticity in the concrete of 2L80, while in (b) this same model is shown, however with the TRM represented. Figure B. 13(c)-(d) follow the same criteria, but for the model 2L200.

On the partially strengthened specimen the modification of the transmission length of the steel did not change the failure mode so drastically as in the previous sections. Instead, excluding small localized failures (explained following), the main failures remained the same, occurring at the same sections, however with different intensities. In both extreme models, the TRM close to the middle column was in part detached from the concrete; this part was the non-anchored portion of the TRM. At the side joints, the confinement provided by the TRM contained the concrete crush in this region during CAA; therefore, concrete crush was observed in the adjacent non-strengthened sections in both specimens. In 2L80, the small localized failures, referred previously, incorporate the yield of the steel outside the left side column, plasticity at the beam/column interface at the middle column, and cracks at the side columns. In 2L200, those were the plasticity at the top of the slab and small cracks along the frame. In both specimens the TRM presented plasticity during the failure events.

B.3.2 Mesh Size (Serie M)

Vertical 'Force vs Deflection' Response

When the mesh size is changed in the partially strengthened specimen, the TCA phase is affected as well as the vertical deflection in which the failure occurs. Figure B. 14 presents all the vertical `Load vs Deflection` responses of Serie M. As in CON, changing the mesh size affects the ratio between the softening bandwidth to the elastic unloading zone causing differences on the curves.

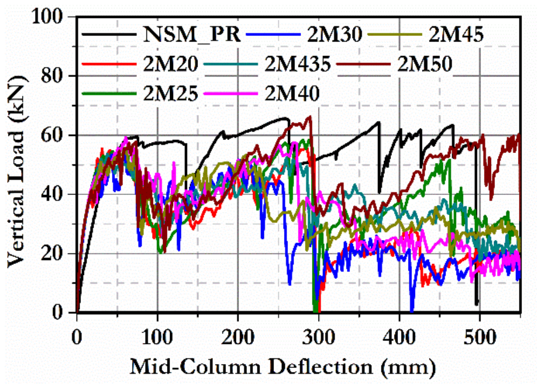

Figure B. 14 – NSM_PR 'Mid-Column Deflection vs Vertical Load' curves of Serie M.

Table B. 13 presents the values of the three key points of all specimens in this Serie. The discrepancy of the loads between models during CAA is small, with the maximum value being 59.3 kN, in 2M40, and the minimum being 54 kN, in 2M30, i.e., 10%. This, however, was not the case for the deflections at the CAA stage, where the difference between maximum and minimum values was 135%. 2M20 presented the smallest deflection at which P_f occurred and 2M50 the largest. Therefore, as explained in previous sections, changes in the mesh imply in changes in the frame behaviour; therefore, the mesh must to be adequate to the model studied and must to be calibrated properly. Values of peak loads, P_{med}, also presented small discrepancy around the mean, while during TCA the difference was bigger.

Mesh Size	CAA		P_{med}		TCA	
	Load (kN)	Deflection (mm)	Load (kN)	Deflection (mm)	Load (kN)	Deflection (mm)
2M20	55.5	31.3	55.6	285.4	29.3	415.7
2M25	56.0	54.5	58.4	280.4	51.7	462.1
2M30	54.0	58.5	51.7	199.9	21.7	530.9
2M35	53.7	37.8	52.3	259.7	38.3	454.5
2M40	59.3	60.6	57.5	268.2	27.8	428.4
2M45	55.8	60.6	53.2	209.9	35.6	444.7
2M50	57.8	73.6	66.2	289.3	60.3	548.0

Table B. 13 – NSM_PR key points of Serie M.

Load Cells Responses

Responses of the load cells presented good agreement between the simulations in Serie M. Figure B. 15 presents the responses of the top columns load cells, LC1 and LC2 (Figure B. 15a), as well as those from the load cells at the beam level, LC3 and LC4 (Figure B. 15b). LC1 and LC2 showed tension during all the vertical deflection, while LC3 and LC4 alternated between compression, during CAA, and tension during TCA. The transition between CAA and TCA in all specimens occurred at similar vertical deflections.

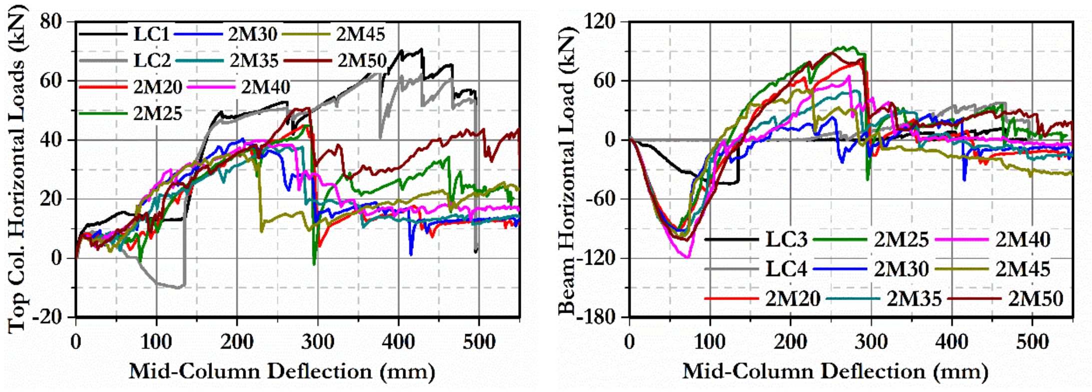

a) b)

Figure B. 15 – NSM_PR load cells responses on Serie M a) LC1 and LC2 b) LC3 and LC4.

Specimen	LC1 (kN)	LC2 (kN)	LC3 (kN)	LC4 (kN)
NSM_PR	14.9	-10.1	-44.7	-1.0
2M20	8.2	8.8	-91.4	-93.6
2M25	7.6	6.1	-91.5	-90.7
2M30	9.7	8.1	-91.8	-100.0
2M35	4.4	8.2	-98.9	-101.3
2M40	12.6	7.9	-119.3	-119.4
2M45	8.3	4.1	-99.0	-102.9
2M50	12.8	9.1	-102.0	-100.8

Table B. 14 – NSM_PR load cells responses of Serie M during CAA.

Table B. 14 shows the readings of the load cells of the Serie M at the peak load, P_f. It is important to remember that negative values represent compression, while positive represent tension. The responses of load Cells LC1 and LC2 show distinct values for different mesh sizes, with an irregular variation, presenting a mean of 9.7 kN and a standard deviation of 2 kN. Again, here the values compared will be the highest between pairs of load cells. Therefore, the maximum registered at LC1-LC2 was 12.8 kN, in 2M50, while the minimum was 7.6 kN, in 2M45; in other words, 68% of difference. The difference at the load cells LC3 and LC4 presented smaller proportion, where 2M40 had 119.4 kN, and 2M25 had 91.5 kN, representing 30%.

Maximum dynamic response and DIF

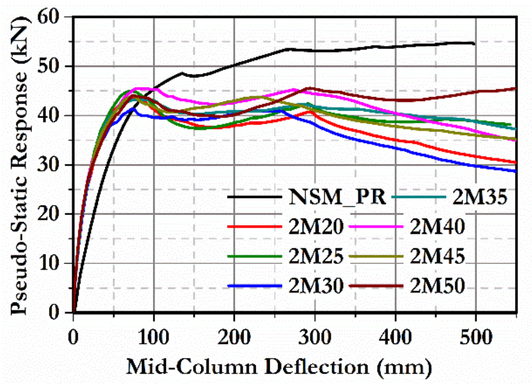

Figure B. 16 – NSM_PR Pseudo-static response of Serie M.

Specimen	Maximum Dynamic Response (kN)		Dynamic Increase Factor (DIF)
	Load (kN)	Deflection (mm)	
NSM_PR	48.5	135.4	1.23
2M20	43.6	73.6	1.27
2M25	44.9	72.5	1.25
2M30	41.4	73.6	1.31
2M35	43.2	83.0	1.24
2M40	45.4	80.7	1.30
2M45	44.1	73.6	1.27
2M50	44.1	73.6	1.31

Table B. 15 – NSM_PR Dynamic response of Serie M.

Figure B. 16 presents the pseudo-static responses of the simulations of Serie M. As observed in the vertical `Load vs Deflection` curve, the part of the curve most affected is that regard to the TCA. Table B. 15 present the values of maximum dynamic responses and its deflections, as well as DIF for the first load peak P_f. The divergence between values was small, as expected due the behaviour of the resistant load at CAA in Table B. 13 – NSM_PR key points of Serie M.

The maximum load registered was in 2M40, where the maximum dynamic response was 45.4 kN, while the minimum was 41.4 kN, in 2M30, being 9% smaller. The difference between deflections outcomes reached 14.4%. The DIF varied in an irregular form with 1.28 as mean value and 0.03 as standard deviation. The difference between extreme values was 6%.

Ductility ratio

In Serie M all simulations presented lower values of ductility ratio than that from the original model (Table B. 16). It emphasizes the importance of the proper calibration of the simulation with trustable results. Between maximum and minimum ratios, the difference was nearly 43% in this Serie, the mean was 4.89 and the standard deviation 0.54.

Specimen	Ductility ratio ($\Delta_{failure}/\Delta_{yield}$)
NSM_PR	2.75
2M20	4.42
2M25	3.88
2M30	4.97
2M35	4.86
2M40	5.35
2M45	5.23
2M50	5.54

Table B. 16 – NSM_PR Ductility ratios of Serie M.

Failure modes

Figure B. 17 shows the failure modes of the two extreme specimens of Serie M, 2M20 and 2M50. The first is presented in (a) and (b), while the second is shown in (c)-(d). In both models the concrete plasticity is presented, however Figure B. 17(b)-(d) show that configuration with the presence of TRM for each model.

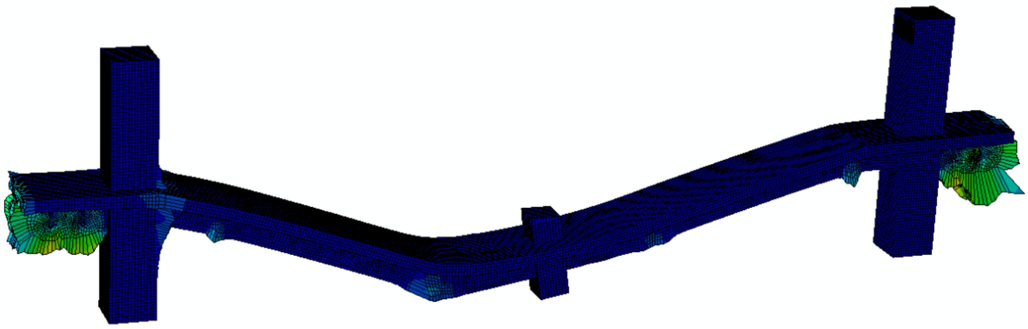

a)

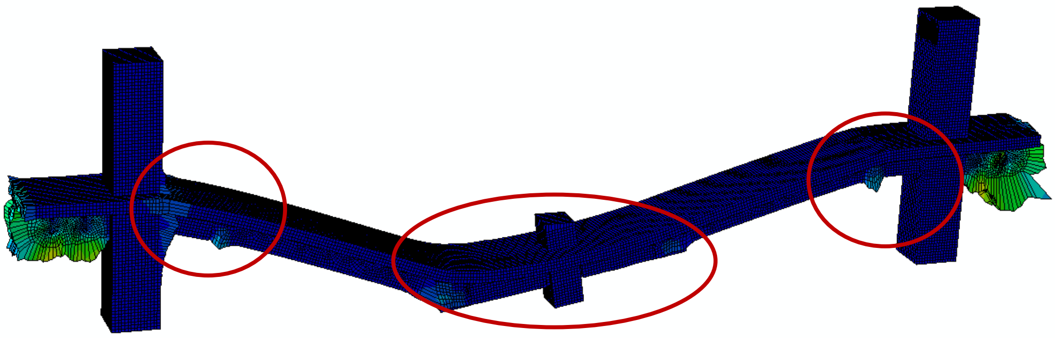

b)

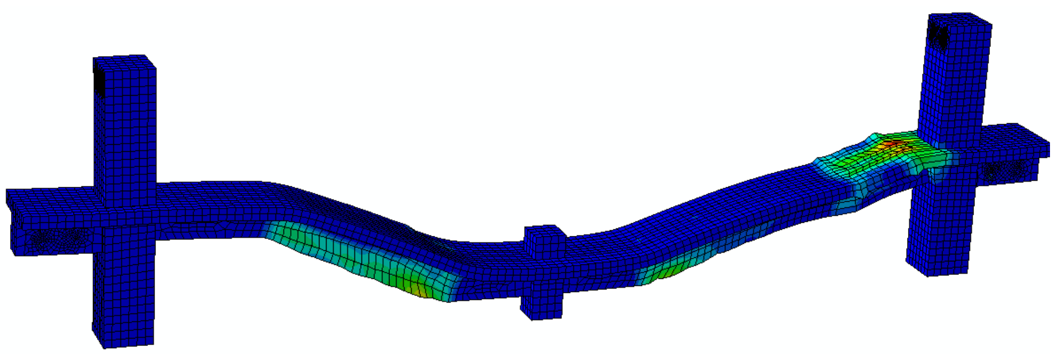

c)

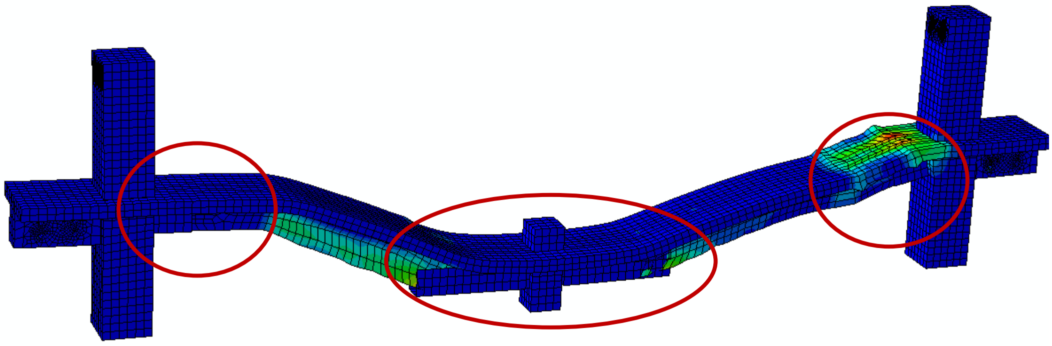

d)

Figure B. 17 – NSM_PR Failure modes of Serie M a) 2M20 b) 2M50.

As observed in CON, Serie M, the failure mode is changed considerably from the model with 20mm to that on with 50 mm of mesh size. The same happened here, however the larger mesh resulted in a more representative model than that with a fine mesh. In 2M20, one of the main failures occurred at an atypical region: that where the concrete is connected with the set-up at the beam level. This `failure` occurred due the small mesh size in that area, in some cases smaller than 20 mm. The differences on the material behaviour associated to difference mesh sizes, mentioned in the previous sections, were expressed here in the region of transference of load. Apart of that, the specimens 2M20 showed also failures of concrete crushing at the bottom of the beam, after the TRM at the side joints, due CAA. Moreover, the TRM was not detached from the concrete in this model, what caused the failure to occur in the non-strengthened region and at the beam/column interface, with rupture of the reinforcement steel. The failure of 2M50 is that of the calibration model in this specimen. It reproduced the failure of the experiment in many details, as at side joints, the TRM detachment, cracks formations, and asymmetrical shear failures.

B.3.3 Viscosity (Serie V)

In this specimen the viscosity did not present influence on the frame behaviour as well. Yet, the vertical load-deflection response (Figure B. 18a) and load cells readings (Figure B. 18(b)-(c)) are presented to confirm.

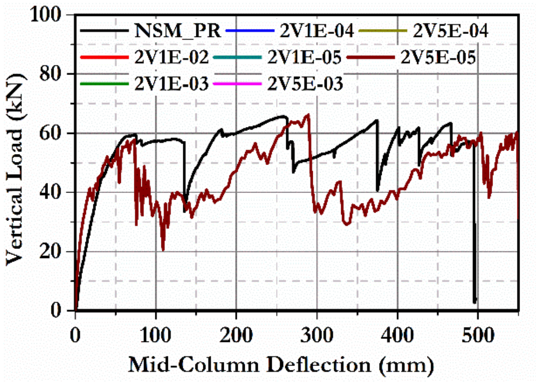

a)

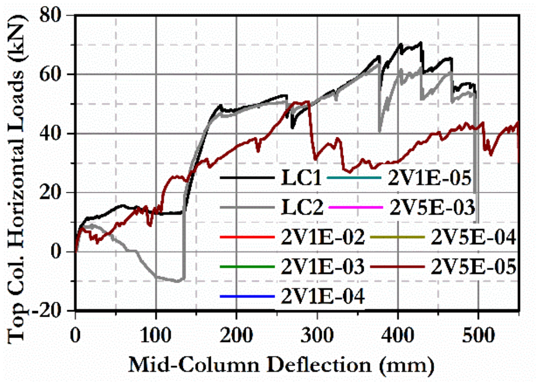

b)

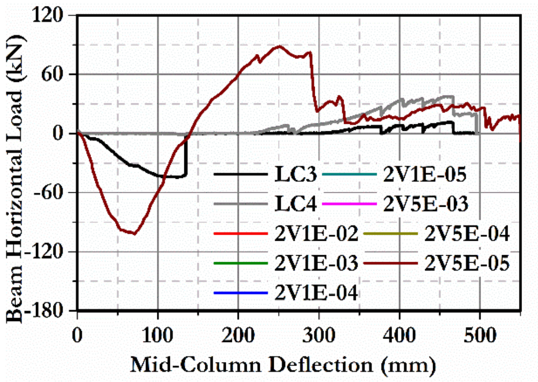

c)

Figure B. 18 – NSM_PR curves of Serie V a)'Mid-Column Deflection vs Vertical Load' b) LC1 and LC2 c) LC3 and LC4.

B.4 TRM_TR

B.4.1 Transmission Length (Serie L)

Vertical 'Force vs Deflection' Response

The vertical load-deflection curve of Serie L of the TRM_TR specimen is presented in Figure B. 19. Once more, the behaviour of the models can be compared up to a certain vertical deflection; in the previous Serie it was 147 mm, here it is 167 mm. Table B. 17 show the values of loads and deflection of Serie L. One can observe the small variation of the loads during CAA, which has 65.5 kN as mean value. The highest value of resistant load during CAA, 68.5 kN, was achieved in the specimen with highest value of transmission length, while the lowest, 62.6 kN, was achieved in 3L80, representing nearly 9% of difference. The deflections had a larger variation around the mean, 71.5 mm, where the minimum was 67.7 mm, achieved in two specimens, 3L100 and 3L160 mm, and the maximum, occurring in 3L200, was 77.4 mm, being therefore 14 % different.

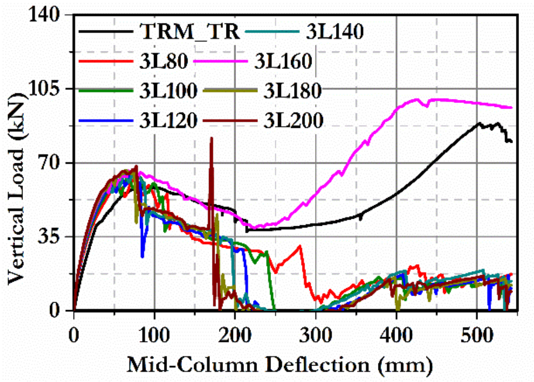

Figure B. 19 – TRM_TR 'Mid-Column Deflection vs Vertical Load' curves of Serie L.

Transm. Length	CAA		P_{min}		TCA	
	Load (kN)	Deflection (mm)	Load (kN)	Deflection (mm)	Load (kN)	Deflection (mm)
3L80	62.6	74.9	-	-	-	-
3L100	64.1	67.7	-	-	-	-
3L120	65.3	72.5	-	-	-	-
3L140	65.7	74.9	-	-	-	-
3L160	66.1	67.7	39.1	224.4	99.9	451.7
3L180	66.3	65.4	-	-	-	-
3L200	68.5	77.4	-	-	-	-

Table B. 17 – TRM_TR key points of Serie L.

Load Cells Responses

The load cells responses of this Serie can be visualized in Figure B. 20. In (a), the readings of load cells LC1 and LC2 are shown, and in (b) LC3 and LC4. The simulations in this Serie presented similar evolution for the top load cells, while at the beam level, a small increment of the transferred load can be seen. Again, here the transition between CAA and TCA could not be observed.

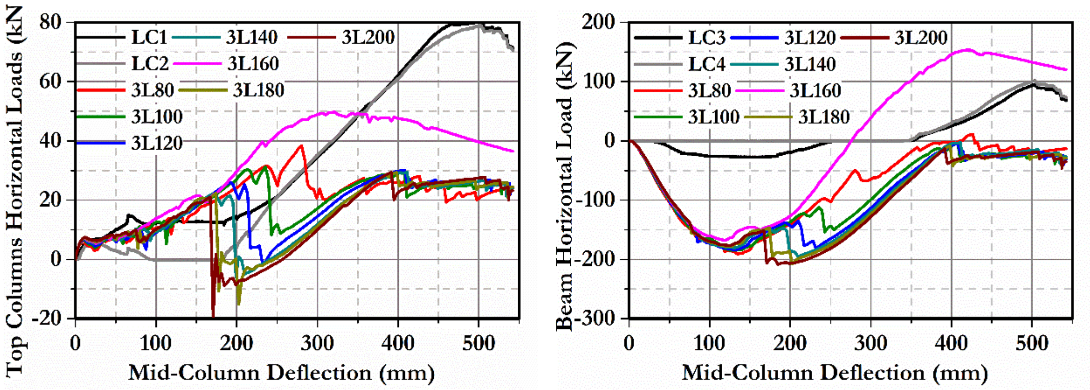

a) b)

Figure B. 20 – TRM_TR load cells responses on Serie L a) LC1 and LC2 b) LC3 and LC4.

Specimen	LC1 - LC2 (kN)	LC3 - LC4 (kN)
TRM_TR	12.6	-27.2
3L80	12.4	-191.0
3L100	13.8	-184.7
3L120	14.1	-183.4
3L140	14.9	-180.3
3L160	16.5	-167.7
3L180	14.4	-178.1
3L200	14.3	-176.7

Table B. 18 – TRM_TR load cells responses of Serie L during CAA.

Table B. 18 shows the values of load acting on the load cells at the vertical deflection of maximum CAA response. Varying the transmission length represented a maximum variation of 33% on the load transferred at the top of the side columns. The maximum value occurred in 3L160 and the more distant the transmission length got from 160 mm the lower was the value of load transferred at the top of side columns. At the beam level this relation was different, more regular, in general the values of transferred load increased for lower values of transmission length, as in the previous specimens. If the extreme value in 3L160 is not considered, the maximum difference of loads, 8%, occurred between 3L80 and 3L200. Considering the value in 3L160, this difference goes up to 14%.

Maximum dynamic response and DIF

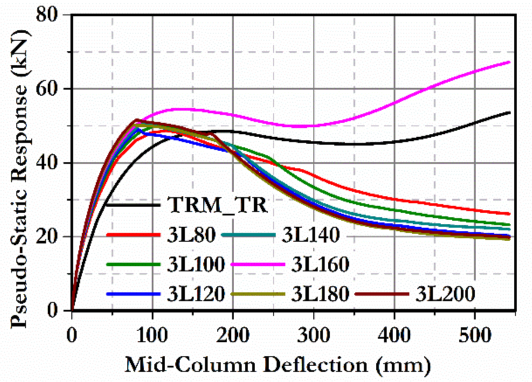

Figure B. 21 – TRM_TR Pseudo-static response of Serie L.

Specimen	Maximum Dynamic Response (kN)		Dynamic Increase Factor (DIF)
	Load (kN)	Deflection (mm)	
TRM_TR	48.5	183.9	1.20
3L80	45.7	79.9	1.31
3L100	47.4	109.8	1.30
3L120	54.5	82.4	1.21
3L140	53.9	90.3	1.30
3L160	55.8	131.1	1.31
3L180	58.4	77.4	1.31
3L200	60.0	79.9	1.33

Table B. 19 – TRM_TR Dynamic response of Serie L.

The evolution of the resistant load with the vertical deflection in a dynamic scenario can be seen in Figure B. 21. Table B. 19 presents the values of maximum dynamic responses, deflections at MDR, as well as the correspondent DIFs. The maximum dynamic response increases with the increment of transmission length, confirming that a better tied steel will disperse more energy inside the concrete. Due the sensibility of the model, values of deflection were in general lower than that from the original model, reaching 69% of difference. Demonstrating a proportionality of the dispersed energy, the DIFs remained, in general, around the same values for all models. Amongst the simulations of this Serie, the difference between higher and lower maximum dynamic responses was 33%, achieved in 3L200 and 3L80 respectively.

Ductility ratio

Specimen	Ductility ratio ($\Delta_{failure}/\Delta_{yield}$)
TRM_TR	3.57
3L80	2.82
3L100	3.77
3L120	2.93
3L140	3.30
3L160	4.30
3L180	2.66
3L200	2.87

Table B. 20 – TRM_TR Ductility ratios of Serie L.

In Serie L, the simulations presented lower ductility ratios than the original model, 3L160, where the variation of the ratio was not so evident as in the Serie L of previous specimens (Table B. 20). Here, values of ductility ratio varied around 3.23 and the standard deviation was 0.55. The maximum value in 3L160 was 62% higher than the lowest in 3L180. It highlights the sensibility of this model, where extreme values of indicators of ductility could be found changing 20 mm on the transmission length.

Failure modes

Figure B. 22 shows the failure modes of the specimens studied with extreme values of transmission length, 3L80 and 3L200. In earlier vertical deflections, the flexural anchors help to avoid major crack formation and propagation, keeping, therefore, the integrity of the frame in the middle join.

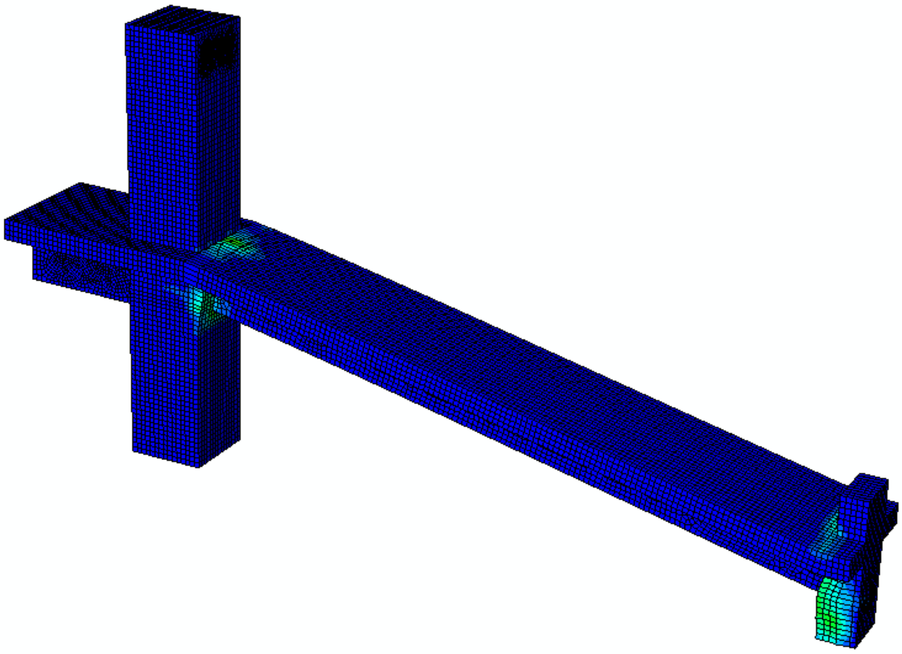

a)

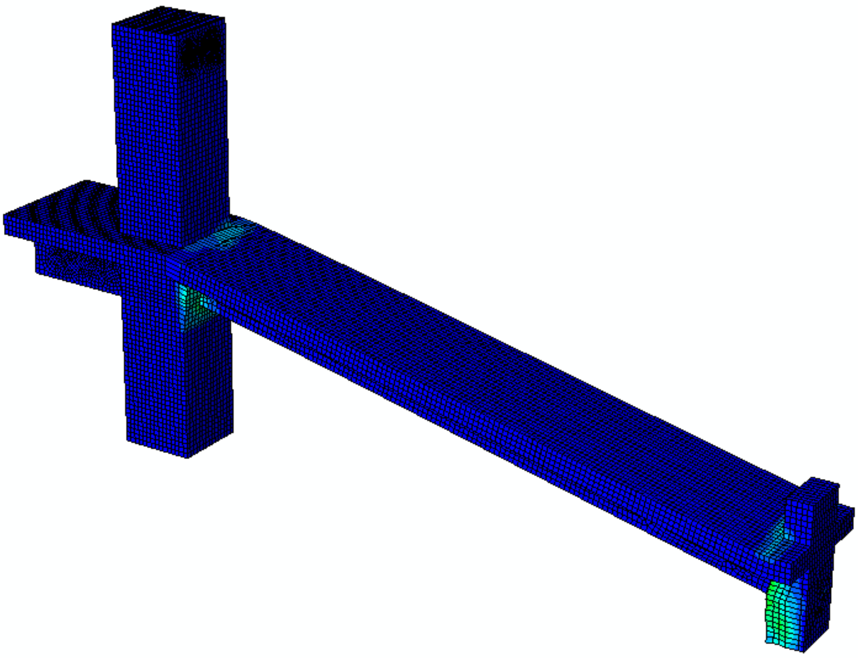

b)

Figure B. 22 – TRM_TR Failure modes of Serie L a) 3L80 b) 3L200.

Moreover, the confined concrete at the side joints does not fail due the high compression in the area. In parallel the TRM prevent shear crack to develop and evolve along the beam. Therefore, the failure mode does not change significantly. The failure is localized at the beam/column interfaces, where the steel is lead to rupture and/or the concrete is pulled out from the column. The TRM experiences cracks along its length, but not in the fibres, only in the mortar.

B.4.2 Mesh Size (Serie M)

Vertical 'Force vs Deflection' Response

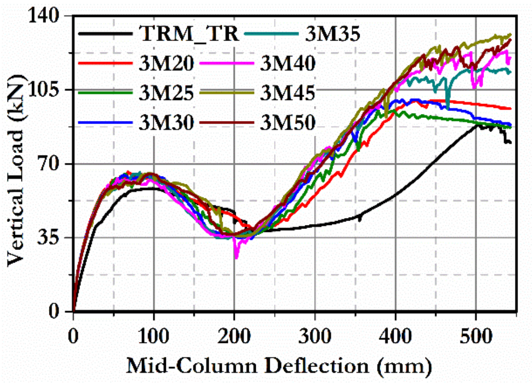

Figure B. 23 – TRM_TR 'Mid-Column Deflection vs Vertical Load' curves of Serie M.

Mesh Size	CAA		P_{min}		TCA	
	Load (kN)	Deflection (mm)	Load (kN)	Deflection (mm)	Load (kN)	Deflection (mm)
3M20	66.1	67.7	39.1	224.4	99.9	451.7
3M25	65.1	63.2	36.0	202.5	95.3	378.2
3M30	64.6	95.7	34.4	220.7	100.3	407.8
3M35	65.9	82.4	34.7	191.7	115.0	513.9
3M40	63.1	54.5	32.2	206.1	123.4	537.9
3M45	65.3	95.7	35.6	209.7	131.1	542.0
3M50	65.2	98.4	36.6	198.9	128.6	542.0

Table B. 21 – TRM_TR key points of Serie M.

Figure B. 23 presents the vertical 'Load vs Deflection' curves for all models in Serie M. The simulations in this Serie had the best fit to the experimental curve. The evolution of the resistant load with the vertical deflection was similar in all specimens up to P_f; differences can be observed from this point onward.

Table B. 21 presents the values of the three key points for the simulations of Serie M. Confirming the stated before, no significant change can be observed in the peak load at CAA when the mesh size is changed. From the maximum to the minimum load between simulations at this stage, the difference is 5%, however major changes are observed in the deflections that it occurs, 81%. It can be explained by the oscillation that occurs in the curve due the speed of convergence adopted, if a lower value of target increment time was chosen less oscillation would be observed. Nevertheless, the time demanded to process this model would increase in a disproportional and undesired way. Values of P_{min} changed in 21%, with the lowest in intermediary models, and P_{TCA} values increased in 38% with the increment of mesh size.

Load Cells Responses

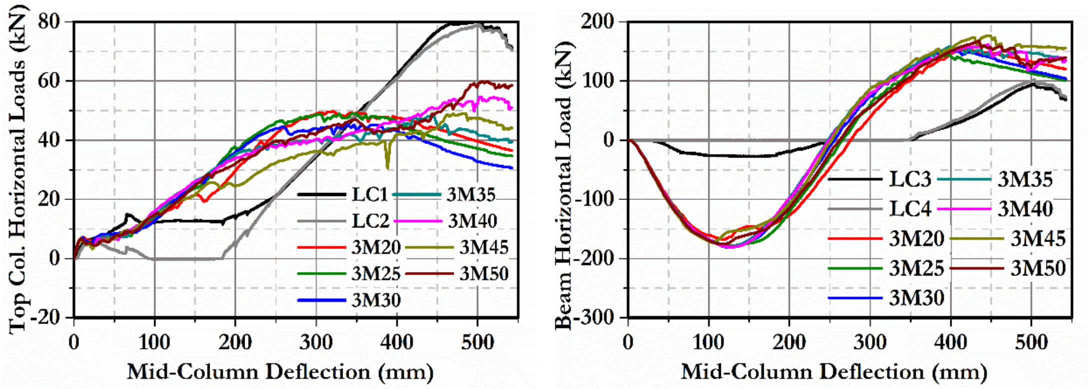

a) b)

Figure B. 24 – TRM_TR load cells responses on Serie M a) LC1 and LC2 b) LC3 and LC4.

On the load cells responses, the similarity of models can also be visualized in early vertical deflections, and major differences occured during TCA. Figure B. 24a presents the curve of transferred loads at the top load cells vs the vertical deflection of the middle column. Similarly, Figure B. 24b shows the readings of LC3 and LC4 with the vertical deflections of the middle column. Here, it can be seen that changing the mesh size does not imply in a considerable change in the deflection where CAA is fully developed and TCA takes place.

Table B. 22 shows the load cells responses when the load peak at CAA is achieved. The major difference at the top load cells was 43%, where the maximum was achieved in 3M35 and the minimum in 3M45. The former had 33% more load than the original model 3M20, at the top load cells, while the later had 7% less. At the beam load cells, the maximum difference between readings was 8%, where 3M30 presented the highest value and 3M20 the lowest. Therefore, changes in the mesh size in NSM_PR affected more the columns and its transference of loads to the adjacent elements.

Specimen	LC1 - LC2 (kN)	LC3 - LC4 (kN)
TRM_TR	12.6	-27.2
3M20	16.5	-167.7
3M25	19.2	-178.2
3M30	19.8	-180.9
3M35	21.9	-179.7
3M40	21.6	-180.6
3M45	15.3	-173.0
3M50	16.6	-175.2

Table B. 22 – TRM_TR load cells responses of Serie M during CAA.

Maximum dynamic response and DIF

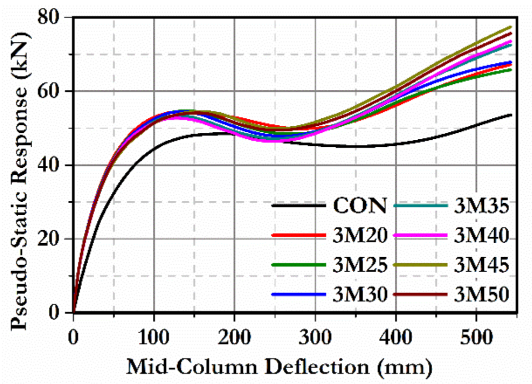

Figure B. 25 – TRM_TR Pseudo-static response of Serie M.

The dynamic response of the frame studied in TRM_TR for different values of mesh size can be seen in Figure B. 25. As it occurred in the load-deflection curve, here the similarity of the dynamic curves is evident up to the peak, after which those start to differ. Table B. 23 presents the values of maximum dynamic response and associated deflections of the simulations for the first load peak P_f, as well as the correspondent DIF. Again, the difference was small compared with other Series, the major difference between of the maximum dynamic response models was 4%, while on the DIF this value was 3%. Values of deflections were constant, having only one model with distinct value.

Specimen	Maximum Dynamic Response (kN)		Dynamic Increase Factor (DIF)
	Load (kN)	Deflection (mm)	
TRM_TR	48.5	183.9	1.20
3M20	54.5	131.1	1.21
3M25	54.6	131.1	1.19
3M30	54.4	131.1	1.19
3M35	53.5	131.1	1.23
3M40	52.7	127.9	1.20
3M45	53.8	131.1	1.21
3M50	53.7	131.1	1.21

Table B. 23 – TRM_TR Dynamic response of Serie M.

Ductility ratio

Specimen	Ductility ratio ($\Delta_{failure}/\Delta_{yield}$)
TRM_TR	3.57
3M20	4.30
3M25	4.38
3M30	4.38
3M35	4.37
3M40	4.12
3M45	4.48
3M50	4.45

Table B. 24 – TRM_TR Ductility ratios of Serie M.

The effect of changing the mesh size is less observed in this specimen. Table B. 24 presents the ductility ratios of Serie M, where only one specimen presented smaller value than the original model, 3M20. The mean and standard deviation in this Serie were 4.35 and 0.11 respectively. The difference between maximum and minimum reached only 2% in those simulations.

Failure modes

Figure B. 26 shows the failure modes of the two extreme models studied in this Serie, 3M20 (a) and 3M50 (b). One can observe that, again, no significant change occurred from one specimen to the other, although, as mentioned before, there are changes when the mesh is modified. As in the previous sections, due the enhanced stiffness of the beam provided by the strengthening, the failures are concentrated in weaker sections, namely the beam/columns interfaces.

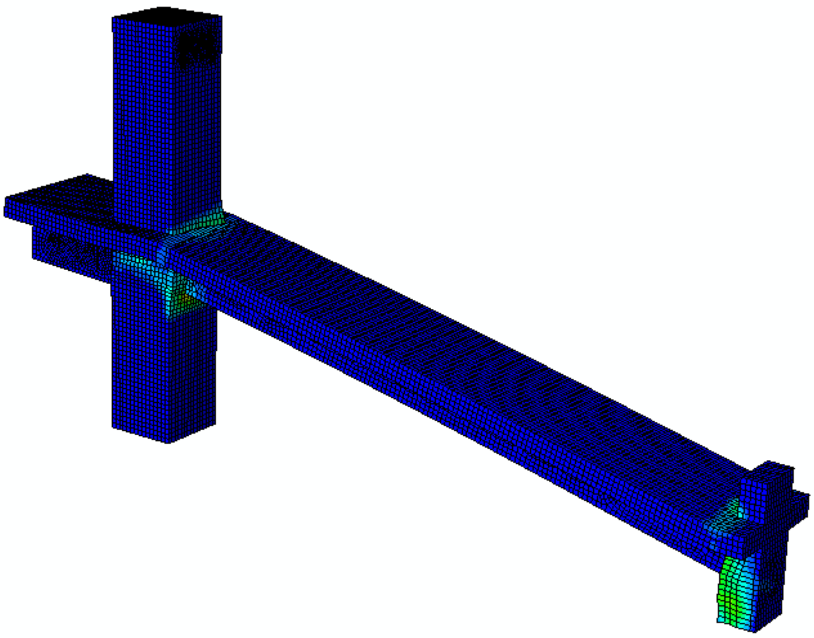

a)

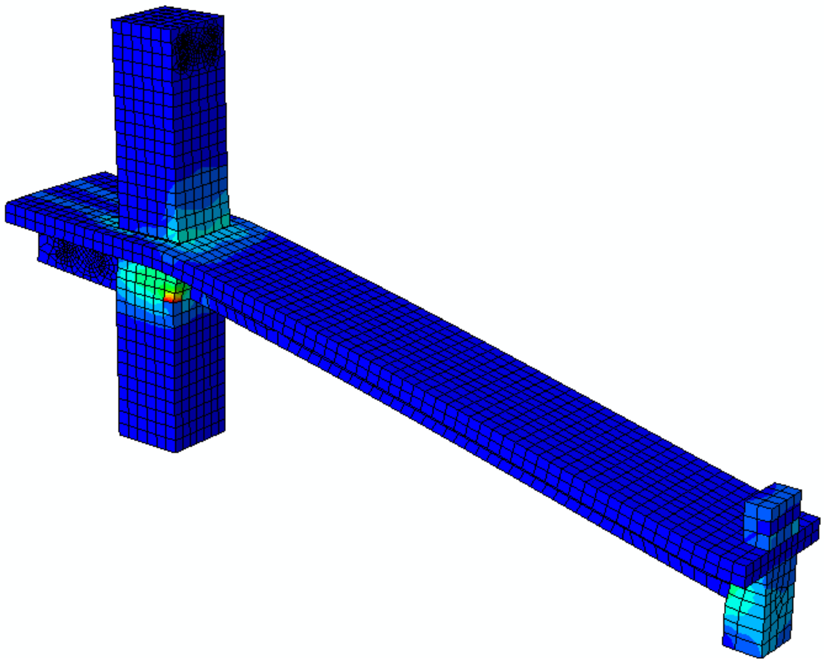

b)

Figure B. 26 – TRM_TR Failure modes of Serie M a) 3M20 b) 3M50.

B.4.3 Viscosity (Serie V)

Here, the parameter viscosity did not cause any change on the frame behaviour, as in the previous specimens. That can be observed in the load-deflection curve (Figure B. 27a), as well as the top (Figure B. 27b) and the beam (Figure B. 27c) load cells curves.

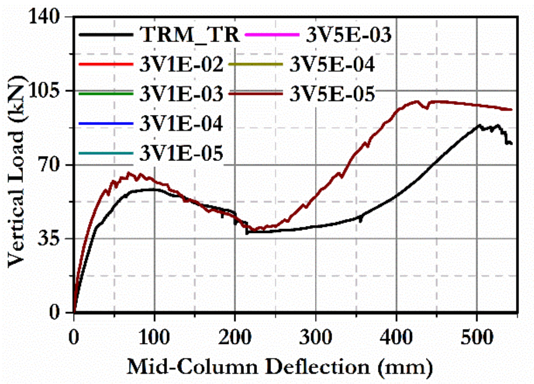

a)

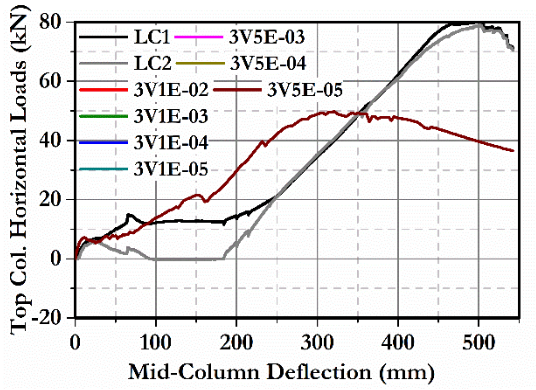

b)

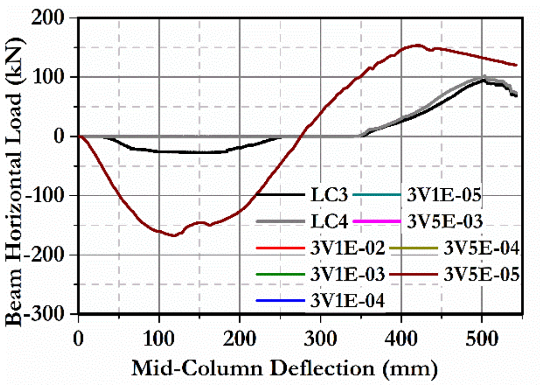

c)

Figure B. 27 – TRM_TR curves of Serie V a)'Mid-Column Deflection vs Vertical Load' b) LC1 and LC2 c) LC3 and LC4.

B.5 NSM_TR

B.5.1 Transmission Length (Serie L)

Vertical 'Force vs Deflection' Response

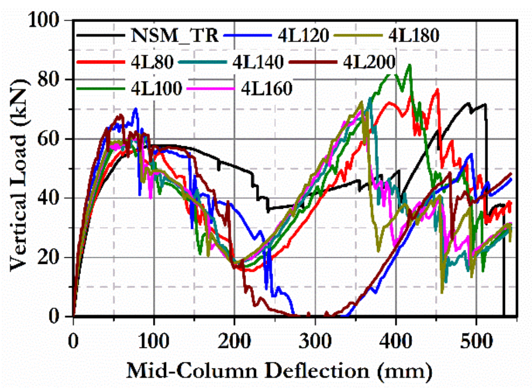

Figure B. 28 – NSM_TR 'Mid-Column Deflection vs Vertical Load' curves of Serie L.

The vertical 'Load vs Deflection' curve of Serie L is presented in Figure B. 28. The alteration of the transmission length presented influence on the development of the curve from the beginning of the simulation up to the end of the TCA phase.

Table B. 25 present the values of load and deflections for the three key points of the load-deflection curve for the simulations of Serie L. The peak load at CAA, P_f, is increased with the increment of transmission length, while the correspondent deflection did not follow the same evolution. The maximum value achieved of P_f was 68.1 kN, in 4L200, which was 21% higher of the minimum, 56.2 kN, achieved in 4L80. The deflections at P_f reached its maximum value, 85.0 mm, in 4L160, nearly 45% higher than the 58.8 mm achieved in 4L200, and 25% higher than that from 4L80.

Transm. Length	CAA		P_{MIN}		TCA	
	Load (kN)	Deflection (mm)	Load (kN)	Deflection (mm)	Load (kN)	Deflection (mm)
4L80	56.2	67.7	15.6	220.7	76.8	451.7
4L100	59.4	63.2	16.9	213.4	84.9	417.2
4L120	65.6	67.7	0.0	300.0	54.8	493.5
4L140	60.3	74.9	18.3	202.5	73.7	367.9
4L160	61.0	85.0	17.9	198.9	69.3	357.4
4L180	61.6	79.9	18.1	198.9	72.4	357.4
4L200	68.1	58.8	0.0	300.0	48.6	467.1

Table B. 25 – NSM_TR key points of Serie L.

Load Cells Responses

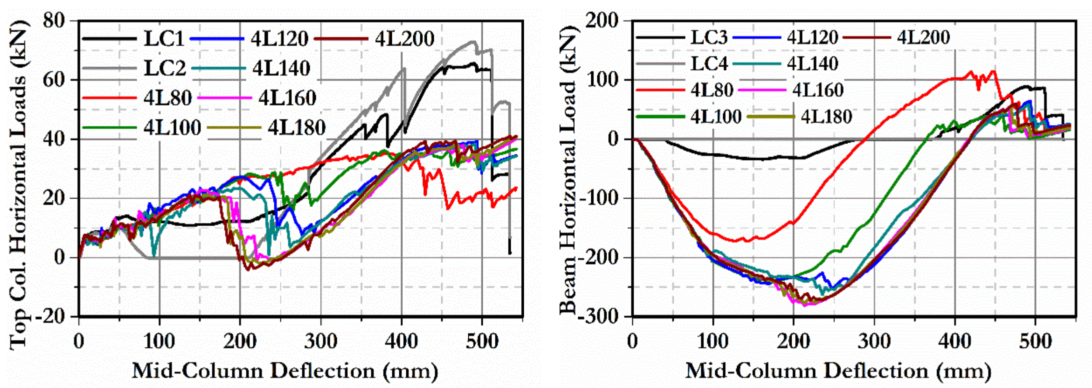

a) b)

Figure B. 29 – NSM_TR load cells responses on Serie L a) LC1 and LC2 b) LC3 and LC4.

Specimen	LC1 (kN)	LC2 (kN)	LC3 (kN)	LC4 (kN)
NSM_TR	11.8	-0.2	-34.1	0.0
4L80	18.3	17.6	-172.6	-170.8
4L100	23.1	22.7	-239.0	-239.3
4L120	23.5	20.0	-243.9	-237.5
4L140	22.7	20.4	-232.2	-231.8
4L160	21.0	21.9	-238.2	-237.5
4L180	19.5	20.4	-240.8	-239.5
4L200	20.4	20.3	-239.8	-238.6

Table B. 26 – NSM_TR load cells responses of Serie L during CAA.

The Serie L presented similar transference of load at the top of the side columns (Figure B. 29a) up to nearly 150 mm of vertical deflection, which is the peak of CAA in the original model (Figure B. 29b). At the beam load cells the similarity was kept on the other models apart the original. Table B. 26 present the values of load cells readings for Serie L. The comparison, as in the Series of NSM_PR, are performed with the highest value of a pair of loads from load cells at the same position. At load cells LC1 and LC2 the maximum load transferred was 23.5 kN, in 4L120, and the minimum was 18.3 kN, in 4L80, i.e., 28% more load in the former. At LC3 and LC4 the load transferred had its peak also in 4L120, with a difference of 41% from the minimum, in 4L80.

Maximum dynamic response and DIF

The dynamic behaviour of Serie L can be found in Figure B. 30. One can see that the curves differ one to the other since the beginning and the peak in the load is increased. This peak is the maximum dynamic response and can be found in Table B. 27 as well as the correspondent deflections and DIF. The former is increased, in general, with the increment of the transmission length, where the highest value, 54 kN, achieved in 4L200, was 16% higher than the lowest, 46.4 kN, in 4L80. With different transmission lengths, the mean value was 117 mm and the standard deviation reached 15.4 mm. The DIF did not vary regularly between models, however around 1.25, with 0.03 of standard deviation.

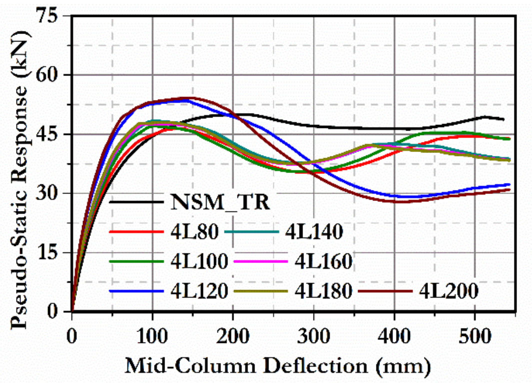

Figure B. 30 – NSM_TR Pseudo-static response of Serie L.

Specimen	Maximum Dynamic Response (kN)		Dynamic Increase Factor (DIF)
	Load (kN)	Deflection (mm)	
NSM_TR	50.0	206.8	1.16
4L80	46.4	137.4	1.21
4L100	47.1	104.1	1.26
4L120	53.4	131.1	1.23
4L140	48.3	106.9	1.25
4L160	47.6	92.9	1.28
4L180	48.0	115.7	1.28
4L200	54.0	131.1	1.26

Table B. 27 – NSM_TR Dynamic response of Serie L.

Ductility ratio

Specimen	Ductility ratio ($\Delta_{failure}/\Delta_{yield}$)
NSM_TR	5.12
4L80	4.61
4L100	3.30
4L120	4.46
4L140	3.40
4L160	2.85
4L180	3.94
4L200	4.81

Table B. 28 – NSM_TR Ductility ratios of Serie L.

Ductility ratios of Serie L presented values in general smaller than the original model, 4L80 (Table B. 28). The exception was 4L200, which achieved 4.81, being 69% higher than the minimum, presented in 4L160. Values of the ratios oscillated around 3.91, with a standard deviation equal to 0.69.

Failure modes

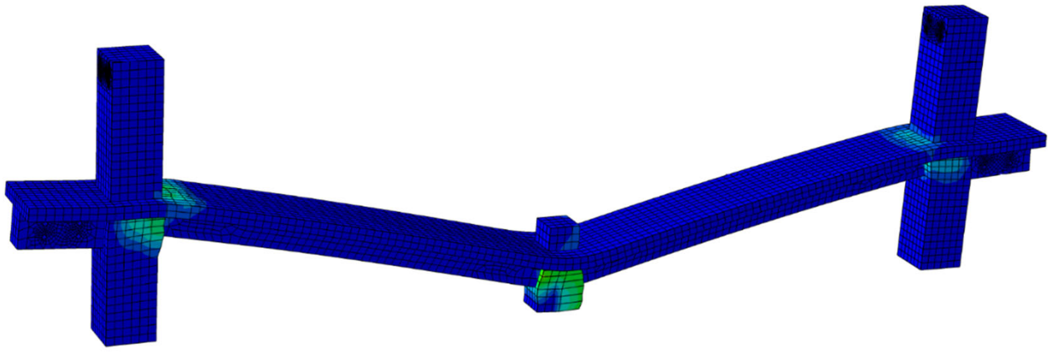

a)

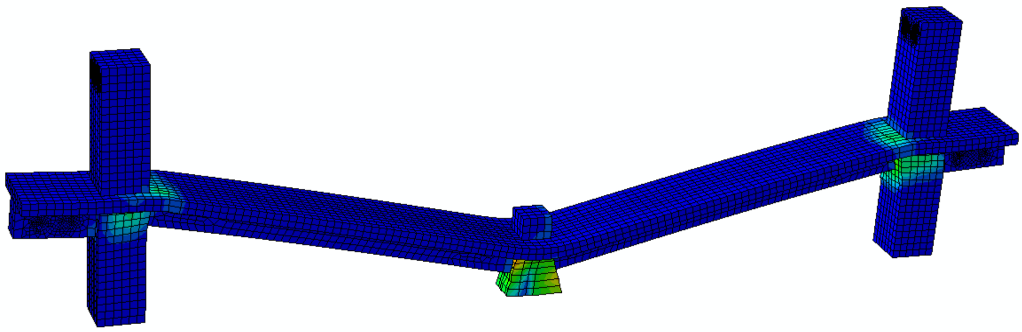

b)

Figure B. 31 – NSM_TR Failure modes of Serie L a) 4L80 b) 4L200.

Figure B. 31 presents the failure modes of models 4L80 (a) and 4L200 (b). As in the fully strengthened specimen TRM_TR it did not change significantly from one model to the other. This is due the improvement provided by the TRM along the beam which prevented shear and provided confinement to the concrete. The NSM reinforcement at the middle joint, increased the flexural resistance of the frame spreading the tension and preventing early crack formations. Moreover, because the NSM is continuous through the middle column, no concrete detachment occurred in this specimen. Nevertheless, there were small changes in the failure mode in this Serie, which are due the better anchorage of the steel inside the concrete. Given that only the plasticity of the concrete is being presented in Figure B. 31, the failures are presented with more intensity at the regions where the damage was more severe. The better anchored steel favoured more cracks formation when it was tensioned, and plasticity beyond side columns can be observed.

B.5.2 Mesh Size (Serie M)

Vertical 'Force vs Deflection' Response

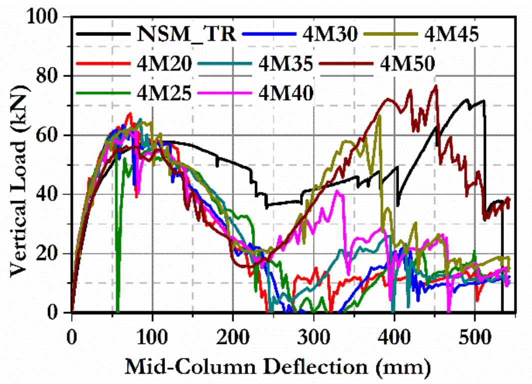

Figure B. 32 – NSM_TR 'Mid-Column Deflection vs Vertical Load' curves of Serie M.

Mesh Size	CAA		P_{MIN}		TCA	
	Load (kN)	Deflection (mm)	Load (kN)	Deflection (mm)	Load (kN)	Deflection (mm)
4M20	67.4	72.5	0.0	260.0	15.1	542.0
4M25	60.7	50.5	0.0	325.0	21.1	417.2
4M30	63.2	63.2	0.0	310.0	22.0	410.9
4M35	65.4	85.0	0.0	246.0	25.9	394.9
4M40	62.0	70.1	15.4	235.5	41.1	328.6
4M45	64.3	98.4	19.8	224.4	66.6	381.6
4M50	56.2	67.7	15.6	220.7	76.8	451.7

Table B. 29 – NSM_TR key points of Serie M.

The development of the resistant load with the vertical deflection of the simulations in Serie M can be seen in Figure B. 32. Major differences on the curves occurred since P_f and perdured up to the end of the simulations. In Table B. 29 one can see that the variation of load peaks during CAA reached 20%, where the maximum, 67.4 kN, was achieved in the simulation with smaller mesh size, and the minimum, 56.2 kN, at 4M50. The associated deflections did not vary regularly, where the major deflection occurred in 4M45 and the minimum in 4M25, representing a difference of 95%, with a mean of 72.5 mm and a standard deviation of 14.5 mm.

Load Cells Responses

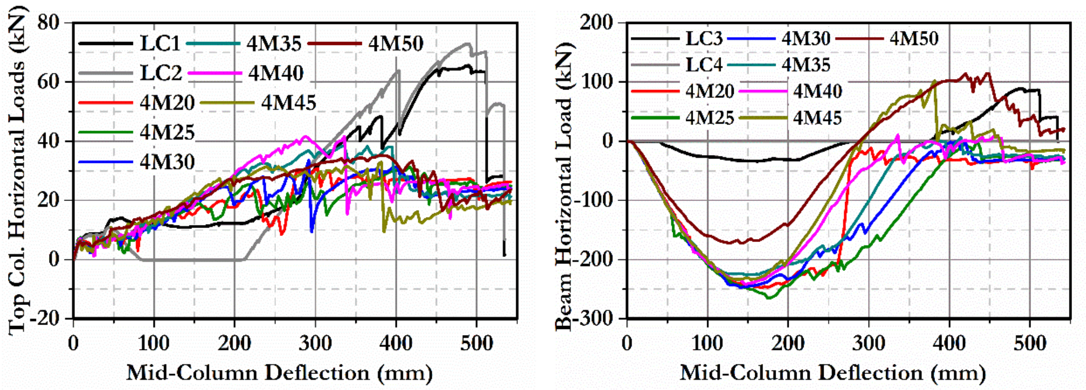

a) b)

Figure B. 33 – NSM_TR load cells responses on Serie M a) LC1 and LC2 b) LC3 and LC4.

Specimen	LC1 (kN)	LC2 (kN)	LC3 (kN)	LC4 (kN)
NSM_TR	11.8	-0.2	-34.1	0.0
4M20	17.6	16.6	-245.6	-242.6
4M25	18.9	16.7	-251.3	-248.2
4M30	16.4	20.9	-248.0	-246.0
4M35	20.7	20.2	-226.0	-228.0
4M40	17.5	19.3	-242.2	-245.0
4M45	21.9	22.0	-234.2	-234.4
4M50	18.3	17.6	-172.6	-170.8

Table B. 30 – NSM_TR load cells responses of Serie M during CAA.

The curves of transference of load at the top of the side columns and at the beam level with the vertical deflection from Serie M can be seen in Figure B. 33. At LC1 and LC2 the difference among mesh sizes plays major role at the TCA, while at the beam level it can be seen from the peak of CAA onward. Table B. 30 shows the values of the load cells readings in Serie M at the vertical deflection correspondent to the peak of load at CAA. At LC1 and LC2 values of transferred load oscillated reaching a maximum in 4M45, 22 kN, and a minimum in 4M20, 17.6 kN, meaning 25% of difference. At LC3 and LC4 this difference was 46% between 4M25 and 4M50 with 251.3 kN and 172.6 kN respectively.

Maximum dynamic response and DIF

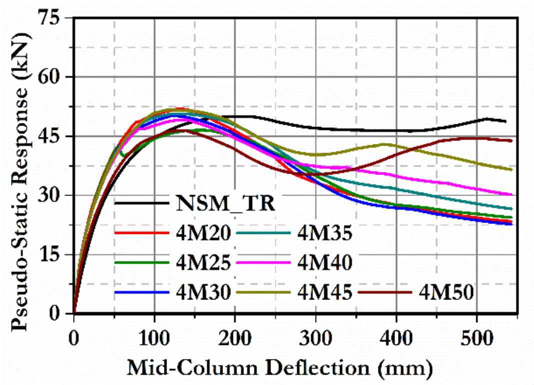

Figure B. 34 – NSM_TR Pseudo-static response of Serie M.

Specimen	Maximum Dynamic Response (kN)		Dynamic Increase Factor (DIF)
	Load (kN)	Deflection (mm)	
NSM_TR	50.0	206.8	1.16
4M20	51.9	131.1	1.30
4M25	46.5	157.1	1.30
4M30	50.2	124.8	1.26
4M35	50.6	131.1	1.29
4M40	49.1	137.4	1.26
4M45	51.7	118.7	1.24
4M50	46.4	137.4	1.21

Table B. 31 – NSM_TR Dynamic response of Serie M.

The pseudo-static response of the simulations in Serie M can be found in Figure B. 34. Differences on the evolution of the dynamic response can be seen from the beginning of the test. However, the major difference amongst maximum dynamic responses was 12%, between 4M20 and 4M50, where values did not evolve regularly with the increment of mesh size (Table B. 31). The associated deflections also evolved irregularly, with different mesh size, however with lower variation, 8.4% around the mean, 134 mm. The DIFs acquired from this Serie varied between 1.21 and 1.30 achieved in 4M50 and 4M20 respectively, where the mean and the standard deviation are 1.27 and 2.5 respectively.

Ductility ratio

Apart from model 4M45, all the other simulations presented higher values of ductility ratio compared to 4M50 (Table B. 32). The mean value of ratios was 5.12 with a standard deviation equal to 0.72. The highest ductility ratio was found in 4M25, being 54% higher than the minimum, registered in 4M45.

Specimen	**Ductility ratio ($\Delta_{failure}/\Delta_{yield}$)**
NSM_TR	5.12
4M20	4.62
4M25	6.69
4M30	4.91
4M35	5.27
4M40	5.37
4M45	4.34
4M50	4.61

Table B. 32 – NSM_TR Ductility ratios of Serie M.

Failure modes

The failure modes of models 4M20 and 4M50 are presented in Figure B. 35(a)-(b) respectively. Both figures show the same failure modes, however with a better representation in that with the model with finer mesh. As in the previous Series the main failure events did not change amongst models due the increased stiffness that the beam achieved with the presence of TRM and NSM. Therefore, the damages were directed to the beam/column interfaces.

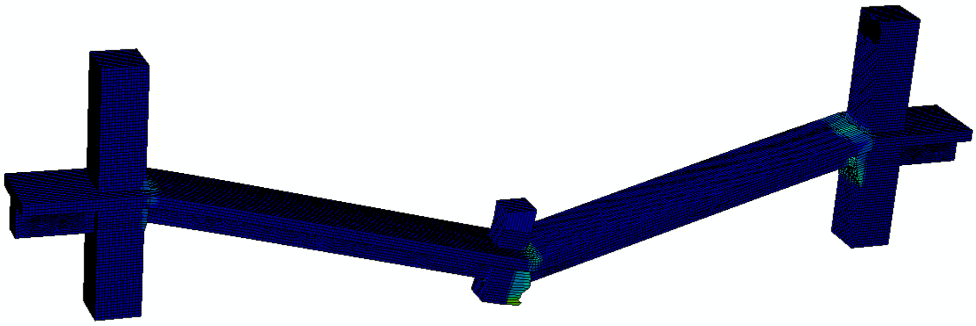

a)

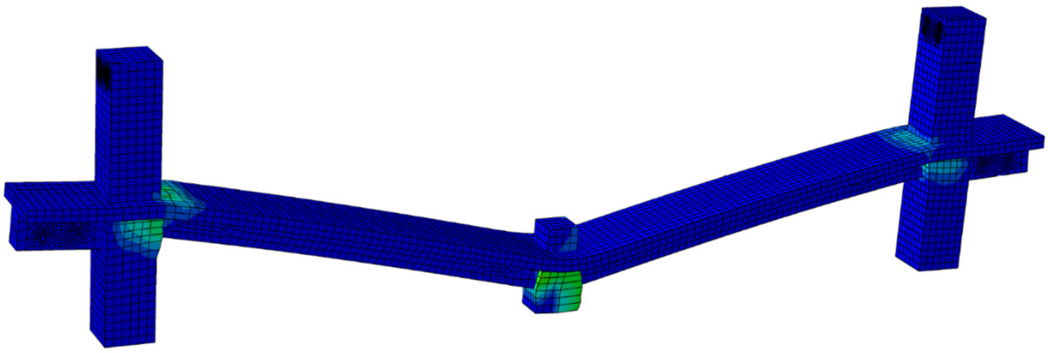

b)

Figure B. 35 – NSM_TR Failure modes of Serie M a) 4M20 b) 4M50.

B.5.3 Viscosity (Serie V)

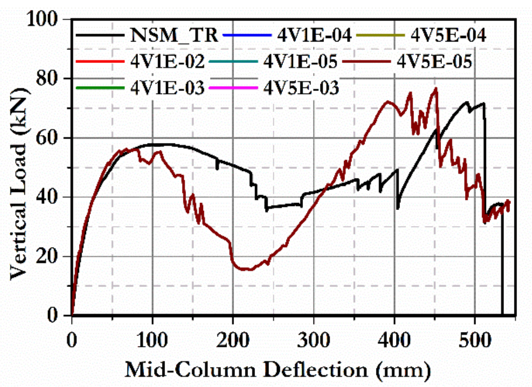

a)

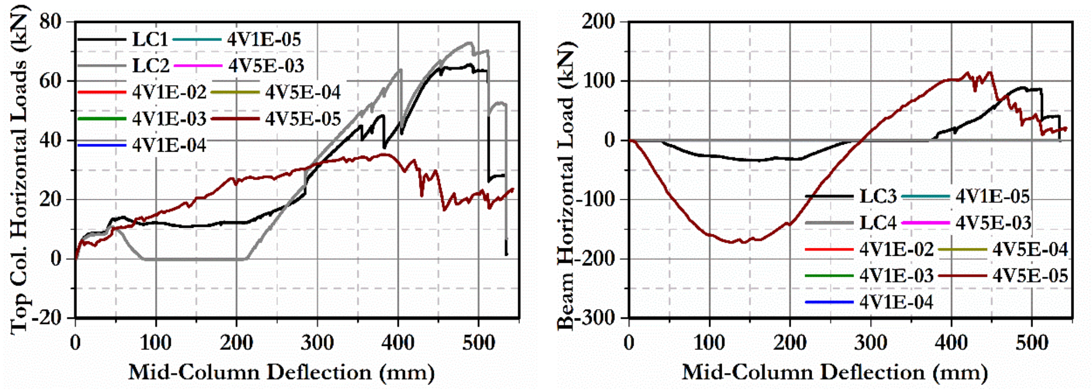

b) c)

Figure B. 36 – NSM_TR curves of Serie V a)'Mid-Column Deflection vs Vertical Load' b) LC1 and LC2 c) LC3 and LC4.

Serie V did not present any modification amongst simulations in NSM_TR as well. Figure B. 36(a)-(c) shows, respectively, the load-deflection, LC1-LC2 response, and LC3-LC4 response curves for this Serie.